A Search for Redshifted Absorption Lines at Radio Frequencies

by

Ting Yan

B.A., Nanjing University, 2003

M.S., Purple Mountain Observatory, Chinese Academy of Sciences, 2006

A thesis submitted to the

Faculty of the Graduate School of the

University of Colorado in partial fulfillment

of the requirements for the degree of

Doctor of Philosophy

Department of Astrophysical and Planetary Sciences

2013

This thesis entitled:
A Search for Redshifted Absorption Lines at Radio Frequencies
written by Ting Yan
has been approved for the Department of Astrophysical and Planetary Sciences

John T. Stocke

Jeremy Darling

John Bally

Erica Ellingson

Kyle McElroy

Date

The final copy of this thesis has been examined by the signatories, and we find that both the content and the form meet acceptable presentation standards of scholarly work in the above mentioned discipline.

Yan, Ting (Ph.D., Astrophysics)

A Search for Redshifted Absorption Lines at Radio Frequencies

Thesis directed by Prof. John T. Stocke

The purpose of this thesis is to conduct a survey to discover new H I and molecular absorption systems at radio frequencies at significant cosmological distances. While such systems offer significant advantages for studying molecular gas at high redshift, only 5 molecular absorbers are known, all at $z < 1$. Various attempts to find more have failed. Finding more such systems will help us study the physical properties of the gas out of which stars form in the early universe. A particularly important use of molecular absorbers is to test whether there is any variation in fundamental physical constants over cosmic time. Radio frequencies have significant advantage over optical frequencies for this purpose.

Because the host galaxies of radio-loud AGN are almost exclusively elliptical galaxies, which are low in neutral gas, we have selected a rare sample of 80 radio-loud AGN that have non-elliptical morphologies in the optical. These could be late-type galaxies, interacting systems or intervening galaxies well foreground to the radio source, all of which potentially have plenty of cold gas. We performed NIR photometry and confirmed that most of the objects are neither unobscured quasars nor elliptical galaxies. In fact, many have late-type galaxy SEDs in the optical and near-IR (NIR) requiring that the AGN are completely "buried" even in the NIR. We have also obtained sub-arc second (VLA and VLBA) radio maps that show that most of the radio sources are compact enough for high optical depth absorption lines to be present. This sample includes a substantial number of Compact Symmetric Objects (CSOs) and Medium-sized Symmetric Objects (MSOs), which are believed to be the "infant" stage of classic double-lobe radio galaxies.

Up to now, we have found 5 H I absorption systems at $z = 0.2$–0.9 but NO molecular absorbers. One of the detections is in an intervening system, and others are all associated absorption systems ($z_{\rm abs} = z_{\rm agn}$). We find a high detection rate among compact sources, especially CSOs, and

radio galaxies (instead of radio quasars). We demonstrate that the most promising candidates to find high-z HI absorbers are optical-faint/radio-loud AGN, for which it is not easy to obtain redshifts. Because "blind" searches are nearly impossible considering the severe radio frequency interference (RFI) at sub-GHz frequencies, the lack of accurate spectroscopic redshifts for these faint sources has proven to be a significant obstacle for this research.

Dedication

To my grandmother, whom I admire, love, and miss deeply.

Acknowledgements

Nothing in this thesis could have been made possible without the guidance of my advisor, Prof. John Stocke. His passion for observations and new discoveries always inspires me to question the facts and seek better answers from the data. I appreciate his patience and understanding when I sometimes spent to much time solving "small" problems rather than the "big" ones. And it gave me a precious opportunity to learn how to think independently and where to focus on. I would like to thank Prof. Jeremy Darling and our collaborators, Emmanuel Momjian and Nissim Kanekar, for their help. This thesis makes use of data obtained from various telescopes around the world. Many thanks to the hard work of all the instrumentalists, scientists, observing assistants, and staff who help us capture and decipher all those photons. Thanks to the diversity of research in CASA, I was able to get a great deal of local help as well, especially from Brain Keeney, Adam Ginsburg, Quyen Hart, and Kyle Willett. I am very grateful to Prof. Rosalba Perna for giving me an opportunity to work on a project about Neutron Stars with her.

Alongside my journey at CU, I also started a journey with my husband Jixia Dai, joined by our son Yian later on. Our journey at CU is finally coming to an end, but our life-long journey still has a lot ahead and I am excitedly looking forward to it. I am forever indebted to my parents. They gave me a life filled with love and set me an example of how valuable life could be. I am also grateful to Qian Yan, my dear brother and best friend. I am incredibly lucky getting to know Juthika Khargharia, Julia Hu, and Tina Zhao at Boulder. Thank you girls for be being there for me in good times and bad times. Lastly, I wish to express my deep gratitude to my grandmother, who never understood what's the point of counting stars (what she believed I was doing). Thank

you for your unconditional love and support, grandma, I'll learn to stay strong, nice, and wise no matter what happens just like what you always did.

My special thanks go to Dr. Elaine Hanson for the enlightening conversations we had in the past year.

Contents

Chapter

Tables

Table

Figures

Figure

Chapter 1

Introduction

The overall goal of this thesis is to find more atomic and molecular absorption systems at radio frequencies, especially these at intermediate to high redshift. The motivation for the search is driven by the potential of using these absorption systems to test whether fundamental physical constants change over cosmic time. In Section 1.1, we review the study of variations in fundamental physical constants, and show why the radio techniques are very promising. This thesis focuses its search on a unique sample of compact radio-loud AGN that are selected to be highly obscured. We review the basics of the unified schemes of AGN in Section 1.2 and compact radio-loud AGN in Sections 1.3. In Section 1.4, the physics of 21 cm lines is briefly discussed. Section 1.6 presents an overview of the thesis project.

1.1 Motivations

A fairly generic feature of most modern higher-dimensional theoretical models (such as Kaluza-Klein theories and superstring theories) is that fundamental constants such as the fine structure constant (α=$e^2/\hbar c$), the electron-proton mass ratio ($\mu \equiv m_{\rm e}/m_{\rm p}$), and the proton gyromagnetic ratio ($g_{\rm p}$), depend on the scale lengths of the extra dimensions of the theory. In the current theoretical framework, it is implausible that these scale lengths remain constant, implying that quantities such as α, μ, and $g_{\rm p}$ should vary with cosmic time. The detection of such changes provides an avenue to probe new and fundamental physics and may provide new constraints on the early evolution and origin of our Universe. Recent terrestrial measurements using atomic clocks

and isotopic abundances do not show any evidence of these time variations. Rosenband et al. (2008) have reported the tightest constraint of $\dot{\alpha}/\alpha = (-1.6 \pm 2.3) \times 10^{-17}$/year using Al^+ and Hg^+ single-ion optical clocks. Astrophysical methods enable us to investigate possible changes over much longer time scales, variations which are non-linear with time, and possible spatial variations. For example, the relative wavelength separation between two transitions of an alkali doublet is proportional to α^2 and has been used to obtain laboratory constraints on the variations of α decades ago (Savedoff 1956). This also can be exploited by measuring quasar absorption lines. As a generalization of the alkali doublet method, the many-multiplet method increases the accuracy of the measurement by utilizing different multiplets and different ions simultaneously (Webb et al. 1999). Using the alkali doublet method on 22 quasar absorbing systems and the many-multiplet method on 143 systems over the redshift range $0.2 < z < 3.7$, Murphy et al. (2003; see also Webb et al. 2011) claimed a detection of $\Delta\alpha/\alpha = (-5.4 \pm 1.2 \times 10^{-6})$. But this result has not been confirmed by others using the same method (Srianand et al. 2004; Chand et al. 2006). Reinhold et al. (2006) report a positive measurement of $\Delta\mu/\mu = 2.0 \pm 0.6 \times 10^{-5}$ using H_2 absorptions over $0 < z < 3$ (a few high-z QSOs contain UV absorption transitions of H_2 and CO thought to be due to cold halo gas like in the Milky Way; e.g., Noterdaeme et al. 2010, Srianand et al. 2008). However, each of these techniques contains many systematic uncertainties such as local velocity shifts between species, wavelength calibration, line blending and so on. Recently Griest et al. (2010) have made a detailed investigation of wavelength calibration techniques in use at the Keck 10m telescope (where the Webb et al. and Murphy et al. detections of $\Delta\alpha$ were obtained). These authors conclude that unexplained wavelength calibration shifts exist even on timescales as short as a few hours and that the ultimate causes of these shifts are not understood. While this analysis casts significant doubts on all of the suggested optical detections and non-detections described above, it does not provide a clear methodology to improve optical spectroscopic wavelength calibration to the level needed to obtain a definitive measurement. In general, optical slit spectroscopy of faint targets is not well-suited to observations requiring meter per second accuracies.

Therefore, a completely independent technique with totally different and hopefully fewer

systematic errors, is needed either to verify or challenge these detections of $\Delta\alpha/\alpha$ and $\Delta\mu/\mu$ made optically. Radio spectroscopy of highly-redshifted atomic and molecular absorption lines provides this independent method. Radio spectroscopy has the advantages of accurate frequency calibration, high spectral resolution and intrinsically narrow lines. Several promising methods have been employed including: comparisons between the H I 21 cm hyperfine line and molecular rotational lines (Carilli et al. 2000, Murphy et al. 2001); 18 cm OH main lines, used alone or compared with H I 21 cm line (Darling 2003; Kanekar et al. 2005; Kanekar et al. 2012); 18 cm OH satellite lines conjugate in emission and absorption (Kanekar et al. 2004; Darling 2004) for $\Delta\alpha/\alpha$; inversion transitions of ammonia (Flambaum & Kozlov 2007; Henkel et al. 2009; Kanekar 2011)), and molecular rotation lines (Wiklind & Combes 1999) for $\Delta\mu/\mu$. These methods have proved to provide comparable or better accuracy to the results from optical techniques based on currently known systems (e.g., the best limit to date is $\Delta\alpha/\alpha < 2.4 \times 10^{-6}$ at $z = 0.765$; Kanekar et al. 2012), but are limited mostly by the number and the redshift of the absorption systems. Unfortunately, the highest redshift radio molecular absorbers are at redshifts less than the redshifts where the many multiplet and H_2 techniques have been employed optically. Those techniques based on ultraviolet transitions can only be applied to higher redshift systems ($z > 1$) that are shifted into the optical wavebands. Therefore radio techniques provide complementary measurements at low redshifts as well as independent measurements at high redshifts. With the highest-z molecular absorber analyzed at $z = 0.765$ up to now, we can not categorically refute Murphy et al. (2003) detection of $\Delta\alpha/\alpha$.

Given the promise of these radio techniques, this thesis focuses on discovering new and higher redshift absorption systems. With this in mind it is worthwhile to consider the nature of the targets, radio-loud AGN.

1.2 Unified Schemes of AGN

Active Galactic Nuclei (AGN) are powered by super-massive black holes (SMBHs) in the centers of galaxies. The accretion onto SMBHs release immense amount of energy all across the

electromagnetic spectrum from radio frequencies to gamma rays. Observational properties vary significantly between AGN at all wavelengths in morphologies, luminosities, line properties, variability, etc. Geometric effects play an important but not singular role in determining the observational properties (Urry & Padovani 1995). The general consensus on the structure of AGN is as follows under the "unified schemes" (Fig. 1.1). The central SMBH is surrounded by an accretion disk which emits thermal light that peaks at the UV–optical wavelengths. Outside the disk, large amount of dust and gas form a torus that is much larger than the disk in width and height. On the rotation axis of the disk, two collimated jets propagate into opposite directions. Scattered clouds of cold gas can be photo-ionized by the radiation of the disk and give off strong emission lines. The clouds closer to the SMBH are revolving faster, so their emission lines have broader velocity dispersions.

Viewing at an angle close to the plane of the disk, observers see the synchrotron emission at radio frequencies from the jets, narrow emission lines in the optical/UV spectrum from the narrow line region, and the reprocessed disk light in the mid/far-infrared from the torus. The disk and broad line region are blocked by the torus, but their presence is sometimes revealed by polarized light scattered by materials above the torus. Viewing at an angle close to the jet axis, both the disk and the broad line region are exposed, and we see the UV-optical continuum and broad emission lines. Because of its relativistic speed, the jet is strongly boosted and exhibits super-luminal motions & boosted continuum luminosity to the observer when aligned with the line-of-sight.

Other than geometric effects, AGN are different intrinsically at the same time. For example, the radio emission is not always present. We call the AGN "radio loud" if the radio emission is strong, and "radio quiet" if weak or not seen. The dichotomy of radio-loud and radio-quiet AGN is not yet well understood. The presence of radio emission seems to be an important factor related to other properties of the AGN. For instance, the host galaxies of the radio-loud AGN are exclusively elliptical galaxies, while those of the radio-quiet AGN are more commonly spiral galaxies.

Different names have been used to represent the various aspects of observing properties of AGN (Fig. 1.1). If the nucleus outshines the host galaxy in the UV–optical wavelengths, we consider it a "quasar". Otherwise it's a "radio galaxy" or "Seyfert galaxy" depending on its radio loudness.

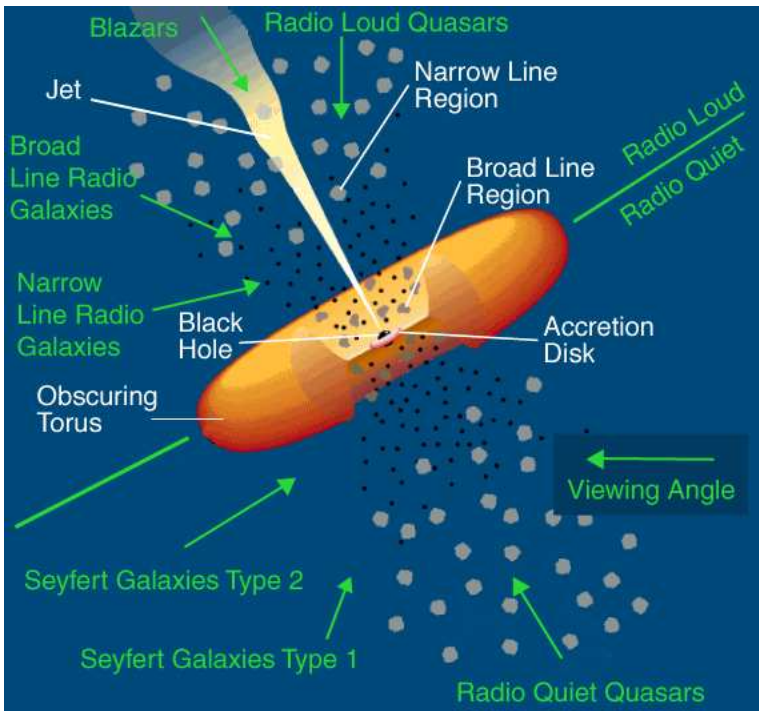

Figure 1.1 A schematic diagram of radio-loud and radio-quiet AGN. Major components of the AGN structure is labeled with white text. Arrows represent the viewing angles of the observer. The classification of AGN types from a certain viewing angle is shown in green text. Credit: reproduced from Urry & Padovani (1995) as modified by the Pierre Auger Cosmic Ray Observatory.

If both broad and narrow emission lines are present, it is called a "type 1" AGN, otherwise it's a "type 2" AGN if only narrow emission lines are seen. If the jet is oriented exactly on the line of sight, we will likely see a "blazar" which is very compact, variable and its spectrum is dominated by a relativistically-boosted non-thermal continuum.

1.3 Compact Radio-loud AGN

The jets of radio-loud AGN can penetrate through the interstellar medium and advance well beyond their host galaxies. Diffuse lobes are formed as the result of interactions between jets and ambient gas. The relative brightness of jets and lobes are related to the radio luminosity of the object (Fanaroff & Riley 1974, FR hereafter). The surface brightness of weak radio objects generally decreases outward from jets to lobes. In contrast, powerful objects often have brighter lobes that are edge-brightened with so-called hotspots which represent the "working fronts" of the jets. Objects with the former morphology are considered "Class I" or FR-I, while the latter "Class II" or FR-II. Meanwhile, many of the compact objects have a core-jet morphology which consists of a bright core and a one-sided jet, consistent with being viewed along the orientation of the jet. To discriminate from the core-jet objects, we call a radio-loud AGN a Symmetric Object (SO) when both sides of it radio emission is detected. Note that "Symmetric" here does not mean the morphology and brightness are exactly the same but rather that the overall radio structure is not core-jet by containing two lobes.

However, beside core-jet objects, a large fraction of compact objects resemble the large scale SOs in morphology except that they are confined within the host galaxies (Phillips & Mutel 1982; Fanti et al. 1990). We adopt the terminology introduced by Fanti et al. (1995) to indicate a size of > 15 kpc, 15 kpc – 1 kpc, and < 1 kpc with the terms Large Symmetric Object (LSO), Medium-size Symmetric Object (MSO), and Compact Symmetric Object (CSO) respectively. In general, 1 kpc is considered a typical size of the narrow-line emission regions, and 15 kpc represents a typical size of the optical host galaxies.

It has been debated whether CSOs and MSOs are young LSOs that have not fully evolved,

or "frustrated" LSOs that are stopped from expanding by dense medium but are as old as LSOs. Observations now prefer the former, i.e., the youth scenario. Firstly, the hotspot advance speeds have been detected in some CSOs (Owsianik & Conway 1998; Gugliucci et al. 2005) and these are sub-luminal (unlike core-jet objects). Kinetic ages are around 10^3–10^4 yr derived from the speed measurements. Secondly, constraints from spectral ages are consistent with kinetic ages (Readhead et al. 1996). Lastly, there is no direct evidence of enough dense gas required to confine the majority of CSOs and MSOs (O'Dea 1998).

The study of CSOs and MSOs is not only important to reveal the evolutionary track of radio-loud AGN, but can also be very helpful to probe the gas content of their host galaxies thanks to their small sizes. In addition, increasing evidence has shown that AGN and their host galaxies co-evolve, so CSOs and MSOs might disclose the link between the central engine and the galactic environment.

1.4 The H I 21 cm line

The ground state of H I is split into two energy levels due to the interaction between the electron spin and proton spin. The spins are either parallel or anti-parallel. The parallel state has higher energy than the anti-parallel state. The energy difference is 5.9 μeV, which corresponds to a wavelength of 21 cm or a frequency of 1420 MHz. The 21 cm line is highly forbidden with a probability of $A_{10} = 2.9 \times 10^{-15}$ s^{-1}, which gives an extremely small critical density of $n_{cr} = A_{10}/C_{10} \sim 3 \times 10^{-5}$ cm^{-3}, where the collisional de-excitation rate $C_{10} \approx \sigma v = 10^{-10}$ cm^3 s^{-1} assuming a thermal velocity v of 100 km s^{-1} and a cross section σ of 10^{-17} cm^{-2} for collisions. However, the 21 cm transition is not necessarily in local thermal equilibrium when the number density $n_{\rm HI} \gg n_{cr}$, for example, due to the cosmic ray background. We define a spin temperature T_s

$$\frac{n_1}{n_0} = \frac{g_1}{g_0} \exp\left(-\frac{h\nu}{kT_s}\right), \tag{1.1}$$

where n_1 and n_0 are the number densities of the upper and lower states, and the statistical weights are $g_1 = 3$ and $g_0 = 1$ for the two states. In local thermal equilibrium, T_s is the same as the kinetic temperature. Because of the small energy difference of the transition, 5.9 μeV or 0.068 K, $h\nu/kT_s \ll 1$, so $n_1 = 3n_0$ and $n_{\rm HI} = n_1 + n_0 = 4n_0$.

H I gas was first detected in emission lines in the disk of the Milky Way (Ewen & Purcell 1951; Muller & Oort 1951) and then in nearby spiral galaxies. The column density can be inferred from these lines by

$$N_{\rm HI} = 1.83 \times 10^{18} \int \left(\frac{T_b}{\rm K}\right) \frac{\tau}{1 - e^{-\tau}} \, {\rm d}\left(\frac{v}{\rm km\ s^{-1}}\right) \ {\rm cm^{-2}}, \tag{1.2}$$

where T_b is the brightness temperature of the emission line and τ is the optical depth at radial velocity v. In optically thin gas, $\tau/(1 - e^{-\tau}) \approx 1$, so the column density is independent of T_s. The flux density S is an integration of T_b over the solid angle of the source

$$S = \frac{2\nu^2 k}{c^2} \int T_b \, {\rm d}\Omega. \tag{1.3}$$

When the H I gas is optically thin, the mass can be estimated from

$$M_{\rm HI} = 2.36 \times 10^5 \left(\frac{D}{\rm Mpc}\right)^2 \int \left(\frac{S}{\rm Jy}\right) {\rm d}\left(\frac{v}{\rm km\ s^{-1}}\right) \ M_\odot, \tag{1.4}$$

where D is the distance of the gas. Because $S \sim D^{-2}$, the detectability decreases rapidly with increasing distance. Emission lines are hardly detected beyond the local universe under the sensitivity of current radio instruments.

For absorption lines, when a flux density of $S_{\rm abs}$ is absorbed over the path through the absorbing gas which blocks a continuum $S_{\rm con}$ in the background, the optical depth is $\tau \equiv -\ln(1 - S_{\rm abs}/S_{\rm con})$ or $\tau \cong S_{\rm abs}/S_{\rm con}$ if the gas is optically thin ($\tau \lesssim 0.1$). A covering factor f has to be considered because the foreground absorber does not necessarily cover the entire background structure. The H I column density of the absorbing gas is

$$N_{\rm HI} = 1.83 \times 10^{18} \left(\frac{1}{f}\right) \left(\frac{T_s}{\rm K}\right) \int \tau \, {\rm d}\left(\frac{v}{\rm km\ s^{-1}}\right) \ {\rm cm^{-2}}. \tag{1.5}$$

The absorbed flux density $S_{\rm abs}$ is distance independent, i.e., the same gas can be detected in absorption lines regardless how far it is given the same background flux density. Therefore, the 21 cm absorption lines are excellent for studying neutral gas at high redshift if suitable background sources can be found. So far about 80 absorbers have been detected at $z > 0.1$ with about half in intervening systems and half in associated systems.

1.5 OH 18 cm Lines

We are particularly interested in finding radio hydroxyl radical (OH) lines because they provide a precise method to estimate changes in α, μ, and $g_{\rm p}$ with reduced systematic errors (Chengalur & Kanekar 2003; Darling 2003; Kanekar et al. 2004). Each rotation state of OH is split into four energy levels (Figure 1.2). First, the interaction between the electron spin and molecular rotation results in Λ-doubling (even parity Λ^+ and odd parity Λ^-). Second, each of the two Λ levels are further split into two levels due to the hyperfine effect. The transition between the two Λ levels forms four lines, two main lines with $\Delta F = 0$ and two satellite lines with $\Delta F = \pm 1$. For the ground state of OH, $^2\Pi_{3/2} J = 3/2$, the main lines are at 1665 MHz and 1667 MHz, while the satellite lines are at 1612 MHz and 1720 MHz.

Under certain circumstances, the $F = 2$ levels or the $F = 1$ levels can be overpopulated and produce conjugate satellite lines, one in emission and one in absorption (Elitzur 1992). The population inversion is caused by the decay from upper rotation levels. For example, if the 120 μ m intra-ladder transition from $^2\Pi_{3/2} J = 5/2$ $(F = 3, 2)$ to $J = 3/2$ $(F = 2, 1)$ dominates, the $F = 2$ levels are overpopulated relative to the $F = 1$ levels due to the selection rule $\Delta F = 0, \pm 1$. The 1720 MHz transition from $\Lambda^+, F = 2$ to $\Lambda^-, F = 1$ is thus seen in emission, while the 1612 MHz transition from $\Lambda^-, F = 2$ to $\Lambda^+, F = 1$ is seen in absorption. On the contrary, when the 79 μm cross-ladder transition from $^2\Pi_{1/2} J = 1/2$ $(F = 1, 0)$ to $^2\Pi_{3/2} J = 3/2$ $(F = 2, 1)$ dominates, the 1612 MHz line is in emission while the 1720 MHz line is in absorption. Which route is more important depends on the physical conditions including the density, temperature, and radiation field. When the pumping line is optically thick, the emission and absorption lines show exactly the

same profile. If the satellite lines are exactly conjugate, it is certain that they originate from the same gas, which is ideal for measuring fundamental physical constants because the uncertainty in relative motions between different species or gas components is a severe problem for other methods.

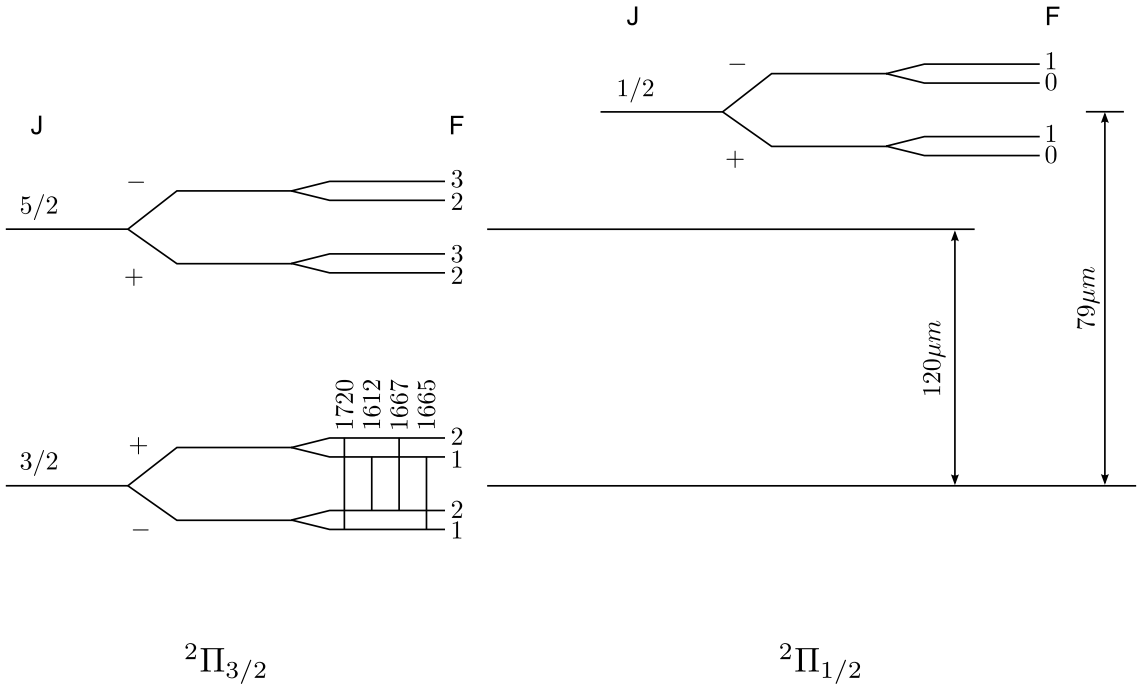

Figure 1.2 The lowest energy levels of the OH molecule. The ground electronic state of OH has two rotational ladders, $^2\Pi_{3/2}$ and $^2\Pi_{1/2}$. Each rotational state is split into four sub-levels due to Λ-doubling and hyperfine splitting.

Conjugate OH satellite lines have been observed toward several extragalactic targets: NGC 4945 (Whiteoak & Gardner 1975), Cen A (van Langevelde et al. 1995), M82 (Seaquist et al. 1997), and NGC 253 (Frayer et al. 1998) in the local universe; PKS 1413+135 ($z = 0.247$, Darling 2004; Kanekar et al. 2004) and PMN J0134−0931 ($z = 0.765$, Kanekar et al. 2005, 2012) at cosmological distances. Cen A, NGC 253, and PKS 1413+135 have perfectly conjugate satellite lines. Unfortunately, in PMN J0134−0931 with the highest redshift, the two lines differ in both strength and shape (Kanekar et al. 2012).

1.6 Thesis Prospectives

In this thesis, we engage in a discovery program for bright background radio sources that are suitable for radio absorption line searches. But suitable sources are hard to find since the absorption we are seeking to detect also absorbs and reddens the AGN continuum. Thus a sample of candidates must be selected carefully. In contrast to previous samples selected at radio frequencies, a unique sample was selected at both radio and optical frequencies to have not only high radio luminosities but also optical obscuration. In this thesis, we study the properties of this sample through multi-wavelength observations and search for absorption lines in the sample.

In Chapter 2, we describe the selection criteria of the sample, present the Near-IR photometry, and study the optical-NIR SEDs. It is found in the optical-NIR SEDs that the majority of the sample are indeed highly-obscured. Because of the large obscuration, this sample is inevitably faint in the optical-NIR and lacks spectroscopic redshifts. Since photometric redshifts are not accurate enough for the radio line searches due to RFI, optical-NIR spectroscopy has also been obtained for some of the bright ones to determine spectroscopic redshifts (Chapter 2). Chapter 3 includes high-resolution VLA and Very Long Baseline Array (VLBA) radio images of these sources to identify those sources containing very compact structures and to identify sources which have radio/optical-NIR position offsets indicative of foreground, not associated absorption. The unique selection criteria prove to be very efficient in selecting compact radio galaxies. A first round of H I 21 cm absorption observations from this sample is presented in Chapter 4. Up to now, 5 H I absorbers have been detected, which yields a high detection rate compared to previous samples. We have also found that the absorbing gas has higher column densities in our sample, again supporting the high obscuration rate. However, no OH lines have been detected so far, though not searched intensively. We summarize the thesis and discuss future work in Chapter 5. We will continue the line searches and studies of this sample. Inspired by the successful selection of this sample, we have selected two new samples, one with higher-z candidates, the other with younger candidates. In Appendix A, optical–NIR images and SEDs are presented for the entire sample including SDSS

3-color composite images, J-band images, K-band images, and u-g-r-i-z-J-H-K-band SEDs. Radio images are presented in Appendix B for the ones observed or reduced by us at VLA-A 4.9 GHz, VLA-A 8.5 GHz, and VLBA 1.4 GHz. For other objects, references can be found for published images in Table 3.1.

The sample was selected originally by Fred Hearty in his thesis project, who also contributed some few Near-IR photometric observations in 2006 and 2007. The observations were conducted by Ting Yan (TY) in Chapter 2, and by Jeremy Darling & TY in Chapters 3 & 4. The data reduction and analysis were mostly carried out by TY. The confirming VLA and GMRT absorption studies were carried out by Emmanuel Momjian and Nissim Kanekar respectively. The content in Chapter 2 was published in the Astronomical Journal, Volume 144, Issue 4. The content in Chapters 3 and 4 will be submitted for publication soon (Fall 2013).

Throughout this thesis, we assume a ΛCDM cosmology with $H_0 = 71$ km s^{-1} Mpc^{-1}, $\Omega_\Lambda = 0.73$, and $\Omega_\mathrm{M} = 0.27$.

Chapter 2

Sample Selection and Near-Infrared Photometry

Previously published in a slightly different version as: Yan, T., Stocke, J. T., Darling, J., & Hearty, F., Invisible Active Galactic Nuclei. I. Sample Selection and Optical/Near-IR Spectral Energy Distributions, 2012, AJ, 144, 124. The GMOS spectra (see Table 2.3 and Figure 2.3) and Near-IR images for the full sample (see Appendix A) are not presented in the published version.

In order to find more examples of the elusive high-redshift molecular absorbers, we have embarked on a systematic discovery program for highly obscured, radio-loud AGN using the VLA Faint Images of the Radio Sky at Twenty centimeters (FIRST) radio survey in conjunction with Sloan Digital Sky Survey (SDSS) to identify 80 strong ($\geq$ 300 mJy) radio sources positionally coincident with late-type, presumably gas-rich galaxies. In this chapter, the basic properties of this sample are described including the selection process and the analysis of the spectral-energy-distributions (SEDs) derived from the optical (SDSS) + near-IR (NIR) photometry obtained by us at the Apache Point Observatory 3.5m. The NIR images confirm the late-type galaxy morphologies found by SDSS for these sources in all but a few cases. Among 80 sources in the sample, 39 show galaxy type SEDs, 17 have galaxy components to their SEDs, 8 have quasar power-law continua, and 16 are significantly reddened quasars. At least 9 sources with galaxy SEDs have K-band flux densities too faint to be giant ellipticals if placed at their photometric redshifts. Photometric redshifts for this sample are analyzed and found to be too inaccurate for an efficient radio-frequency absorption line search; spectroscopic redshifts are required. A few new spectroscopic redshifts for these sources are presented here but more will be needed to make significant progress in this field.

2.1 Introduction

While most strong radio sources are identified with luminous elliptical galaxies or optical/UV point sources (quasars), a small number of these sources lie behind obscuring screens of gas and dust becoming invisible to us at optical/UV and possibly also at near-IR wavelengths. Identifying highly obscured, "invisible AGN" can lead to the detection and study of highly-redshifted radio-frequency atomic and molecular absorption line systems, which can provide important information about the early universe unobtainable in other ways. Radio absorption lines provide unparalleled velocity resolution and detailed physical diagnostics. And, where the background radio source is spatially-resolved, very-long baseline interferometry maps in the H I absorption line can provide the best spatial resolution ($\sim$ 10 pc at z=1–2) of the gas distribution in distant galaxies; magnetic field structures also can be mapped using Faraday rotation measures of a polarized background source (Gaensler 2007), or using Zeeman splitting in the 21 cm line itself in the future. Atomic plus molecular absorption can provide much additional information. First, molecules trace the gas that supplies star formation so that the strengths and ratios of their absorption lines can be used to determine the physical conditions (e.g., temperature, pressure, density, chemical abundance and magnetic field strength) of the locations where most stars have formed over cosmic time. Second, the combination of various H I and molecular absorption/emission lines makes it possible to probe whether and by how much dimensionless fundamental physical constants have changed as the universe evolves.

So far there are about 80 H I 21 cm absorbers detected at $z > 0.1$. Only five of them are molecular absorbers[1]. The first system, PKS 1413+135, was detected in H I absorption in 1992 at $z = 0.25$ (Carilli et al. 1992), in CO absorption in 1994 1994 and subsequently in nearly a dozen species 1994. This source is a BL Lac object residing in an edge-on spiral galaxy and the nucleus is highly obscured ($A_V > 20$; Stocke et al. 1992; Carilli et al. 1992). Then B3 1504+377 was found at $z = 0.67$ (Wiklind & Combes 1996a), which is also an intrinsic molecular absorption system. The other three molecular absorbers are all in gravitational lens systems: B0218+357 at $z_{em} = 0.94$

with the lensing object at $z_{\rm abs} = 0.69$ (Wiklind & Combes 1995, Menten & Reid 1996, Gerin et al. 1997), PKS 1830-211 at $z_{\rm em} = 2.5$ with the lensing object at $z_{\rm abs} = 0.89$ (Wiklind & Combes 1996b) and PMN J0134-0931 at $z_{\rm em} = 2.2$ with the lensing object at $z_{\rm abs} = 0.77$ (Kanekar et al. 2005, 2012). OH lines are detected in all five systems but only two have conjugate OH molecular absorption/emission lines (PKS 1413+135, Darling 2004, Kanekar et al. 2004; PMN J0134-0931, Kanekar et al. 2012) important for fundamental constants work (Darling 2003).

Although "blind" searches of samples of strong radio sources have been undertaken to find molecular absorption, mostly they have led to negative results, although a few new H I 21 cm absorbers have been found (Curran et al. 2011b; Gupta et al. 2009). Some of the unsuccessful surveys for high-z molecular absorbers include: millimeter observations of strong sources with known redshifts (Willett, Kanekar, & Carilli, private communication), cm- and m-wave observations of reddened quasars and radio galaxies, sources with damped Lyα absorbers, and type-2 quasars, etc. (Curran et al. 2006; Curran & Whiting 2010; Curran et al. 2011b). While a few new H I 21 cm absorbers have been discovered, no new molecular absorbers have been discovered in these searches. This suggests both that high-z molecular absorbers are very rare and that rather standard techniques cannot be used to discover molecular absorbers (e.g., searches using samples containing damped Ly α absorbers; Gupta et al. 2009); i.e., the obscuration we are trying to find significantly absorbs and reddens the quasar optical-UV continuum so that it is not detectable in most cases. Thus, optically-bright quasars are not a good sample to use to search for radio-frequency molecular absorption (Curran et al. 2008, 2011a).

With the overall goal of discovering new examples of high-z molecular absorbers, we have embarked on an extensive discovery program using a new selection method devised specifically for this task. In this chapter we describe the first steps towards the ultimate goal of discovering a substantial sample of high-z radio absorption line systems. In Section 2.2 we describe this new

[1] In this thesis molecular absorption refers to the multitude of species seen in the radio-frequency spectra of giant molecular clouds, not the UV absorption transitions of H_2 and CO absorption arising in cool halo gas probed by far-UV spectroscopy in the Milky Way and high-z QSO spectra of intervening galaxies (Noterdaeme et al. 2010; Srianand et al. 2008).

selection method which combines Very Large Array (VLA) Faint Images of the Radio Sky at Twenty centimeters (FIRST; Becker et al. 1995) radio source detections with Sloan Digital Sky Survey (SDSS; York et al. 2000) photometry and morphologies for the coincident galaxies designed to select strong radio sources which are associated with late-type galaxies. In Section 2.3 we describe new broad-band near-IR (NIR) imaging of this sample obtained by us at the Apache Point Observatory's 3.5m telescope (APO hereafter) which allows us to search for nuclear point sources which are obscured optically and to extend the spectral energy distributions (SEDs) of these sources from the SDSS optical photometry to longer wavelengths. The analysis of the NIR images and of the optical/NIR SEDs is described in Section 2.4. A few new spectroscopic redshifts obtained in the progress of this work are also reported in this Section. Individual results for some representative and also unusual objects are presented in Section 2.5 and candidates for finding atomic and molecular absorption are identified. We conclude with a summary of the observational results and discuss the future work using our on-going survey in Section 2.6.

2.2 Sample Selection

2.2.1 Background

The host galaxies of radio-loud AGN are almost exclusively giant ellipticals (e.g. Urry & Padovani 1995, McLeod 2006). This is true for all the subclasses of radio-louds including quasars, FRI and II type radio galaxies and BL Lac Objects. While we might generically expect radio sources associated with a spiral or irregular host galaxy or with a merger to possess foreground absorption, their occurrence is extremely rare. But recent large surveys allow us to find rare objects that do not obey the general tendency for radio-loud AGN to be hosted by giant ellipticals for specific reasons. For example, Wilson & Colbert (1995) have suggested that the origin of radio-loud AGN is in the merger of two supermassive Black Holes (SMBHs) when two disk systems merge to form an elliptical galaxy (Mihos & Hernquist 1996). If the Wilson & Colbert (1995) scenario is correct, the merger of the SMBHs first creates a luminous but small-scale ($\sim$ 1kpc) radio-loud AGN termed a "Compact

Symmetric Object" (CSO; Begelman 1996; Perlman et al. 2001) which can then evolve into a large-scale classical double through subsequent outbursts. And if the CSO forms quite quickly after the merger, it can be accompanied by remnant gas and dust from the merger (Willett et al. 2010). This circumstance can cause the galaxy's optical morphology to appear distorted and provide gas for foreground absorption at the same time. Indeed, some CSOs have disturbed optical morphologies (Perlman et al. 2001) and a high fraction ($\sim$ 20–40%) of compact radio sources including CSOs have H I absorption in their radio spectra (van Gorkom et al. 1989; Vermeulen et al. 2003; Gupta et al. 2006; Chandola et al. 2011; but see Curran & Whiting 2010). PKS 1413+135, the first molecular absorber detected, is also a CSO (Perlman et al. 1996) with intrinsic absorption.

Besides the two intrinsic molecular absorbers, known gravitational lenses have provided 3 other known molecular absorbers, B2 0218+357, PKS 1830-211 and PMN J0134-0934. Gravitational lenses possess unusual optical morphology due both to their multiple images and to the presence of a foreground galaxy. It is also possible that a foreground, gas-rich galaxy can produce atomic and/or molecular absorption even without producing multiple images (Narayan & Schneider 1990). Again, a correlation between unusual optical morphology and foreground absorption can result, although in this case the absorbing gas is external to the AGN and its host.

Another rare class of radio-loud AGN which possesses unusual optical morphology is the so-called "alignment effect" radio galaxy (2 known examples are in our sample) in which UV emission lines from the gas surrounding the radio jets are redshifted to the optical and are responsible for a non-elliptical morphology in certain wavebands (e.g., Zirm et al. 2003). This circumstance has not led to the discovery of molecular absorbers, probably due to the very extended radio source structure required to create the "alignment effect". On the other hand, the first two classes described above often include radio sources with compact radio structure. Compact structure facilitates the detection of atomic and molecular absorption because the absorption detection does not get diluted by flux which does not go through the absorbing gas (see Chapter 3).

2.2.2 The Radio-loud Late-type Galaxy Sample

The 1.4 GHz VLA FIRST survey covers over 9,000 square degrees of the North and South Galactic Caps. FIRST has a typical flux density rms of 0.15 mJy, and a resolution of 5″. The Data Release 5 (DR5) of SDSS covers about 8,000 square degrees of almost exactly the same area of the sky as FIRST. This field includes approximately 1500 FIRST sources with flux densities > 300 mJy. Among these sources, 808 are associated with SDSS sources, i.e., one or more optical objects are detected within 1.″5 of the radio centroid; thus, it is possible that some of the associated SDSS sources are **not** the AGN host galaxy. Excluding 467 sources classified as stars which might actually be QSOs, 341 are probably the host galaxies of the radio sources. Note that star-galaxy separation is robust down to $r \sim 21.5$ mag in the SDSS (Lupton et al. 2001). To select non-elliptical galaxies, two standards are used. The first is that the best-fit of the radial profile is exponential (typical for spiral galaxies) rather than De Vaucouleurs (typical for elliptical galaxies; 94 sources). The other is that the core compactness parameter[2] is smaller than 2.6 (also typical for spiral galaxies; 200 sources). These two criteria also eliminate quasars and point-source (AGN) dominated galaxies as well. The combination of the two standards makes the selection fairly reliable (Strateva et al. 2001) but there could still be some mis-classified cases. All SDSS classifications employed the i-band images (rest-frame g-band at the median photometric redshift of the sample, $z \approx 0.6$), which typically have the highest signal-to-noise images for our sample.

Overall, 82 objects in SDSS DR5 meet both these criteria (see Table 2.1). Two nearby galaxies are excluded because their intrinsic radio luminosities are much lesser than typical radio-loud AGN (J1413−0312 = NGC 5506 and J1352+3126 = UGC 8782). None of these sources has more than one optical counterpart, although the possibility remains that some of the optical sources are actually merged images of two or more galaxies. Because we were interested in obtaining a representative sample of these rare AGN, we did not conduct any completeness tests for this sample, nor did we obtain a new sample using later SDSS data releases. Our sample selection is demonstrably

[2] The ratio of the Petrosian radii containing 90% and 50% of the galaxy light. Same as the the concentration index defined in (Strateva et al. 2001).

successful because all the three possible situations mentioned above have a few known examples in the sample. PKS 1413+135 (J1415+1320) is the first discovered high-z molecular absorber and a CSO. B2 0748+27 (J0751+2716) is a gravitational lens (Lehar et al. 1997). And 4C +23.27 (J1120+2327, @ z=1.819) is the well-known "alignment effect" radio galaxy 3C 256 (Zirm et al. 2003) just mentioned. There are a couple of other known CSOs and Compact Steep Spectrum Sources (CSSs; slightly larger in physical extent of 1–20 kpc but similar to CSOs; de Vries et al. 1998) present and more have been found in the course of this work (Chapter 3). A few host galaxies appear to be merging with another galaxy.

The full list of all 80 sources in our sample is found in Table 2.1. This Table includes by columns: (1) coordinate style designation for the source which is used in this thesis; (2) the commonly used radio source name for the source; (3) the 20 cm continuum flux density from FIRST in Jy; (4) the associated SDSS name for the optical counterpart which also provides an accurate (RA,DEC) centroid position; (5) the SDSS r-band "model magnitude" and its associated error (Stoughton et al. 2002), which results from an extrapolation of the best-fit (for this sample) exponential radial profile; (6) the photometric redshift and error from Data Release 8 (DR8) using an empirical method called "kd-tree nearest neighbor fit" (Csabai et al. 2007); and (7) the spectroscopic redshift where available. The spectroscopic redshifts come from references in the NASA/NED database except for the cases noted with an asterisk; these new spectroscopic redshifts were obtained by us and are described in Section 2.3.

Table 2.1. Basic Source Data.

Object	Radio Name	$F_{20\mathrm{cm}}$ (Jy)	SDSS Name	SDSS r	SDSS z_{phot}	z_{spec}[a]
J0000−1054	PKS 2358−111	0.40	J000057.65−105432.1	22.01 ± 0.18	0.37 ± 0.14	
J0003−1053	PKS 0001−111	0.40	J000356.30−105302.4	21.70 ± 0.15	0.57 ± 0.12	1.474*
J0134+0003	4C −00.11	0.89	J013412.70+000345.2	22.74 ± 0.16	0.77 ± 0.12	0.879
J0249−0759	PKS 0247−08	0.62	J024935.38−075921.2	21.63 ± 0.15	0.41 ± 0.16	
J0736+2954	TXS 0733+300	0.49	J073613.67+295422.2	22.49 ± 0.17	0.09 ± 0.05	
J0747+4618	4C +46.16	0.52	J074743.57+461857.7	21.38 ± 0.07	0.19 ± 0.06	2.926
J0749+2129	TXS 0746+216	0.42	J074948.75+212932.9	20.94 ± 0.08	0.46 ± 0.01	
J0751+2716	B2 0748+27	0.60	J075141.51+271631.7	22.23 ± 0.13	0.72 ± 0.22	0.349[b]
J0759+5312	TXS 0755+533	0.33	J075906.52+531247.8	21.75 ± 0.09	0.64 ± 0.24	
J0805+1614	PKS 0802+16	0.63	J080502.18+161404.9	20.54 ± 0.06	0.54 ± 0.12	0.632:*
J0807+5327	TXS 0803+536	0.33	J080740.73+532739.8	20.48 ± 0.04	0.30 ± 0.12	
J0824+5413	TXS 0820+543	0.39	J082425.46+541349.0	19.95 ± 0.05	0.46 ± 0.12	0.639*
J0834+1700	4C +17.45	1.64	J083448.22+170042.4	22.01 ± 0.14	0.27 ± 0.15	
J0839+2403	4C +24.18	0.66	J083957.90+240311.4	21.15 ± 0.09	0.79 ± 0.17	
J0843+4215	B3 0840+424A	1.46	J084331.63+421529.4	21.39 ± 0.14	0.42 ± 0.15	
J0901+0304	PKS 0859+032	0.38	J090150.96+030423.0	18.19 ± 0.01	0.29 ± 0.04	0.287*
J0903+5012	4C +50.28	0.95	J090349.81+501235.5	22.19 ± 0.22	0.40 ± 0.22	
J0905+4128	B3 0902+416	0.48	J090522.18+412839.8	21.83 ± 0.09	0.65 ± 0.16	
J0907+0413	4C +04.30	0.70	J090750.74+041337.3	22.57 ± 0.19	0.69 ± 0.11	
J0910+2419	4C +24.19	0.83	J091022.55+241919.5	20.92 ± 0.06	0.74 ± 0.14	
J0915+1018	TXS 0912+105	0.35	J091512.95+101827.4	22.01 ± 0.12	0.31 ± 0.03	
J0917+4725	B3 0914+476	0.35	J091727.16+472525.6	21.82 ± 0.12	0.81 ± 0.22	
J0920+1753	4C +18.29	1.08	J092011.12+175324.7	22.43 ± 0.16	0.70 ± 0.11	
J0920+2714	B2 0917+27B	0.46	J092045.05+271406.6	18.04 ± 0.01	0.17 ± 0.01	0.206*
J0939+0304	PKS 0937+033	0.47	J093945.16+030426.4	20.44 ± 0.05	0.47 ± 0.02	
J0945+2640	B2 0942+26	0.57	J094530.97+264052.9	21.86 ± 0.12	0.09 ± 0.03	
J0951+1154	TXS 0948+121	0.37	J095133.84+115459.6	21.81 ± 0.09	0.60 ± 0.10	
J1008+2401	B2 1005+24	0.43	J100832.62+240119.6	22.35 ± 0.16	0.82 ± 0.20	
J1010+4159	B3 1007+422	0.42	J101024.79+415933.3	20.69 ± 0.07	0.49 ± 0.14	
J1019+4408	B3 1016+443	0.34	J101948.17+440824.5	22.27 ± 0.18	0.09 ± 0.05	
J1023+0424	TXS 1021+046	0.33	J102337.55+042413.9	21.62 ± 0.08	0.67 ± 0.11	

Table 2.1 (continued)

Object	Radio Name	$F_{20\mathrm{cm}}$ (Jy)	SDSS Name	SDSS r	SDSS z_{phot}	z_{spec}[a]
J1033+3935	B2 1030+39	0.41	J103322.03+393551.0	21.45 ± 0.09	0.20 ± 0.02	1.095:
J1034+1112	TXS 1031+114	1.21	J103405.08+111231.6	22.21 ± 0.17	0.39 ± 0.14	
J1043+0537	4C +05.45	0.67	J104340.30+053712.6	22.37 ± 0.17	0.53 ± 0.16	
J1045+0455	TXS 1043+051	0.38	J104551.74+045551.1	21.62 ± 0.08	0.43 ± 0.13	
J1048+3457	4C +35.23	1.05	J104834.24+345724.9	20.83 ± 0.04	0.39 ± 0.09	1.594
J1120+2327	4C +23.27	1.38	J112043.02+232755.2	21.81 ± 0.16	0.58 ± 0.24	1.819
J1125+1953	PKS 1123+201	0.43	J112555.22+195344.0	21.18 ± 0.10	0.26 ± 0.12	
J1127+5743	TXS 1124+579	0.65	J112743.71+574316.2	21.29 ± 0.08	0.53 ± 0.02	
J1129+5638	TXS 1126+569	0.50	J112904.15+563844.4	21.89 ± 0.20	0.67 ± 0.10	0.8922*
J1142+0235	TXS 1139+028	0.38	J114206.38+023533.5	20.90 ± 0.05	0.53 ± 0.05	
J1147+4818	4C +48.33	0.50	J114752.27+481849.5	22.21 ± 0.20	0.17 ± 0.05	
J1148+1404	TXS 1145+143	0.33	J114825.43+140449.3	21.66 ± 0.11	0.40 ± 0.14	
J1202+1207	TXS 1200+124	0.37	J120252.09+120720.6	20.62 ± 0.04	0.33 ± 0.13	
J1203+4632	B3 1200+468	0.42	J120331.80+463255.6	22.23 ± 0.13	0.50 ± 0.12	
J1207+5407	4C +54.26	0.60	J120714.13+540754.5	22.11 ± 0.18	0.77 ± 0.14	
J1215+1730	4C +17.54	1.03	J121514.70+173002.2	21.77 ± 0.10	0.07 ± 0.03	0.268
J1228+5348	4C +54.28	0.53	J122850.60+534801.6	22.52 ± 0.20	0.35 ± 0.19	
J1238+0845	TXS 1235+090	0.41	J123819.26+084500.4	21.52 ± 0.10	0.75 ± 0.10	
J1300+5029	TXS 1258+507	0.38	J130041.24+502937.0	21.55 ± 0.07	0.27 ± 0.14	1.561
J1312+1710	TXS 1310+174	0.34	J131235.21+171055.7	22.52 ± 0.16	0.47 ± 0.16	
J1315+0222	TXS 1312+026	0.52	J131516.93+022221.1	20.99 ± 0.13	0.51 ± 0.17	
J1341+1032	4C +10.36	0.69	J134104.36+103207.3	21.99 ± 0.14	0.38 ± 0.11	
J1345+5846	4C +59.20	0.42	J134538.32+584654.6	22.01 ± 0.17	0.58 ± 0.22	
J1347+1217	4C +12.50	4.86	J134733.35+121724.2	15.35 ± 0.00	0.18 ± 0.05	0.122
J1348+2415	4C +24.28	0.56	J134814.88+241550.3	22.31 ± 0.18	0.21 ± 0.17	2.879
J1354+5650	4C +57.23	0.72	J135400.10+565005.1	22.60 ± 0.20	0.21 ± 0.08	
J1357+0046	PKS 1355+01	2.00	J135753.71+004633.3	22.05 ± 0.11	0.57 ± 0.18	
J1410+4850	TXS 1408+490	0.33	J141036.04+485040.4	20.99 ± 0.05	0.52 ± 0.09	0.5927*
J1413+1509	TXS 1411+154	0.50	J141341.70+150939.9	20.96 ± 0.09	0.43 ± 0.11	
J1414+4554	B3 1412+461	0.41	J141414.84+455448.7	20.16 ± 0.03	0.48 ± 0.03	0.186:
J1415+1320	PKS 1413+135	1.18	J141558.81+132023.7	19.05 ± 0.02	0.29 ± 0.05	0.247

Notice that most of these sources are quite faint in the optical ($\sim$ 75% fainter than r=21) so that the application of the Strateva et al. (2001) morphology discriminators is not without some uncertainty. Since the original galaxy classification was made using SDSS DR5, we have revisited the sample selection process using DR8. In almost all cases the original classification is confirmed but in a few cases (5 in number) the DR8 compactness parameter (C) exceeds the $C < 2.60$ cut suggested by Strateva et al. (2001) for late-type systems. In one other case (J1421−0246) the r-band SDSS galaxy image is much better fit by a De Vaucouleurs $r^{1/4}$-law than an exponential disk. Because the possibility of being late-type cannot be ruled out completely and to retain a complete sample selected from SDSS DR5 and the April, 2003 version of FIRST, we still include these 5 objects in the sample.

2.3 Observations

2.3.1 Near-IR Imaging

In order to check the SDSS galaxy classifications, to complement the SDSS photometry (and thus to provide an optical/NIR SED), and to search for an extincted point-source indicative of an imbedded AGN, we obtained NIR photometry of this sample using the Near-Infrared Camera & Fabry-Perot Spectrometer (NIC-FPS; Hearty et al. 2005) in its imaging mode on the APO 3.5 m. In the last several years almost all of the objects in this sample were observed in the J and $K_{\rm short}$ bands with all objects detected in $K_{\rm short}$ and most in J-band. H-band observations were made for fewer of these sources, particularly where the H-band photometry was important in evaluating the nature of the source. During these observations, the seeing varied from sub-1″to 2″with a median seeing value of $\sim 1\farcs3$. This image quality is approximately the same or, in many cases, better than the image quality for the SDSS.

The images were reduced in the standard manner with flat-field and dark images obtained the same night. Because all of these images were obtained using a 5-point dither pattern on the sky, the science images were used to create a sky-flat by median-filtering. Following flat-fielding the

Table 2.1 (continued)

Object	Radio Name	$F_{20\mathrm{cm}}$ (Jy)	SDSS Name	SDSS r	SDSS z_{phot}	z_{spec}[a]
J1421−0246	4C −02.60	0.55	J142113.54−024646.0	20.34 ± 0.10	0.50 ± 0.03	
J1424+1852	4C +19.47	0.70	J142409.71+185253.5	21.49 ± 0.08	0.52 ± 0.11	
J1502+3753	B2 1500+38	0.34	J150234.77+375353.0	20.50 ± 0.06	0.40 ± 0.09	
J1504+5438	TXS 1503+548	0.38	J150451.19+543839.7	20.29 ± 0.05	0.53 ± 0.10	0.621
J1504+6000	TXS 1502+602	1.55	J150409.21+600055.7	20.00 ± 0.02	0.47 ± 0.16	1.024*
J1523+1332	4C +13.54	0.35	J152321.74+133229.2	21.76 ± 0.12	0.46 ± 0.18	
J1527+3312	B2 1525+33	0.32	J152750.89+331253.0	22.04 ± 0.10	0.44 ± 0.14	
J1528−0213	PKS 1525−020	0.47	J152821.99−021319.0	21.75 ± 0.15	0.63 ± 0.07	
J1548+0808	TXS 1545+082	0.63	J154809.05+080834.7	21.78 ± 0.14	0.65 ± 0.12	
J1551+6405	TXS 1550+642	0.68	J155128.19+640537.8	22.10 ± 0.15	0.47 ± 0.15	
J1559+4349	4C +43.36	0.75	J155931.21+434916.6	21.11 ± 0.07	0.42 ± 0.09	1.232*
J1604+6050	TXS 1603+609	0.59	J160427.40+605055.5	21.44 ± 0.10	0.59 ± 0.05	0.5585*
J1616+2647	PKS 1614+26	1.41	J161638.32+264701.3	22.46 ± 0.17	0.44 ± 0.03	0.7548*
J1625+4134	4C +41.32	1.72	J162557.68+413440.8	22.35 ± 0.16	0.58 ± 0.18	2.550
J1629+1342	4C +13.60	0.71	J162948.42+134205.7	22.34 ± 0.18	0.44 ± 0.18	
J1633+4700	4C +47.43	0.46	J163315.02+470016.9	21.44 ± 0.12	0.57 ± 0.19	
J1724+3852	B2 1722+38	0.37	J172400.53+385226.7	22.14 ± 0.12	0.11 ± 0.05	1.5439*
J2203−0021	4C −00.79	0.61	J220358.31−002148.1	21.21 ± 0.13	0.57 ± 0.10	0.729*

[a]Redshifts noted with superscript "*" were obtained recently by us using DIS II or TripleSpec at the APO 3.5m telescope (see Figures 2.1 & 2.2). Others come from the NASA/NED database. Redshifts noted with ":" are uncertain.

[b]Gravitational lensing system with background quasar at $z = 3.2$ and foreground galaxy at $z = 0.349$.

images were aligned and stacked; astrometric positions for source centroids were set to the World Coordinate System using 5-10 SDSS stars identified in these images. Most of the objects in this project are faint, so, in order to reduce the photometric error and for consistency with the SDSS optical photometry, we first measure the magnitude in an aperture of $2''(m_{2''})$. This magnitude is similar to the fiber magnitude $m_{\rm fiber}$ in SDSS (Stoughton et al. 2002). SDSS also gives the "model magnitude" $m_{\rm model}$ as the best estimated magnitude for extended sources. Assuming an unchanged radial profile between the optical and NIR images, the "model NIR magnitude" is $m = m_{2''} + (m_{\rm model} - m_{\rm fiber})$ and is the NIR equivalent of the SDSS model magnitudes to facilitate a consistent source SED.

These are the magnitudes that we quote in Table 2.2. Table 2.2 lists our NIC-FPS photometry for the 70 sources in the trimmed sample including by column: (1) source name as in Table 2.1; (2–4) the next three columns list the J, H and $K_{\rm short}$ band magnitudes. The listed statistical errors include a contribution from photon statistics as well as the zero-point errors from the 5-10 2MASS stars in the field. Column (5) lists the UT date of the observations in the format YY-MM-DD; all observations of any one source were obtained sequentially on the UT date listed. Column (6) lists the classification of the source based on its optical/NIR SED. These classifications are discussed in the next Section in detail. Abbreviations include: G = galaxy; Q = quasar and $Q + abs$ = possible reddened quasar; $G + Q$ = galaxy + quasar. Column (7) lists $z_{\rm fit}$, the best-fit photometric redshifts based on optical + NIR SEDs for G-type sources only. Column (8) lists the Hubble type for the best-fitting SED galaxy template (see next Section for discussion) used for the classification in Column (7). The entries in the last three columns will be discussed in detail in the next Section.

Table 2.2. NIR photometry and optical-NIR SED.

Object	J	H	$K_{\rm short}$	Observation Date	SED Type[a]	$z_{\rm fit}$	Hubble Type[b]
J0000−1054	20.03 ± 0.25	19.30 ± 0.26	18.55 ± 0.26	UT081102	Q+abs		
J0003−1053	17.69 ± 0.28	16.46 ± 0.28	16.19 ± 0.31	UT071213	Q+abs		
J0134+0003	18.88 ± 0.38	17.76 ± 0.39	16.91 ± 0.39	UT071213	G	0.92	Sa
J0249−0759	19.19 ± 0.21	18.30 ± 0.22	17.40 ± 0.21	UT081102	G+Q		
J0736+2954	19.62 ± 0.27	18.57 ± 0.27	17.60 ± 0.27	UT081228	G+Q		
J0747+4618	19.40 ± 0.14		17.95 ± 0.14	UT091228	Q+abs		
J0749+2129	18.22 ± 0.13		16.37 ± 0.13	UT080120	G	0.52	S0
J0751+2716	19.84 ± 0.18	19.41 ± 0.18	18.18 ± 0.17	UT070304	G	0.42	Sc
J0759+5312	19.66 ± 0.17	18.65 ± 0.17	18.09 ± 0.17	UT080218	G+Q		
J0805+1614	18.12 ± 0.11	16.78 ± 0.11	15.87 ± 0.12	UT080218	G	0.67	Sc
J0807+5327	19.13 ± 0.09		17.73 ± 0.09	UT080120	Q+abs		
J0824+5413	17.67 ± 0.09		15.81 ± 0.10	UT080120	G+Q		
J0834+1700	20.10 ± 0.23	> 19.42 ± 0.36	> 19.05 ± 0.32	UT081228	Q+abs		
J0839+2403	18.83 ± 0.15	18.60 ± 0.15	17.63 ± 0.15	UT070304	G+Q		
J0843+4215	18.59 ± 0.24		16.51 ± 0.25	UT080120	G	0.60	Sb
J0901+0304	16.17 ± 0.03	15.18 ± 0.02	14.45 ± 0.03	UT080120	G	0.21	Sc
J0903+5012	19.16 ± 0.35	17.95 ± 0.35	17.44 ± 0.35	UT080218	G+Q		
J0905+4128	19.46 ± 0.17	19.14 ± 0.17	17.48 ± 0.17	UT080218	G+Q		
J0907+0413	19.32 ± 0.33	18.59 ± 0.33	17.51 ± 0.33	UT070304	G	1.10	Sc
J0910+2419	18.04 ± 0.10		17.19 ± 0.11	UT080120	G+Q		
J0915+1018	20.02 ± 0.23	19.31 ± 0.23	18.33 ± 0.23	UT081228	G+Q		
J0917+4725		18.54 ± 0.22	17.61 ± 0.22	UT081228	G+Q		
J0920+1753	19.00 ± 0.31	18.49 ± 0.31	17.53 ± 0.31	UT090116	G	0.68	Sc
J0920+2714	15.91 ± 0.04	14.94 ± 0.05	14.36 ± 0.06	UT060611	G	0.23	S0
J0939+0304	17.80 ± 0.09	17.01 ± 0.09	16.46 ± 0.10	UT060611	G	0.34	S0
J0945+2640	19.33 ± 0.21		18.63 ± 0.21	UT080418	Q		
J0951+1154	18.86 ± 0.17	18.24 ± 0.17	17.37 ± 0.17	UT081228	G	0.65	Sc
J1008+2401	19.41 ± 0.35	18.76 ± 0.36	17.80 ± 0.36	UT081228	G	0.62	Sc
J1010+4159	17.79 ± 0.12	17.09 ± 0.12	16.79 ± 0.13	UT060611	G	0.71	Sc
J1019+4408	20.05 ± 0.27	19.07 ± 0.27	17.95 ± 0.27	UT081228	Q+abs		
J1023+0424	18.74 ± 0.15	18.56 ± 0.15	17.63 ± 0.15	UT060611	G	0.71	Sc

Table 2.2 (continued)

Object	J	H	$K_{\rm short}$	Observation Date	SED Type[a]	$z_{\rm fit}$	Hubble Type[b]
J1033+3935	18.40 ± 0.17	17.67 ± 0.17	16.78 ± 0.17	UT060611	G	0.80	Sc
J1034+1112	20.19 ± 0.29		17.94 ± 0.29	UT090116	G+Q		
J1043+0537	19.75 ± 0.29		17.96 ± 0.29	UT090116	G	0.42	E
J1045+0455	19.67 ± 0.15	18.76 ± 0.15	18.53 ± 0.15	UT081228	Q+abs		
J1048+3457	18.39 ± 0.08	17.74 ± 0.13	17.31 ± 0.12	UT060611	Q+abs		
J1120+2327	> 19.07 ± 0.27	> 18.30 ± 0.28	> 18.64 ± 0.29	UT070304	Q		
J1125+1953	20.13 ± 0.17		> 19.08 ± 0.26	UT090116	Q		
J1127+5743	18.78 ± 0.12	17.83 ± 0.12	17.12 ± 0.15	UT060611	G	0.49	Sb
J1129+5638	18.57 ± 0.31	18.02 ± 0.31	17.38 ± 0.31	UT081228	G	0.64	Sa
J1142+0235	18.90 ± 0.09	17.30 ± 0.08	17.04 ± 0.09	UT060611	G	0.37	Sa
J1147+4818	19.92 ± 0.28		17.23 ± 0.28	UT090116	Q		
J1148+1404	19.35 ± 0.20		17.72 ± 0.20	UT090116	G	0.54	Sc
J1202+1207	19.36 ± 0.08		17.27 ± 0.10	UT090116	G+Q		
J1203+4632	19.71 ± 0.25	18.69 ± 0.25	18.02 ± 0.25	UT081228	G	0.36	E
J1207+5407	18.92 ± 0.31	18.26 ± 0.31	17.58 ± 0.31	UT081228	G	0.61	Sc
J1215+1730	19.78 ± 0.16	19.04 ± 0.16	18.11 ± 0.17	UT080120	Q+abs		
J1228+5348	19.31 ± 0.36		19.03 ± 0.36	UT090116	G+Q		
J1238+0845	17.93 ± 0.16	17.58 ± 0.16	16.88 ± 0.17	UT060611	G	0.65	Sc
J1300+5029	19.27 ± 0.13		17.60 ± 0.13	UT080517	Q		
J1312+1710	19.55 ± 0.37	19.02 ± 0.37	18.18 ± 0.37	UT080218	G	0.63	Sc
J1315+0222		16.91 ± 0.23	16.30 ± 0.23	UT060611	G	0.85	Sc
J1341+1032	20.02 ± 0.25	> 19.24 ± 0.39	17.79 ± 0.25	UT081228	Q+abs		
J1345+5846	18.86 ± 0.30		18.25 ± 0.30	UT091228	G+Q		
J1347+1217	13.23 ± 0.06	12.25 ± 0.08	11.37 ± 0.10	UT060611	G	0.18	Sa
J1348+2415	> 20.05 ± 0.34		> 18.69 ± 0.35	UT080517	Q		
J1354+5650	19.82 ± 0.30		18.14 ± 0.30	UT080517	G	0.65	Sc
J1357+0046	19.77 ± 0.19	18.63 ± 0.19	18.09 ± 0.19	UT081228	G+Q		
J1410+4850		18.39 ± 0.10	17.08 ± 0.10	UT060630	G+Q		
J1413+1509	18.63 ± 0.16		17.37 ± 0.18	UT080120	G	0.22	S0
J1414+4554	17.62 ± 0.06	16.63 ± 0.06	16.15 ± 0.06	UT070603	G	0.38	S0
J1415+1320	> 16.62 ± 0.20	16.06 ± 0.22	14.93 ± 0.11	2MASS[c]	G	0.30	Sa

Usually there are 5-10 non-saturated objects from the Two Micron All-Sky Survey (2MASS) catalog in the $\sim 5' \times 5'$ NIC-FPS field, which are used to provide zero-points for the magnitudes listed in Table 2.2. The magnitude error budget includes amounts from the image photon-statistics (usually $\sigma_{2''} < 0.05$), the 2MASS magnitude system error ($\sigma < 0.1$) and slightly larger and less well-defined errors accrued in placing the NIR magnitudes onto the SDSS "model magnitude" scale ($\sigma_{\rm model} \sim 0.1$ and $\sigma_{\rm fiber}$ varies from 0.05 to 0.3). Sources which show NIR point sources, and so have more centrally-concentrated surface brightness profiles than their optical images, may have NIR "model magnitudes" which have been under-estimated systematically by 0.1–0.2 mags. For non-detected objects, we set a 3σ flux level recorded as a model magnitude limit in Table 2.2. Blank spaces in Table 2.2 mean that the source was not observed in that band.

The systematic astrometric error of an SDSS frame is on the order of 50 mas per coordinate. For objects brighter than $r = 20$ mag, the object controiding for a point source gives a random error of about 20 mas. About 5-10 SDSS stars with $r < 20$ mag were selected in each NIR field for astrometric calibration, yielding a total positional uncertainty in the range of 50 - 100 mas. For bright FIRST radio sources the astrometric error is smaller than 50 mas so that the optical/NIR positional errors dominate the accuracy with which the SDSS, NIR and VLA/VLBA images can be registered. All sources have coincident NIR and optical positions although discrepancy exists between optical/NIR and radio positions for some of the sources mostly due to extended structure of the radio sources. More details will be discussed in Chapter 3.

Specific unusual circumstances involving morphology, relative positional offsets and unusual or inconclusive SEDs are discussed source by source in Section 2.5.

Due to the faint and diffuse nature of most of the target galaxies in this sample, spectroscopic redshifts are available for only 17 of them. Originally it was thought that a reliance on the SDSS photometric redshifts would be sufficient for this program given the wide bandwidths available on current generation sub-GHz radio receivers. However, this has not proven to be the case. First, the special defining qualities of this sample make photometric redshifts (photo-z hereafter) less reliable than for most galaxy samples (i.e., optical objects can be combinations of starlight plus extincted

Table 2.2 (continued)

Object	J	H	$K_{\rm short}$	Observation Date	SED Type[a]	$z_{\rm fit}$	Hubble Type[b]
J1421−0246	17.45 ± 0.14		15.60 ± 0.14	UT080120	G	0.49	E
J1424+1852	19.26 ± 0.17	18.97 ± 0.18	17.77 ± 0.19	UT080218	Q+abs		
J1502+3753	18.37 ± 0.10	17.87 ± 0.09		UT060630	Q+abs		
J1504+5438	18.09 ± 0.09	17.00 ± 0.09	16.15 ± 0.09	UT080218	G	0.51	Sc
J1504+6000	18.06 ± 0.07	18.46 ± 0.05	17.60 ± 0.06	UT070528	Q		
J1523+1332		18.51 ± 0.21	18.26 ± 0.21	UT070528	Q+abs		
J1527+3312			18.11 ± 0.21	UT080517	G	0.32	Sb
J1528−0213		17.62 ± 0.25	16.75 ± 0.25	UT070528	G	0.54	E
J1548+0808	18.77 ± 0.25	17.72 ± 0.25	16.83 ± 0.25	UT070528	G	0.51	E
J1551+6405			18.88 ± 0.27	UT110518	G+Q		
J1559+4349	18.55 ± 0.13	17.70 ± 0.12	16.78 ± 0.12	UT060630	Q+abs		
J1604+6050	18.94 ± 0.18	17.74 ± 0.18	16.89 ± 0.18	UT080218	G	0.42	S0
J1616+2647		18.59 ± 0.27	18.10 ± 0.27	UT070528	G	0.72	Sc
J1625+4134	19.21 ± 0.26	17.98 ± 0.26	16.80 ± 0.26	UT060630	Q		
J1629+1342	18.88 ± 0.32	18.50 ± 0.32	17.38 ± 0.32	UT070528	G	0.74	Sc
J1633+4700	19.10 ± 0.20	18.49 ± 0.20	17.73 ± 0.20	UT080218	Q+abs		
J1724+3852	19.96 ± 0.09	18.50 ± 0.09	18.72 ± 0.09	UT081102	Q+abs		
J2203−0021	18.54 ± 0.18	17.36 ± 0.18	16.85 ± 0.18	UT081102	G	0.71	Sc

[a]The optical-NIR SED is classified as G if it drops at the blue end, Q if it keeps increasing or $Q + abs$ if it flattens out at the blue end, and $G + Q$ if there is flux excess at the red end on top of Q feature at the blue end. See Section 2.4.2 for details.

[b]Sources classified as G are fit with template spectra (Figure 2.9) to estimate the Hubble type of the host galaxy. See section 4.2 for details.

[c]Data from the 2MASS survey.

AGN). And second, the difficult radio frequency interference (RFI) environments now present at all terrestrial radio telescope sites make even typical photo-z accuracy insufficient for a sensitive H I and molecular line search; i.e., without an accurate spectroscopic redshift, the presence of intense, receiver-saturating RFI means that it is not possible to determine definitively whether an absorption is present without a specific frequency prediction. Due to this circumstance we initiated a program for obtaining optical and/or NIR redshifts using the spectrographs at the APO 3.5m.

2.3.2 Optical and Near-IR Spectroscopy

The Dual Imaging Spectrograph (DIS II) was used in its standard low dispersion mode to obtain $\sim$ 150 km s^{-1} resolution spectra in the 4000–9000 Å wavelength region (1.8 Å pix^{-1} shortward of 5500 Å and 2.4 Å pix^{-1} longward; see Oke & Gunn 1982 for original design). TripleSpec is a cross-dispersed NIR spectrograph that provides simultaneous R $\sim$ 3500 spectra in a continuous wavelength coverage from 0.95–2.46 μm in five spectral orders. The instrument is described in more detail in Wilson et al. (2004). Where we have successfully obtained DIS II spectra, emission lines are detected and redshift errors are $\pm$30–60 km s^{-1} and $\pm$90 km s^{-1} where absorption and only weak emission is detected. TripleSpec NIR spectra have similar resolution but the signal-to-noise ratio is much lower so that the DIS II redshifts are preferred where we have obtained both optical and NIR spectroscopy. We have also obtained redshifts for 5 objects using the Gemini Multi-Object Spectrographs (GMOS) on the Gemini North telescope with low-resolution spectroscopy (R150 grating).

These new redshifts led to the detection of redshifted H I 21 cm in 4 cases. Despite observing many more objects which possessed only photometric redshifts only one new redshifted H I 21 cm absorption detection was made based on a photo-z alone: J1357+0046 (PKS 1355+01) possesses two H I components at $z_{\rm HI}$=(0.7971, 0.7962); i.e., at a significantly higher z than the SDSS $z_{\rm phot}$=0.57. The spectra we have obtained thus far for this project are listed in Table 2.3 with the instrument used, the redshift obtained including measurement errors and the emission lines detected. These spectra are shown in Figures 2.1–2.3.

Table 2.3. New Spectroscopic Redshifts.

Object	$z_{\rm spec}$	$z_{\rm phot}$	$z_{\rm fit}$[a]	Instrument Used
J0003−1053	1.474 ± 0.001	0.42		TripleSpec
J0805+1614	0.632: ± 0.002	0.49	0.67	TripleSpec
J0824+5413	0.6385 ± 0.0003	0.46		DIS II, TripleSepc
J0901+0304	0.2872 ± 0.0001	0.29	0.21	DIS II
J0920+2714	0.2064 ± 0.0002	0.17	0.23	DIS II
J1129+5638	0.8922 ± 0.0006	0.67	0.64	GMOS-N
J1410+4850	0.5927 ± 0.0005	0.52		GMOS-N
J1504+6000	1.024 ± 0.001	0.67		DIS II
J1559+4349	1.232 ± 0.001	0.42		TripleSpec
J1604+6050	0.5585 ± 0.0004	0.59	0.42	GMOS-N
J1616+2647	0.7548 ± 0.0002	0.44	0.72	GMOS-N
J1724+3852	1.5439 ± 0.0006	0.11		GMOS-N
J2203−0021	0.729 ± 0.001	0.57	0.71	TripleSpec

[a]Same as in Table 2.2.

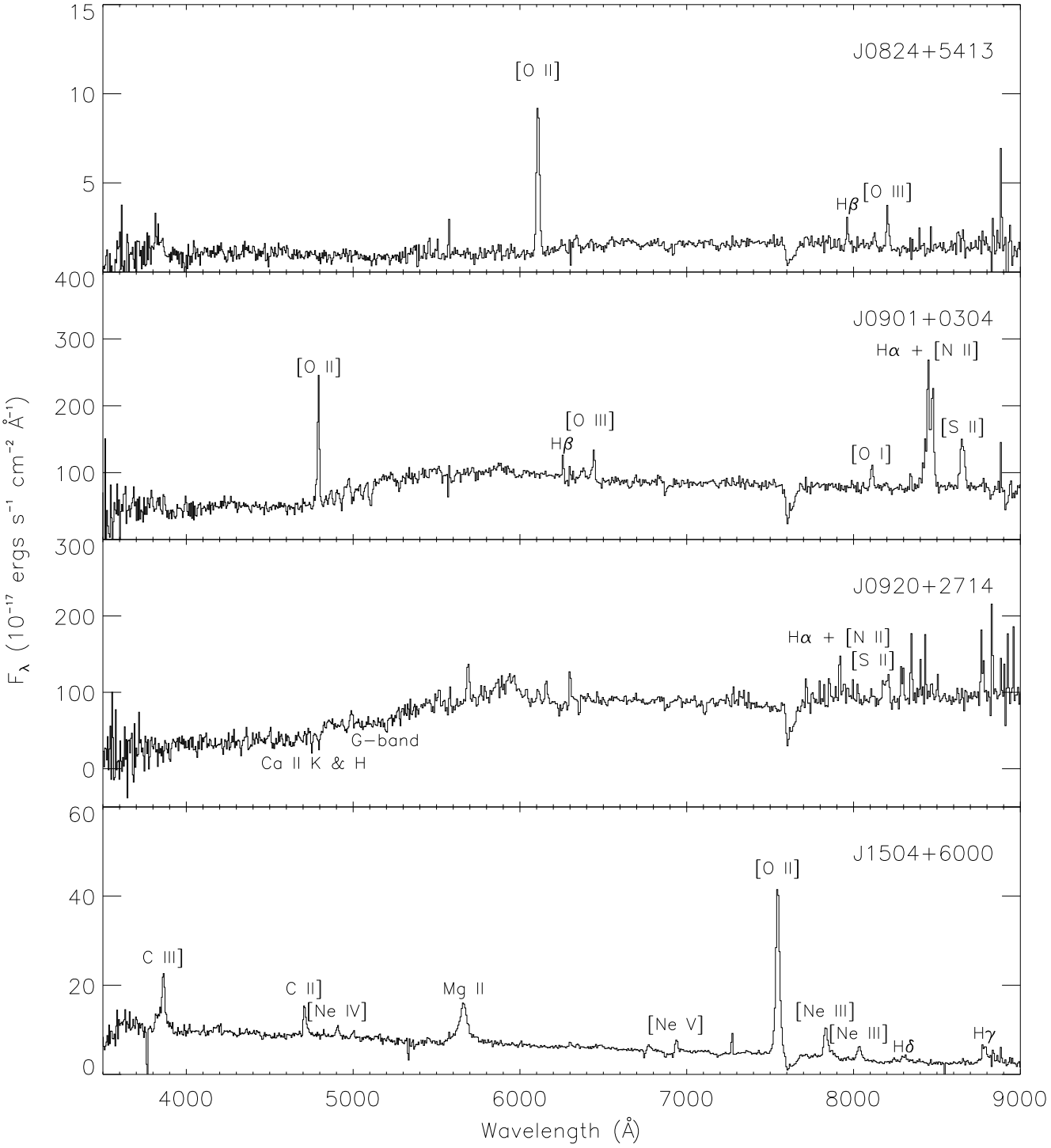

Figure 2.1 The APO/DIS optical spectra with prominent emission/absorption lines marked.

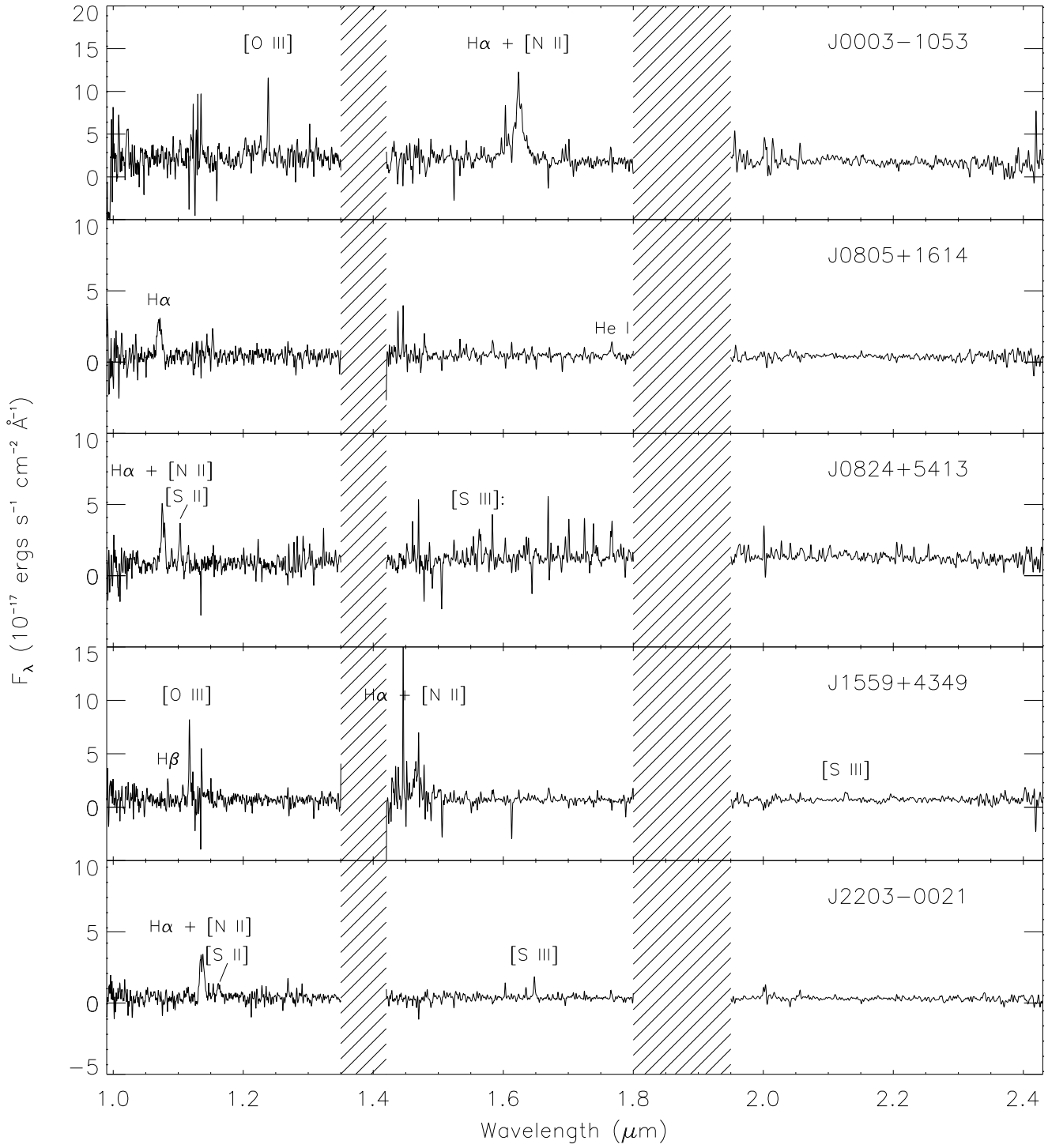

Figure 2.2 The APO/TripleSPEC near-IR spectra with prominent emission lines marked. The shaded regions are regions of significant atmospheric absorption.

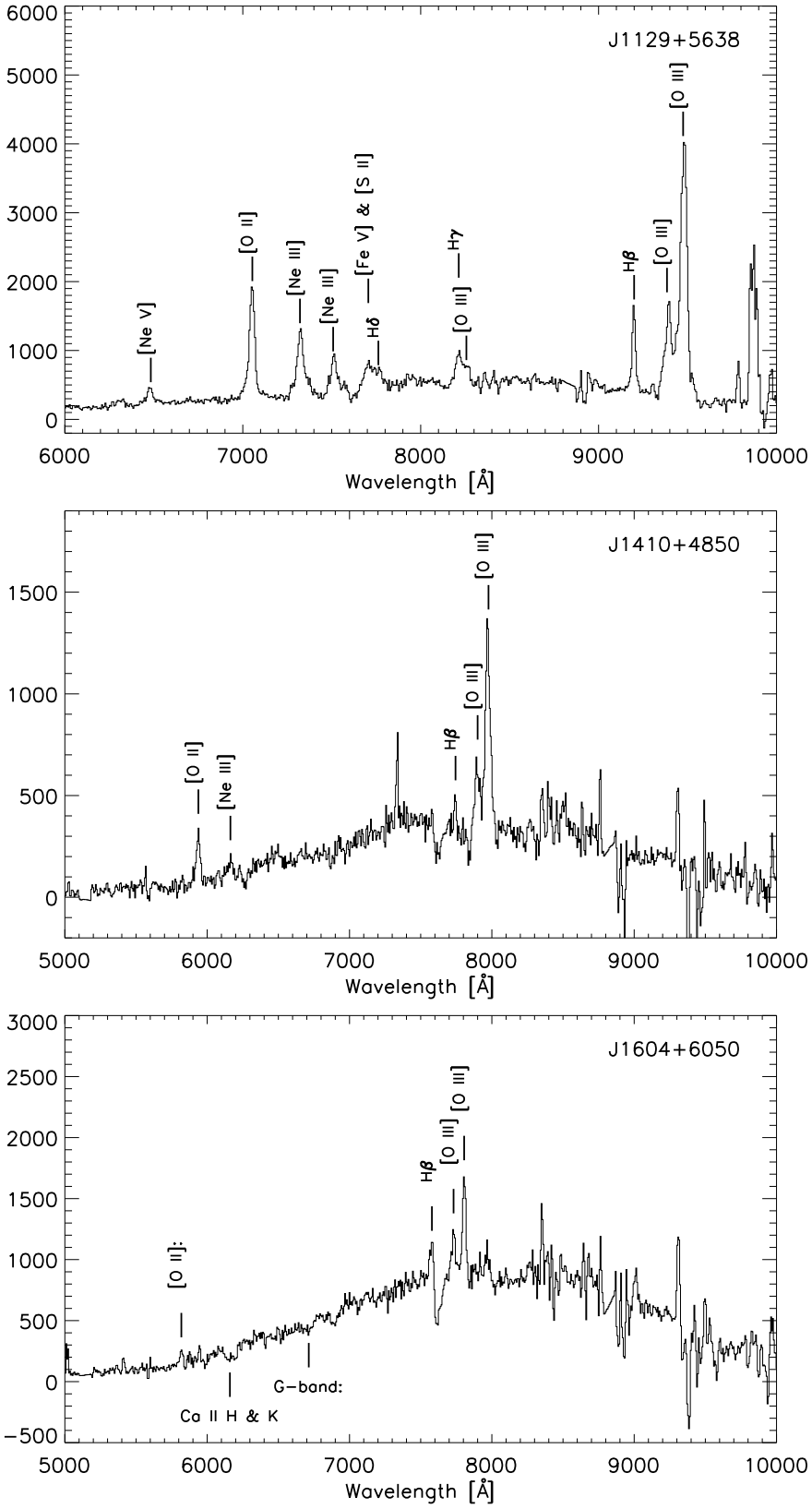

Figure 2.3 The Gemini/GMOS-N optical spectra with prominent emission/absorption lines marked. No flux calibration has been applied so the vertical scale is in detector counts. Unidentified spikes are residual cosmic rays and sky lines.

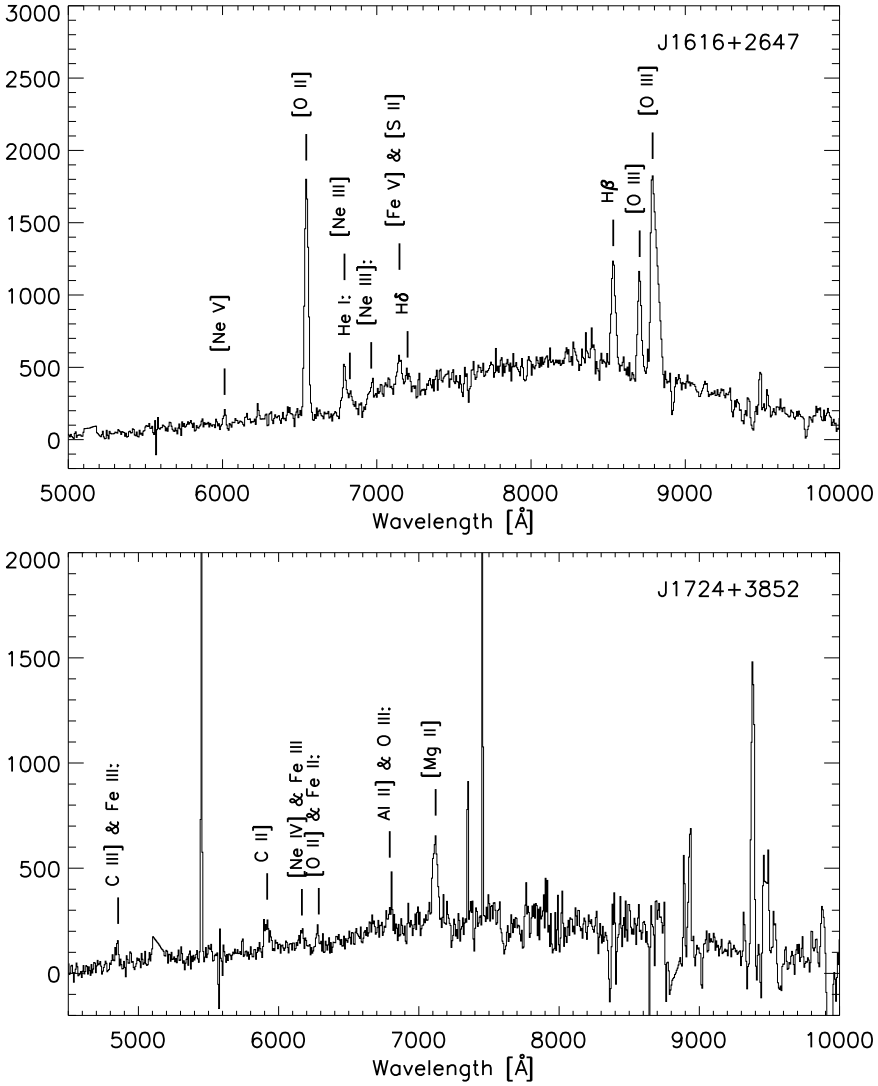

Figure 2.3 Continued.

2.4 NIR Morphology, Magnitudes and Optical/NIR SEDs

With multi-band observations, we are now able to better understand these sources despite their faintness. In this Section we use the NIR magnitudes to examine the NIR morphology of the source, use the NIR magnitudes to create an optical-NIR SED and compare these with template galaxy spectra. The $K_{\rm short}$ magnitudes are then used to place these objects on the $K-z$ diagram for which many radio-loud sources show a strong correlation.

2.4.1 Near-IR (NIR) Morphology

The NIC-FPS (JHK) imaging provides an independent check of the SDSS galaxy morphology classifier. In general, these images provide ample confirmation of the galaxy morphology in that virtually all of them are diffuse sources in moderate seeing conditions (median $\sim 1\farcs3$). See Figure 2.4 for a few representative images and Figure A.1 for the full sample. For a few sources, particularly some of the optically red sources, the NIR images suggest that an elliptical galaxy morphology is possible so that the Strateva et al. (2001) classification may be incorrect. The few sources which show a centrally-concentrated structure in our NIR images are J1354+5650, J0749+2129, J0920+2714, J1043+0537, J1019+4408,and J0003−1053. These are not removed from the sample because they may still be extincted, although this is less likely compared to the more diffuse galaxies (e.g., J0920+2714 is detected in redshifted H I 21 cm absorption). Otherwise, the optical morphology classifications for these sources made by the SDSS is confirmed.

2.4.2 Optical-NIR Spectral Energy Distributions (SEDs)

These sources have a wide variety of optical-NIR SEDs due to three factors: variations in host galaxy type, the relative importance of the host galaxy and the AGN as a function of wavelength, and the amount of nuclear obscuration. In an attempt to categorize their SEDs we have placed each source into one of the following three categories, listed these in Table 2.2 and show a few examples of each type in Figures 2.5–2.7):

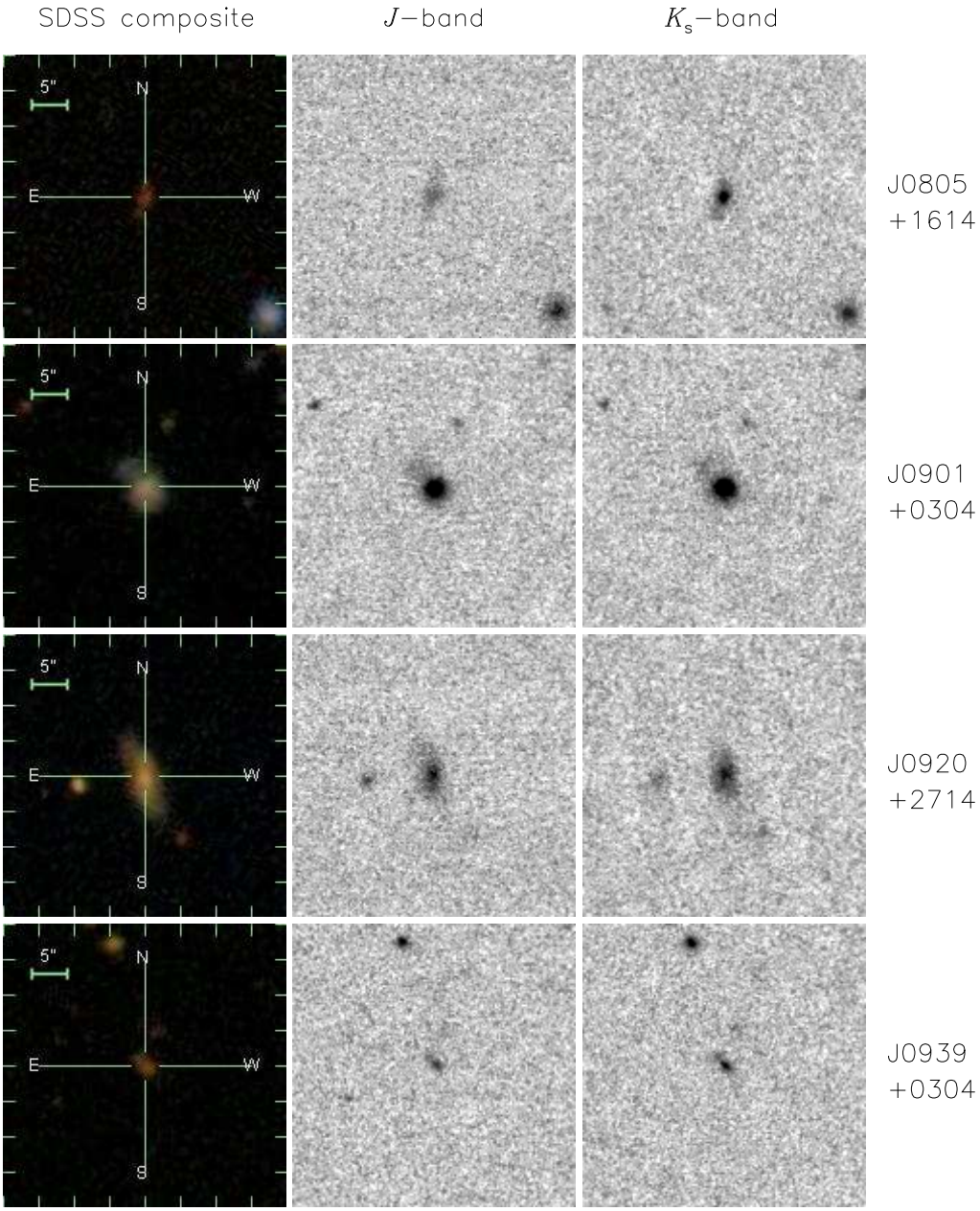

Figure 2.4 Representative optical and NIR images from our sample all shown at the same scale and orientation as indicated in left-hand column. Shown are the SDSS composite images (*left*; blue: g-band, green: r-band, red: i-band), and the APO 3.5m J-band (*middle*) and K_s band (*right*) images of (from top to bottom) J0805+1614, J0901+0304, J0920+2714, and J0939+0304.

- Quasar (Q in column 6 of Table 2.2) or obscured quasar (Q+abs). The Q SED is approximated by a single power-law declining from blue to red in F_λ, although in some cases contributions from emission lines to specific flux bands are evident. Almost all previously known quasars in our sample have Q-type SEDs. Sources classified as Q+abs show evidence for a flattening in flux at the blue end. In some cases the SDSS u-band flux is only an upper limit making the classification uncertain between Q+abs and a galaxy G-type SED; i.e., it is uncertain whether the near-UV flux continues to decline or not. See Figure 2.5 for examples.

- Galaxy (G). This galaxy-like SED peaks in the middle bands and declines toward both the blue and the red ends. See Figure 2.6 for examples. If the turn-down at the blue-end is not explicitly observed (u and sometimes g-band fluxes are upper limits), the source SED could either be Q+abs or G. Sources are classified as Q+abs if the NIR slope is too steep to be a galaxy, otherwise these sources are classified as G.

- Galaxy + Quasar (G+Q). The SED is a power-law Q component with a bump in the middle bands which could be a galaxy G component. Sources missing the flattening at the red end are labeled as G+Q since the absence of a flattening or turn-down in the NIR could be due to contributions from a nuclear source that is obscured at shorter wavelengths. See Figure 2.7 for an example.

Our classifications are largely confirmed by the sources for which optical and/or near-IR spectroscopy is in-hand. Overall there are 39 sources in the G class (including 11 SEDs best-fit by early-type galaxies and 28 by late-type galaxies), 17 in $G + Q$, 8 in Q and 16 in $Q + abs$. While our NIR photometry was obtained several years after the SDSS optical photometry, we do not see strong effects in the SEDs arising from any AGN variability that may have occurred over that time period. The SDSS and NIR images (as in Figure 2.4) and the SEDs (as in Figures 2.5–2.7) are shown for the entire sample in Appendix A. Due to the strong possibility that the 39 sources in the G class are actually rather simple in ther overall SEDs, in this next Section we concentrate on

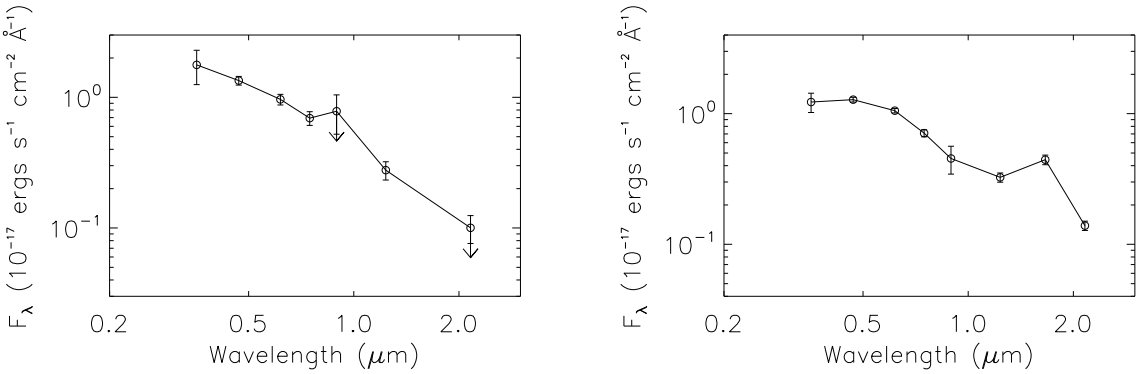

Figure 2.5 SED classified as Q (*left*, J1125+1953) and $Q + abs$ (*right*, J1724+3852).

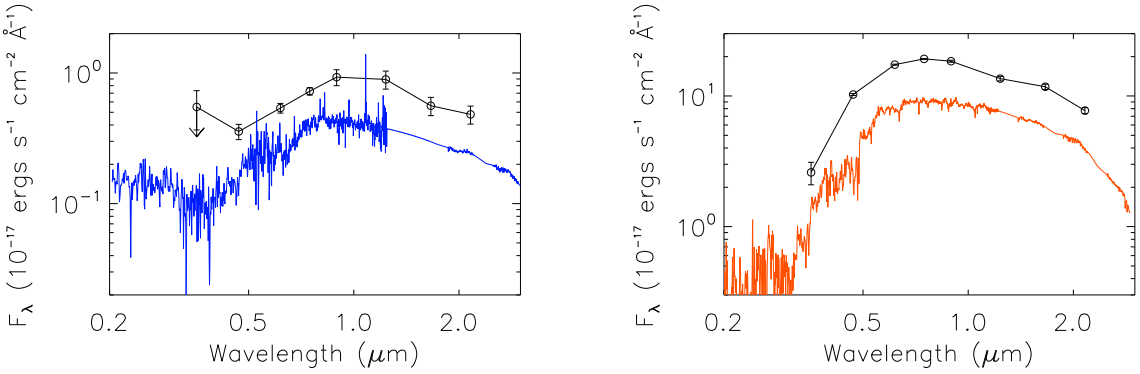

Figure 2.6 SED classified as G (*left*, J0951+1154; *right*, J0920+2714). The spectra are template galaxies of Sc type at $z = 0.65$ (*left*) and S0 type at $z = 0.23$ (*right*).

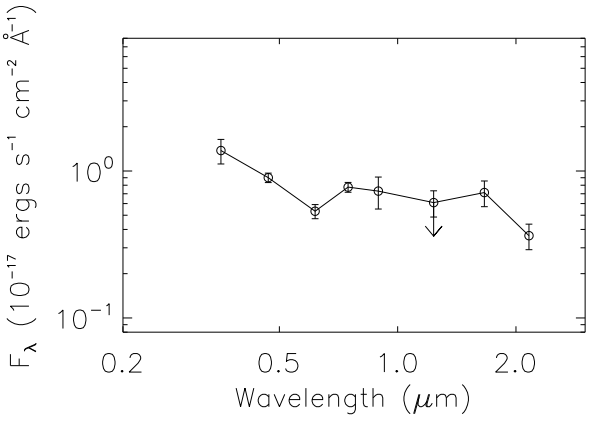

Figure 2.7 SED classified as $G + Q$ (J0917+4725).

G-class sources in a further scrutiny of their photometric properties.

2.4.3 Photometric and Spectroscopic Redshifts

Since up to now this program has relied primarily on the SDSS photo-zs, a brief review of their basic properties is in order. Before Data Release 7 (DR7), SDSS photo-zs are derived from fits using typical SDSS resolution spectra of various galaxy types (Budavári et al. 2000; Csabai et al. 2003). A new algorithm is used in DR7 which utilizes SDSS spectroscopic catalog as a training set to determine photo-zs from spectroscopic objects with similar SEDs (Csabai et al. 2007). However, objects in this training set are brighter and closer on average than typical objects in our sample. A fainter and deeper training set more representative of our sources is included in DR8 which has r-band magnitudes mostly between $r = 20$–22, redshifts mostly between 0.2–0.8, and the improved average error is 0.10–0.12 (Csabai, private communication). Although these redshifts are a good potential match to our own sample, the correlation between the spectroscopic and photo-zs we have in-hand is less compelling. Figure 2.8a shows sources with known spectroscopic redshifts compared with their photometric redshifts from DR8. Only half (8 out of 16) of these sources appear reasonably well-fit by the DR8 algorithm to the 1σ accuracy noted above. But even for the 8 with $z_{\rm phot} \simeq z_{\rm spec}$, the photometric redshift systematically underestimates the redshift by $\Delta z \sim$ 0.05–0.1 (see Figure 2.8a), i.e., the offset of H I absorption can be as large as 70 MHz. We note that the only source (J1414+4554) to the left of the solid line in Figure 2.8a has an uncertain redshift of $z = 0.186$ (Falco et al. 1998). Given its unique and unusual location in this plot we doubt the accuracy of this spectroscopic redshift (Falco et al. did not publish their spectrum) and do not use it further.

In the poorly-fit 7 sources at $z > 1$, three are classified as Q SED types and 4 are classified as $Q + abs$. It is understandable in these cases that the SDSS photo-z classifier obtains an unreliable redshift by trying to fit a galaxy template to a reddened quasar SED. An emission line spectrum with weak continuum may also pose a problem for the photo-z algorithms. Thus, those source with $z_{\rm spec} >> z_{\rm phot}$ are not representative of the remainder of the sample and photo-zs for Q and

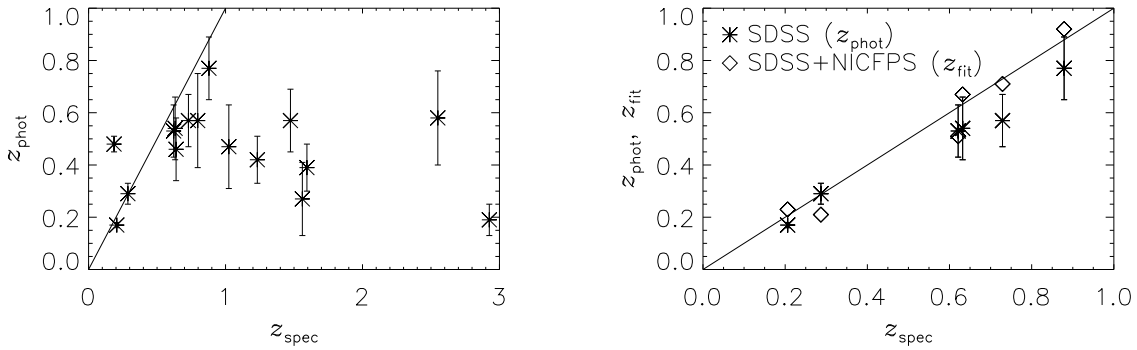

Figure 2.8 *Left* (a): Spectroscopic redshifts compared with photometric redshifts from DR8 for those 16 sources with spectroscopic redshifts. The line shows $z_{\rm spec} = z_{\rm phot}$, illustrating that the fitting algorithm does not work for high-z ($z \gtrsim 1$) quasars. Even for those sources not classified as quasars, the $z_{\rm phot}$ is systematically lower than $z_{\rm spec}$ by $\Delta z = 0.05$–0.1 at $z \sim 0.5$–1. *Right* (b): Photometric redshifts from DR8 (asterisks with error bars) and from our fitting routine (diamonds) using SDSS+NIR photometry for sources with spectroscopic redshifts and classified as G. See Section 2.4.3 for discussion.

$Q + abs$ type sources in particular should not be used.

Given the potential complexities of the SEDs for these galaxies, it would be very helpful if we could use our NIR photometry to further constrain source redshifts. But given the results shown in Figure 2.8a we restrict this analysis to only those sources classified as G-types in Figure 2.8b. Using the SED templates in Figure 2.9 we have used a least-squares approach to determine the best-fit Hubble types and redshifts ($z_{\rm fit}$) for the G sources based on their SDSS + NIR SEDs and listed them in Table 2.2 column 7 & 8. We searched parameter space in redshift, peak flux density and discrete Hubble types (Figure 2.9) to find the best-fit values that give the least difference between the observed flux points and the template SEDs. As shown in Figure 2.8b using data on G-type sources only, a photo-z can be estimated to $\pm$ 0.2 at high confidence ($\sim$ 90%). While this is true both for those sources with well-fit SDSS + NIR SEDs, and for those sources with SDSS photo-zs only, there is a slight systematic difference between $z_{\rm fit}$ and $z_{\rm phot}$. This slight systematic underestimate of $\Delta z \sim 0.05$–0.1 is the same as in Figure 2.8a, suggesting that the SDSS+NIR SEDs are a slightly better indication of the true redshift of these sources. However, we caution that this conclusion is based on a training set of < 10 sources. Even with this improvement in the precision, photo-zs are inadequate for a successful redshifted H I 21cm absorption since the above quoted precision ($\Delta z \sim 0.1$) can provide a search frequency accurate to no better than $\sim$ 40 MHz at $z \sim 1$. Given current levels of RFI at large radio telescopes world-wide this is still inadequate for a conclusive H I search (i.e., RFI-free regions are typically much smaller than this at $\nu < 1$ GHz) so that spectroscopic redshifts are still required.

But before we can accept that the photo-zs for all G-type sources are accurate to ± 0.1 in Δz, we need to scrutinize them further using previous results for luminous radio galaxies. The G-type sources can be plotted on the well-known $K - z$ diagram that relates the K-magnitude and the redshift (van Breugel et al. 1998). Willott et al. (2003) observed 49 radio galaxies with 151-MHz flux densities greater than 0.5 Jy and gave a $K - z$ relation fitted by a second-order polynomial

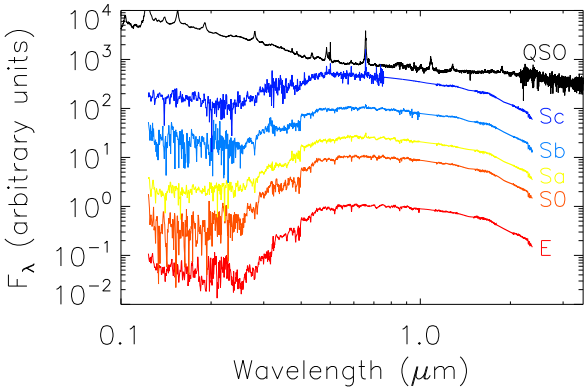

Figure 2.9 Template spectra for typical galaxies (Mannucci et al. 2001) and unreddeded QSOs (Vanden Berk et al. 2001; Glikman et al. 2006).

between K-magnitude and $\log_{10}z$,

$$K = 17.37 + 4.53\log_{10}z - 0.31(\log_{10}z)^2. \tag{2.1}$$

The dispersion in the correlation between these two quantities for radio-loud AGN is reported to be 0.58 mag up to $z = 3$. If a galaxy is formed at $z > 5$, undergoes an instantaneous starburst, then evolves passively and has a luminosity of $3L^*$ (typical giant elliptical galaxy hosting a radio-loud AGN) at present, the K-magnitude evolution of such a galaxy is close to the observed $K - z$ relation presented here. The observed $K - z$ values from our sample (excluding all Q and $Q + abs$ type sources) are plotted in Figure 2.10 together with the $K - z$ relation from Equation 2.1.

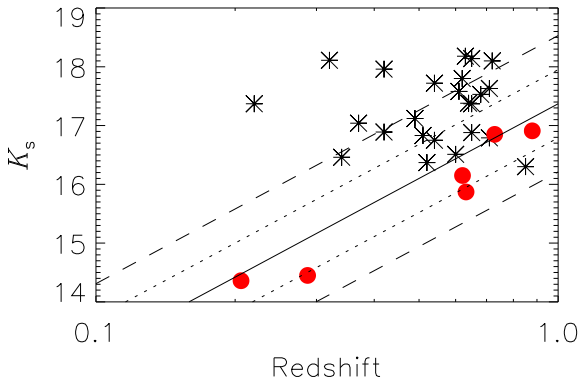

Figure 2.10 The observed $K_s - z$ diagram for objects whose SED is classified as G. The red dots represent objects with known spectroscopic redshifts. For the remainder, photometric redshifts are used (black asterisks). The black line is the best fit $K - z$ relation from Willott et al. (2003) with the dotted lines indicating the 1σ dispersion and the dashed lines indication the 2σ dispersion. Table 2.4 lists 9 sources which are fainter in K than the 2σ dispersion in the $(K - z)$ relation. See Section 2.4.3 for discussion.

While some sample sources conform quite well to the relationship (including all those with spectroscopic redshifts), there are a significant number which should have $z \gtrsim 1$ based on their $K-$band magnitudes and instead have $z_{\rm phot} < 1$. While we will not understand these discrepancies fully until spectroscopic redshifts are obtained, there are several possibilities including: (1) the host galaxies of some radio-loud AGN are not giant ellipticals; (2) the host galaxy, or at least the inner bulge of the host, is heavily extincted ($A_V > 20$) even at K-band (unlikely); (3) the SDSS galaxy is

not the AGN host but is rather a lensing, or simply a foreground, galaxy close to the sightline; and (4) the photo-zs are systematically too low due to the SDSS source being a composite of quasar and galaxy. Regardless of the solution for each case, the source offset from the $K-z$ relation can be used as a diagnostic that there is some unusual circumstance for that particular source and that the photo-z is unreliable. This appears to be the case for a large fraction of the sample.

Given Equation (1) and that the photo-zs are < 1, almost all G-type sources in Table 2.2 with $K \geq 17$ would be discrepant in Figure 2.10. Approximately 2/3 of the sources falls into this magnitude range and so have $z_K >> z_{\rm fit}$, where z_K is the redshift calculated in Equation (1) from the K-band mags in Table 2.2. The 21 discrepant objects in our sample have diffuse morphology in the NIR and so are either extincted even at K-band, are underluminous hosts, or are foreground galaxies unrelated to the AGN. *Spitzer Space Observatory* mid-IR photometry of these objects can determine if they are still extincted at K-band. In any case these sources are good candidates for foreground absorption. In Table 2.4 we list those 9 sources that are more than 2σ fainter than expected in K-band based on their photo-zs. Table 2.4 contains the following information by column: (1) source name; (2) $z_{\rm fit}$ from Table 2.2 column (7); (3) Hubble type from Table 2.2 column (8); (4) K-band magnitude from Table 2.2 column (4); (5) $z_{\rm K}$; and (6) the amount of redshift discrepancy, $\Delta z = z_K - z_{\rm fit}$.

2.5 Discussion of Selected Unusual Sources

J0003−1053 This is one of the reddest sources in our sample with $(r - Ks) = 5.5 \pm 0.3$. Although the flattening of the SED longward of 1 micron is comparable to what is expected for a $z \sim 2$ elliptical, the observed blue flux density is much too faint for this interpretation. So this source must be heavily obscured and is an excellent candidate for absorption studies at $z = 1.474$.

J0134+0003. The optical spectroscopic redshift of z=0.879 is from Drinkwater et al. (1997). Curran et al. (2006) observed this source for H I absorption but severe RFI was present around the expected frequency for H I at z=0.879.

J0751+2716 This source is a well-known "Einstein Ring" gravitational lens system with

Table 2.4. Sources with Discrepant Redshift Estimates.

Object	$z_{\rm fit}$[a]	Hubble Type[b]	$K_{\rm short}$[c]	$z_{\rm K}$	Δz
J1008+2401	0.62	Sc	17.80	1.25	0.63
J1043+0537	0.42	E	17.96	1.35	0.93
J1142+0235	0.37	Sa	17.04	0.85	0.48
J1148+1404	0.54	Sc	17.72	1.20	0.66
J1312+1710	0.63	Sc	18.18	1.52	0.89
J1354+5650	0.65	Sc	18.14	1.49	0.84
J1413+1509	0.22	S0	17.37	1.00	0.78
J1527+3312	0.32	Sb	18.11	1.46	1.14
J1616+2647	0.72	Sc	18.10	1.46	0.74

[a,b,c]Same as in Table 2.2.

$z_{\rm lens}$=0.35 and $z_{\rm QSO}$=3.2. While this source has been searched for redshifted H I 21 cm absorption by us, RFI was present which rendered the search inconclusive.

J0901+0304 Our DIS II spectrum yields $z = 0.2872$ based on strong narrow emission lines (Table 2.3; Figure 2.1) and led to the discovery of two components of redshifted H I 21 cm absorption at z=(0.2886, 0.2869). See Chapter 4.

J0920+2714 While this source is apparently associated with a rather normal bright (K=14.3) galaxy at $z_{\rm spec} = 0.2064$ (see Table 2.3), the FIRST radio source position is offset from the SDSS galaxy position by 1.7 arcsecs, an offset we have confirmed using new VLA and VLBA maps (see Chapter 3). An H I 21 cm absorption has been discovered at z= 0.2067 (see Chapter 4), consistent with the optical/NIR galaxy; i.e., the radio-loud AGN is background to the galaxy which creates the absorption.

J0939+0304 There is a point source seen only in the $K_{\rm s}$ image of this source but not at the center of the "host" galaxy (Figure 2.4). Regardless of whether the AGN is in an interacting system or whether the nuclear offset is due to a foreground galaxy, this source is an excellent candidate for absorption studies.

J1357+0046 The optical and NIR images show a faint linear string of knots, one of which is coincident with the radio source (see Chapter 3). Despite the absence of a spectroscopic redshift, we have detected H I 21 cm redshifted absorption at z=(0.7971, 0.7962). See Chapter 4 for details.

J1502+3753 A 5 GHz MERLIN image shows that the very blue optical/NIR counterpart sits in the center of a very extended, double-lobed source (Bolton et al. 2006). It is an unlikely candidate for radio absorption studies because the radio source structure is so extended, with only a weak compact, core component.

2.6 Discussion and Conclusions

With the goal of finding more high-z molecular absorbers, we have selected 80 strong radio sources with non-elliptical morphology in the optical and obtained NIR images at the APO 3.5m

telescope to further characterize their basic nature. Selection from the FIRST survey at $f_{20\mathrm{cm}} > 300$ mJy assures that we are targeting radio-loud AGN. An SDSS associated galaxy classification as non-elliptical gives us the greatest probability of finding plentiful gas, regardless of the reason for the late-type morphologies; e.g., the observed galaxy could either be a very young radio galaxy like a CSO or a foreground galaxy like in a gravitational lens system. In this first chapter we have presented a selection method for finding highly-obscured AGN and the optical-NIR data necessary both to confirm their morphology and judge the amount of obscuration present.

We have obtained NIR images of the sample to supply us with morphological information to check the SDSS classification, to extend the SDSS optical SEDs into the near-IR and to search for heavily obscured nuclei. Our NIR observations are consistent morphologically and photometrically with the expectation that many of these sources are heavily obscured systems. Analysis of the NIR morphology and of the optical/NIR SEDs provides a consistent picture of a heavily obscured, radio-loud AGN in most cases (see detailed discussion in Section 2.4.2). Also we have made a comparison between the photomeric redshifts and redshifts estimated from the K-band magnitudes. Because radio-loud AGN exhibit a significant "Hubble diagram" type correlation out to $z \sim$3, we can use the K-band magnitudes as a crude redshift indicator. For nine sources these K-band derived redshifts are significantly greater than their photo-zs (see Table 2.4 and Figure 2.8), indicating either that the host galaxy is not a giant elliptical or that the SDSS detected galaxy is forground to the AGN. In either case, these are excellent candidates for finding foreground absorption. However, this analysis also makes it clear that it is not advisable to use photometric redshifts of Q or Q+*abs*-type sources to conduct an efficient H I 21 cm absorption-line search. Additionally, Figure 2.8b shows that even when just the G-type sources are used, there is a systematic offset ($\Delta z \sim 0.05 - 0.1$) between the SDSS-derived photometric redshifts and the spectroscopic redshifts on top of the standard statistical errors present in the SDSS photo-z measurement ($\Delta z \sim$ 0.1–0.12). While it may be possible to conduct an H I 21 cm search of sources with G-type SEDs using photometric redshifts derived using both SDSS+NIR photometry (called z_{fit} herein), the statistical errors present (see Figure 2.8b) are too large to make such a search successful in the presence of the typical RFI

environment found at ground-based radio telescopes. Again a more accurate spectroscopic redshift is required.

While the optical/NIR properties described herein are compelling that most of the sources within sample are obscured, 'invisible AGN', it is also important to continue to scrutinize the basic properties of the radio sources against which absorption might be observed. Regardless of the amount of obscuration between us and the nucleus of an AGN, its radio spectrum is unlikely to show strong absorption lines if the radio source contains mostly geometrically-extended flux. This is because we are viewing the large majority of the source flux along unobscured lines-of-sight that avoid going through the host galaxy (and its obscured nucleus) entirely. VLA A-configuration and VLBA maps are in-hand and will provide identification of the most compact radio sources in this sample. These high resolution maps also will be used to make an accurate comparison between the radio source structure and the optical/NIR galaxy positions to identify potential intervening absorption candidates. These maps and their analysis will be presented in Chapter 3. Not only will VLA/VLBA observations discover new examples of CSOs and CSSs but they will also identify those obscured nuclei which are likely to show the strongest absorption due to possessing very compact radio continuum structures. Hopefully, some of the absorptions we discover will be molecular lines.

Chapter 3

High Resolution Radio Maps

This is the second part of the thesis aimed at finding redshifted absorption lines at radio frequencies. We selected a sample of 80 obscured radio-loud active galactic nuclei and presented their basic optical/NIR properties in Chapter 2. In this chapter, we present high-resolution radio images of these sources. All the sources were observed at 4.9 GHz and 8.5 GHz using the Very Large Array in A-configuration. We find that 52 sources are compact or have compact components with size $< 0\farcs5$ and flux density > 0.1 Jy at 4.9 GHz. The most compact sources were then observed with the Very Long Baseline Array at 1.4 GHz. Based on possessing components with high flux densities, 60 sources are good candidates for absorption-line searches. Eight new Compact Symmetric Object candidates have been identified. Together with 5 CSOs and 3 candidates already known, the detection rate of CSOs is $\sim$ two times higher than the detection rate previously found in flux-limited samples. We have also identified 2 candidates for gravitational lens systems and 5 candidates for intervening systems.

3.1 Introduction

Finding redshifted absorption lines at radio frequencies is an important yet challenging work. In fact, there are only 5 known systems with $z \gtrsim 0.2$ that have molecular absorption lines detected at radio frequencies. More detections will in general help us understand local physical properties of cold dense gas, its impact on the environment, and population statistics in space and time. A specific and promising application is to study a question with deep physical consequences: whether

there is spacial or temporal variation in fundamental physics parameters such as the fine-structure constant and the proton-to-electron mass ratio. To this end we have embarked on a systematic search using obscured active galactic nuclei (AGNs). In Chapter 2, we described the selection techniques of the sample and presented our near-infrared (NIR) photometry. After confirming that most of the objects are heavily obscured, in this chapter, using high-resolution radio images we identify sources that are compact enough at radio frequencies for absorptions to occur. By this we mean that a source dominated by a compact component will not have its absorption diluted by flux which comes to us unabsorbed.

Study of radio-loud AGNs shows that their host galaxies are almost exclusively ellipticals (e.g. Urry & Padovani 1995; Best et al. 2005) with little cold gas. But recent large surveys make it possible to find a group of rare cases that do not obey this rule. We selected a sample of 80 objects that only make up $\sim 5\%$ of luminous radio objects in the Faint Images of the Radio Sky at Twenty-cm (FIRST) survey (Becker et al. 1995). Sky regions of the FIRST survey are also covered by the Sloan Digital Sky Survey (SDSS; York et al. 2000). There are ~ 1500 sources with flux densities greater than 300 mJy in the April, 2003 version of the FIRST survey. About half of them have coincident optical galaxies detected by the SDSS Data Release 5 (DR5). The majority of these optical objects have typical elliptical morphology, i.e., a De Vaucouleurs radial profile and a large concentration index (Strateva et al. 2001). Only 80 of them have late-type morphology, suggesting they could be late-type galaxies, interacting galaxies or occasionally intervening systems with an object at a different redshift not related to the radio source. Either way the AGNs might be obscured and become "invisible" in the optical.

In Chapter 2, we also presented our NIR observations in three bands. The data were taken using the Astrophysical Research Consortium 3.5-m telescope at the Apache Point Observatory, which is also the site of the SDSS 2.5-m telescope. Our observing conditions were slightly better than the SDSS observing conditions. The morphology is largely consistent in NIR images compared to optical images. Analysis of the optical-NIR spectral energy distributions (SEDs) in Chapter 2 indicates that only a small number of sources have pure elliptical or un-reddened quasar-like SEDs.

Many of them show late-type SEDs or have significant absorption of quasar-like SEDs.

This sample may catch a unique evolutional phase or subclass of radio galaxies. The study of their host galaxies and multi-wavelength properties of the central AGNs could shed light on the formation and evolution of radio galaxies.

In Section 3.2, we describe our observing strategy and data reduction process. Observational results are presented in Section 3.3. We classify the radio morphologies in Section 3.4 and the radio spectral types in Section 3.5. Section 3.6 studies statistical relations between radio morphologies, radio spectral types, and optical+NIR SEDs. We then discuss intervening systems and gravitational lens systems in Section 3.7 and Section 3.8 respectively. Section 3.9 lists other special objects of interest that don't fit into previous categories. We then discuss and summarize the results of this chapter in Section 3.10.

3.2 Observation and Data Reduction

Except when archive data were available, we observed all the sources at 4.9 GHz and 8.5 GHz using the Very Large Array of NRAO [1] in its most extended A-configuration (VLA-A). Overall, we obtained data for 35 sources at both frequencies, 14 at 4.9 GHz only, and 8 at 8.5 GHz only. Our data were taken during June 2007 to August 2007 in the transitional period from VLA to Expanded VLA (EVLA; currently the Karl G. Jansky Very Large Array). The observations were made with an effective bandwidth of 100 MHz in full polarization centered at 4.860 GHz and 8.460 GHz. Typical on-source observing time was 4–5 minutes for each object at one frequency. We bracketed each target or a group of close-by targets with a single phase calibrator. Phase calibrators were point sources chosen from the VLA calibrator manual and close to targets. All phase calibrators have position accuracy better than $0\farcs002$, except the phase calibrator 1224+035 for objects J1202+1207 and J1238+0845, which has position accuracy of $0\farcs002$–$0\farcs01$, still quite small compared to $\sim 0\farcs1$–$0\farcs2$, the typical optical and NIR position uncertainty. Most phase calibrators have amplitude

[1] The National Radio Astronomy Observatory is a facility of the National Science Foundation operated under cooperative agreement by Associated Universities, Inc.

closure errors smaller than 3%, and a few have 3–10%. A target was usually observed in both bands before switching to the next sky position. One of the flux calibrators, 3C286, 3C147, or 3C48, was observed before or after each session.

VLA data were edited, calibrated, and imaged using the Astronomical Image Processing System (AIPS) Version 31DEC12 developed by the National Radio Astronomy Observatory. First, antenna gains are roughly estimated by comparing raw data of the flux calibrator and its model. Phase and amplitude corrections are then derived from the phase calibrator assuming point source structure, and absolute flux density is bootstrapped from the flux calibrator. After applying these corrections to the target source, an initial image is made by imaging and cleaning using the task "IMAGR". Finally, several iterations of self-calibrations are carried out to correct the spacial and temporal changes at the target position in real time. We have also reduced archive data when maps are not available in the literature.

We used the Very Long Baseline Array (VLBA) to obtain 1.4 GHz images for sources that are unresolved or have compact components in VLA-A images. Overall, 36 sources were observed in December 2009 and January 2010. The observations were centered at 1.446 GHz with an effective bandwidth of 32 MHz in full polarization. For each object, an $\sim$ 15-minute observing scan was conducted at three well-separated hour angles over a time span of 3–10 hours to achieve best *uv*-coverage. The target source was phase-referenced every 4–5 minutes by a phase calibrator within 5 degrees on the sky. The phase calibrators were selected from the VLBA Calibrator List. One of the strong, compact "fringe finders", DA193, 3C345, and 4C39.25, was observed before and after each of the four 10-hour observing sessions.

The data reduction of the VLBA observations was carried out in AIPS Version 31Dec10 following standard calibration and imaging procedures. Online measurements of antenna gains and system temperatures are used for the amplitude calibration. Offsets of sampler voltage is corrected by autocorrelation. We also apply corrections of ionosphere and Earth Orientation Parameters before delay, rate, and phase calibration. After the antenna parallactic angles are corrected, the "fringe finders" are used to correct instrumental phases and delays as well as bandpass shapes.

Fringe fitting is done on the phase-reference source to determine delays & rates and apply these corrections to the target and the phase-reference source itself. The data are then averaged over channels and IFs. The following imaging process is similar to VLA except self-calibration is also applied to phase calibrators because these are usually not point source under the high-resolution of VLBA. In each of the above steps, the results are carefully inspected and edited.

Please note that the VLA-A 8.5 GHz images have problematic astrometry in many cases. We initially reduced all VLA data using the Common Astronomy Software Applications (CASA) Version 2.3.1; then we found the center of many images was shifted from the pointing center to the brightest point probably due to problems in the self-calibration process. Reduction was only rectified using AIPS for 4.9 GHz data. This problem does not affect our conclusions because the relative structure of the 8.5 GHz images remains correct. However, caution must be exercised in identifying individual component correlation between frequencies. For this reason we display the 8.5 GHz images only in relative coordinates.

During the transitional period, there were problems in VLA-EVLA baselines including phase jumps and closure errors. Among the 27 antennas, 10 were EVLA antennas in June and July 2007, and 11 in August 2007. EVLA antennas were excluded for 4.9 GHz reduction in AIPS. Therefore the sensitivity is reduced by a factor of ~ 1.6.

The observing log is shown in Table 3.1 together with brief comments about individual sources. For the archive data, if a image is available in the literature, the reference paper is cited; otherwise we processed the archive data by ourselves and cite the project ID as a reference in Table 3.1. In the "Comments" column, "No flux cal." means the flux calibrator is completely flagged or not observed. In this case, a rough flux calibration is done by setting the flux density of the phase calibrator to its flux density reported in the VLA Calibrator Manual; "No flux detected" means the object is too faint/extended to be detected, or a few shortest baselines have signals but they are not sufficient to make a synthesized image.

Table 3.1. Observing Summary of the Radio Imaging.

Object	Radio Name	VLA 4.9 GHz		VLA 8.5 GHz		VLBI		Notes[a]
		Date	Ref.	Date	Ref.	Date	Ref.	
J0000−1054	PKS 2358-111	08/12/07	[1]	08/12/07	[1]			
J0003−1053	PKS 0001-111	08/12/07	[1]	08/12/07	[1]			
J0134+0003	4C -00.11	08/11/07	[1]					N1
J0249−0759	PKS 0247-08	08/11/07	[1]	08/11/07	[1]			N1,N2
J0736+2954	TXS 0733+300	07/08/07	[1]					N3
J0747+4618	4C +46.16		[13]		[13]			
J0749+2129	TXS 0746+216	06/16/07	[1]	06/16/07	[1]			
J0751+2716	B2 0748+27		[15]		[15]			N2
J0759+5312	TXS 0755+533	06/16/07	[1]	06/16/07	[1]	12/10/09	[1]	
J0805+1614	PKS 0802+16	09/13/87	[3]	07/08/07	[1]	12/08/09	[1]	
J0807+5327	TXS 0803+536	06/16/07	[1]	06/16/07	[1]	12/10/09	[1]	
J0824+5413	TXS 0820+543	06/16/07	[1]	06/16/07	[1]	12/10/09	[1]	N4
J0834+1700	4C +17.45			07/08/07	[1]	12/08/09	[1]	
J0839+2403	4C +24.18	07/08/07	[1]					
J0843+4215	B3 0840+424A				[16]		[14]	
J0901+0304	PKS 0859+032	07/06/07	[1]			01/03/10	[1]	
J0903+5012	4C +50.28	06/16/07	[1]	06/16/07	[1]			
J0905+4128	B3 0902+416		[13]		[13]		[12]	
J0907+0413	4C +04.30	12/17/84	[8]					
J0910+2419	4C +24.19	07/08/07	[1]					
J0915+1018	TXS 0912+105	02/07/85	[8]					
J0917+4725	B3 0914+476	06/16/07	[1]	06/16/07	[1]	12/10/09	[1]	
J0920+1753	4C +18.29	07/08/07	[1]			12/08/09	[1]	N4
J0920+2714	B2 0917+27B	06/17/07	[1]	06/17/07	[1]	12/08/09	[1]	
J0939+0304	PKS 0937+033	12/17/84	[8]			01/03/10	[1]	
J0945+2640	B2 0942+26	01/26/01	[9]			12/08/09	[1]	
J0951+1154	TXS 0948+121	02/08/85	[8]	07/06/07	[1]			
J1008+2401	B2 1005+24	07/08/07	[1]			12/08/09	[1]	N4
J1010+4159	B3 1007+422		[13]		[13]		[12]	
J1019+4408	B3 1016+443		[13]		[13]		[12]	
J1023+0424	TXS 1021+046	04/22/86	[4]	07/06/07	[1]	01/03/10	[1]	

Table 3.1 (continued)

Object	Radio Name	VLA 4.9 GHz		VLA 8.5 GHz		VLBI		Notes[a]
		Date	Ref.	Date	Ref.	Date	Ref.	
J1033+3935	B2 1030+39				[16]		[14]	
J1034+1112	TXS 1031+114	06/17/07	[1]	06/17/07	[1]			
J1043+0537	4C +05.45	07/06/07	[1]			01/03/10	[1]	N4
J1045+0455	TXS 1043+051	06/17/07	[1]	06/17/07	[1]			
J1048+3457	4C +35.23	03/08/86	[2]			12/08/09	[1]	
J1120+2327	4C +23.27							
J1125+1953	PKS 1123+201	07/06/07	[1]			12/08/09	[1]	
J1127+5743	TXS 1124+579	06/16/07	[1]	06/16/07	[1]	12/10/09	[1]	
J1129+5638	TXS 1126+569	06/16/07	[1]	06/16/07	[1]	12/10/09	[1]	
J1142+0235	TXS 1139+028	02/08/85	[8]	07/08/07	[1]	01/03/10	[1]	N4
J1147+4818	4C +48.33	06/17/07	[1]	06/17/07	[1]	12/10/09	[1]	
J1148+1404	TXS 1145+143	04/08/86	[4]	07/06/07	[1]	01/03/10	[1]	
J1202+1207	TXS 1200+124	06/17/07	[1]	06/17/07	[1]	01/03/10	[1]	
J1203+4632	B3 1200+468	07/08/07	[1]					
J1207+5407	4C +54.26	06/16/07	[1]	06/16/07	[1]			
J1215+1730	4C +17.54				[16]		[14]	
J1228+5348	4C +54.28	06/16/07	[1]	06/16/07	[1]			
J1238+0845	TXS 1235+090	06/17/07	[1]	06/17/07	[1]	01/03/10	[1]	
J1300+5029	TXS 1258+507				[17]		[14]	
J1312+1710	TXS 1310+174	04/08/86	[4]	07/08/07	[1]	12/08/09	[1]	
J1315+0222	TXS 1312+026	12/17/84	[8]	07/08/07	[1]			
J1341+1032	4C +10.36	06/17/07	[1]	06/17/07	[1]			
J1345+5846	4C +59.20	06/17/07	[1]	06/17/07	[1]	12/10/09	[1]	
J1347+1217	4C +12.50							
J1348+2415	4C +24.28		[11]				[10]	
J1354+5650	4C +57.23	06/17/07	[1]	06/17/07	[1]			
J1357+0046	PKS 1355+01	06/17/07	[1]	06/17/07	[1]	01/03/10	[1]	
J1410+4850	TXS 1408+490	07/15/07	[1]	07/15/07	[1]	12/10/09	[1]	
J1413+1509	TXS 1411+154	07/15/07	[1]					
J1414+4554	B3 1412+461				[17]		[18]	
J1415+1320	PKS 1413+135						[19]	

We have an almost complete set of VLA-A 4.9 GHz images from our own data, the literature, and archive data processed by us. A few exceptions without VLA-A images are objects that have been well studied or proven to be unresolved in VLA-A 8.5 GHz image so are likely unresolved at 4.9 GHz as well. The 8.5 GHz data we summarize in Table 3.1 include our own data, and data from the literature or archives that would help us understand the nature of the source. That is to say, if a source was of little interest based on its VLA-A 4.9 GHz image (for example, consisting of two well-separated lobes with an optical/NIR source right between them), we did not process its archive data.

3.3 Observational Results

Basic image parameters are listed in Table B.1 of Appendix B including $r.m.s.$ (σ) and maximum flux densities, as well as the major and minor axis sizes, and position angle (P.A.) of the restored beam. The median $r.m.s.$ is 0.19, 0.12, and 0.36 mJy at 4.9 GHz, 8.5 GHz, and 1.4 GHz respectively. Dynamical range of a few hundreds is easily reached through self-calibration. The median major axis value of the restored beam is $0\farcs5$, $0\farcs3$, and 15 miliarc seconds at 4.9 GHz, 8.5 GHz, and 1.4 GHz respectively for the restored beam. For a few VLBA 1.4 GHz observations, the data were tapered to exclude long baselines with no signal.

Our VLA and VLBA images are shown in Figure B.1 of Appendix B. Each image has five contour levels ranging from 3σ to $0.8S_{\rm m}$ and logarithmically spaced, where $S_{\rm m}$ is the maximum flux density, i.e., assuming $R = 0.8S_{\rm m}/3\sigma$, the contour levels are (1, $R^{1/4}$, $R^{2/4}$, $R^{3/4}$, R)$\times 3\sigma$. A negative 3σ value is shown as a dashed line. In the 4.9 GHz and 1.4 GHz images, the optical centroid position in the r-band is labeled in blue with uncertainties along the RA and Dec axes. The red cross is the NIR centroid position (usually K_s-band) with uncertainties. A green rectangle in a 4.9 GHz image represents the boundary of the object's 1.4 GHz VLBA image where available. Therefore even if an object's NIR and/or optical position crosses are completely or partly outside of its 1.4 GHz image, their relative positions can be inferred from the crosses and rectangle in its 4.9 GHz image. Center coordinates of the 4.9 GHz and 1.4 GHz images are shown at the bottom

Table 3.1 (continued)

Object	Radio Name	VLA 4.9 GHz		VLA 8.5 GHz		VLBI		Notes[a]
		Date	Ref.	Date	Ref.	Date	Ref.	
J1421−0246	4C -02.60	07/10/07	[1]	07/10/07	[1]			
J1424+1852	4C +19.47	07/10/07	[1]	07/10/07	[1]			
J1502+3753	B2 1500+38	07/15/07	[1]	07/15/07	[1]			
J1504+5438	TXS 1503+548				[16]		[14]	
J1504+6000	TXS 1502+602	06/17/07	[1]	06/17/07	[1]	01/11/10	[1]	
J1523+1332	4C +13.54	07/10/07	[1]	07/10/07	[1]	01/11/10	[1]	
J1527+3312	B2 1525+33	07/15/07	[1]	07/26/91	[6]	01/11/10	[1]	N5
J1528−0213	PKS 1525-020	07/10/07	[1]	07/10/07	[1]			
J1548+0808	TXS 1545+082	07/15/07	[1]	07/15/07	[1]	01/11/10	[1]	
J1551+6405	TXS 1550+642				[16]		[14]	
J1559+4349	4C +43.36	06/23/99	[7]			01/11/10	[1]	
J1604+6050	TXS 1603+609	06/17/07	[1]	06/17/07	[1]	01/11/10	[1]	
J1616+2647	PKS 1614+26	07/15/07	[1]	05/04/90	[5]	01/11/10	[1]	N2
J1625+4134	4C +41.32				[16]		[14]	
J1629+1342	4C +13.60	07/15/07	[1]	07/15/07	[1]			
J1633+4700	4C +47.43	07/15/07	[1]	07/15/07	[1]	01/11/10	[1]	
J1724+3852	B2 1722+38	07/15/07	[1]	07/15/07	[1]	01/11/10	[1]	
J2203−0021	4C -00.79	08/11/07	[1]					N1

References. — [1] This work; [2] VLA project AA052; [3] VLA project AA073; [4] VLA project AB375; [5] VLA project AB568; [6] VLA project AB611; [7] VLA project AB922; [8] VLA project AH167; [9] VLA project AS704; [10] Cai et al. (2002); [11] Chambers et al. (1996); [12] Dallacasa et al. (2002a); [13] Fanti et al. (2001); [14] Helmboldt et al. (2007); [15] Lehar et al. (1997); [16] Myers et al. (2003); [17] Patnaik et al. (1992); [18] Peck & Taylor (2000); [19] Perlman et al. (2002).

[a]N1–N5 in this column mean: N1, no flux calibration on the VLA-A 4.9 GHz image; N2, no flux calibration on the VLA-A 8.5 GHz image; N3, not detected on the VLA-A 4.9 GHz image; N4, not detected on the VLBA 1.4 GHz image; N5, all data are flagged on the VLA-A 4.9 GHz image.

of each plot. Relative positions along RA and Dec are labeled on the X and Y axes respectively. Please note that absolute 8.5 GHz astrometry is problematic and the central coordinates of the 8.5 GHz images are for this reason not given.

The 4.9 GHz images are overlaid with NIR images (see Chapter 2). K_s-band images are used with two exceptions. J1125+1953 was not detected in the Ks-band so its J-band image is used. J1502+3753 was not observed in the Ks-band so its H-band image is used. NIR images have been re-gridded and smoothed by cubic interpolation to match the astrometry of the 4.9 GHz images. Pixel counts are displayed by grayscale with the following approach. On a grayscale of 0 (white) to 1 (dark), 1 represents the maximum pixel count of the object; 0 and 0.2 represent the -2.5σ and $+2.5\sigma$ noise of the sky background respectively; between 0 to 0.2 and 0.2 to 1, the gray shade scales linearly with pixel counts.

For each radio image, we fit major components with elliptical Gaussian profiles and report the results in Tables B.2, B.3, and B.4 of Appendix B for the 4.9 GHz, 8.5 GHz, and 1.4 GHz images respectively. Tables B.2 and B.4 list (1) object name, (2) component ID, (3,4) RA and Dec of the component, (5,6) peak and integrated flux density, and (7,8,9) deconvolved major axis, minor axis, and P.A. of the Gaussian component. The 8.5 GHz results are shown in Table B.3 without coordinates information for the reason mentioned in Section 3.2. Without reliable astrometry, we match components at 4.9 GHz and 8.5 GHz images by eye and mark the same component with the same letter ID. The associations are unambiguous in all cases. Spectral index data for each component in Column (8) of Table B.1 is calculated between 4.9 GHz and 8.5 GHz. In cases in which one component at 4.9 GHz is resolved into several components in 8.5 GHz, each sub-component is named by the letter ID at 4.9 GHz followed by a number and their flux densities are summed in calculating the spectral index. Note well, that because the beam sizes differ between 4.9 GHz and 8.5 GHz in our observations, these spectral indices should be treated as estimates. The Gaussian profile may not be a good estimate for resolved components with complicated structures, but we make sure total flux density is conserved during the fit.

3.4 Morphological Classification

We find that 52 out of the 80 sources are compact or have compact components with size $< 0\farcs5$ and flux density > 0.1 Jy at 4.9 GHz. Twenty-nine objects are unresolved in VLA-A images and their morphological types are determined by very-long-baseline-interferometry (VLBI) observations. Depending on the jet inclination angle, there are two major types, double-lobe and core-jet objects. Morphological classification is shown in Column (15) of Table 3.2.

Table 3.2. Summary of the Radio Properties.

Object	z	SED Type	G Type	S_{365} (Jy)	$S_{1.4}$ (Jy)	$S_{4.9}$ (Jy)	$\alpha_{\rm l}$	$\alpha_{\rm h}$	Spec. Type	LAS ($''$)	LLS (kpc)	Freq. (GHz)	Telescope	Morph. Type	CAND	INT
(1)	(2)	(3)	(4)	(5)	(6)	(7)	(8)	(9)	(10)	(11)	(12)	(13)	(14)	(15)	(16)	(17)
J0000−1054		Q+abs		2.20	0.40	0.07	−1.28	-1.41	USS	1.5	< 12.9	4.9	VLA-A	MSO	Y	
J0003−1053	1.474 [a]	Q+abs		1.47	0.40	0.14	−0.97	-0.84	SS	2.3	20.0	4.9	VLA-A	CPLX	Y	C
J0134+0003	0.879	G	Sa	1.11	0.89	0.46	−0.17	-0.53	GPS	0.018	0.140	2.3	VLBI	CSO:	Y	
J0249−0759		G+Q		2.34	0.62	0.19	−0.99	-0.95	SS	1.9	< 16.3	4.9	VLA-A	LSO	N	
J0736+2954		G+Q		0.35	0.49	0.52	0.26	0.05	FS	0.014	< 0.118	5	VLBI	CJ	Y	
J0747+4618	2.926	Q+abs		2.00	0.52	0.13	−1.00	-1.09	USS				VLA-A	LSO	N	
J0749+2129	0.52 *	G	S0	1.13	0.42	0.12	−0.73	-1.05	SS	2.6	~ 16.1	4.9	VLA-A	CPLX	Y	
J0751+2716	3.200 [b]	G	Sc	1.47	0.60	0.21	−0.66	-0.83	SS				VLA-A	GA	Y	Y
J0759+5312		G+Q		1.12	0.33	0.15	−0.91	-0.63	SS	1.4	< 11.9	4.9	VLA-A	MSO	Y	
J0805+1614	0.632 :	G	Sc	1.78	0.63	0.20	−0.77	-0.94	SS	0.45	: 3.10	8.5	VLA-A	MSO	Y	
J0807+5327		Q+abs		0.83	0.33	0.11	−0.69	-0.92	SS	1.1	< 9.1	4.9	VLA-A	MSO	Y	C
J0824+5413	0.639	G+Q		1.12	0.39	0.15	−0.79	-0.77	SS	1.8	12.4	4.9	VLA-A	MSO	Y	
J0834+1700		Q+abs		5.64	1.64	0.58	−0.92	-0.84	SS		$<$		VLA-A	SL	Y	Y
J0839+2403		G+Q		1.77	0.66	0.23	−0.73	-0.84	SS	4.1	< 35.3	4.9	VLA-A	LSO	N	
J0843+4215	0.60 *	G	Sb	2.50	1.46	0.58	−0.40	-0.74	SS✓	0.021	~ 0.143	5	VLBI	CJ	Y	
J0901+0304	0.287	G	Sc	0.56	0.38	0.26	−0.28	-0.31	GPS✓	0.011	0.047	1.4	VLBI	PS	Y	
J0903+5012		G+Q		2.78	0.95	0.31	−0.80	-0.90	SS	3.4	< 29.0	4.9	VLA-A	LSO	N	
J0905+4128		G+Q		1.10	0.48	0.16	−0.61	-0.90	SS	0.330	< 2.824	1.66	VLBI	MSO	Y	
J0907+0413	1.10 *	G	Sc	1.85	0.70	0.19	−0.72	-1.04	SS	2.6	~ 21.4	4.9	VLA-A	LSO	N	
J0910+2419		G+Q		2.72	0.83	0.21	−0.89	-1.12	SS	4.2	< 36.0	4.9	VLA-A	LSO	N	

Table 3.2 (continued)

Object	z	SED Type	G Type	S_{365} (Jy)	$S_{1.4}$ (Jy)	$S_{4.9}$ (Jy)	$\alpha_{\rm l}$	$\alpha_{\rm h}$	Spec. Type	LAS ($''$)	LLS (kpc)	Freq. (GHz)	Telescope	Morph. Type	CAND	INT
(1)	(2)	(3)	(4)	(5)	(6)	(7)	(8)	(9)	(10)	(11)	(12)	(13)	(14)	(15)	(16)	(17)
J0915+1018		G+Q		0.97	0.35	0.18	−0.76	-0.56	SS	1.9	< 16.5	4.9	VLA-A	LSO	Y	
J0917+4725		G+Q		1.21	0.35	0.13	−0.91	-0.81	SS	0.6	< 5.0	4.9	VLA-A	SL	N	Y
J0920+1753	0.68 *	G	Sc	3.45	1.08	0.27	−0.86	-1.11	SS	0.4	~ 3.0	4.9	VLA-A	MSO	Y	
J0920+2714	[c]	G	S0	1.60	0.46	0.13	−0.93	-1.04	SS	2.9	< 24.7	4.9	VLA-A	LSO	Y	Y
J0939+0304	0.34 *	G	S0	0.75	0.47	0.23	−0.35	-0.56	FS:	0.230	~ 1.107	1.4	VLBI	CJ	Y	
J0945+2640		Q		1.56	0.57	0.20	−0.74	-0.86	SS	5.3	< 45.7	4.9	VLA-A	LSO	N	
J0951+1154	0.65 *	G	Sc	1.25	0.37	0.11	−0.90	-0.99	SS	2.9	~ 20.1	4.9	VLA-A	LSO	N	
J1008+2401	0.62 *	G	Sc	1.36	0.43	0.12	−0.85	-1.05	SS	2.0	~ 13.6	4.9	VLA-A	MSO	Y	
J1010+4159	0.71 *	G	Sc	1.40	0.42	0.14	−0.90	-0.88	SS	0.265	~ 1.904	1.66	VLBI	MSO	Y	
J1019+4408		Q+abs		1.04	0.34	0.07	−0.82	-1.27	SS	0.155	< 1.326	1.66	VLBI	CSO	Y	
J1023+0424	0.71 *	G	Sc	0.90	0.33	0.11	−0.75	-0.89	SS	0.56	~ 4.03	8.5	VLA-A	MSO	Y	
J1033+3935	1.095 :	G	Sc	0.82	0.41	0.65	−0.52	0.37	FS	0.005	0.039	5	VLBI	CJ	Y	
J1034+1112		G+Q		4.59	1.21	0.36	−0.99	-0.98	SS	4.9	< 41.7	4.9	VLA-A	LSO	N	
J1043+0537	0.42 *	G	E	2.67	0.67	0.20	−1.03	-0.97	USS	6.6	~ 36.5	4.9	VLA-A	LSO	N	
J1045+0455		Q+abs		1.18	0.38	0.14	−0.84	-0.82	SS	2.9	< 24.8	4.9	VLA-A	LSO	N	
J1048+3457	1.594	Q+abs		2.44	1.05	0.38	−0.63	-0.81	SS				VLBI	CPLX	Y	
J1120+2327	1.819	Q		5.48	1.38	0.36	−1.02	-1.09	USS				VLA-A	LSO	N	
J1125+1953		Q		1.60	0.43	0.15	−0.98	-0.83	SS		$<$	4.9	VLA-A	CJ	Y	
J1127+5743	0.49 *	G	Sb	1.70	0.65	0.19	−0.71	-1.00	SS	0.49	~ 2.95	8.5	VLA-A	MSO	Y	
J1129+5638	0.892	G	Sa	1.25	0.50	0.12	−0.68	-1.16	SS	0.080	0.622	1.4	VLBI	CSO:	Y	

Table 3.2 (continued)

Object	z	SED Type	G Type	S_{365} (Jy)	$S_{1.4}$ (Jy)	$S_{4.9}$ (Jy)	$\alpha_{\rm l}$	$\alpha_{\rm h}$	Spec. Type	LAS ($''$)	LLS (kpc)	Freq. (GHz)	Telescope	Morph. Type	CAND	INT
(1)	(2)	(3)	(4)	(5)	(6)	(7)	(8)	(9)	(10)	(11)	(12)	(13)	(14)	(15)	(16)	(17)
J1142+0235	0.37 *	G	Sa	0.89	0.38	0.20	−0.63	-0.50	SS✓	1.5	~ 7.7	4.9	VLA-A	MSO	Y	
J1147+4818		Q		1.89	0.50	0.12	−0.99	-1.18	SS	1.0	< 8.3	4.9	VLA-A	CJ/GA	Y	C
J1148+1404	0.54 *	G	Sc	1.00	0.33	0.10	−0.84	-0.97	SS	1.5	~ 9.3	4.9	VLA-A	MSO	Y	
J1202+1207		G+Q		1.01	0.37	0.16	−0.75	-0.69	SS	0.098	< 0.840	1.4	VLBI	CSO:	Y	
J1203+4632	0.36 *	G	E	0.52	0.42	0.20	−0.17	-0.58	GPS	0.040	~ 0.200	5	VLBI	CSO:	Y	
J1207+5407	0.61 *	G	Sc	2.58	0.60	0.16	−1.09	-1.05	USS	1.4	~ 9.7	4.9	VLA-A	MSO	Y	
J1215+1730	0.268	Q+abs		2.40	1.03	0.62	−0.63	-0.41	SS✓	0.135	0.551	5	VLBI	CSO:	Y	
J1228+5348		G+Q		1.94	0.53	0.15	−0.96	-1.02	SS	4.9	< 41.7	4.9	VLA-A	LSO	N	
J1238+0845	0.65 *	G	Sc	1.25	0.41	0.08	−0.82	-1.32	SS	3.2	~ 22.0	4.9	VLA-A	LSO	N	
J1300+5029	1.561	Q		0.67	0.38	0.39	−0.43	0.03	FS			4.9	VLA-B	CJ	Y	
J1312+1710	0.63 *	G	Sc	0.95	0.34	0.11	−0.78	-0.90	SS	0.056	~ 0.385	1.4	VLBI	CSO:	Y	
J1315+0222	0.85 *	G	Sc	1.33	0.52	0.16	−0.70	-0.93	SS	2.4	~ 18.2	4.9	VLA-A	LSO	Y	
J1341+1032		Q+abs		2.62	0.69	0.17	−1.00	-1.12	USS	1.0	< 8.7	4.9	VLA-A	MSO	Y	C
J1345+5846		G+Q		1.81	0.42	0.12	−1.08	-1.00	USS	2.3	< 19.3	4.9	VLA-A	LSO	N	
J1347+1217	0.122	G	Sa	8.31	4.86	3.09	−0.40	-0.36	FS	0.100	0.217	1.66	VLBI	CSO	Y	
J1348+2415	2.879	Q		2.74	0.56	0.14	−1.19	-1.14	USS			4.9	VLA-A	LSO	N	
J1354+5650	0.65 *	G	Sc	1.86	0.72	0.28	−0.71	-0.76	SS	2.5	~ 17.4	4.9	VLA-A	LSO	N	
J1357+0046		G+Q		4.74	2.00	0.49	−0.64	-1.11	SS	0.086	0.647	1.4	VLBI	CSO:	Y	
J1410+4850	0.592	G+Q		0.76	0.33	0.11	−0.63	-0.86	SS	0.043	0.284	1.4	VLBI	CSO:	Y	
J1413+1509	0.22 *	G	S0	< 0.25	0.50	0.41	> 0.52	-0.16	GPS✓	0.015	~ 0.051	5	VLBI	CSO	Y	

Table 3.2 (continued)

Object	z	SED Type	G Type	S_{365} (Jy)	$S_{1.4}$ (Jy)	$S_{4.9}$ (Jy)	$\alpha_{\rm l}$	$\alpha_{\rm h}$	Spec. Type	LAS ($''$)	LLS (kpc)	Freq. (GHz)	Telescope	Morph. Type	CAND	INT
(1)	(2)	(3)	(4)	(5)	(6)	(7)	(8)	(9)	(10)	(11)	(12)	(13)	(14)	(15)	(16)	(17)
J1414+4554	0.38 *	G	S0	0.40	0.41	0.21	0.02	-0.53	GPS	0.031	~ 0.162	5	VLBI	CSO	Y	
J1415+1320	0.247	G	Sb	2.74	1.18	0.84	-0.63	-0.27	FS	0.117	0.450	1.66	VLBI	CSO	Y	
J1421−0246	0.49 *	G	E	1.73	0.55	0.16	-0.85	-0.97	SS	3.5	~ 21.2	4.9	VLA-A	LSO	N	
J1424+1852		Q+abs		2.69	0.70	0.19	-1.00	-1.06	USS	1.6	< 13.8	4.9	VLA-A	MSO	Y	
J1502+3753		Q+abs		1.11	0.34	0.12	-0.89	-0.81	SS	2.0	< 17.5	4.9	VLA-A	LSO	N	
J1504+5438	0.621	G	Sc	0.78	0.38	0.17	-0.53	-0.64	SS			5	VLBI	PS	Y	
J1504+6000	1.024	Q		5.22	1.55	0.44	-0.90	-1.01	SS	0.62	5.0	8.5	VLA-A	MSO	Y	
J1523+1332		Q+abs		1.59	0.35	0.11	-1.13	-0.92	USS	3.7	< 32.0	4.9	VLA-A	LSO	N	
J1527+3312	0.32 *	G	Sb	0.75	0.32	0.11	-0.64	-0.89	SS		$\sim$		VLBI	CPLX	Y	
J1528−0213	0.54 *	G	E	1.06	0.47	0.16	-0.61	-0.85	SS	1.4	~ 8.8	4.9	VLA-A	MSO	Y	
J1548+0808	0.51 *	G	E	1.79	0.63	0.21	-0.78	-0.89	SS	0.246	~ 1.513	1.4	VLBI	MSO	Y	
J1551+6405		G+Q		0.59	0.68	0.21	0.10	-0.96	GPS	0.074	< 0.630	5	VLBI	CJ	Y	
J1559+4349	1.232	Q+abs		2.08	0.75	0.19	-0.76	-1.12	SS	0.8	6.6	4.9	VLA-A	MSO/GA	Y	C
J1604+6050	0.559	G	S0	0.64	0.59	0.20	-0.06	-0.88	GPS	0.014	0.089	1.4	VLBI	CSO:	Y	
J1616+2647	0.755	G	Sc	1.71	1.41	0.70	-0.14	-0.56	GPS	0.124	0.915	1.4	VLBI	CSO	Y	
J1625+4134	2.550	Q		2.47	1.72	1.36	-0.27	-0.19	FS	0.006	0.049	5	VLBI	CJ	Y	
J1629+1342	0.74 *	G	Sc	1.95	0.71	0.23	-0.75	-0.92	SS	5.1	~ 37.4	4.9	VLA-A	LSO	N	
J1633+4700		Q+abs		1.46	0.46	0.15	-0.87	-0.91	SS	5.2	< 44.5	4.9	VLA-A	LSO	N	
J1724+3852	1.542	Q+abs		0.88	0.37	0.14	-0.64	-0.77	SS	0.040	0.340	1.4	VLBI	CSO:	Y	
J2203−0021	0.729	G	Sc	1.71	0.61	0.18	-0.77	-0.98	SS	0.9	6.4	4.9	VLA-A	MSO	Y	

In Table 3.2, we list each object's largest angular size in Column (11) and largest linear size in Column (12). Because the size is frequency and resolution dependent, we also list the observing frequency in Column (13) and telescope/configuration in Column (14). When an object's spectroscopic redshift is not available, its photometric redshift is used to estimate its linear size. In Chapter 2, we fit photometric redshifts and Hubble types from optical+NIR SEDs for objects with galaxy-like SEDs, and the redshift uncertainties are within $\sim$ 0.1–0.2. For objects with a quasar-like signature in their optical+NIR SEDs, due to the uncertain amount of quasar contribution and extent of obscuration, it is implausible to obtain a reliable photometric redshift. In this case, an upper limit is set by using the maximum angular scale possible over cosmic time, 8.6 kpc/$''$ at $z \sim 1.6$. We show redshifts, optical+NIR SED types, and Hubble types in Column (2), (3), and (4) respectively in Table 3.2.

Most of the objects show classic double-lobe structure with or without a core. The separation of the two lobes ranges from tens of parsecs to tens of kilo-parsecs. We adopt the terminology introduced by Fanti et al. (1995) to indicate a separation of $>$ 15 kpc, 15 kpc – 1 kpc, and $<$ 1 kpc with the terms Large Symmetric Object (LSO), Medium-size Symmetric Object (MSO), and Compact Symmetric Object (CSO) respectively. In general, 1 kpc is considered a typical size of the narrow-line emission regions around AGNs, and 15 kpc represents a typical size of the optical host galaxies. LSOs are classic FRI or FRII objects with extended radio emission that could expand to scales much larger than their host galaxies. These objects are not likely to be intrinsic absorbers due to their extended structure and large scale, unless a strong core is present. In contrast, MSOs and CSOs are better candidates because of their compact structure and small scale close-in to the gas-rich galaxy with which they are identified. We find 24 LSOs, 22 MSOs, and 16 CSOs in the sample. However, from its morphology at one-band alone, a CSO can hardly be discriminated from a core-jet object if there are multiple jet components without spectral index data on such a small scale. Therefore 10 of the CSOs remain candidates as multi-wavelength and multi-epoch observations are necessary to pin down "true" CSOs. CSOs are discussed in detail in Section 3.4.1.

Table 3.2 (continued)

Object	z	SED Type	G Type	S_{365} (Jy)	$S_{1.4}$ (Jy)	$S_{4.9}$ (Jy)	$\alpha_{\rm l}$	$\alpha_{\rm h}$	Spec. Type	LAS ($''$)	LLS (kpc)	Freq. (GHz)	Telescope	Morph. Type	CAND	INT
(1)	(2)	(3)	(4)	(5)	(6)	(7)	(8)	(9)	(10)	(11)	(12)	(13)	(14)	(15)	(16)	(17)

Note. — Columns list: (1) object name, (2) redshift of the radio source, where suffix (*) indicates a photometric redshift fit by its optical-NIR SED in Chapter 2, and suffix (:) means the redshift is uncertain, (3) optical+NIR SED type from Chapter 2, (4) Hubble type for "G"-type objects in column (3), (5) flux density at 365 MHz, (6) flux density at 1.4 GHz, (7) flux density at 4.9 GHz, (8) spectral index between 365 MHz and 1.4 GHz, (9) spectral index between 1.4 GHz and 4.9 GHz, (10) spectral type, where the check mark ✓ means the classification has been modified using more information in addition to the spectral indices in column (8) and (9), (11) largest angular size between major components, (12) largest linear size corresponding to column (6), where "∼" means a photometric redshift is used and "<" means $z = 1.6$ is used to obtain largest size possible, (13) and (14) frequency and telescope with which the LAS and LLS are measured, (15) morphological classification, where CPLX means complex, CJ means core-jet, GA means gravitational arc, PS means point source and SL means single lobe, (16) whether the object remains a good candidate (CAND) for absorption-line search in radio frequencies, and (17) whether it is an intervening (INT) system (Y) or candidate (C), see Sections 3.7–3.9 for more details.

[a]Likely the redshift of the background radio object in an intervening system.

[b]The redshift of the background radio object gravitationally-lensed by a foreground galaxy at $z = 0.349$.

[c]This is an intervening system. The foreground galaxy has a redshift of 0.206. The radio source is in the background and its redshift is unknown.

If the jet of a radio source is inclined toward us, the radiation close to the core could be strongly boosted due to relativistic beaming of the jet. Radio structure of these sources generally consists of a compact core and some extended jet components aligned on one side of the core (core-jet morphology). Sometimes a weak counterjet is also detected. These are also good candidates for absorption-line searches.

Morphological classifications are listed in Table 3.2. Except for the double-lobe and core-jet types mentioned above, there are four minor types: single-lobe, gravitational-arc, complex, and point-source objects. J0834+1700 and J0917+4725 have a single, extended component in their VLA-A images. We call them single-lobe objects since they are very likely one of the two lobes in a classic double-lobe structure. J0834+1700 and J0917+4725 are discussed in detail in Sections 3.9 and respectively. J0751+2716 is a gravitational-lens system with an arc shape in its radio image (Lehar et al. 1997). We find two more objects showing gravitational arcs, J1147+4818 and J1559+4349. Four objects are classified as complex objects for their atypical morphologies. All the above sources will be discussed in detail in subsequent sections. The point-source objects, J0901+0304 and J1504+5438, are unresolved in their VLBI images and most likely core-jet objects without the jet components detected.

3.4.1 Compact Symmetric Objects (CSOs)

CSOs have symmetric double-lobe structure fully within 1 kpc. Rather than "frustrated" jets obstructed by a dense inter-stellar medium (ISM), they are now believed to be young objects with age $\lesssim 10^4$ yr that will evolve into classic FRI or FRII objects (Fanti et al. 1995; Begelman 1996; Readhead et al. 1996). The hotspot advance speed of CSOs is found to be sub-luminal (Owsianik & Conway 1998), in contrast to core-jet objects. CSOs also have low variability in brightness and low polarization. All of these are consistent with the speculation that the jets are propagating nearly perpendicular to the line of sight. CSO candidates are often selected based on their morphologies in one band. But further observations are often needed to confirm a CSO because they usually have complicated structures caused by frequent central activities and interactions with various ISM

components around AGNs. It is preferred that a flat-spectrum core between the symmetric lobes is identified using multi-wavelength observations. However, the cores of CSOs are often weak or undetected. In this case, the advance speed of hotspots and jet components can be measured to make sure there is no strong beaming effect and the jet-propagating axis has a large inclination angle. The detection rate of H I 21 absorption is exceptionally high in CSOs, $\sim 50\%$. One of the two known intrinsic atomic and molecular absorbers, J1415+1320, is a CSO Perlman et al. (1996, 2002).

There are 5 known CSOs in our sample. J1019+4408 was observed by Dallacasa et al. (2002b) at 1.67 GHz and exhibits all the typical CSO features in morphology, i.e., symmetric, edge-brightened, and S-shaped lobes. J1347+1217 is an ultra-luminous infrared galaxy at $z = 0.122$ with ongoing merging activity. It was observed using VLBI by Stanghellini et al. (1997) at 5 GHz, and a core was confirmed by Stanghellini et al. (2001) at 15 GHz and Xiang et al. (2002) at 1.66 GHz although luminosities of the two lobes are quite asymmetric especially at high frequency. Lister et al. (2003) found that J1347+1217 has atypical CSO features including superluminal motions and large linear polarization, suggesting a smaller-than-typical inclination angle. H I 21-cm absorption is detected towards the weak lobe (Morganti et al. 2004). J1413+1509 was classified by Helmboldt et al. (2007) as a CSO candidate at 5 GHz and later confirmed by Tremblay (2011) using VLBI observations at 4.8 GHz, 8.3 GHz, and 15 GHz. J1414+4554 also has typical CSO morphology; Gugliucci et al. (2005) did not detect motions between the two hotspots from 1997 to 2002 and set an upper limit of 0.014 mas yr^{-1}.This indicates a relative projected velocity of 0.24 c assuming a photometric redshift $z = 0.38$ (Chapter 2). J1415+1320 is an atomic and molecular absorber at radio frequencies. Perlman et al. (1996) identified the core using multifrequency VLBI observations. Gugliucci et al. (2005) measured the motion of the hotspots and estimate an age as young as 130±47 yr.

We have identified one new CSO (J1616+2647) and 7 new CSO candidates in our 1.4 GHz images. All of them are compact in 8.5 GHz VLA-A images, i.e., there is no extended flux detected at or larger than $\sim 0\farcs1$ level. For 7 of the 8 objects, 70%–85% of the flux density detected by the

FIRST survey is accounted for in our 1.4 GHz VLBA images. J1312+1710 has only 52% of its FIRST flux detected, indicating it may have a second set of weak lobes further out from the core.

Three CSOs candidates were previously observed with VLBI. J0134+0003 is a VLBA calibrator and was observed by the VLBA Calibrator Survey (Beasley et al. 2002). J1215+1730 and J1203+4632 were selected by Helmboldt et al. (2007) as CSO candidates in 5 GHz. Tremblay (2011) claim there is no structure seen in the counterjet of J1215+1730 and refutes it as a CSO candidate. But we still consider it a candidate based on our CSO-selection criteria.

See Table 3.3 for a summary of the CSOs and candidates. The detection rate of CSOs is 20% in our sample if all the 10 CSO candidates are successfully confirmed as CSOs. Conservatively, assuming a 50% success rate, the detection rate is 14%, still nearly twice higher than the 7.5% detection rate found by Polatidis et al. (1999) in a flux-limited sample with flux density $\geqslant 0.7$ Jy at 5 GHz. We will show in Section 3.6 the most of the CSO candidates, implying a high success rate close to 1. The success rate should be close to 1. The high CSO detection rate might be caused by our selection of non-elliptical galaxies, consistent with the fact that disturbed optical structure is often seen in nearby CSOs (Perlman et al. 2001). But it could also be that our sample-selection criteria tend to select compact objects that have radio emission centered within $1\farcs5$ of the optical objects, i.e., LSOs with angular size larger than the $5''$resolution of the FIRST survey are not selected. While selecting at high frequencies tends to include more compact object than that at low frequencies, our selecting frequency is 1.4 GHz compared to 5 GHz in Polatidis et al. (1999). Once confirmation of these CSO candidates is obtained, our sample will return a much higher frequency of CSOs than other selection techniques.

3.5 Radio SED types

To classify radio SEDs, flux densities at three frequency bands are used: 365 MHz, 1.4 GHz, and 5 GHz. The Texas Survey of Radio Sources at 365 MHz (Douglas et al. 1996) detected all objects in the sample, except J1413+1509 for which the flux density limit of the survey, 25 mJy, is used as an upper limit. Flux densities at 1.4 GHz from the FIRST survey are compared with those

Table 3.3. Summary of CSOs and CSO Candidates

Object	z	LAS (mas)	LLS (pc)	z Ref.	CSO Ref.	Status
(1)	(2)	(3)	(4)	(5)	(6)	(7)
J0134+0003	0.879	18 [a]	140	[5]	[3]	?
J1129+5638	0.892	80	622	[1]	This work	?
J1202+1207		98	< 840		This work	?
J1203+4632	0.36*	40	~ 200	[2]	[12]	?
J1215+1730	0.268	135 [b]	551	[12]	[12]	?
J1312+1710	0.63*	56	~ 385	[2]	This work	?
J1357+0046		86	< 738		This work	?
J1410+4850	0.592	43	284	[1]	This work	?
J1604+6050	0.559	14	89	[1]	This work	?
J1724+3852	1.542	40	340	[1]	This work	?
J1019+4408		155 [c]	< 1326		[4]	Y
J1347+1217†	0.122	100 [d]	217	[6]	[10], [13], [8]	Y
J1413+1509	0.22*	14 [e]	~ 49	[2]	[12]	Y
J1414+4554	0.38*	31 [f]	~ 160	[2]	[7]	Y
J1415+1320†	0.247	117 [g]	450	[11]	[9], [7]	Y
J1616+2647	0.755	124	915	[1]	This work	Y

Note. — The table is separated into two sessions by a horizontal line. The top session summarizes 10 CSO candidates and the bottom session lists 6 known/confirmed CSOs. Columns list: (1) object name; (2) redshift, where suffix "*" indicates photometric redshift fit by optical-NIR SED in Paper I; (3) largest angular size between major components; (4) largest linear size, where "$\sim$" means photometric redshift is used and "$<$" means $z = 1.6$ is used to obtain largest size possible; (5) redshift reference; (6) CSO reference; (7) status, where "?" means CSO candidate and "Y" means confirmed CSO.

References. — [1] Table 2.3; [2] photometric redshift derived by fitting the optical–NIR SED (Section 2.4.3); [3] Beasley et al. (2002); [4] Dallacasa et al. (2002b); [5] Drinkwater et al. (1997); [6] Grandi (1977); [7] Gugliucci et al. (2005); [8] Lister et al. (2003); [9] Perlman et al. (1996); [10] Stanghellini et al. (2001); [11] Stocke et al. (1992); [12] Tremblay (2011); [13] Xiang et al. (2002).

[a]Measured at 2.3 GHz (Beasley et al. 2002).

[b,e,f]Measured at 5 GHz (Helmboldt et al. 2007).

[c]Measured at 1.66 GHz (Dallacasa et al. 2002b).

[d]Measured at 1.66 GHz (Xiang et al. 2002).

[g]Measured at 1.66 GHz (Perlman et al. 1996).

from other lower-resolution (45″) surveys such as the NRAO VLA Sky Survey (Condon et al. 1998) to make sure all the flux densities are accounted for by FIRST. In fact, the differences are within $\sim 10\%$, equivalent to their uncertainties. All the sources with declination higher than 2.°5 are in the 87GB catalog of radio sources (Gregory & Condon 1991) at 5 GHz. For those lower than 2.°5, flux densities at 5 GHz are cited from the Parkes-MIT-NRAO surveys (Griffith et al. 1994, 1995) or the Parkes Catalog (Wright & Otrupcek 1990).

First, we define α_l as the spectral index between 365 MHz and 1.4 GHz, and α_h as between 1.4 GHz and 5 GHz ($S_\nu \propto \nu^\alpha$). While slightly different criteria are adopted by different authors, the following empirical criteria are commonly used at the above frequencies: flat-spectrum (FS) objects ($\alpha_h \geqslant -0.5$; e.g., Healey et al. 2007), steep-spectrum (SS) objects ($\alpha_h < -0.5$ and $\alpha_l < -0.5$), gigahertz-peaked-spectrum (GPS) objects ($\alpha_h < -0.5$, $\alpha_l \geqslant -0.5$, and $\alpha_l - \alpha_h \geqslant 0.3$; e.g. O'Dea 1998), and ultra-steep-spectrum (USS) objects ($\alpha_l \leqslant -1.0$; e.g. Roettgering et al. 1994).

Typical radio SEDs are single power-law with $\alpha \sim -0.5$ to -1.0 over a wide frequency span, $\sim$ 50 MHz – 5 GHz. This non-thermal spectrum is considered to be the synchrotron radiation from shock-accelerated electrons. A low-frequency turnover is sometimes present due to the synchrotron self-absorption or free-free absorption. The flattened spectrum is usually $\alpha > 0$ at low frequencies, and can be as large as +2.5 in a homogenous source. The turnover is smooth over about one order of magnitude in frequency. Our classifying standards above can be interpreted as a turnover frequency $\nu_m \lesssim 400$ MHz for SS objects and $\nu_m \gtrsim 400$ MHz for GPS objects. A small fraction of SS objects are USS with $\alpha < 1.0$ due to extreme energy loss probably caused by electron depletion or inverse-Compton radiation. It has been found that USS objects are excellent candidates for finding high-z radio galaxies (Miley & De Breuck 2008). When the radiation becomes opaque, the spectrum has a shallower and often bumpy slope, which makes a FS object.

We have double-checked the radio SED types using flux densities measured from other radio frequencies, with help from the NASA/IPAC Extragalactic Database. Two FS objects, J0901+0304 and J1413+1509, are re-classified as GPS objects because their turnover frequencies ($\nu_{\rm m}$) are between 5 GHz and 8.5 GHz. Two FS objects, J1215+1730 and J1142+0235, are re-classified as

SS because their SEDs are straight from 365 MHz to 8.5 GHz with $\alpha \simeq -0.5$. One GPS object, J0843+4215, is re-classified as SS because $\nu_m \leqslant 500$ MHz with $\alpha_l = -0.4$ and $\alpha_h = -0.7$. One object, J0939+0304, does not fall into any of the four categories listed above. It has $\alpha_h < -0.5$, $\alpha_l > -0.5$, and $(\alpha_l - \alpha_h) < 0.3$. Flux densities at higher or lower frequencies are needed to pin down the SED types of objects like J0939+0304. It could be either FS or GPS as there is no flux density available > 5 GHz, so it is marked as "FS:".

Overall, there are 6 FS objects, 8 GPS objects, 55 SS objects, 10 USS objects, and one uncertain object (FS or GPS). The reliability of the original classification method is 60% for FS objects, 83% for GPS objects. A spectral index between ~ 1 GHz and ~ 10 GHz might be a better choice for α_l to classify FS and GPS objects than the one between ~ 1 GHz and ~ 5 GHz used here. For SS and USS objects, 100% of them are indeed steep spectrum, although the critical spectral index -1.0 is rather arbitrarily chosen. The radio spectral types are shown in Column (10) of Table 3.2.

Using the NASA/IPAC Extragalactic Database, we have made 3rd-order polynomial fits to NED SEDs with turnover frequencies clearly present. The turnover frequency and peak flux density can be inferred from the fit as well as the spectral indices of optically thin and thick regions.

3.6 Statistical Properties

In this section, we study the statistical properties of our sample including radio morphologies, radio SEDs, and optical+NIR SEDs. To study a homogeneous sample with only intrinsic obscurations, intervening systems and candidates should be excluded. Column (17) of Table 3.2 lists 4 intervening systems and 5 suspicious objects (see Sections 3.7–3.9 for more details). Excluding these 9 objects gives us a sample of 71 objects.

The optical+NIR SEDs were derived into four classes in Chapter 2: quasar (Q), quasar with extinction signatures in bluer bands ($Q + abs$), galaxy with a quasar signature in bluer bands ($G+Q$), and pure galaxy (G). We have also fit G-type objects with template spectra of five Hubble types (E, S0, Sa, Sb, and Sc), and give the best-fit Hubble-types and redshifts. See Appendix A

for more details. The MIR SEDs of this sample will be studies in the future (Section 5.1).

3.6.1 Radio Morphologies and SEDs

We summarize the number of objects with each radio morphological type and SED type in Table 3.4. The following statistical trends are clearly shown in the data.

- There is not a single MSO or LSO among the FS and GPS objects. That is to say, $\nu_m \gtrsim 1$ GHz almost guarantees a small-scale core-jet object, CSO, or point-source object. On the other hand, 75% of the core-jet objects and 50% of the CSOs are FS or GPS objects.

- FS objects are mostly core-jet objects (5 out of 7). Interestingly enough, both of the two FS CSOs, J1347+1217 and J1415+1320, have atypical CSO features that are instead core-jet characteristics.

- Most of the GPS objects (6 out of 8) are CSOs. GPS objects are an excellent source for finding CSOs (Stanghellini et al. 1997; Liu et al. 2007).

- Steep spectrum (SS) CSOs have a larger median size (622 pc) than GPS CSOs (162 pc). Meanwhile, most of the SS CSOs have $\nu_m \sim 365$ MHz – 1.4 GHz, which means that ν_m varies inversely with the size. This should also apply to MSOs and LSOs, but their ν_m might have shifted to frequencies lower than the 365 MHz band. See Section 3.6.4 for more details on the inverse correlation.

In summary, double-lobe objects in the sample have $\nu_m < 10$ GHz and their sizes are inversely proportional to ν_m, while FS objects don't have a turnover frequency up to at least 10 GHz (O'Dea 1998). It is also worth noting that the intervening systems/candidates are exclusively SS objects, i.e., the radio objects in these systems are the most common objects compared to the ones with intrinsic obscurations.

Table 3.4. Statistics of Morphological Types and Radio Spectral Types

Radio SED \ Morphology		CJ	CSO	MSO	LSO	PS	CX
		8	16	18	24	2	3
FS	7	5	2	0	0	0	0
GPS	8	1	6	0	0	1	0
SS	47	2	8	15	18	1	3
USS	9	0	0	3	6	0	0

Note. — This table shows the number of objects with a particular morphological type and spectral type. The row header lists morphological types and the column header lists spectral types. Total number of objects for each type are shown in the first row and the first column.

Table 3.5. Statistics of Radio Morphologies and Optical+NIR SEDs

OIR SED \ Morphology		CJ	CSO	MSO	LSO	PS	CX
		8	16	18	24	2	3
G	37	3	10	12	8	2	2
G+Q	16	2	3	3	8	0	0
Q+abs	11	0	3	2	5	0	1
Q	7	3	0	1	3	0	0

Note. — This table shows the number of objects with a particular radio morphology and optical+NIR SED. The row header lists radio morphological types and the column header lists optical+NIR SED types. Total number of objects for each type are shown in the first row and the first column.

3.6.2 Radio Morphologies and Optical+NIR SEDs

Similar to Table 3.4, Table 3.5 summarizes the number of objects with a particular radio morphology and optical+NIR SED type. We find the following statistical properties in the data.

- Core-jet objects have a high percentage of quasar-type SEDs (Q, $Q + abs$, and ,$G + Q$) $\sim$ 60%. Since our sample-selection criteria are inclined to choose non-stellar objects, the actual fraction should be much higher than 60% in traditionally-selected samples, indicating that core-jet objects are predominantly non-obscured quasars bright in the optical.

- CSOs and MSOs have a high percentage of galaxy-type SEDs (G and $G + Q$), $>$ 80%, implying that their central engines are mostly obscured in the optical.

- With increasing size (CSOs, MSO, LSOs), the fraction of G-type objects decreases and that of Q-type objects increases, suggesting optical obscuration reduces with increasing radio size or AGN age.

In summary, AGNs of double-lobe radio sources are mostly obscured in the optical and their sizes are inversely proportional to the extent of obscuration, while AGNs of core-jet radio sources

are often unobscured in the optical (Best et al. 2005).

3.6.3 Radio SEDs and Optical+NIR SEDs

Table 3.6 summarizes the number of objects with a particular radio SED type and optical+NIR SED type. Following the discussions in Section 3.6.1 and 3.6.2, we find that GPS objects are associated with G or $G + Q$-type objects, while 2 out of the 7 FS objects show Q-type optical-NIR SEDs. Note again that the fraction of quasars in FS objects should be much higher in traditionally selected samples. We conclude that there is a good correspondence between radio morphological types, radio SED types and optical-NIR SED types: CSO-GPS-G, MSO-CSS-G, LSO-SS-G, Cj-FS-Q, where "CSS" stands for Compact Steep Spectrum objects, a name that combines morphological and SED features (Fanti et al. 1990). Although SEDs types are easier to classify, they have the problem of representing inhomogeneous groups. For instance, CSOs can be FS, GPS, or SS objects depending on the turnover frequencies. Therefore our radio images are crucial to reveal the nature of these objects.

USS objects are often associated with quasar-like SEDs. Among the 9 USS objects, 7 have quasar-type SEDs; additionally, all of them are MSOs or LSOs. Redshifts for only 3 USS objects are available, all at z =1.8–2.9. For comparison, the other two objects with $z \geqslant 1.8$ are the gravitational-lens system J0751+2716 and a FS core-jet object J1625+4134. In objects with $\alpha_l < -0.9$, only J0920+2714 has a G-type SED, and we will show in Section 3.7 that this is an intervening absorption system with a foreground galaxy at $z = 0.206$ much brighter than the AGN host galaxy in the optical+NIR. Our findings are consistent with the fact that many of the USS objects are at high-z (e.g., Ishwara-Chandra et al. 2010).

3.6.4 Turnover Frequency versus Largest Linear Size

Fanti et al. (1990) found that there is an anti-correlation between turnover frequencies and the source sizes in Compact Steep Spectrum objects (CSS's; mostly MSOs). In a combined sample of CSS's and Giga-Hertz Peaked Objects (GPS's), O'Dea & Baum (1997) found the same trend.

Table 3.6. Statistics of Optical+NIR SEDs and Radio Spectral Types

OIR SED \ Radio SED		FS	GPS	SS	USS
		7	8	47	9
G	37	4	7	24	2
G+Q	16	1	1	13	1
Q+abs	11	0	0	7	4
Q	7	2	0	3	2

Note. — This table shows the number of objects with a particular optical-NIR SED type and radio SED type. The row header lists radio SED types and the column header lists optical-NIR SED types. Total number of objects for each type are shown in the first row and the first column.

In Figure 3.1a, we plot the turnover frequencies versus largest liner size for our objects that have spectroscopic redshifts and peak frequencies detected. We find that the slope in our sample is consistent with O'Dea & Baum (1997), but the turnover frequency is systematically lower. The best linear fit of our data gives

$$\log\left(\frac{\nu_m}{\mathrm{GHz}}\right) \simeq -0.47(\pm0.15) - 0.61(\pm0.18) \times \log\left(\frac{LLS}{\mathrm{kpc}}\right), \tag{3.1}$$

whereas O'Dea & Baum (1997) found

$$\log\left(\frac{\nu_m}{\mathrm{GHz}}\right) \simeq -0.21(\pm0.05) - 0.65(\pm0.05) \times \log\left(\frac{LLS}{\mathrm{kpc}}\right). \tag{3.2}$$

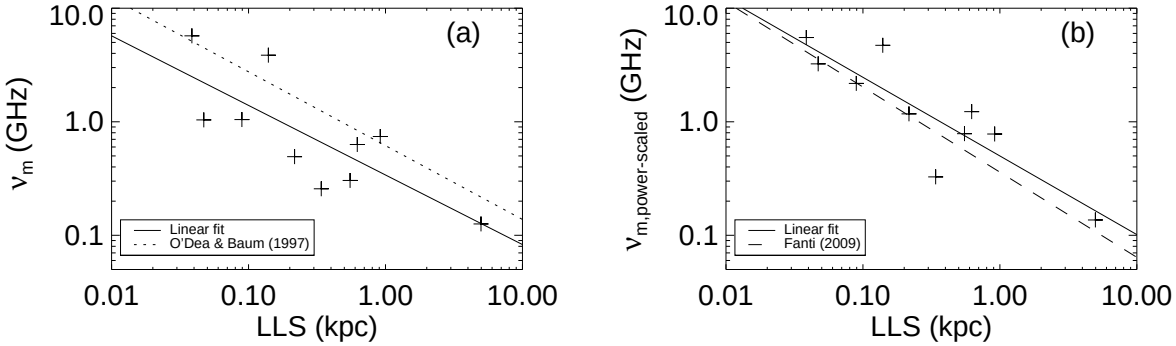

Figure 3.1 Turnover frequencies (a) and power-scaled turnover frequencies (b) vs projected linear sizes for objects that have spectroscopic redshifts and peak frequencies detected. Solid lines are the best linear fit of our data. Dotted and dashed lines are the relations found by O'Dea & Baum (1997) and Fanti (2009) respectively.

If the low-frequency turnover is caused by the synchrotron self absorption, it can be used to estimate the magnetic field. For the synchrotron radiation of relativistic elections with a power-law energy distribution ($N(E) \sim E^{-p}$), the emission coefficient

$$j_\nu \sim B^{(p+1)/2}\nu^{-(p-1)/2}, \tag{3.3}$$

and the absorption coefficient

$$\alpha_\nu \sim B^{(p+2)/2}\nu^{-(p+4)/2}. \tag{3.4}$$

where B is the magnetic field and ν is the frequency (Rybicki & Lightman 1979). The specific intensity of a uniform gas with length l is

$$I_\nu = \frac{j_\nu}{\alpha_\nu}(1 - e^{-\alpha_\nu l}). \tag{3.5}$$

At the turnover frequency, the optical depth $\tau = \alpha_\nu l \sim 1$, thus

$$I_{\nu_m} \sim \frac{j_{\nu_m}}{\alpha_{\nu_m}} \sim B^{1/2}\nu_m^{5/2}. \tag{3.6}$$

For a source with solid angle Ω, the observed flux density at frequency ν'_m is $S_{\nu'_m} = I_{\nu_m}\Omega(1+z)^2$. Assuming an angular size of θ, we get

$$\nu'_m \sim B^{1/5}S_{\nu'_m}^{2/5}\theta^{-4/5}(1+z)^{1/5}. \tag{3.7}$$

The coefficient is weakly dependent on p, a precise calculation gives (e.g., Kellermann & Pauliny-Toth 1981)

$$\left(\frac{\nu'_m}{\mathrm{GHz}}\right) \approx 8\left(\frac{B}{\mathrm{Gauss}}\right)^{1/5}\left(\frac{S_{\nu'_m}}{\mathrm{Jy}}\right)^{2/5}\left(\frac{\theta}{\mathrm{mas}}\right)^{-4/5}(1+z)^{1/5}. \tag{3.8}$$

Instead of observed quantities, we can write the specific intensity of Equation 3.6 in intrinsic quantities, $I_\nu = L_\nu/\pi^2 l^2$, where L_ν is the specific luminosity and l is the size of the emitting region. The intrinsic turnover frequency is thus

$$\nu_m \sim B^{1/5}L_{\nu_m}^{2/5}l^{-4/5}, \tag{3.9}$$

compared to Equation 3.7. A precise calculation gives (Fanti 2009)

$$\log\left(\frac{\nu_m}{\mathrm{GHz}}\right) \approx -0.44 - 0.75\log\left(\frac{LLS}{\mathrm{kpc}}\right) + 0.35\log\left(\frac{L_{5\mathrm{GHz}}}{10^{27}\ \mathrm{W\ Hz^{-1}}}\right), \tag{3.10}$$

where $L_{5\mathrm{GHz}}$ is the specific luminosity at 5 GHz in the optically thin region of the SED. Several assumptions are used in deriving Equation 3.10: (1) the radiation field (i.e. hotspots) is a fraction (30%) of the source size Jeyakumar & Saikia (2000) for all sources, $l = 0.3LLS$; (2) the source has minimum energy density, i.e., in equipartition, so that $B \sim L^{2/7}l^{-6/7}$, L is the total luminosity of the radio sources; (3) the peak luminosity L_{ν_m} is proportional to the total luminosity; (4) the spectral

index in the optically thin region is -0.7. By scaling the luminosity at 5 GHz to 10^{27} W Hz^{-1}, the scaled frequency roughly follows the relation in Equation 3.10 with LLS (Figure 3.1b). The best linear fit gives

$$\log\left(\frac{\nu_m}{\mathrm{GHz}}\right) + 0.35\log\left(\frac{L_{5\mathrm{GHz}}}{10^{27}\ \mathrm{W\ Hz^{-1}}}\right) \approx -0.30(\pm0.11) - 0.69(\pm0.13)\log\left(\frac{LLS}{\mathrm{kpc}}\right). \quad (3.11)$$

We conclude that the discrepancy between Equation 3.1 and Equation 3.2 (Figure 3.1a) can be fully accounted considering our sample has a lower average luminosity than the sample of O'Dea & Baum (1997). Therefore, the result is consistent with that the low-frequency turnover is due to SSA. However, it has been suggested that the turnover frequency in some compact objects is produced by the free-free absorption (FFA) instead of SSA (e.g., Perlman et al. 1994). Under the model of FFA, the turnover frequency should be affected by the ISM density in addition to the source power (Bicknell et al. 1997). We will demonstrate in Chapter 4 that our sample has a denser ISM which would increase the turnover frequency for a fixed source size. If the turnover is caused by FFA, the relation between ν_m and LLS in our sample may be able to place constraints on the model of FFA.

3.7 Position Offsets

In Chapter 2, we detected a NIR counterpart for every optical object, i.e., the offset of the NIR and optical centroid positions is within 5σ of their uncertainties combined. The position uncertainties of the optical/NIR objects are of order $\sim 0\farcs1$–$0\farcs2$ and the size is $\lesssim 2''$except for a few objects (~ 5). In contrast, the resolution of the FIRST survey is $\sim 5''$, insufficient to determine a precise offset between the optical/NIR and radio positions. So with high-resolution radio images we scrutinize each object to see whether there is a significant offset which might indicate unusual systems such as intervening or interacting systems. The most interesting objects are discussed as follows.

J0003−1053 has four components in its 4.9 GHz and 8.5 GHz images. Its NIR centroid position is coincident with the "C" component, which has an inverted spectral index. All other

components have steep spectral indices $\alpha < -0.5$. Its optical centroid position is close to the "B" component. A redshift of 1.474±0.001 is obtained from emission lines in the NIR (see Chapter 2), but the photometric redshift given by SDSS DR8 is 0.57 ± 0.12. Its optical-NIR SED is very red with $r - K_{\rm s} = 5.5 \pm 0.3$, redder that typical elliptical galaxies, and classified as $Q + abs$. We suggest that the object at $z = 1.474$ is heavily obscured either intrinsically or by a foreground galaxy/quasar. Either is favorable to the detection of absorption lines.

J0807+5327 has a double-lobe radio structure. However, the entire radio structure is to the south of the optical and NIR centroid positions by $\sim 1.5''$, which makes it possible that the radio source is not associated with the optical+NIR object. If this is a core-jet object with a core in the 'A" component, the core is still $\sim 0.5''$away from the NIR centroid position.

J0917+4725 shows extended structure in its 4.9 GHz and 8.5 GHz images, and the radio center is $1\farcs3$ away from its NIR center. We overlay the FIRST field with r-band image in Figure 3.2. A second radio lobe is seen in the northeast $\sim 40''$away. It is unknown which is the optical counterpart of the radio source. Absorption lines are unlikely to be detected due to the position offset even if the optical+NIR object is in the foreground of the radio source.

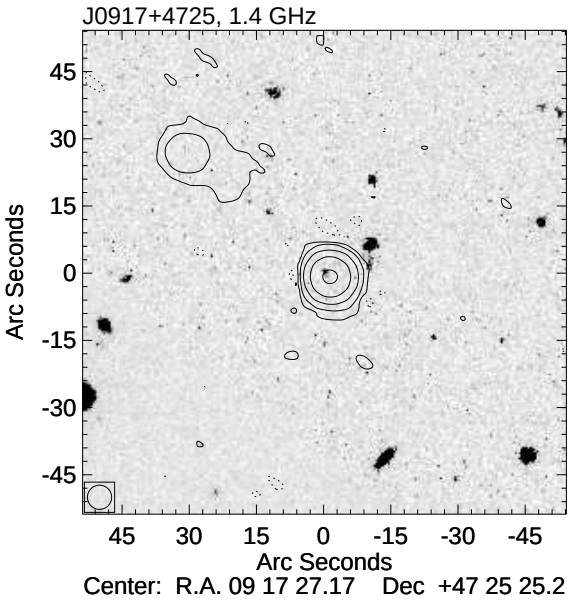

Figure 3.2 The 1.4 GHz contour of the field of J0917+4725, overlaid with optical image in r-band. The contour levels are −0.45, 0.45, 2.3, 11, 54, and 267 mJy.

J0920+2714 is a LSO with the brighter lobe overlapping with but not centered on an elliptical galaxy at $z = 0.209$ ($1\farcs5$ away from optical center). An H I absorption line has been detected at the redshift of the elliptical galaxy (Chapter 4). We conclude that the optical–NIR galaxy is not the counterpart to the radio source.

J1341+1032 is also an MSO which is offset from its optical+NIR center similar to J0807+5327 and J0920+2714. This makes it a good candidate to detect absorption lines at the redshift of the offset foreground galaxy.

3.8 Gravitational Lens Systems

If well aligned, the foreground galaxy in an intervening system can substantially bend the light from the background source and form a gravitational lens system, although the positional offset of the two objects might be less significant than the objects we discussed in Section 3.7. In this case, an arc-like structure of the radio source could help us to discover candidates for lensing systems. There are three objects showing arc-like feature in the sample including J0751+2716, a previously known gravitational lens system (Lehar et al. 1997).

J1559+4349 has a NIR redshift of 1.232±0.001 (Chapter 2) and an optical photometric redshift of 0.42±0.09 according to SDSS DR8. We classify its optical+NIR SED as $Q + abs$ because it is bluer than a Sc-type galaxy. Figure 3.3 shows that the K-band center is close to the radio core. If the radio structure is part of an Einstein ring with radius $0\farcs64$, the center of the ring is close to the r-band center. Therefore, we suggest that the foreground lens is dominant in the optical, while the background object at $z = 1.232$ is dominant in the NIR. J1559+4349 has two components in its VLA-A 4.9 GHz and 8.5 GHz images with spectral indices -1.0 and -1.2 respectively. However, extrapolated to 1.4 GHz, only $\sim 50\%$ of the total flux density of "A" is detected and $\sim 20\%$ of "B" in the VLBA image.

J1147+4818 is classified as core-jet object based on its VLA-A images. No emission from component "B" is detected in the 1.4 GHz VLBA image. We show in Figure 3.4 that the arc-like VLBA component lies on a circle with radius $0\farcs20$. The optical and NIR centroid positions

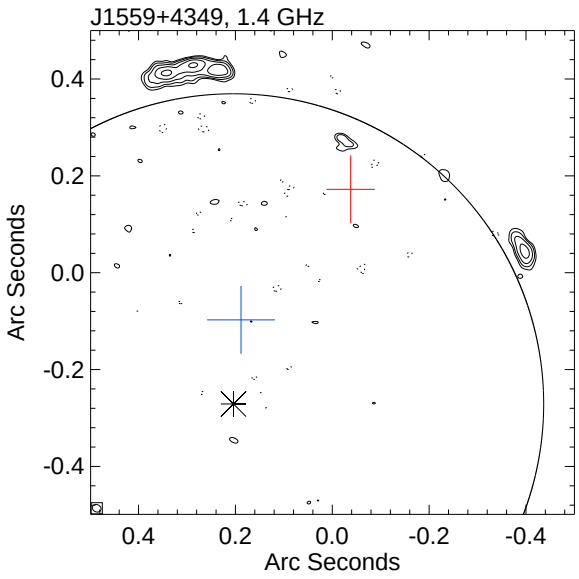

Figure 3.3 The 1.4 GHz contour of J1559+4349. Black arc is part of a circle with radius 0.″64 centered at the position labeled with an asterisk. (This plot is otherwise the same as the 1.4 GHz plot in Figure B.1.)

are coincident and both are in the vicinity of the arc although their uncertainties are as large as the radius of the ring. J1147+4818 is a Q-type object but DR8 gives a photometric redshift of $z = 0.17 \pm 0.05$ assuming it is a galaxy. Compared to J1559+4349, J1147+4818 is less likely a gravitational system due to lacking evidence of two distinct optical-NIR objects. Plus, radio sources often show modest curvature of core-jet components.

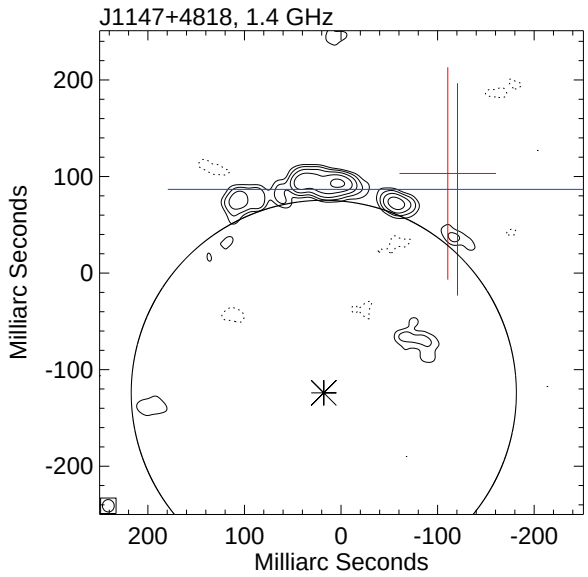

Figure 3.4 The 1.4 GHz contour of J1147+4818. Black arc is part of a circle with radius 0.″20 centered at the position labeled with an asterisk. (This plot is otherwise the same as the 1.4 GHz plot in Figure B.1.)

3.9 Other Objects of Interest

J0834+1700 is one lobe in a double-lobe structure 25″apart (see Figure 3.5), similar to another single-lobe object J0917+4725. The radio source is so well aligned with the optical+NIR object that no significant position offset is present, unlike in the case of J0917+4725. Absorption lines may be detected if the radio source is in the background, although the large amount of extended radio flux makes this a poor absorption candidate.

J1048+3457 is a Broad-Absorption-Lines (BAL) quasar at $z = 1.6$. Although its radio jet is very likely oriented toward the line of sight, it does not show a typical core-jet structure.

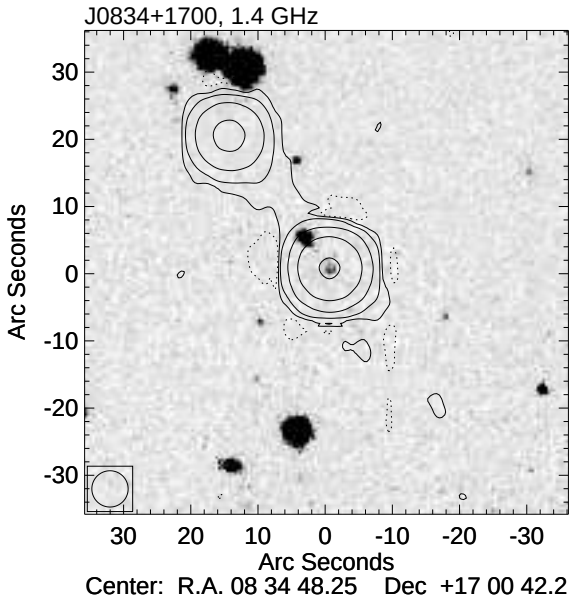

Figure 3.5 The 1.4 GHz contour of the field of J0834+1700, overlaid with optical image in r-band. The contour levels are -0.9, 0.9, 5.5, 33, 203, and 1239 mJy.

Instead, it has complicated sub-arcsec scale structure with many components which might indicate jet precessions and interactions with a dense ISM at an early stage of its radio activity (Kunert-Bajraszewska & Marecki 2007; Kunert-Bajraszewska et al. 2010).

J1527+3312 is unresolved in the 8.5 GHz VLA-A image, but very extended in the higher-resolution 1.4 GHz VLBA image for which only 25% of the total flux density is accounted. While further observations are needed to detect the diffuse radio emission, this "missing flux" makes J1527+3312 a poor absorption candidate.

3.10 Discussion and Conclusions

We selected a sample of high-obscured AGNs that are radio loud in hopes of finding new redshifted absorption systems at radio frequencies. After demonstrating that most of the objects remain obscured in the NIR in Chapter 2, we find in this chapter that their radio properties are also promising a search for absorption lines. There are 52 objects that have a compact component with a size $0\farcs5$, facilitating a high covering factor for any absorbing gas that might be present. We also have identified 9 intervening systems and 16 CSOs in our sample including candidates. There are 20 MSOs and 8 core-jet objects, which are also good targets for absorption-line searches. In fact, only LSOs not in intervening systems or without a bright core should be excluded for further searches, and there are only 14 of them.

Line searches are under way, and so far there have been five 21 cm absorption systems detected, which include both associated and intervening systems (Chapter 4). The detection rate is exceptionally high, consistent with our expectations based on the results of Chapter 2 and this chapter.

Chapter 4

Line Searches

We have embarked on a systematic search for atomic and molecular absorption lines at radio frequencies by selecting a sample which includes highly-obscured nuclei in radio-loud galaxies (Yan et al. 2012, Chapter 2). Here we report the detection of H I 21 cm absorption lines in 5 systems from this sample at redshift 0.2–0.9. Four out of six objects which have usable data at their spectroscopic redshifts shows 21 cm absorption lines, and one shows a tentative detection. We have also searched 14 objects near their photometric redshifts, and made only one detection. No molecular absorption has been detected. The high detection rate of 21 cm absorption lines confirms that our selection criteria are finding highly-obscured nuclei and predicts the detection of more H I absorption systems and possibly molecular absorption systems in the sample. A strong correlation is found between the detection rate and the optical+ SED type, i.e., H I absorptions are rarely found in optical-bright AGN.

4.1 Introduction

It is well known that radio-loud AGN are almost exclusively found in elliptical host galaxies. But with the help of large surveys like SDSS and FIRST, we have selected a sample of rare radio-loud AGN that show late-type morphologies in the optical. In Chapter 2, we obtained NIR photometric data to confirm that the optical+NIR SEDs are consistent with these objects being heavily obscured. We also made high-resolution radio maps to study the correlation between radio structures and optical morphologies (Yan et al. 2013; Chapter 3), which may shed light on the evolution of AGN.

In this chapter, we focus on using this sample to search for new atomic and molecular absorption systems at radio frequencies.

Up to now there have been $\sim$ 80 H I absorption systems detected at cosmological distances ($z > 0.1$), among which about half are associated absorption systems, i.e., $z_{\rm abs} = z_{\rm em}$. The detection rate is $\sim$ 30% in compact radio sources (Vermeulen et al. 2003) and can be as high as 50% in CSO/GPS sources (e.g., Pihlström et al. 2003; Gupta et al. 2006). However, this seems only valid at $z < 1$. Except for two H I absorbers found at $z > 1.5$, various surveys have failed to find more absorption systems at high-z (e.g., Curran et al. 2008, 2011a; Darling et al. 2013). Meanwhile, there are only 5 known molecular absorption systems at $z > 0.1$ (one detected only in OH), all at $z < 1$. Studying this current sample will help us find the key factors for detecting H I and molecular absorptions at radio frequencies.

4.2 Observation and Data Reduction

At the Robert C. Byrd Green Bank Telescope (GBT) of NRAO [1] , observations were conducted with the two prime focus receivers PF1 ($\sim$ 510–690 or $\sim$ 680–920 MHz) and PF2 ($\sim$ 901–1230 MHz) at the appropriate frequency bands depending on the spectroscopic or photometric redshift of the target (see Table 4.1). The spectrometer was set to the narrow-bandwidth, high resolution mode with dual linear polarizations and multiple spectral windows taking spectra simultaneously. Usually 4 spectral windows were used with each having a 50 MHz bandwidth and 4096 channels. Position-switched scans were performed on the target and a sky reference position. Each scan was about 5 minutes in duration with 2 seconds for each integration. For a typical object of 0.8 Jy at 900 MHz, 5 position-switched pairs were carried out to detect a $\tau = 0.01$ absorption line at 5σ significance. The total observing time for each target ranges from $\sim$ 20 minutes to $\sim$ 2 hours due to the large flux density span. Fluxes are calibrated using the noise tube calibrator, which is turned on half of the time for each integration. The uncertainty of this "standard" flux calibration is $\pm$

[1] The National Radio Astronomy Observatory is a facility of the National Science Foundation operated under cooperative agreement by Associated Universities, Inc.

10%. Nonetheless, only relative fluxes (optical depths) are of interest to this work. The data were reduced using GBTIDL, an interactive package for the reduction and analysis of spectral line data taken with GBT. Each integration and polarization was calibrated separately and then averaged together. However, the radio frequency interferences (RFIs) present a severe problem due to mobile phones and TV stations. Figure 4.1 shows two RFI monitoring scans for the PF1 680-920 MHz and PF2 receivers. The RFIs could be intermittent or persistent, and are always variable. Therefore a median spectrum of all integration for each polarization is calculated to eliminate sporadic RFIs not present in most integrations. The noise of a median spectrum is $\pi/2$ larger than that of a mean spectrum if the frequency range is FRI-free or slightly contaminated. If a possible absorption line is identified, each integration is carefully inspected to flag those with RFIs. A final spectrum is obtained by averaging all the remaining integrations.

At the Arecibo Observatory (AO), 6 objects were observed with the 800 MHz receiver ($\sim$ 700–800 MHz) in dual polarization. The Mock Spectrometer contains 14 independent boxes. Each box was configured to have 8192 channels and a bandwidth of 12 MHz with some overlapping to cover the entire 100 MHz frequency range of the receiver. Double-position-switched scans were performed to cancel residual standing waves, which means an observing sequence containing four scans: on-target, off-target, on-reference, and off-reference. The reference source was observed close to the target source in space and time. Each scan was 3-5 minute long, and the total observing time was 1-2 hours for each source. The data were reduced by IDL routines provided by AO. The reference sources are also used as flux calibrators. The Arecibo observations took advantage of a period which was relatively RFI-free just prior to the inception of digital television in Puerto Rico. This observing window has now been closed.

Observations of the HI 21 cm absorption lines toward J0901+0304 were carried out with the Very Large Array (VLA) of NRAO on 2009 December 28 to confirm the detection of H I absorption in the RFI-contaminated spectrum at GBT. The array was in the D-configuration, and the total observing time was 1 hr. These observations used 21 of the antennas that were converted to the Expanded VLA (EVLA) standards. The data were correlated using the old VLA correlator. The

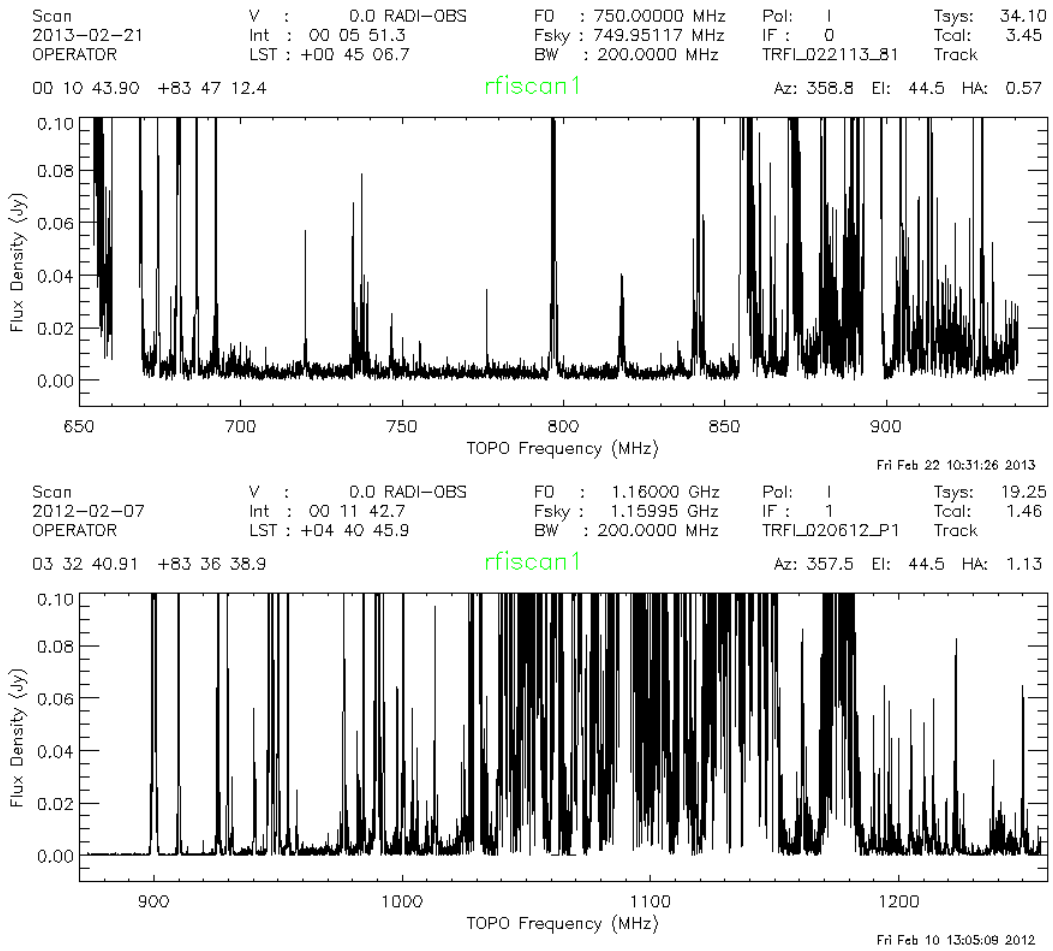

Figure 4.1]
The RFI monitoring scans at GBT for the PF1 680-920 MHz receiver in February, 2013 (*top*) and PF2 receiver in February, 2012 (*bottom*) at GBT.

aliasing that was known to affect the lower 0.5 MHz of the bandwidth for EVLA data which were correlated with the old VLA correlator was avoided by properly placing the frequencies of the two redshifted HI 21 cm lines within a more restrictive 3.125 MHz band. The calibrator source 3C147 (J0542+4951) was used to set the absolute flux density scale, while the compact source J0925+0019 was used as the complex gain calibrator. The editing, calibration, and imaging of the VLA data were carried out using the Astronomical Image Processing System (AIPS) of the NRAO. After applying the amplitude and phase corrections of J0925+001 on J0901+0304. The HI line-free channels were split, and the continuum emission from J0901+0304 was self-calibrated in both phase and amplitude in a succession of iterative cycles. The final phase and amplitude solutions were then applied on the spectral-line data set. The continuum emission was subtracted in the UV-domain, and a Stokes I image cube was made with a synthesized beam width of $97'' \times 67''$ (position angle = -26.60).

The Giant Metrewave Radio Telescope (GMRT) was also used to confirmed the detection of H I absorption in J0901+0304. The observations were carried out on January 28, 2010, using 23 antennas and the GMRT hardware correlator. A 4 MHz band, sub-divided into 128 channels, was used for the observations with two circular polarizations; this yielded a velocity resolution of 8.5 km s^{-1}, and a velocity coverage of ≈ 1100 km s^{-1}. 3C147 and 3C286 were used to calibrate the flux density scale and the system passband, while the compact sources 0823+033 and 0922+005 were used for phase calibration. The GMRT data were analysed in AIPS including standard data flagging and standard calibration procedures to obtain the antenna-based complex gains. A series of iterative self-calibration procedures were then used to determine the antenna gains and the final image. 3-D imaging techniques were used by sub-dividing the field into 13 facets to correct for the non-coplanarity of the array. The final continuum image was then subtracted out from the calibrated visibility data, after which a first-order polynomial was fit to the visibility spectra on each interferometer baseline and subtracted. The residual U-V data were then shifted to the barycentric frame and imaged in all channels to obtain the final spectral cube. A cut through this cube at the target location yielded the HI 21cm spectrum. The target flux density was measured to

be 402.39 ± 0.92 mJy, from a single-Gaussian fit with the AIPS task JMFIT, while the root mean square noise on the spectrum was measured to be 0.9 mJy per 8.5 km s^{-1} channel from off-line regions.

See Table 4.1 for the observing logs at all telescopes used.

Table 4.1. Observing Log.

Object	z	z ref	Line(s) searched	Telescope/Receiver	Date	Line(s) detected
(1)	(2)	(3)	(4)	(5)	(6)	(7)
J0003−1053	*0.42±0.02 & 1.474±0.001	Table 2.3	HI	GBT/PF2	28-Sep-09	
J0003−1053	*0.42±0.02 & 1.474±0.001	Table 2.3	HI	GBT/PF2	30-Sep-09	
J0134+0003	0.879	NED	HI	Arecibo/800-MHz	09-Oct-09	
J0134+0003	0.879	NED	HI, OH	GBT/PF1 680–920MHz	07-Feb-13	
J0751+2716	0.34937 & 3.2	NED	HI	GBT/PF2	08-Oct-09	
J0805+1614	:0.632±0.002	Table 2.3	HI	GBT/PF1 680–920MHz	10-Feb-13	
J0805+1614	:0.632±0.002	Table 2.3	OH	GBT/PF2	08-Jun-09	
J0805+1614	:0.632±0.002	Table 2.3	OH	GBT/PF2	13-Oct-09	
J0824+5413	0.6385±0.0003	Table 2.3	HI	GBT/PF1 680–920MHz	21-May-09	
J0839+2403	*0.88±0.19		HI	GBT/PF1 680–920MHz	22-May-09	
J0839+2403	*0.88±0.19		HI	Arecibo/800-MHz	14-Mar-11	
J0839+2403	*0.88±0.19		HI	Arecibo/800-MHz	15-Mar-11	
J0901+0304	0.2872±0.0001	Table 2.3	HI	GBT/PF2	09-Oct-09	HI
J0901+0304	0.2872±0.0001	Table 2.3	HI	VLA	28-Dec-09	HI
J0901+0304	0.2872±0.0001	Table 2.3	HI	GMRT	28-Jan-10	HI
J0910+2419	*0.70±0.06		HI	GBT/PF1 680–920MHz	21-May-09	
J0920+2714	0.2064±0.0002	Table 2.3	HI	GBT/L-band	10-Sep-06	HI
J0939+0304	*0.47±0.03		HI	GBT/PF2	08-Jun-09	
J0951+1154	*0.62±0.26		HI	GBT/PF1 680–920MHz	01-Jul-09	
J1008+2401	*0.88±0.22		HI	GBT/PF1 680–920MHz	01-Jul-09	

Table 4.1 (continued)

Object	z	z ref	Line(s) searched	Telescope/Receiver	Date	Line(s) detected
(1)	(2)	(3)	(4)	(5)	(6)	(7)
J1023+0424	*0.63±0.15		HI	GBT/PF1 680–920MHz	22-May-09	
J1023+0424	*0.63±0.15		HI	Arecibo/800-MHz	15-Mar-11	
J1033+3935	1.095±0.002	NED	HI	GBT/PF1 510–690 MHz	03-Nov-09	
J1043+0537	*0.87±0.29		HI	GBT/PF1 680–920MHz	22-May-09	
J1043+0537	*0.87±0.29		HI	Arecibo/800-MHz	14-Mar-11	
J1129+5638	0.892±0.002	Table 2.3	HI	GBT/PF1 680–920MHz	15-Apr-12	HI
J1238+0845	*0.83±0.14		HI	GBT/PF1 680–920MHz	22-May-09	
J1238+0845	*0.83±0.14		HI	Arecibo/800-MHz	14-Mar-11	
J1238+0845	*0.83±0.14		HI	Arecibo/800-MHz	15-Mar-11	
J1315+0222	*0.55±0.48		HI	GBT/PF1 680–920MHz	01-Jul-09	
J1357+0046	*1.00±0.17		HI	GBT/PF1 680–920MHz	22-May-09	HI
J1357+0046	*1.00±0.17		HI	GBT/PF1 680–920MHz	01-Jul-09	HI
J1357+0046	*1.00±0.17		OH	GBT/PF2	08-Jun-09	
J1410+4850	0.592±0.001	Table 2.3	HI	GBT/PF1 680–920MHz	08-Feb-13	
J1414+4554	:0.186±0.002	NED	HI	GBT/L-band	12-Mar-09	
J1421−0246	*0.53±0.02		HI	GBT/PF2	05-Jun-09	
J1424+1852	*0.53±0.02		HI	GBT/PF1 680–920MHz	22-May-09	
J1504+5438	0.62244±0.00013	NED, SDSS	HI	GBT/PF1 680–920MHz	21-May-09	
J1604+6050	0.559±0.001	Table 2.3	HI	GBT/PF1 680–920MHz	08-Feb-13	HI:
J1616+2647	0.755±0.001	Table 2.3	HI	GBT/PF1 680–920MHz	15-Apr-12	HI

4.3 Observational Results

At the GBT, twelve objects were searched for H I absorption at their spectroscopic redshift, but six are in RFI-rich regions, precluding a sensitive search at $z_{\rm spec}$. In the six objects with usable data, four detections have been made (the absorption in J0901+0304 was contaminated by RFI, but confirmed later by VLA and GMRT observations) as well as one tentative detection. A clean upper limit was obtained for only one source, J0134+0003. Fourteen objects were searched for 21 cm absorption lines at their photometric redshifts with wide bandwidths, which led to only one detection in J1357+0046.

At the AO, J0134+0003 was searched for H I at its spectroscopic redshift, but an upper limit was obtained with less sensitivity compared to its GBT observations. Four objects were searched at their photometric redshifts using the 705-800 MHz receiver. These four objects were also searched by GBT using the 680-920 MHz receiver. No detection was made.

The GMRT and VLA observations confirmed the detection of H I absorption in J0901+0304.

No OH absorption line has been detected in any source. With usable data, we obtained upper limits for the main line in J2203−0021 and satellite lines in J0751+2716 and J1357+0046.

When a flux density of $S_{\rm abs}$ is absorbed over the path through the absorbing gas which blocks a continuum $S_{\rm con}$ in the background, the optical depth is $\tau \equiv -\ln(1 - S_{\rm abs}/S_{\rm con})$ or $\tau \cong S_{\rm abs}/S_{\rm con}$ for optically thin gas ($\tau \lesssim 0.1$). A covering factor f has to be considered because the foreground absorber does not necessarily cover the entire background structure. The desire to maintain $f \simeq 1$ in the sources selected for observation is the primary reason for observing sources dominated by very compact flux. By integrating the optical depth over the velocity dispersion of the absorption line, we get the H I column density of the absorbing gas

$$N_{\rm HI} = 1.8 \times 10^{18} \frac{T_s}{f} \int \tau {\rm d}v, \tag{4.1}$$

where T_s is the spin temperature of H I, which could be $\sim$ 100–1000 K for neutral gas depending

Table 4.1 (continued)

Object	z	z ref	Line(s) searched	Telescope/Receiver	Date	Line(s) detected
(1)	(2)	(3)	(4)	(5)	(6)	(7)
J2203−0021	0.729±0.001	Table 2.3	HI	Arecibo/800-MHz	09-Oct-09	
J2203−0021	0.729±0.001	Table 2.3	OH	GBT/PF2	01-Oct-09	

Note. — Columns list: (1) object name in IAU convention; (2) redshift used for line search, either obtained by us or in the literature, while prefix "*" means photometric redshifts from SDSS DR6, ":"means uncertain redshift, and "&" is followed by redshift of the background object; (3) redshift reference; (4) line(s) searched; (5) telescope/receiver used; (6) observing date; (7) line(s) detected.

on the local conditions. The column densities of OH are

$$N_{\rm OH,m} = 2.38 \times 10^{14} \frac{T_x}{f} \int \tau {\rm d}v \tag{4.2}$$

for the main lines at 1665 MHz and 1667 MHz and

$$N_{\rm OH,s} = 2.14 \times 10^{15} \frac{T_x}{f} \int \tau {\rm d}v \tag{4.3}$$

for the satellite lines at 1612 MHz and 1720 MHz, where T_x is the excitation temperature of OH.

For a Gaussian profile with a peak optical depth of τ_p and a rest-frame velocity FWHM of ΔV, the integrated optical depth $\int \tau {\rm d}v$ is approximately $1.0645 \tau_p \Delta V$ for optically thin gas. For non-detections, an upper limit is given by setting $\tau_p = 3 \times rms / S_{\rm con}$, assuming $\Delta V = 100$ km s^{-1}, and resampling the spectrum to a resolution of 10 km s^{-1}.

Table 4.2 lists the H I detections, Table 4.3 lists H I upper limits at their spectroscopic redshifts, and Table 4.4 lists OH upper limits at their spectroscopic redshifts.

Table 4.2. H I Detections.

Object	Comp. ID	Resolution (kHz)	rms (mJy)	Center (MHz)	FWHM (km s^{-1})	τ_p	z	$\int \tau \mathrm{d}v$ (km s^{-1})	N_{HI} (10^{20}cm^{-2})
(1)	(2)	(3)	(4)	(5)	(6)	(7)	(8)	(9)	(10)
J0901+0304 [a]	A	24	1.5	1102.277 (2)	46 (2)	-0.0775 (23)	0.288611 (3)	3.79 ± 0.17	6.82 ± 0.31
	B								
	Int[b]							3.82 ± 0.10	6.88 ± 0.18
J0901+0304 [c]	A	65	2.0	1102.267 (8)	54 (5)	-0.0560 (47)	0.288623 (10)	4.70 ± 0.22	8.46 ± 0.39
	B			1103.486 (15)	92 (10)	-0.0387 (36)	0.287199 (18)	5.52 ± 0.31	9.94 ± 0.56
	Int							10.22 ± 0.38	18.40 ± 0.68
J0901+0304 [d]	A	48	2.0	1102.341 (6)	34 (4)	-0.0608 (62)	0.288536 (7)	3.04 ± 0.17	5.47 ± 0.30
	B			1103.625 (13)	68 (9)	-0.0401 (44)	0.287036 (15)	4.03 ± 0.22	7.26 ± 0.39
	Int							7.07 ± 0.27	12.73 ± 0.49
J0920+2714	A	24	1.8	1177.131 (2)	13 (1)	-0.0819 (107)	0.206668 (2)	1.10 ± 0.19	1.97 ± 0.34
	B	24	1.8	1177.072 (13)	33 (5)	-0.0405 (47)	0.206728 (13)	1.42 ± 0.26	2.56 ± 0.47
	Int							2.61 ± 0.12	4.70 ± 0.21
J1129+5638	A	12	5.0	750.764 (15)	104 (12)	-0.0276 (68)	0.891947 (38)	3.07 ± 0.83	5.52 ± 1.49
	B	12	5.0	751.033 (193)	170 (109)	-0.0063 (24)	0.891270 (487)	1.13 ± 0.85	2.04 ± 1.53
	Gfit[e]	12	5.0	750.788 (6)	127 (6)	-0.0285 (11)	0.891886 (15)	3.85 ± 0.22	6.93 ± 0.40
	Int							4.16 ± 0.14	7.49 ± 0.24
J1357+0046 [f]	A	24	2.8	790.764 (5)	80 (5)	-0.0130 (6)	0.796246 (11)	1.12 ± 0.08	2.01 ± 0.15
	B	24	2.8	790.396 (7)	71 (6)	-0.0088 (7)	0.797081 (16)	0.66 ± 0.08	1.19 ± 0.14
	Int							1.82 ± 0.04	3.28 ± 0.07
J1357+0046 [g]	A	24	3.7	790.767 (5)	90 (4)	-0.0140 (6)	0.796239 (10)	1.34 ± 0.08	2.41 ± 0.15

4.4 Notes on Individual Objects

4.4.1 J0901+0304

See Figure 4.2 for the 21 cm spectra of J0901+0304. We first observed this object using the GBT and found two tentative absorption features. One feature is in a small RFI-free window, and the other is badly contaminated by RFI. We later confirmed both features using the VLA and GMRT.

J0901+0304 has a Sc-type optical+NIR SED (Figure A.1). Its optical and NIR images indicate that this is an interacting system (Figure 4.3) with some diffuse structure extending to the NE of the main galaxy. J0901+0304 is not resolved on our VLBA map with a resolution of ~ 10 mas at 1.4 GHz, which means it could either be a CSO or a core-jet object. Its radio SED shows a gigahertz-peaked-spectrum (GPS), which is commonly found in CSOs. However, higher-resolution radio maps are needed to determine its radio morphology.

We observed J0901+0304 using the Dual Imaging Spectrograph (DIS) and obtained a redshift of 0.2872 ± 0.0001 from emission lines (Figure 2.1). We plotted the line ratios on the BPT diagram (Baldwin et al. 1981) to discriminate whether the narrow emission lines are emitted from a Seyfert galaxy, a low-ionization narrow emission-line region (LINER) galaxy, or a starburst galaxy. According to the classification suggested by (Kewley et al. 2006), J0901+0304 is a LINER galaxy. Weak absorption lines from the star light might be present including the Ca II H & K, G-band, and Mg I λ5175 lines.

Two H I absorption lines are detected, one at the optical redshift, the other redshifted with a velocity of 328 km/s. This leaves the narrow component as an infalling high-velocity cloud (HVC). Since the broad line has a velocity consistent with the nucleus, we identify this absorption as galactic disk gas. This is similar to the circumstances found by Keeney et al. (2011) in PKS 1327−206, which is behind a spiral arm in an interacting galaxy; i.e., the broader H I absorption is a detection in the galaxy disk. The broad H I line could also originate from a circumnuclear disk as in 4C 31.04 (Mirabel 1990) and 3C 190 (Ishwara-Chandra et al. 2003). It is worth noting that LINERs can be

Table 4.2 (continued)

Object	Comp. ID	Resolution (kHz)	rms (mJy)	Center (MHz)	FWHM (km s^{-1})	τ_p	z	$\int \tau \mathrm{d}v$ (km s^{-1})	$N_{\rm HI}$ (10^{20}cm^{-2})
(1)	(2)	(3)	(4)	(5)	(6)	(7)	(8)	(9)	(10)
	B	24	3.7	790.410 (8)	59 (7)	-0.0068 (7)	0.797049 (18)	0.42 ± 0.07	0.76 ± 0.12
	Int							1.74 ± 0.05	3.14 ± 0.09
J1604+6050	Gfit	6	3.0	911.025 (2)	8 (2)	-0.0142 (25)	0.559130 (4)	0.12 ± 0.03	0.22 ± 0.06
	Int							0.14 ± 0.02	0.25 ± 0.04
J1616+2647	Gfit	49	3.4	809.133 (34)	447 (30)	-0.0084 (5)	0.755467 (73)	3.98 ± 0.35	7.16 ± 0.63
	Int							4.00 ± 0.16	7.21 ± 0.28

Note. — Columns list: (1) object name in IAU convention; (2) ID of the absorbing component, where "Gfit" means there is only one component and "Int" means integrated value for all components; (3) spectral resolution of the spectrum; (4) rms measured from continuum-subtracted background; (5) (6) (7) (8) Gaussian fit results of the line center in frequency, FWHM in rest-frame velocity, peak of optical depth, and redshift of line center; (9) integrated optical depth $\int \tau \mathrm{d}v$ either from Gaussian fit or in case of "Int", directly measured from the data; (10) column density of the absorbing component assuming full covering factor and a spin temperature of 100 K.

[a]GBT observation.

[b]"A" component only.

[c]GMRT observation.

[d]VLA observation.

[e]Gaussian fit of single compoent.

[f]GBT observation on May 22, 2009.

[g]GBT observation on July 01, 2009.

Table 4.3. H I Upper Limits.

Object	Search Freq. (MHz)	rms (mJy)	$\tau_{3\sigma}$	$N_{\rm HI}$ (10^{20}cm^{-2})	RFI
J0134+0003 [a]	755.94	11.6	< 0.030	< 5.8	
J0134+0003 [b]	755.94	5.4	< 0.010	< 2.0	
J0751+2716	1052.64				RFI
J0805+1614	870.35				RFI
J0824+5413	866.89				RFI
J1033+3935	678.00				RFI
J1410+4850	892.21				RFI
J1504+5438	875.48				RFI

Note. — Assuming $T_s = 100$ K, $f = 1$, $\Delta V = 100$ km s^{-1}. In calculating rms, a resolution of 10 km s^{-1} is used.

[a]AO observation.

[b]GBT observation.

Table 4.4. OH Upper Limits.

Object	OH 1612 MHz				OH 1667 MHz				OH 1720 MHz			
	ν (MHz)	rms (mJy)	Con. (Jy)	$N_{\rm OH}/10^{14}$ ($\rm cm^{-2}$)	ν (MHz)	rms (mJy)	Con. (Jy)	$N_{\rm OH}/10^{14}$ ($\rm cm^{-2}$)	ν (MHz)	rms (mJy)	Con. (Jy)	$N_{\rm OH}/10^{14}$ ($\rm cm^{-2}$)
J0751+2716	1195	2.3	0.78	$< 19.8\ T_x$	1236	N/A			1275	N/A		
J0805+1614	988	RFI			1022	RFI			1054	RFI		
J1129+5638	852	RFI?			881	RFI?			909	RFI?		
J1357+0046	898	N/A			928	RFI			958	2.5	2.77	$< 6.1\ T_x$
J2203−0021	932	1.8	0.77	$< 16.1\ T_x$	964	1.7	0.74	$< 1.6\ T_x$	995	1.7	0.72	$< 16.2\ T_x$
J0134+0003	858	RFI?			887	RFI?			916			

Note. — Assuming $T_x = 100$ K, $f = 1$, $\Delta V = 100$ km s^{-1}. In calculating rms, a resolution of 10 km s^{-1} is used.

found in extranuclear starburst regions that have large scale outflows with velocities of hundreds of km s^{-1} (Lípari et al. 2004). It's possible that the LINER and the absorption line gas in J0901+0304 arise in the same region.

4.4.2 J0920+2714

See Figure 4.4 for the 21 cm spectrum from the GBT where we observed J0920+2714 in 2006 through an exploratory program. We later obtained an optical redshift in 2009 and found that the 21 cm absorption feature is slightly redshifted with respect to the optical redshift.

This is an intervening system with a double-lobe radio source in the background and a galaxy at $z = 0.2064 \pm 0.0002$ in the foreground (Figure 4.5). The intervening determination was made based upon the significant offset between the radio core and the galaxy nucleus (see Chapter 3). The foreground galaxy has an S0-type optical+NIR SED (Figure A.1). A DIS spectrum shows absorption lines from star light and weak emission lines (Figure 2.1). The radio object is an LSO with a steep spectrum (Chapter 3).

We fit two Gaussian lines to the blended feature. The deep narrow line is not resolved and a shallower line has a FWHM of 33 km/s. Both are redshifted with respect to the systemic redshift by 66 and 81 km/s respectively. However, the rotation curve of the S0 galaxy is redshifted toward the southwest where the strongest radio source component lies. Therefore, these absorptions are consistent with being normal disk gas.

4.4.3 J1129+5638

See Figure 4.6 for the 21 cm spectrum of J1129+5638. It is a CSO candidate according to our VLBA observations (Figure 4.7). Its optical/NIR SED is best fit by a Sc-type spiral galaxy template (Figure A.1). It was observed by Gemini/GMOS to obtain a redshift of 0.8925 ± 0.0008 from narrow emission lines (Figure 2.3). The presence of the high ionization [Ne V] line suggests that this source is a narrow line radio galaxy.

The 21 cm absorption is quite broad, FWHM = 318 km s^{-1} if fit by a single Gaussian

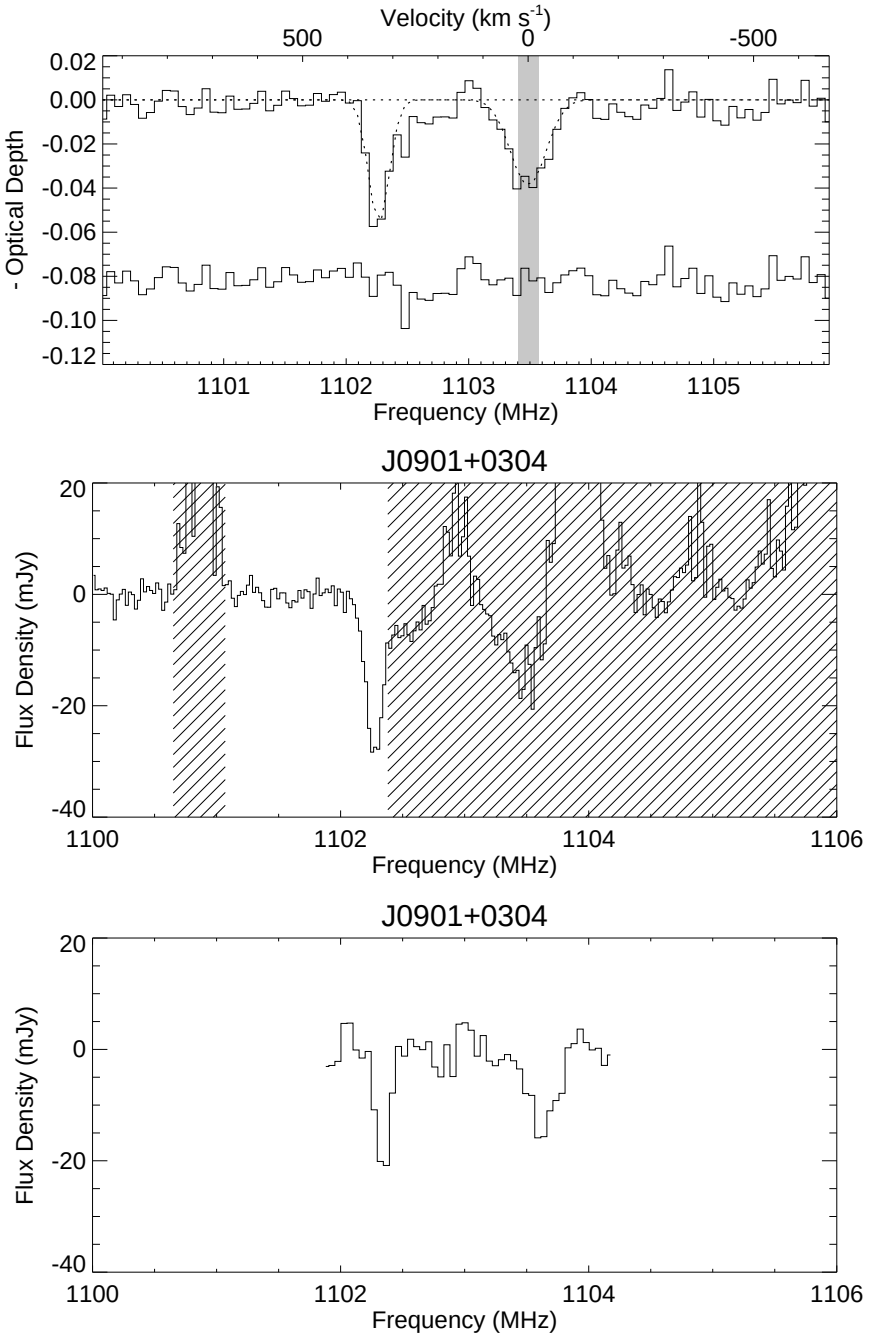

Figure 4.2 The H I 21 cm spectrum in J0901+0304 as observed by GMRT (top), GBT (middle), and VLA (bottom). On the GMRT plot, a Gaussian fit to the two absorption components are shown in dotted lines. Residuals are displayed with an offset in y for clarity. Zero velocity is set to the redshift of the optical galaxy at $z = 0.2872 \pm 0.0001$, with uncertainties shown in gray shade. The hatched regions are contaminated by RFI in the GBT spectrum.

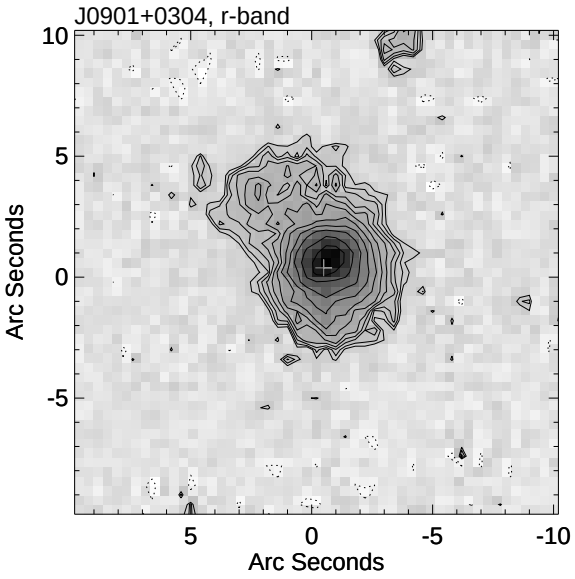

Figure 4.3 Image of J0901+0304 at the r-band. The plus sign marks the peak of the 1.4 GHz VLBA image. The images is sky-subtracted, and the lowest contour levels are 1.5 times of the sky variation.

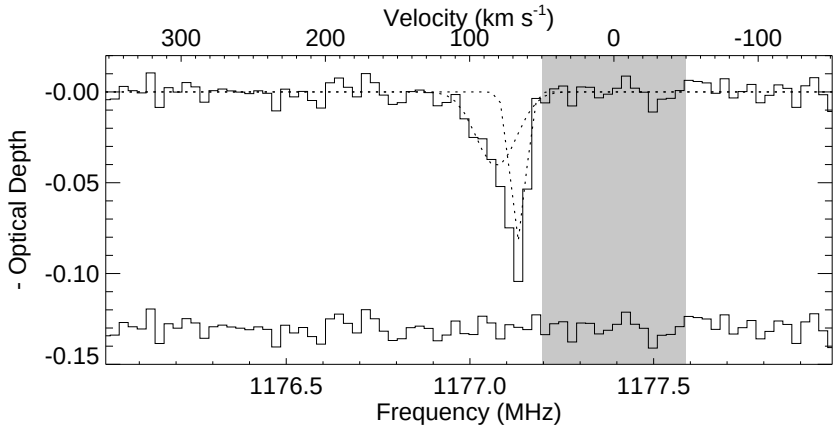

Figure 4.4 H I 21 cm spectrum in J0920+2714 observed by GBT. We fit the absorption feature with two Gaussian components. The narrow component is not resolved (FWHM $\sim$ 2 spectral channels by Gaussian fit). A Gaussian fit to the two absorption components are shown in dotted lines. Residuals are displayed with an offset in y for clarity. Zero velocity is set to the redshift of the optical galaxy, with uncertainties shown in gray shade.

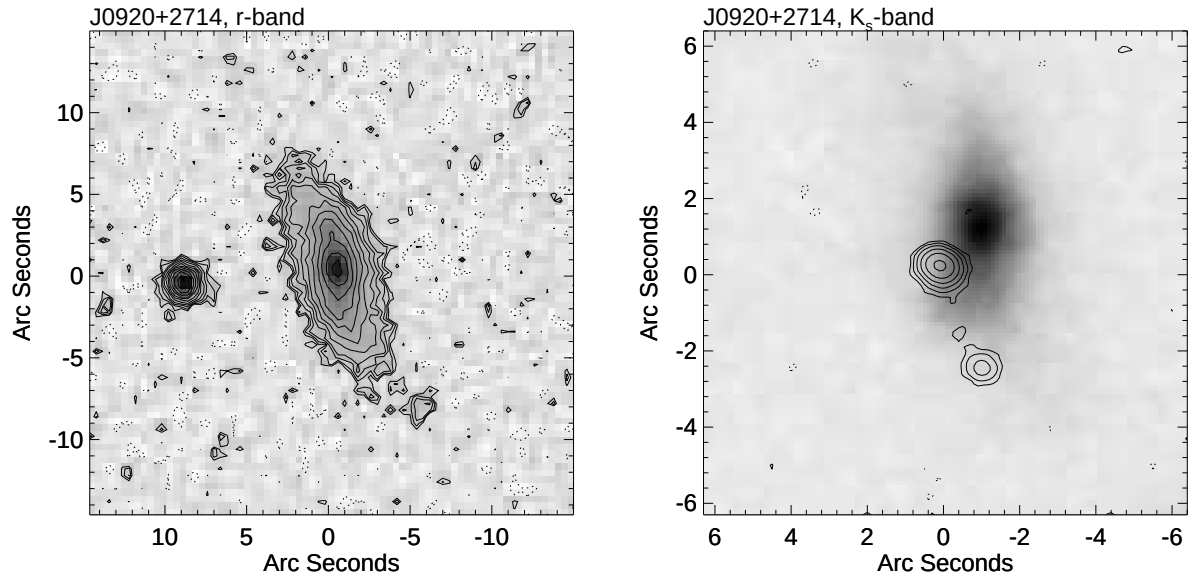

Figure 4.5 Images of J0920+2714 at the r-band (*left*), $K_{\rm s}$-band (*right*, grayscale), and the VLA-A 4.9 GHz (*right*, contours). The r-band and $K_{\rm s}$-band images are sky-subtracted. In the r-band image, the lowest contour levels are 1.5 times of the sky variation. The $K_{\rm s}$-band image has been re-gridded and smoothed by cubic interpolation to match the astrometry of the higher-resolution VLA-A 4.9 GHz image. Pixel counts are displayed by grayscale with the following approach. On a grayscale of 0 (white) to 1 (dark), 1 represents the maximum pixel counts of the object; 0 and 0.2 represents -2.5σ and 2.5σ noise of the sky background respectively; between 0 to 0.2 and 0.2 to 1, it scales linearly with pixel counts. In the VLA-A 4.9 GHz image, the lowest contour level is 3 times the rms.

profile. The redshift of the absorption is consistent with the redshift of the optical emission lines. However, the uncertainty in the optical redshift corresponds to ~ 240 km s^{-1} in velocity. Given the slight (1σ) offset in velocity between the H I absorption and the narrow emission line redshift, this detection is consistent either with normal disk gas or outflowing material. However, the CSO-type radio morphology is not consistent with an outflow in our direction. Therefore, we interpret this detection as being disk gas.

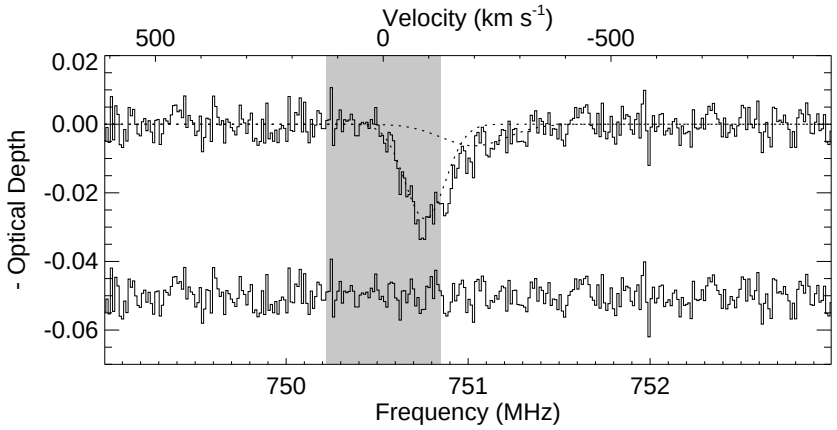

Figure 4.6 H I 21 cm spectrum in J1129+5638 observed by the GBT. Although an asymmetry is present in the feature, the shallower component is not well detected ($< 2\sigma$ for a two-component Gaussian fit). We have also fit the feature with a single component which gives a slightly larger χ^2. A Gaussian fit to the two absorption components are shown in dotted lines. Residuals are displayed with an offset in y for clarity. Zero velocity is set to the redshift of the optical galaxy, with uncertainties shown in gray shade.

4.4.4 J1357+0046

See Figure 4.8 for the 21 cm GBT spectrum. This is the only successful detection without an optical/NIR spectroscopic redshift. J1357+0046 is a CSO candidate by our VLBA observations (Figure 4.9). Its optical+NIR SED is classified as $G+Q$ (Figure A.1). The two lines have a velocity separation of 140 km/s, and FWHMs of 80 km/s and 70 km/s respectively. Without an accurate spectroscopic redshift an assignment of these as disk gas, infall or outflow is not possible.

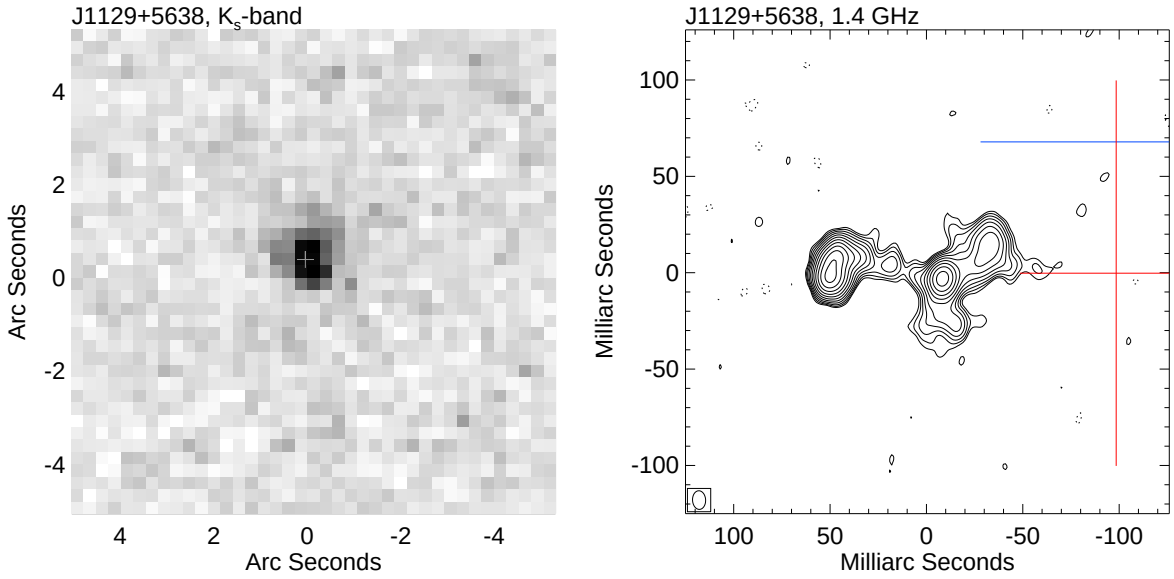

Figure 4.7 Images of J1129+5638 at the K_s-band (*left*) and the VLBA 1.4 GHz (*right*). The K_s-band image is sky-subtracted, and the lowest contour levels are 1.5 times of the sky variation. The plus sign marks the center of the 1.4 GHz image. In the 1.4 GHz image, the centroid positions at the r-band and K_s-band are marked with uncertainties in blue and red respectively. The irregular morphology in the optical/NIR plus the large positional errors in the VLBA map still can be consistent with an associated, not intervening absorber. The lowest contour levels are 3 times the rms.

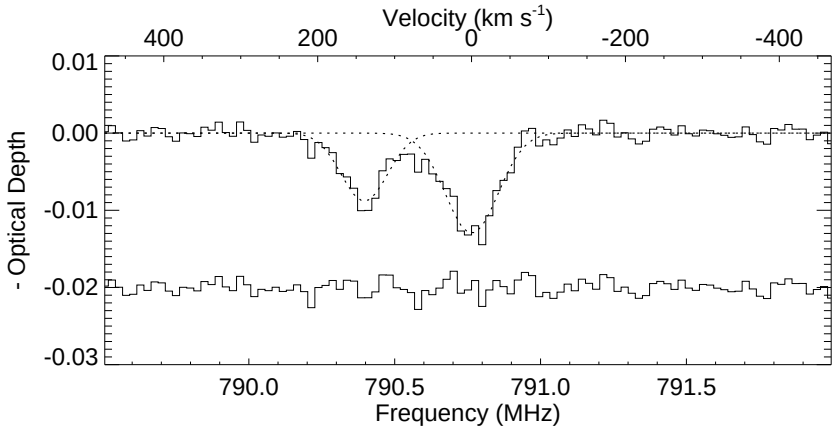

Figure 4.8 H I 21 cm spectra in J1357+0046 observed by GBT. J1357+0046 does not have a spectroscopic redshift in the optical. A Gaussian fit to the two absorption components are shown in dotted lines. Residuals are displayed with an offset in y for clarity. The zero velocity is set to the center of the low redshift H I component ($z = 0.7962$). Only a photometric redshift available for this source.

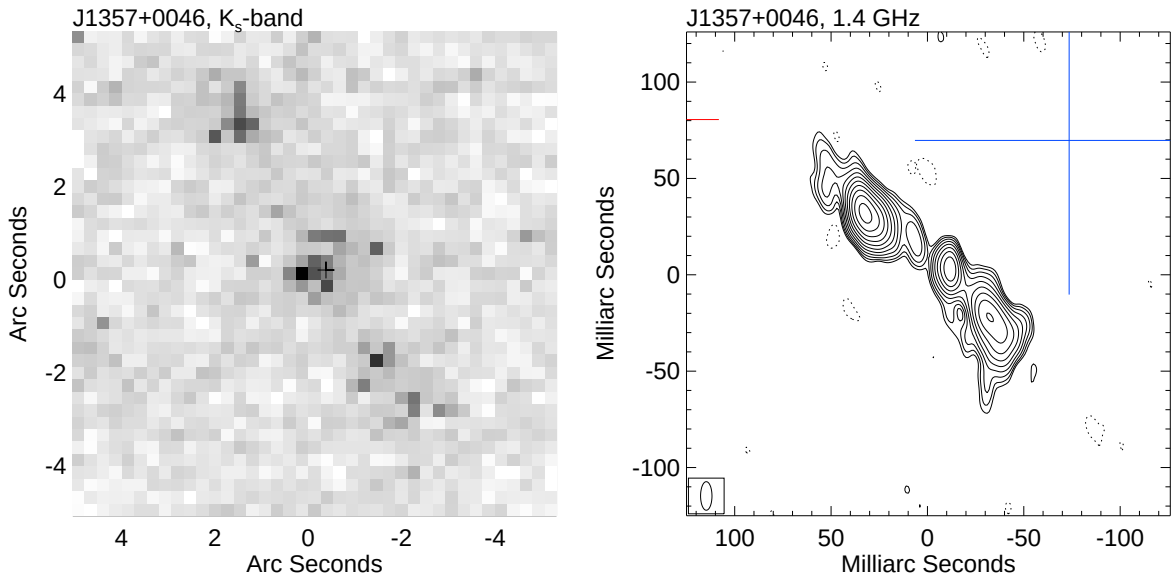

Figure 4.9 Images of J1357+0046 at the K_s-band (*left*) and the VLBA 1.4 GHz (*right*). The K_s-band image is sky-subtracted, and the lowest contour levels are 1.5 times of the sky variation. The plus sign marks the center of the 1.4 GHz image. In the 1.4 GHz image, the centroid positions in r-band and K_s-band are marked with uncertainties in blue and red respectively. The lowest contour level is 3 times of the rms.

4.4.5 J1604+6050

See Figure 4.10 for a tentative narrow 21 cm absorption component at the optical redshift. The redshift of J1604+6050 was obtained by Gemini-GMOS (Figure 2.3). The redshift of the narrow emission lines is 0.5590 ± 0.0004, and that of absorption lines is 0.5627 ± 0.0015. J1604+6050 is a CSO in our VLBA map (Figure 4.11). Its optical+NIR SED is best fit by a S0-type template (Figure A.1). The tentative line is extremely narrow line with an FWHM of only 8 km/s.

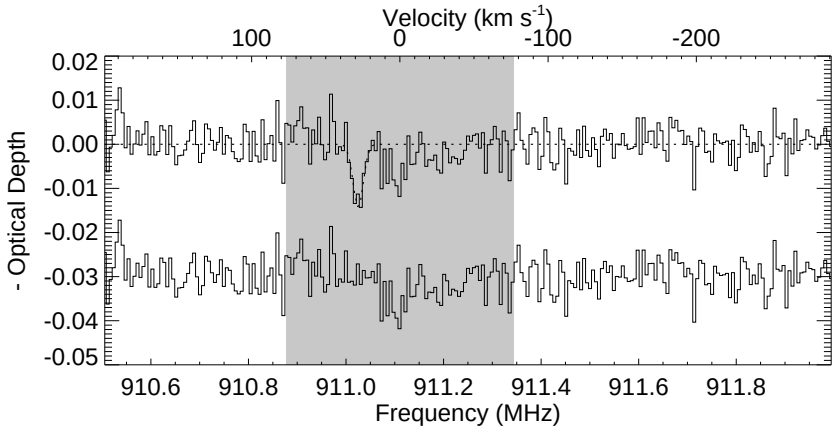

Figure 4.10 H I 21 cm spectrum in J1604+6050 observed by GBT. There is a tentative absorption system at 911.025 MHz. A Gaussian fit to the absorption component is shown in dotted lines. Residuals are displayed with an offset in y for clarity. Zero velocity is set to the redshift of the optical galaxy determined from emission lines, with uncertainties shown in gray shade.

4.4.6 J1616+2647

See Figure 4.12 for the 21 cm spectrum. J1616+2647 is a CSO according to our VLBA observations (Figure 4.13). Its optical+NIR SED is best fit by a Sc-type galaxy template (Figure A.1).It was observed by Gemini/GMOS to obtain a redshift of 0.7553 ± 0.0003 from narrow emission lines (Figure 2.3).

J1616+2647 is one of the broadest absorption systems detected so far with an FWHM of 447 km/s. There are four objects that have 21 cm absorption lines broader than 400 km/s, including 3C 84 and PKS 2322−12, cD galaxies close to the center of galaxy clusters (Inoue et al. 1996; Sarazin et al. 1995). While it would be natural to associate the absorptions with out-flowing gas,

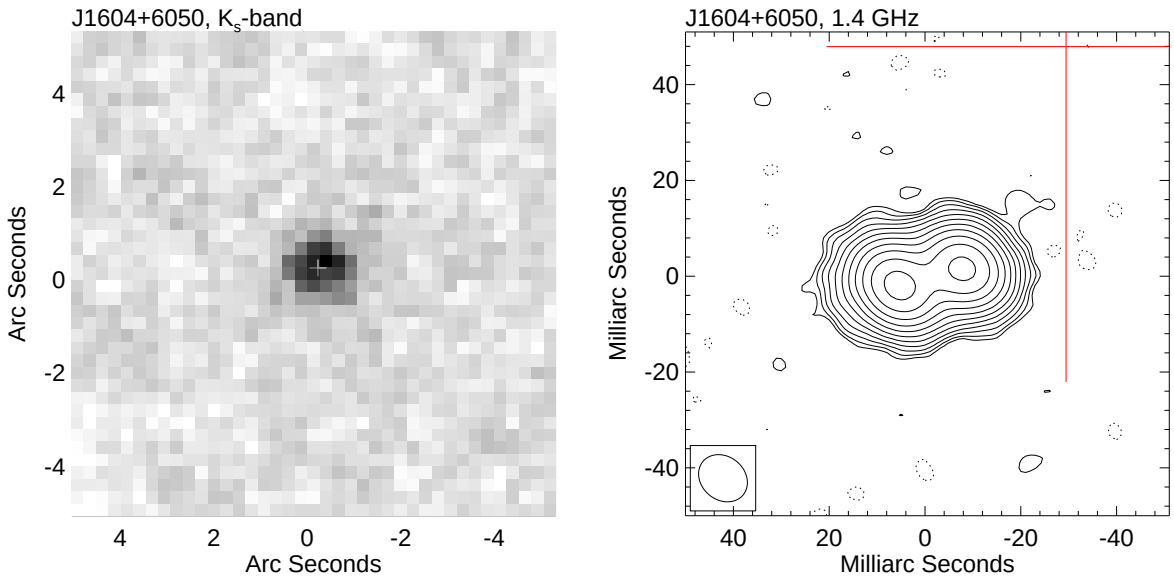

Figure 4.11 Images of J1604+6050 at the $K_{\rm s}$-band (*left*) and the VLBA 1.4 GHz (*right*). The $K_{\rm s}$-band image is sky-subtracted, and the lowest contour levels are 1.5 times of the sky variation. The plus sign marks the center of the 1.4 GHz image. In the 1.4 GHz image, the centroid positions in r-band and $K_{\rm s}$-band are marked with uncertainties in blue and red respectively. The lowest contour level is 3 times of the rms.

the absorption in J1616+2647 is centered at the systemic redshift and could also be partly or largely disk gas.

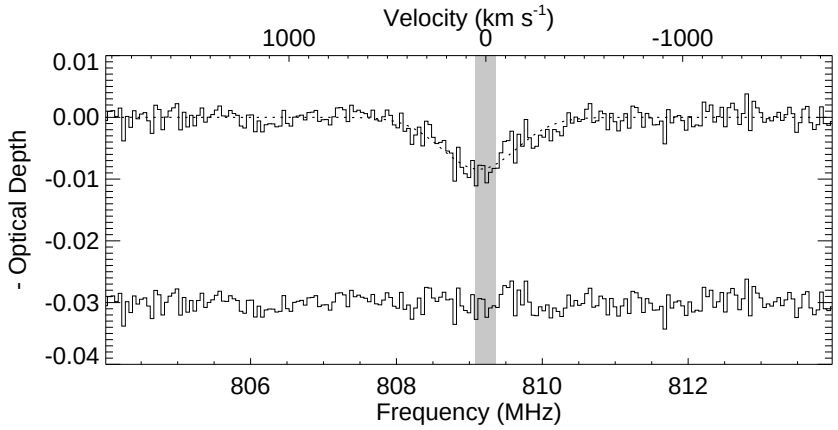

Figure 4.12 H I 21 cm spectrum in J1616+2647 observed by GBT. This absorption system has large velocity dispersion ($\sim$ 500 km s^{-1} in rest frame from Gaussian fit). A Gaussian fit to the absorption component is shown in dotted lines. Residuals are displayed with an offset in y for clarity. Zero velocity is set to the redshift of the optical galaxy, with uncertainties shown in gray shade.

4.5 Associated H I Absorbers ($z_{\rm abs} = z_{\rm em}$)

In this section we investigate the key factors, among various source properties such as radio sizes, AGN types, and UV luminosity that impact the properties of associated absorption lines such as detection rates and column densities. We made three detections, one tentative detection, and one non-detection among 5 objects that have been searched at their spectroscopic redshifts. The absorption lines in J1357+0046 are very likely associated, although we have not obtained a spectroscopic redshift. Overall, our sample has a high detection rate of associated H I absorbers.

4.5.1 Radio Luminosity

It has been found that radio luminosities do not effect the detection rates or column densities of H I absorbers. Our sample has a lower radio luminosity compared to previous samples at the same redshift range. Although it could be possible that objects with lower radio luminosities have more gas content, present data are not sufficient to make a conclusion.

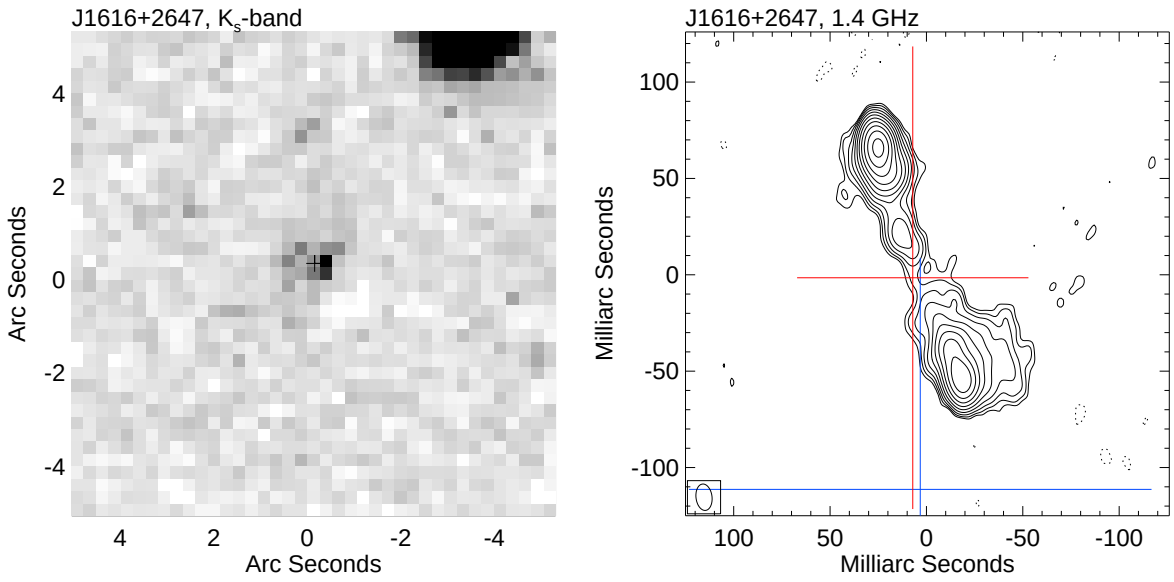

Figure 4.13 Images of J1616+2647 at the K_s-band (*left*) and the VLBA 1.4 GHz (*right*). The K_s-band image is sky-subtracted, and the lowest contour levels are 1.5 times of the sky variation. The plus sign marks the center of the 1.4 GHz image. In the 1.4 GHz image, the centroid positions in r-band and K_s-band are marked with uncertainties in blue and red respectively. The lowest contour level is 3 times of the rms.

Table 4.5. Properties of the objects searched for H I absorption.

Object	Redshift	Optical+NIR SED	Radio Morphology	LLS (kpc)	Radio SED	Turnover Freq. (MHz)
(1)	(2)	(3)	(4)	(5)	(6)	(7)
J0901+0304	0.2872 ± 0.0001	G/Sc	PS[a]	0.047	GPS	807
J1129+5638	0.8925 ± 0.0008	G/Sc	CSO	0.622	SS	334
J1357+0046	0.7971,0.7962[b]	G+Q	CSO	0.647	SS	< 365
J1616+2647	0.7553 ± 0.0003	G/Sc	CSO	0.915	GPS	423
J1604+6050 [c]	0.5590 ± 0.0004	S0	CSO	0.089	GPS	670
J0134+0003 [d]	0.8790	Sa	CSO	0.140	GPS+SS[e]	2054
J0920+2714 [f]	0.2064 ± 0.0002	S0[g]	LSO[h]	<24.717	SS	< 74

Note. — Columns list: (1) object name; (2) redshift; (3) optical+SED type and Hubble type; (4) radio morphology type; (5) largest projected linear size; (6) radio SED type; (7) turnover frequency of the radio SED.

[a]With a resolution of 15 mas at 1.4 GHz.

[b]Redshifts of the two 21 cm absorption lines.

[c]Tentative detection.

[d]Non detection.

[e]GPS at high frequencies and SS at low frequencies. The cut-off frequency is 515 MHz.

[f]Intervening absorber.

[g]The foreground object.

[h]The background object.

4.5.2 Compactness

Absorptions are rarely detected in LSOs unless they have strong core or jet components. We have shown that for most of the objects in our sample, the radio emission is confined within their host galaxies. The objects we searched for associated absorptions are all compact with projected linear size < 1 kpc. Vermeulen et al. (2003) found a high detection rate (33%) of H I absorptions in compact radio sources. Their sample includes both radio-loud galaxies and radio-loud quasars, CSOs (< 1 kpc) and MSOs (> 1 kpc, < 15 kpc). Further examination is needed for sub-groups because their detection rates are different.

A fractional compactness can be calculated from the ratio of the peak flux density in the brightest component to the integrated flux density. We plot these ratios for our 4.9 GHz VLA-A images and for 1.4 GHz VLBA images in Figure 4.14 against radio sizes. From this Figure we infer that sources with VLBA fractional compactness $> 15\%$ are the most likely to produce H I 21 cm absorption lines. And since many sources with high compactness in VLA-A images have low compactness in VLBA images, VLBA mapping is essential to use for this compactness discrimination.

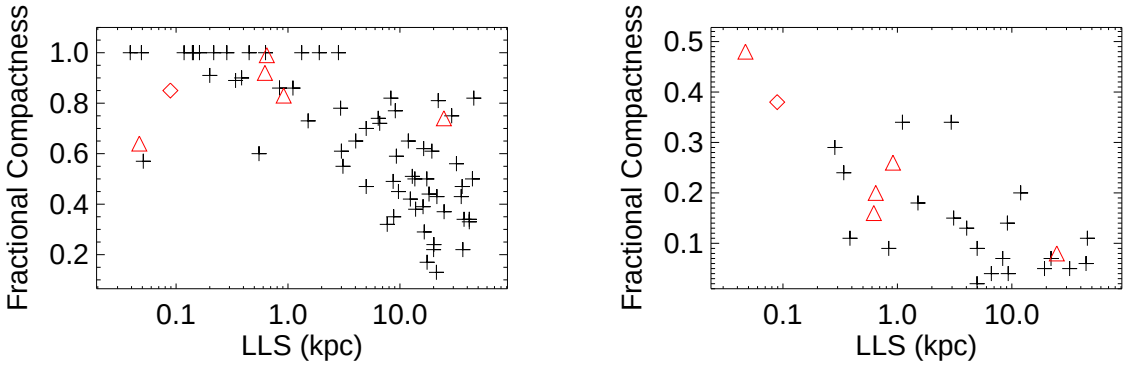

Figure 4.14 Fractional compactness vs projected linear sizes for 4.9 GHz VLA-A images (left) and 1.4 GHz VLBA images (right). The total flux densities are from the FIRST survey (1.4 GHz) and other low-resolution surveys (4.9 GHz). The triangles represent H I detections, and the diamond represents the tentative detection.

4.5.3 The Unified Scheme of AGN

It has been found that the detection rate is higher in radio-loud galaxies than radio-loud quasars, and higher in GPS objects than flat-spectrum (FS) objects. This is largely consistent with the unified scheme of AGN where radio-loud galaxies are viewed close to the plane of the circum-nuclear disk and torus while radio-loud quasars are viewed closer to the jet propagation direction (Best et al. 2005). Our data are consistent with the unified schemes of AGN. Among our 4 detections of associated absorption, 3 have G-type optical+NIR SEDs best fit by an Sc-type template, 3 are CSOs, and 3 have radio SEDs peaking between 300 MHz and 800 MHz.

The two high-z H I absorbers known so far were both detected serendipitously. MG J0414+0534 at $z = 2.6$ is an ultraluminous IR galaxy strongly magnified in a gravitational-lens system (Moore et al. 1999; Downes & Solomon 2003). B2 0902+34 is a giant elliptical galaxy at $z = 3.4$ with an R-band magnitude of 23.5 (Uson et al. 1991; Adams et al. 2009).

4.5.4 UV Luminosity

However, the geometry of the absorbing gas does not seem to match the geometry of the circum-nuclear dust that blocks the thermal light from AGN. And there is increasing evidence that many of the absorption lines are induced by the interaction between the jets and ISM. The turbulence induced by strong interactions can naturally explain the wide span of both the velocity offsets (up to a few thousand km/s) and the line widths (from $\sim$ 10 km/s to $\sim$ 500 km/s) of H I absorption lines found by ourselves and others. Moreover, Curran & Whiting (2010) find a critical UV luminosity, $L^c_{UV} = 10^{23}$ W Hz^{-1}, above which no 21 cm absorption system has been detected. They also questioned the unified schemes of AGN because they find no difference between the detection rates in AGN types once $L_{UV} < L^c_{UV}$. UV luminosities may be an indicator of the extent of obscuration, either by circum-nuclear dust or by the interstellar medium (ISM).

Our selection criteria tend to select objects at $z < 1$ with low UV luminosity. To demonstrate, we plot in Figure 4.15, the UV luminosity as a function of redshift for objects with 19th magnitude

in the r-band. 19th mag is the bright limit of our sample (except a few galaxies at $z = 0.1 - 0.3$, which all have $L_{UV} < 10^{23}$ W Hz^{-1}). We can see from Figure 4.15 that all types of galaxies have UV luminosity much lower than 10^{23} W Hz^{-1}, while quasars exceed this luminosity at $z \sim 1$. Therefore, if correctly selected, all of the objects in our sample have $L_{UV} < 10^{23}$ W Hz^{-1} except a few intervening systems. Our detection rate seems to be higher than the 50% found by Curran & Whiting (2010). We will show in Section 4.5.5 that the ISM is denser in our sample, which may contribute to the high detection rate.

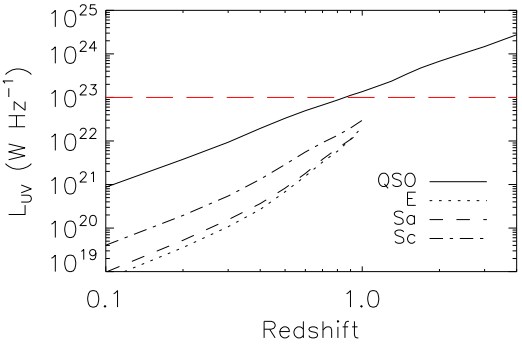

Figure 4.15 UV luminosities vs. redshifts for objects with $r = 19$ mag. The redshift range of galaxies in our sample spans from 0.1–1, due to the selection criteria which require that the object is detected in the Sloan Digital Sky Survey.

4.5.5 The Interstellar Medium (ISM) in This Sample

Pihlström et al. (2003) found an anti-correlation between H I column densities and radio size (0.01–10 pc). In Figure 4.16, we can see our four associated absorbers tend to have column densities higher than the relation in Pihlström et al. (2003). We used the same assumptions of the spin temperature (100 K) and covering factor (100%) as in Pihlström et al. (2003). A dense ISM is also suggested for a larger sub-group of our sample through the separation ratio and the flux density ratio of the lobes on each side of the core. We plot these ratios for the LSOs and MSOs in this sample in Figure 4.17. The centroid position of the K_s-band image is used to identify the core component. CSOs are not included because a core is generally not identified in their radio

images and the position uncertainty of their K_s-band image are too large to be used as the core position. There is a trend that the brighter lobe tends to be closer to the core. A similar trend has been found previously (Saikia et al. 2001; Rossetti et al. 2006), but is much stronger in our sample, which implies the ISM is denser in this sample.

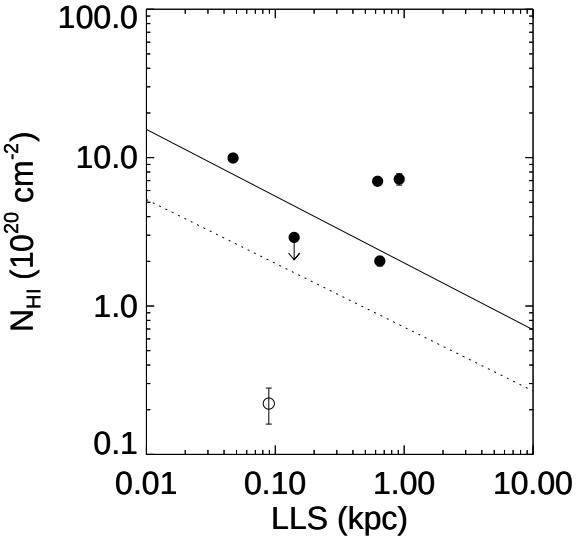

Figure 4.16 H I column densities vs projected linear sizes for objects searched for associated H I absorptions. The tentative detection is shown as an open circle. The upper limit is shown with an arrow for one clean non-detection. The solid line is the anti-correlation found by Pihlström et al. (2003) for H I absorptions, and the dashed line includes both detections and upper limits (Pihlström et al. 2003).

4.6 Search for OH Lines

We only obtained limited data on the search of OH lines, and no detection has been made. Since the successful detection of four redshifted molecular absorption systems by Wiklind and Combes in the 1990s (Wiklind & Combes 1994, 1995, 1996a,b), only one absorber has been detected, a $z_{\rm abs} = 0.765$ absorber toward the gravitational lensed PMS J0134−0931 (Kanekar et al. 2005). In this absorption system, only OH 18 cm lines are detected, unlike the above four sources which were first found in millimeter lines such as the rotational lines of CO, HCO, and HCN, and then searched in OH 18 cm lines. Different approaches have all failed to find more molecular systems

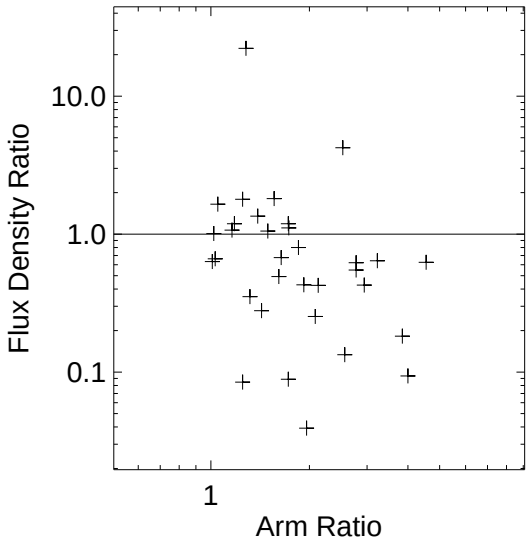

Figure 4.17 Flux density ratios vs arm (separation) ratios of the two lobes for LSOs and MSOs (Core-jet Objects and CSOs not included). The brighter lobe tends to be closer to the core.

((Combes 2008; Curran et al. 2011b)). The two known associated OH absorbers are quite similar: both have large jet inclination angles; both are in edge-on disk galaxies; and both are very red. A radio-loud galaxy in a late-type galaxy is inevitably rare and the alignment of the radio emission and disk gas adds to that rarity. We believe our sample will be ideal for this search because of the late-type morphology.

4.7 Discussion and Conclusions

After selecting the best candidates, we have completed the first round of searches for absorption lines at radio frequencies. Five new H I absorption systems have been detected among the seven objects with usable data. The detection rate is higher than previously selected samples, and consistent with previous finding that H I 21 cm absorptions are most likely detected in compact radio galaxies. However, the number of searched objects is still small, and more observations in this sample with help us understand the most important factor in detecting redshifted absorption systems. While we acknowledge that these absorptions could be due to gas associated with an AGN torus, they are most consistent with disk gas in the spiral host galaxies. Evidence favoring this interpretation includes the concordance of optical/NIR and H I 21 cm redshifts and the indication that these sources contain H I absorptions only slightly dense than previous H I detections (Pihlström et al. 2003). This early result suggests that the eventual detection of molecular gas will allow us to probe star formation sites, not AGN torus, and different redshifts.

A thorough search is hindered by the lack of accurate redshift for most objects at this point. Large 10-m telescopes are needed to obtain optical/NIR spectroscopy for these faint sources. Alternatively, the newly-operated Atacama Large Millimeter/sub-millimeter Array (ALMA) can be used to obtain mm/sub-mm spectroscopy for the mm/sub-mm bright objects. Meanwhile, the severe RFI conditions are also preventing us from obtaining usable data even when a spectroscopic redshift is available. Therefore a large pool of objects with accurate redshift is essential for continuing the search.

Chapter 5

Future Work

This thesis studies a sample of obscured AGN in hopes of finding new absorption systems at radio frequencies at cosmological distances. The sample is well selected to have a bright radio background and a gas-rich environment along the sightline, i.e., radio AGN with a late-type optical morphology. Four new H I 21 cm absorption systems have been detected in six objects with usable data, in addition to one detection in broadband searches using photometric redshifts where the existence of the 21 cm absorption can not be made conclusively due to wide spread RFIs. Although no molecular absorption systems have been detected, we have demonstrated that this is a very promising sample for finding these exceptional rare systems. We will continue the search to hopefully find about 20 more H I 21 cm absorption systems and 2–3 molecular absorption systems in the full sample. This sample has proved to be very efficient in finding young radio galaxies (CSOs) as well. Young radio galaxies are very important to study the onset of radio activity and its interacting with ISM. We will continue the study of young radio galaxies in the sample as well as selecting new candidates for higher-z or even younger objects.

5.1 Mid-Infrared Photometry

We have obtained 3.6 and 4.5 μm images using the Infrared Array Camera (IRAC) on the Spitzer Space Telescope for the full sample of 80 objects to achieve 1-σ noise level of 1 μJy. Sixty five objects have also been detected by the Wide-field Infrared Survey Explorer (WISE) with images in 3.4, 4.6, 12 and 22 μm wavelength bands. Extending the optical–NIR SED into the mid-infrared

(MIR) would provide more information on the obscuration of AGN and the star formation region.

For early-type galaxies with only old stars, their SEDs decline in the MIR (see Figure 5.1 left-band panel). As for late-type galaxies, a MIR bump would show up from the gas in the star formation region. A good example is the ultra-luminous infrared galaxy 4C +12.50 (J1347+1217) in the sample. A quasar obscured in the optical would emerge in the IR like in the case of PKS 1413+135 (J1415+1320). In this case (see example in Figure 5.1 right-hand panel), the high extinction indicates a large gas screen in front of the AGN. Therefore, it is very useful to identify IR-bright objects in the sample using the optical–NIR–MIR SEDs like in Figure 5.1. The data are now being analyzed.

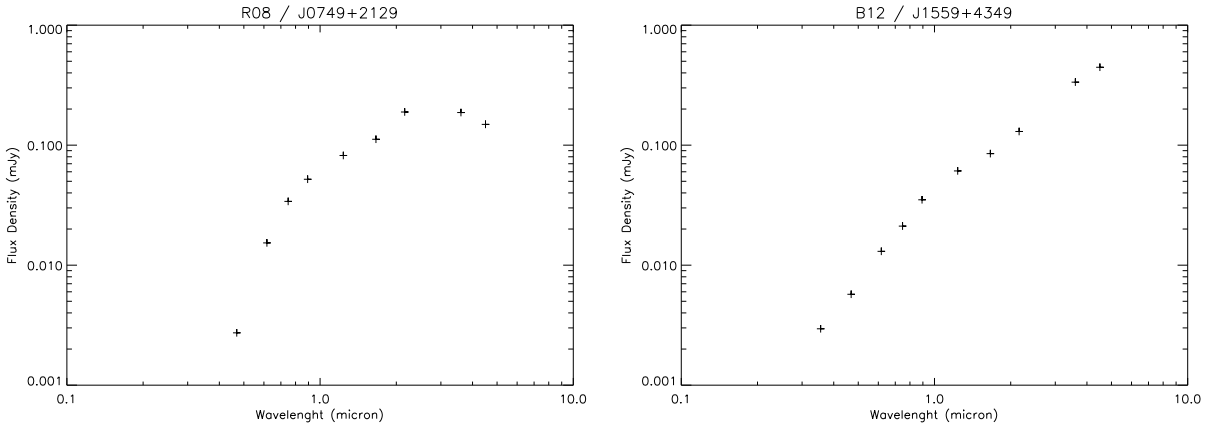

Figure 5.1 The optical–IR SEDs of J0749+2129 and J1559+4349 at the SDSS u,g,r,i,z-bands, NICFPS J,H,K-bands, and IRAC 3.6, 4.5 μm bands.

5.2 Line Searches

We will continue the search of H I 21 cm absorption lines in the sample. As discussed in Chapter 4, the two obstacles are (1) lacking spectroscopic redshifts, (2) limited RFI-clean windows at sub-GHz bands. To obtain more spectroscopic redshifts, we will propose to take optical/NIR spectroscopy with 10-m telescopes such as Gemini. The emission lines will also help us to determine the physical conditions of the emitting gas such as its origin, density, and temperature. Once the redshift is determined for an object, we will select an RFI-clean radio telescope at the redshifted

21 cm wavelength range for line searches. OH 18 cm lines will be searched once H I 21 cm lines are found. Millimeter molecular absorption lines will also be searched toward mm-bright objects, but only for flat-spectrum sources with sufficient continuum flux at mm wavelengths. Or conversely, a redshift could be determined by mm spectroscopy first with the unprecedented capability of ALMA or CCAT.

5.3 VLBI Spectral Mapping of the H I Absorbers

The H I 21 absorption lines have a variety of origins including the AGN torus, AGN disk, jet/cloud interaction, giant molecular clouds, high velocity clouds, and outflow/infall gas, resulting in various line depths, widths, and velocity offsets. VLBI spectral mapping of the 21 cm line can pin down the location of the H I absorption components and study the physical conditions of the absorbing gas (e.g., Perlman et al. 2002; Conway 1999; Araya et al. 2010). For example, the mapping of J1616+2647 would reveal whether the broad absorption feature is from the core, from the lobes, prevailing through the entire radio structure, or made up of multi-components from multiple locations. Unfortunately such mapping is possible only at the specific receiver bands available at EVLA or GMRT, and only at low-z for the VLBA.

5.4 VLBI Mapping of CSOs

VLBA continuum mapping will be used to locate/detect weak cores to confirm CSOs. A central core would have flat spectrum while the lobes have steep spectrum. Multifrequency observations up to $\sim$ 10 GHz (X-band) will be carried out simultaneously because the core component might be variable over a few months/years. It is also possible to measure the jet advance speed in the smallest angular size CSOs ($\sim$ 15 mas), J0134+0003, J1413+1509, and J1414+4554 by multiple epoch observations over $\sim$ ten years.

5.5 A Sample of Red Radio-loud AGN

Here we propose to select a sample of "red" radio-loud AGN from the FIRST, SDSS, and WISE surveys, which are good candidates for high-z CSOs/MSOs or highly-obscured radio quasars. In the 2012 February 16 version of the FIRST survey, there are 3072 objects that have $S_{1.4\mathrm{GHz}} >$ 300 mJy. Among them, 2895 are in the sky coverage of the SDSS DR8 catalog. About half of the FIRST objects (1555) do not have an counterpart in SDSS DR8 (within $1\farcs5$). To select the most compact radio objects, we set $2''$ upper limit for the deconvolved major axis of FIRST objects, compared to the $\sim 5''$ survey resolution. This gives 443 objects remaining in the sample. These are then cross-referenced with the WISE survey, and we find that 157 objects are detected in WISE (again within $1\farcs5$). We scrutinize each object in the SDSS DR10 catalog and exclude 10 objects not included in the database yet as well as 24 objects that have possible counterparts. Therefore, a final sample of red radio-loud AGN includes 123 objects that are radio bright, optically faint, and IR bright. The average detection limit of the SDSS survey is $\sim$ 6.0, 4.8, 4.8, 11.0, and 22.4 μJy at the u, g, r, i, z-band respectively (Stoughton et al. 2002). The WISE photometric sensitivity is $\sim$ 0.068, 0.098, 0.86 and 5.4 mJy at 3.4 (W1-band), 4.6 (W2-band), 12 (W3-band) and 22 (W4-band) μm in unconfused regions (Wright et al. 2010).

Nearly all the CSOs/MSOs identified so far are at $z < 1$ due to the fact that they reside in radio galaxies instead of radio quasars. The brightest W1-band object in this sample, 87GB 081856.9+512216, has a radio SED peaking around 150 MHz, which corresponds to $\sim$ 450 MHz in the rest frame if located at $z \sim 2$, making it a good candidate for a high-z CSO. These objects could also be radio quasars that are highly obscured in the optical, which would be good candidates for absorption-line searches as well.

5.6 A Sample of Flat Spectrum Radio Galaxies

The majority of the CSOs are found in GPS objects with radio SEDs peaking around 0.5–5 GHz. From the the anti-correlation between turnover frequencies and sources sizes, we know that

smaller objects should peak at higher frequencies. Because the hotspot advance speed ($\sim$ 0.1–0.2 c) is almost independent of the source size, smaller objects are also younger. The youngest CSO detected so far is VII Zw 485 at $z = 0.107$ with a kinematic age of $\sim$ 200 years, a size of 9.6 pc, and a turnover frequency of $\sim$ 2 GHz (Polatidis 2009).

In a flux-limited sample, the ratio of radio quasars versus radio galaxies increases rapidly with increasing frequencies because radio quasars have flatter spectra than radio galaxies. However, we have known that CSOs are mostly found in radio galaxies while radio quasars are mostly core-jet objects. For example, in a sample of high-frequency-peakers (HFPs, $\nu_m > 5$ GHz) studied by Dallacasa et al. (2000), only a few identified CSOs are present out of the 55 objects. This fraction is much higher in a sample of GPS objects in the southern sky studies by (Snellen et al. 2002) because only radio galaxies are selected.

The Combined Radio All-Sky Targeted Eight GHz Survey (CRATES, Healey et al. 2007) is an 8.4 GHz survey of bright ($S_{4.8\mathrm{GHz}} > 65$ mJy), flat-spectrum ($\alpha^{4.8\mathrm{GHz}}_{1.4\mathrm{GHz}} > -0.5$) radio sources with nearly uniform extragalactic coverage. Spectroscopic redshifts have been determined for 1226 objects ($R < 23$ mag) by the Candidate Gamma-Ray Blazar Survey (CGRaBS, Healey et al. 2008) in the over 11,000 CRATES objects. These results show only 16 NLRGs ($\nu_{\mathrm{FWHM}} < 1000$ km s^{-1}) and 12 galaxies (objects with small line equivalent widths and large H/K break contrasts) in the sample.

We propose that these 28 objects are good candidates to detect CSOs younger than $\sim$ 100 years. In fact, 2 objects already studied in the sample have ages $<$ 500 years, and there are only 10 CSOs with ages $<$ 500 years detected so far (Giroletti & Polatidis 2009). They are CGRaBS J0111+3906 at $z = 0.199$ (Owsianik et al. 1998; Taylor et al. 2000) and CGRaBS J2203+1007 at $z = 1.005$ (Gugliucci et al. 2005; An & Baan 2012). CGRaBS J0111+3906 is also found to be a H I 21 cm absorber (Carilli et al. 1998; Curran et al. 2011b).

In summary, based upon the current survey work, new surveys of the numerous radio bright AGN never before investigated in detail undoubtedly harbor new examples of atomic and molecular absorbers. Eventually some of these will be found at $z > 1$ allowing the ultimate goal of this work

to be realized.

Bibliography

Adams, J. J., Hill, G. J., & MacQueen, P. J. 2009, ApJ, 694, 314

An, T., & Baan, W. A. 2012, ApJ, 760, 77

Araya, E. D., Rodríguez, C., Pihlström, Y., et al. 2010, AJ, 139, 17

Baldwin, J. A., Phillips, M. M., & Terlevich, R. 1981, PASP, 93, 5

Beasley, A. J., Gordon, D., Peck, A. B., et al. 2002, ApJS, 141, 13

Becker, R. H., White, R. L., & Helfand, D. J. 1995, ApJ, 450, 559

Begelman, M. C. 1996, in Cygnus A – Studay of a Radio Galaxy, ed. C. L. Carilli & D. E. Harris, 209

Best, P. N., Kauffmann, G., Heckman, T. M., et al. 2005, MNRAS, 362, 25

Bicknell, G. V., Dopita, M. A., & O'Dea, C. P. O. 1997, ApJ, 485, 112

Bolton, R. C., Chandler, C. J., Cotter, G., et al. 2006, MNRAS, 367, 323

Budavári, T., Szalay, A. S., Connolly, A. J., Csabai, I., & Dickinson, M. 2000, AJ, 120, 1588

Cai, Z., Nan, R., Schilizzi, R. T., et al. 2002, A&A, 381, 401

Carilli, C. L., Menten, K. M., Reid, M. J., Rupen, M. P., & Yun, M. S. 1998, ApJ, 494, 175

Carilli, C. L., Perlman, E. S., & Stocke, J. T. 1992, ApJ, 400, L13

Carilli, C. L., Menten, K. M., Stocke, J. T., et al. 2000, Physical Review Letters, 85, 5511

Chambers, K. C., Miley, G. K., van Breugel, W. J. M., et al. 1996, ApJS, 106, 247

Chand, H., Srianand, R., Petitjean, P., et al. 2006, A&A, 451, 45

Chandola, Y., Sirothia, S. K., & Saikia, D. J. 2011, MNRAS, 418, 1787

Chengalur, J. N., & Kanekar, N. 2003, Physical Review Letters, 91, 241302

Combes, F. 2008, Ap&SS, 313, 321

Condon, J. J., Cotton, W. D., Greisen, E. W., et al. 1998, AJ, 115, 1693

Conway, J. E. 1999, New A Rev., 43, 509

Csabai, I., Dobos, L., Trencséni, M., et al. 2007, Astronomische Nachrichten, 328, 852

Csabai, I., Budavári, T., Connolly, A. J., et al. 2003, AJ, 125, 580

Curran, S. J., & Whiting, M. T. 2010, ApJ, 712, 303

Curran, S. J., Whiting, M. T., Murphy, M. T., et al. 2006, MNRAS, 371, 431

Curran, S. J., Whiting, M. T., Wiklind, T., et al. 2008, MNRAS, 391, 765

Curran, S. J., Whiting, M. T., Combes, F., et al. 2011a, MNRAS, 416, 2143

Curran, S. J., Whiting, M. T., Murphy, M. T., et al. 2011b, MNRAS, 413, 1165

Dallacasa, D., Fanti, C., Giacintucci, S., et al. 2002a, A&A, 389, 126

Dallacasa, D., Stanghellini, C., Centonza, M., & Fanti, R. 2000, A&A, 363, 887

Dallacasa, D., Tinti, S., Fanti, C., et al. 2002b, A&A, 389, 115

Darling, J. 2003, Physical Review Letters, 91, 011301

—. 2004, ApJ, 612, 58

Darling, J., Grasha, K., Bolatto, A., Leroy, A., & Stocke, J. 2013, to be submitted

de Vries, W. H., O'Dea, C. P., Perlman, E., et al. 1998, ApJ, 503, 138

Douglas, J. N., Bash, F. N., Bozyan, F. A., Torrence, G. W., & Wolfe, C. 1996, AJ, 111, 1945

Downes, D., & Solomon, P. M. 2003, ApJ, 582, 37

Drinkwater, M. J., Webster, R. L., Francis, P. J., et al. 1997, MNRAS, 284, 85

Elitzur, M. 1992, Astronomical masers, Vol. 170 (Springer)

Ewen, H. I., & Purcell, E. M. 1951, Nature, 168, 356

Falco, E. E., Kochanek, C. S., & Munoz, J. A. 1998, ApJ, 494, 47

Fanaroff, B. L., & Riley, J. M. 1974, MNRAS, 167, 31P

Fanti, C. 2009, Astronomische Nachrichten, 330, 120

Fanti, C., Fanti, R., Dallacasa, D., et al. 1995, A&A, 302, 317

Fanti, C., Pozzi, F., Dallacasa, D., et al. 2001, A&A, 369, 380

Fanti, R., Fanti, C., Schilizzi, R. T., et al. 1990, A&A, 231, 333

Flambaum, V. V., & Kozlov, M. G. 2007, Physical Review Letters, 98, 240801

Frayer, D. T., Seaquist, E. R., & Frail, D. A. 1998, AJ, 115, 559

Gaensler, B. 2007, in From Planets to Dark Energy: the Modern Radio Universe

Gerin, M., Phillips, T. G., Benford, D. J., et al. 1997, ApJ, 488, L31

Giroletti, M., & Polatidis, A. 2009, Astronomische Nachrichten, 330, 193

Glikman, E., Helfand, D. J., & White, R. L. 2006, ApJ, 640, 579

Grandi, S. A. 1977, ApJ, 215, 446

Gregory, P. C., & Condon, J. J. 1991, ApJS, 75, 1011

Griest, K., Whitmore, J. B., Wolfe, A. M., et al. 2010, ApJ, 708, 158

Griffith, M. R., Wright, A. E., Burke, B. F., & Ekers, R. D. 1994, ApJS, 90, 179

—. 1995, ApJS, 97, 347

Gugliucci, N. E., Taylor, G. B., Peck, A. B., & Giroletti, M. 2005, ApJ, 622, 136

Gupta, N., Salter, C. J., Saikia, D. J., Ghosh, T., & Jeyakumar, S. 2006, MNRAS, 373, 972

Gupta, N., Srianand, R., Petitjean, P., Noterdaeme, P., & Saikia, D. J. 2009, MNRAS, 398, 201

Healey, S. E., Romani, R. W., Taylor, G. B., et al. 2007, ApJS, 171, 61

Healey, S. E., Romani, R. W., Cotter, G., et al. 2008, ApJS, 175, 97

Hearty, F., Beland, S., Green, J., et al. 2005, in Society of Photo-Optical Instrumentation Engineers (SPIE) Conference Series, Vol. 5904, Society of Photo-Optical Instrumentation Engineers (SPIE) Conference Series, ed. J. B. Heaney & L. G. Burriesci, 199–211

Helmboldt, J. F., Taylor, G. B., Tremblay, S., et al. 2007, ApJ, 658, 203

Henkel, C., Menten, K. M., Murphy, M. T., et al. 2009, A&A, 500, 725

Inoue, M. Y., Kameno, S., Kawabe, R., et al. 1996, AJ, 111, 1852

Ishwara-Chandra, C. H., Dwarakanath, K. S., & Anantharamaiah, K. R. 2003, Journal of Astrophysics and Astronomy, 24, 37

Ishwara-Chandra, C. H., Sirothia, S. K., Wadadekar, Y., Pal, S., & Windhorst, R. 2010, MNRAS, 405, 436

Jeyakumar, S., & Saikia, D. J. 2000, MNRAS, 311, 397

Kanekar, N. 2011, ApJ, 728, L12

Kanekar, N., Chengalur, J. N., & Ghosh, T. 2004, Physical Review Letters, 93, 051302

Kanekar, N., Langston, G. I., Stocke, J. T., Carilli, C. L., & Menten, K. M. 2012, ApJ, 746, L16

Kanekar, N., Carilli, C. L., Langston, G. I., et al. 2005, Physical Review Letters, 95, 261301

Keeney, B. A., Stocke, J. T., Danforth, C. W., & Carilli, C. L. 2011, AJ, 141, 66

Kellermann, K. I., & Pauliny-Toth, I. I. K. 1981, ARA&A, 19, 373

Kewley, L. J., Groves, B., Kauffmann, G., & Heckman, T. 2006, MNRAS, 372, 961

Kunert-Bajraszewska, M., Janiuk, A., Gawroński, M. P., & Siemiginowska, A. 2010, ApJ, 718, 1345

Kunert-Bajraszewska, M., & Marecki, A. 2007, A&A, 469, 437

Lehar, J., Burke, B. F., Conner, S. R., et al. 1997, AJ, 114, 48

Lípari, S., Mediavilla, E., Garcia-Lorenzo, B., et al. 2004, MNRAS, 355, 641

Lister, M. L., Kellermann, K. I., Vermeulen, R. C., et al. 2003, ApJ, 584, 135

Liu, X., Cui, L., Luo, W.-F., Shi, W.-Z., & Song, H.-G. 2007, A&A, 470, 97

Lupton, R., Gunn, J. E., Ivezić, Z., et al. 2001, in Astronomical Society of the Pacific Conference Series, Vol. 238, Astronomical Data Analysis Software and Systems X, ed. F. R. Harnden, Jr., F. A. Primini, & H. E. Payne, 269

Mannucci, F., Basile, F., Poggianti, B. M., et al. 2001, MNRAS, 326, 745

McLeod, K. K. 2006, in Planets to Cosmology: Essential Science in the Final Years of the Hubble Space Telescope, ed. M. Livio & S. Casertano, 73

Mihos, J. C., & Hernquist, L. 1996, ApJ, 464, 641

Miley, G., & De Breuck, C. 2008, A&A Rev., 15, 67

Mirabel, I. F. 1990, ApJ, 352, L37

Moore, C. B., Carilli, C. L., & Menten, K. M. 1999, ApJ, 510, L87

Morganti, R., Oosterloo, T. A., Tadhunter, C. N., et al. 2004, A&A, 424, 119

Muller, C. A., & Oort, J. H. 1951, Nature, 168, 357

Murphy, M. T., Webb, J. K., & Flambaum, V. V. 2003, MNRAS, 345, 609

Murphy, M. T., Webb, J. K., Flambaum, V. V., et al. 2001, MNRAS, 327, 1244

Myers, S. T., Jackson, N. J., Browne, I. W. A., et al. 2003, MNRAS, 341, 1

Narayan, R., & Schneider, P. 1990, MNRAS, 243, 192

Noterdaeme, P., Petitjean, P., Ledoux, C., et al. 2010, A&A, 523, A80

O'Dea, C. P. 1998, PASP, 110, 493

O'Dea, C. P., & Baum, S. A. 1997, AJ, 113, 148

Oke, J. B., & Gunn, J. E. 1982, PASP, 94, 586

Owsianik, I., & Conway, J. E. 1998, A&A, 337, 69

Owsianik, I., Conway, J. E., & Polatidis, A. G. 1998, A&A, 336, L37

Patnaik, A. R., Browne, I. W. A., Wilkinson, P. N., & Wrobel, J. M. 1992, MNRAS, 254, 655

Peck, A. B., & Taylor, G. B. 2000, ApJ, 534, 90

Perlman, E. S., Carilli, C. L., Stocke, J. T., & Conway, J. 1996, AJ, 111, 1839

Perlman, E. S., Stocke, J. T., Carilli, C. L., et al. 2002, AJ, 124, 2401

Perlman, E. S., Stocke, J. T., Conway, J., & Reynolds, C. 2001, AJ, 122, 536

Perlman, E. S., Stocke, J. T., Shaffer, D. B., Carilli, C. L., & Ma, C. 1994, ApJ, 424, L69

Phillips, R. B., & Mutel, R. L. 1982, A&A, 106, 21

Pihlström, Y. M., Conway, J. E., & Vermeulen, R. C. 2003, A&A, 404, 871

Polatidis, A., Wilkinson, P. N., Xu, W., et al. 1999, New A Rev., 43, 657

Polatidis, A. G. 2009, Astronomische Nachrichten, 330, 149

Readhead, A. C. S., Taylor, G. B., Xu, W., et al. 1996, ApJ, 460, 612

Reinhold, E., Buning, R., Hollenstein, U., et al. 2006, Physical Review Letters, 96, 151101

Roettgering, H. J. A., Lacy, M., Miley, G. K., Chambers, K. C., & Saunders, R. 1994, A&AS, 108, 79

Rosenband, T., Hume, D. B., Schmidt, P. O., et al. 2008, Science, 319, 1808

Rossetti, A., Fanti, C., Fanti, R., Dallacasa, D., & Stanghellini, C. 2006, A&A, 449, 49

Rybicki, G. B., & Lightman, A. P. 1979, Radiative processes in astrophysics

Saikia, D. J., Jeyakumar, S., Salter, C. J., et al. 2001, MNRAS, 321, 37

Sarazin, C. L., Burns, J. O., Roettiger, K., & McNamara, B. R. 1995, ApJ, 447, 559

Savedoff, M. P. 1956, Nature, 178, 688

Seaquist, E. R., Frayer, D. T., & Frail, D. A. 1997, ApJ, 487, L131

Snellen, I. A. G., Lehnert, M. D., Bremer, M. N., & Schilizzi, R. T. 2002, MNRAS, 337, 981

Srianand, R., Chand, H., Petitjean, P., & Aracil, B. 2004, Physical Review Letters, 92, 121302

Srianand, R., Noterdaeme, P., Ledoux, C., & Petitjean, P. 2008, A&A, 482, L39

Stanghellini, C., Dallacasa, D., O'Dea, C. P., et al. 2001, A&A, 377, 377

Stanghellini, C., O'Dea, C. P., Baum, S. A., et al. 1997, A&A, 325, 943

Stocke, J. T., Wurtz, R., Wang, Q., Elston, R., & Jannuzi, B. T. 1992, ApJ, 400, L17

Stoughton, C., Lupton, R. H., Bernardi, M., et al. 2002, AJ, 123, 485

Strateva, I., Ivezić, Ž., Knapp, G. R., et al. 2001, AJ, 122, 1861

Taylor, G. B., Marr, J. M., Pearson, T. J., & Readhead, A. C. S. 2000, ApJ, 541, 112

Tremblay, S. E. 2011, PhD thesis, The University of New Mexico

Urry, C. M., & Padovani, P. 1995, PASP, 107, 803

Uson, J. M., Bagri, D. S., & Cornwell, T. J. 1991, Physical Review Letters, 67, 3328

van Breugel, W. J. M., Stanford, S. A., Spinrad, H., Stern, D., & Graham, J. R. 1998, ApJ, 502, 614

van Gorkom, J. H., Knapp, G. R., Ekers, R. D., et al. 1989, AJ, 97, 708

van Langevelde, H. J., van Dishoeck, E. F., Sevenster, M. N., & Israel, F. P. 1995, ApJ, 448, L123

Vanden Berk, D. E., Richards, G. T., Bauer, A., et al. 2001, AJ, 122, 549

Vermeulen, R. C., Pihlström, Y. M., Tschager, W., et al. 2003, A&A, 404, 861

Webb, J. K., Flambaum, V. V., Churchill, C. W., Drinkwater, M. J., & Barrow, J. D. 1999, Physical Review Letters, 82, 884

Webb, J. K., King, J. A., Murphy, M. T., et al. 2011, Physical Review Letters, 107, 191101

Whiteoak, J. B., & Gardner, F. F. 1975, ApJ, 195, L81

Wiklind, T., & Combes, F. 1994, A&A, 286, L9

—. 1995, A&A, 299, 382

—. 1996a, A&A, 315, 86

—. 1996b, Nature, 379, 139

Willett, K. W., Stocke, J. T., Darling, J., & Perlman, E. S. 2010, ApJ, 713, 1393

Willott, C. J., Rawlings, S., Jarvis, M. J., & Blundell, K. M. 2003, MNRAS, 339, 173

Wilson, A. S., & Colbert, E. J. M. 1995, ApJ, 438, 62

Wilson, J. C., Henderson, C. P., Herter, T. L., et al. 2004, in Society of Photo-Optical Instrumentation Engineers (SPIE) Conference Series, Vol. 5492, Society of Photo-Optical Instrumentation Engineers (SPIE) Conference Series, ed. A. F. M. Moorwood & M. Iye, 1295–1305

Wright, A., & Otrupcek, R. 1990, in PKS Catalog (1990), 0

Wright, E. L., Eisenhardt, P. R. M., Mainzer, A. K., et al. 2010, AJ, 140, 1868

Xiang, L., Stanghellini, C., Dallacasa, D., & Haiyan, Z. 2002, A&A, 385, 768

Yan, T., Stocke, J. T., Darling, J., & Hearty, F. 2012, AJ, 144, 124

Yan, T., Stocke, J. T., Darling, J., & Momjian, E. 2013, to be submitted

York, D. G., Adelman, J., Anderson, Jr., J. E., et al. 2000, AJ, 120, 1579

Zirm, A. W., Dickinson, M., & Dey, A. 2003, ApJ, 585, 90

Appendix A

Optical–NIR Images and SEDs

Optical–NIR images and SEDs are shown in Figure A.1 for the entire sample. For each row of Figure A.1, columns from left to right are: (1) SDSS composite images, (g-band in blue, r-band in green, and i-band in red); (2) the APO 3.5m J-band images; (3) the APO 3.5m K_s band images; and (4) optical–NIR SEDs. All images are shown at the same scale and orientation as indicated on the SDSS composite images. Pixel counts of J and K_s images are displayed by grayscale with the following approach: on a grayscale of 0 (white) to 1 (dark), 1 represents the maximum pixel counts of the object or 5σ noise of the sky background if the signal to noise ratio is smaller than 5; 0 and 0.5 represents -2.5σ and 2.5σ noise of the sky background respectively; between 0 to 0.5 and 0.5 to 1, it scales linearly with pixel counts. J0917+4725 was not observed in the J-band by us and an J-band image is not available. For the well-known molecular absorber, J1415+1320, its J and K_s images from the 2MASS survey are shown as it was not observed by us. SED types are shown for Q, $Q + abs$, and $G + Q$-type objects on the SED plots. For G-type objects, Hubble types are shown as well as the best-fit template spectra. See Section 2.4.2 for more details about the SED and Hubble types. Note that the y-axis of all SED plots extends over two orders of magnitude for comparison. Some objects were observed on multiple dates. The data on SED plots are from a single date for each object as listed in Table 2.2. As for J-band and K_s-band images, the ones with the best signal-to-noise ratio are selected and the dates are shown on the images.

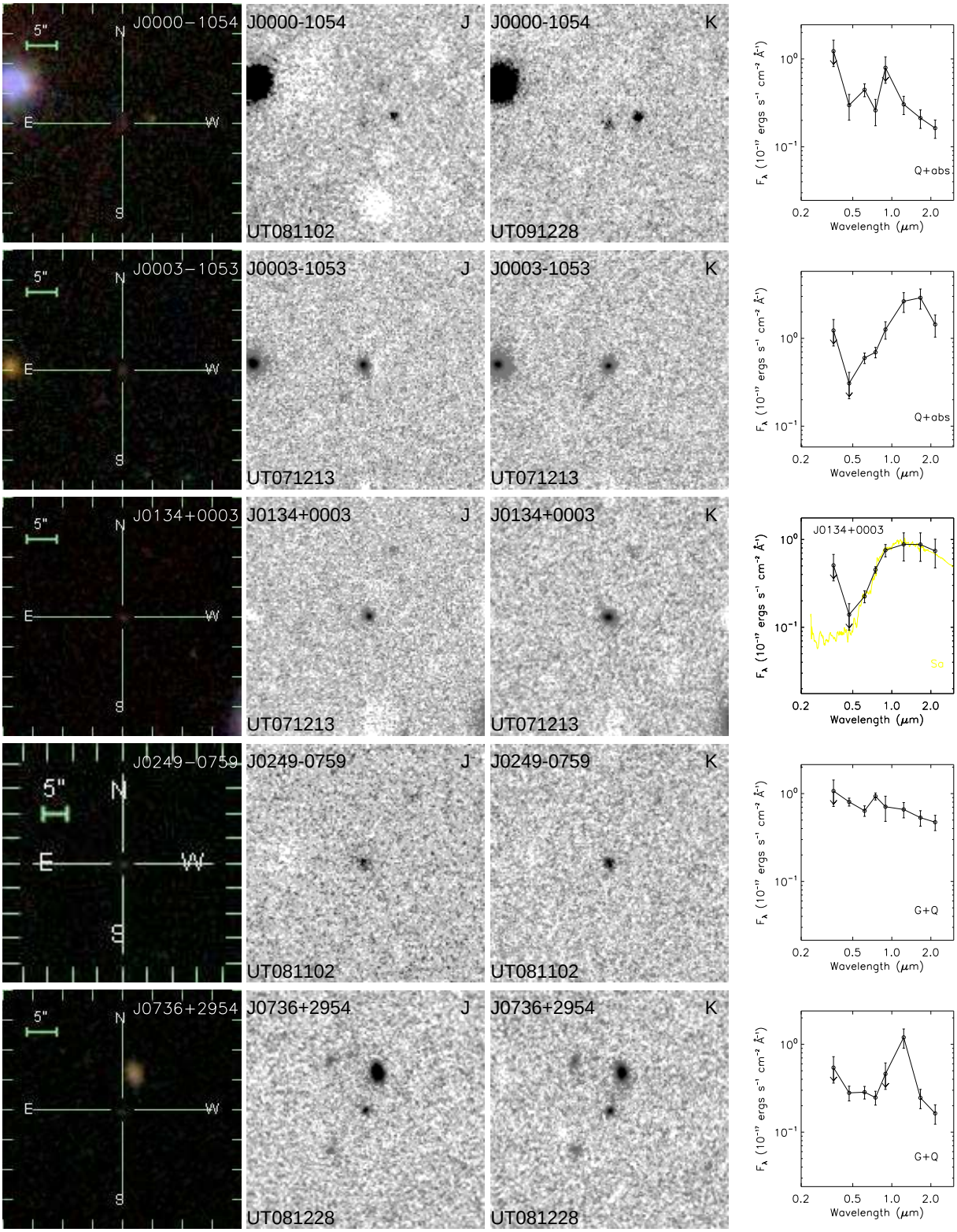

Figure A.1 Optical–NIR images and SEDs.

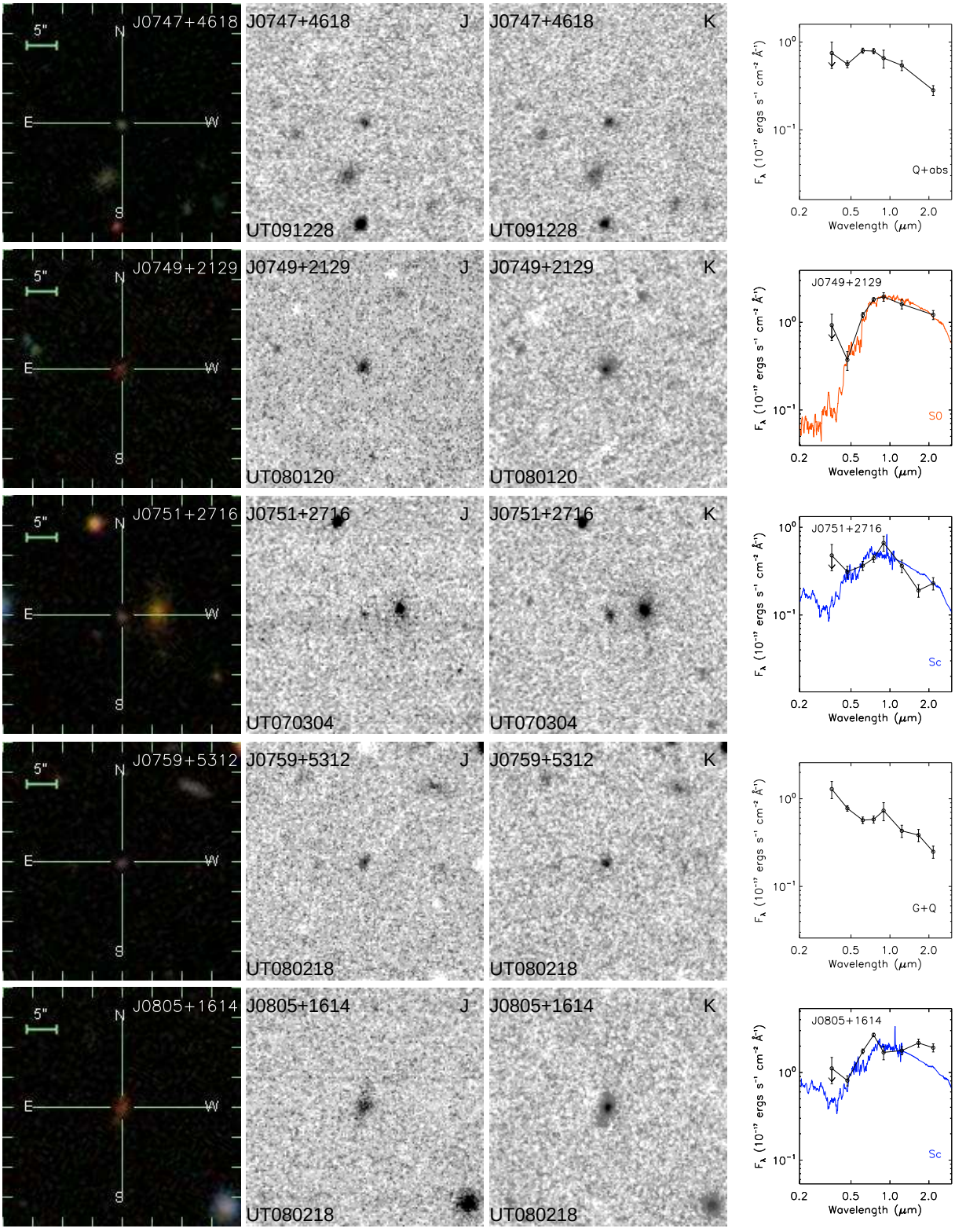

Figure A.1 Continued.

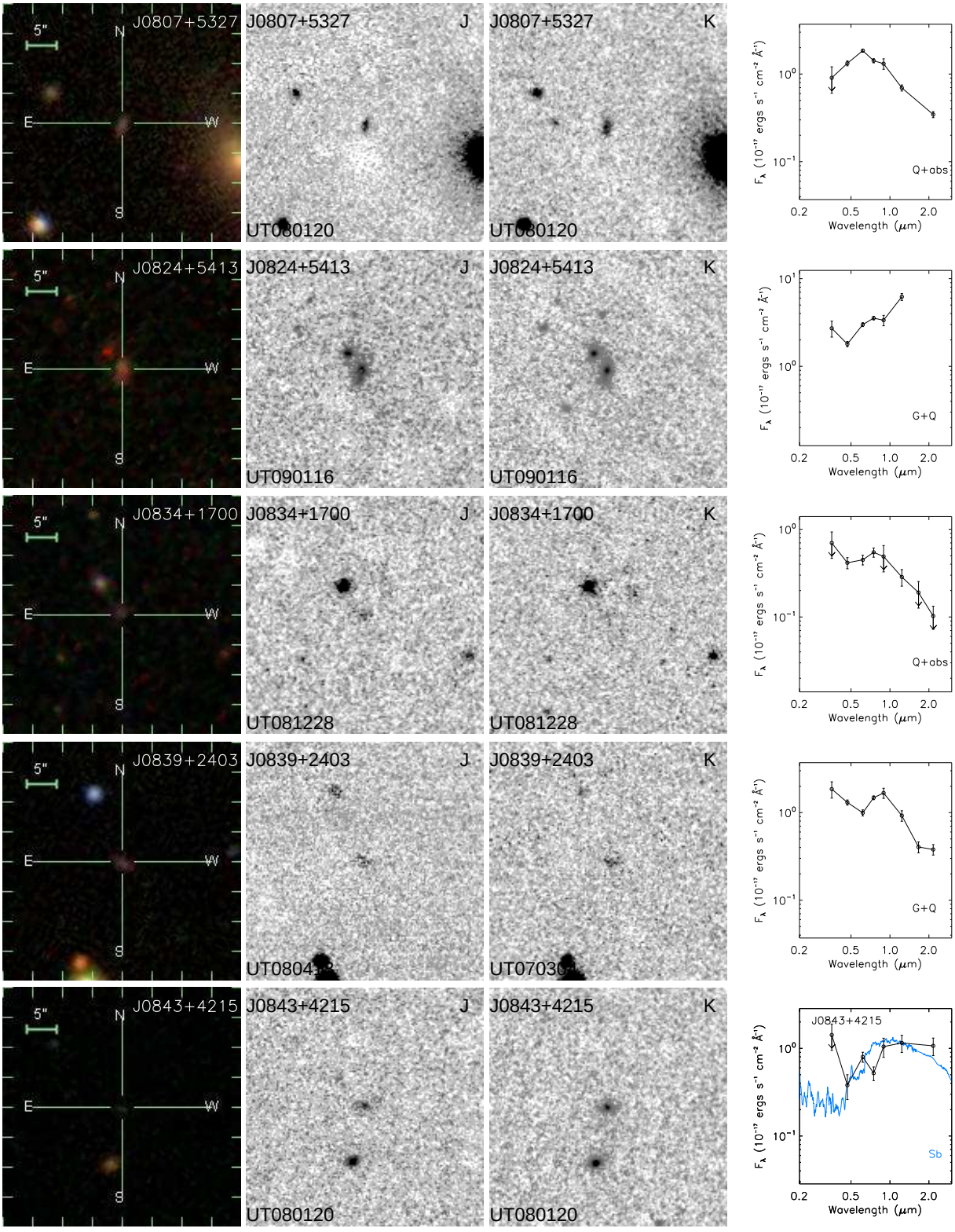

Figure A.1 Continued.

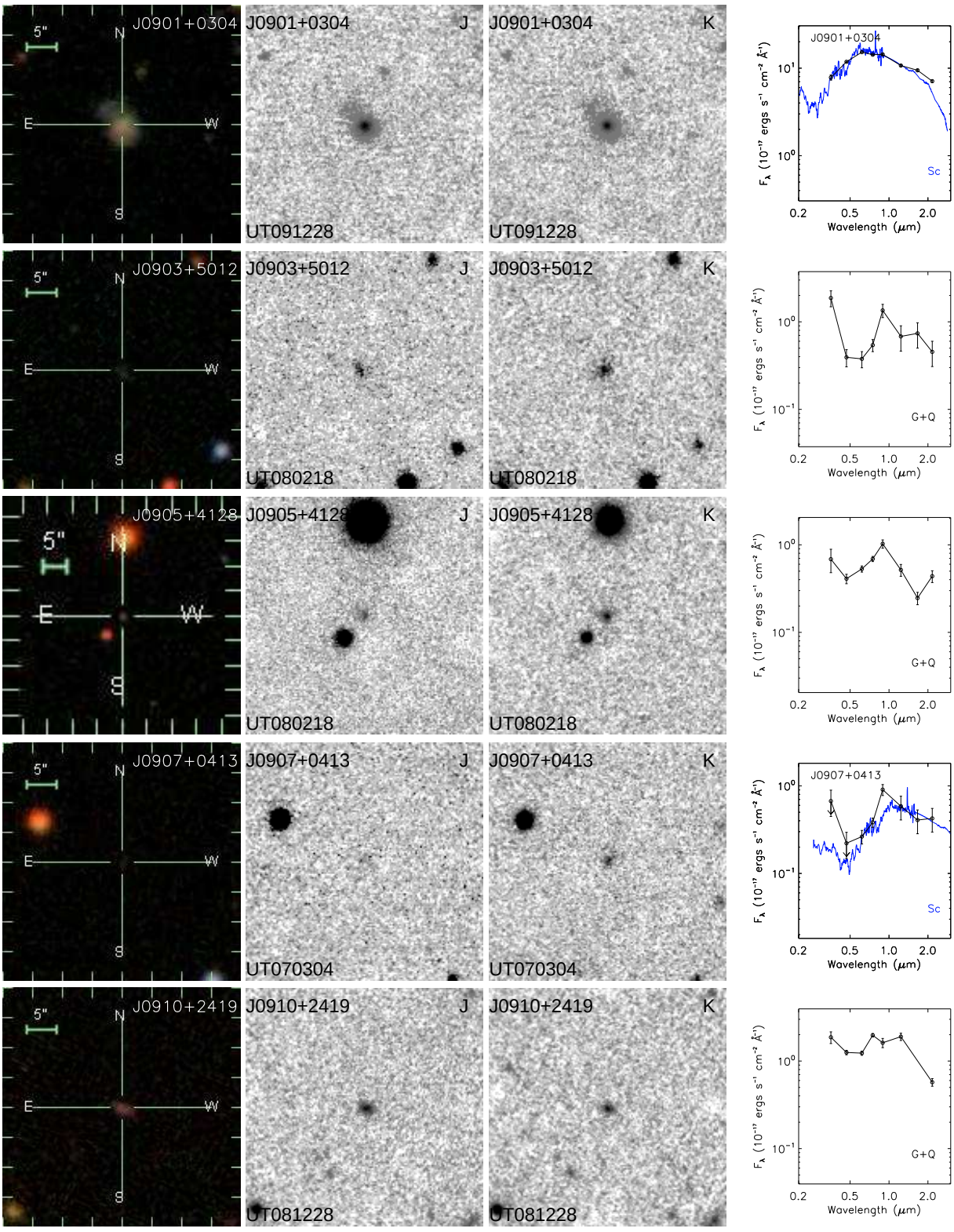

Figure A.1 Continued.

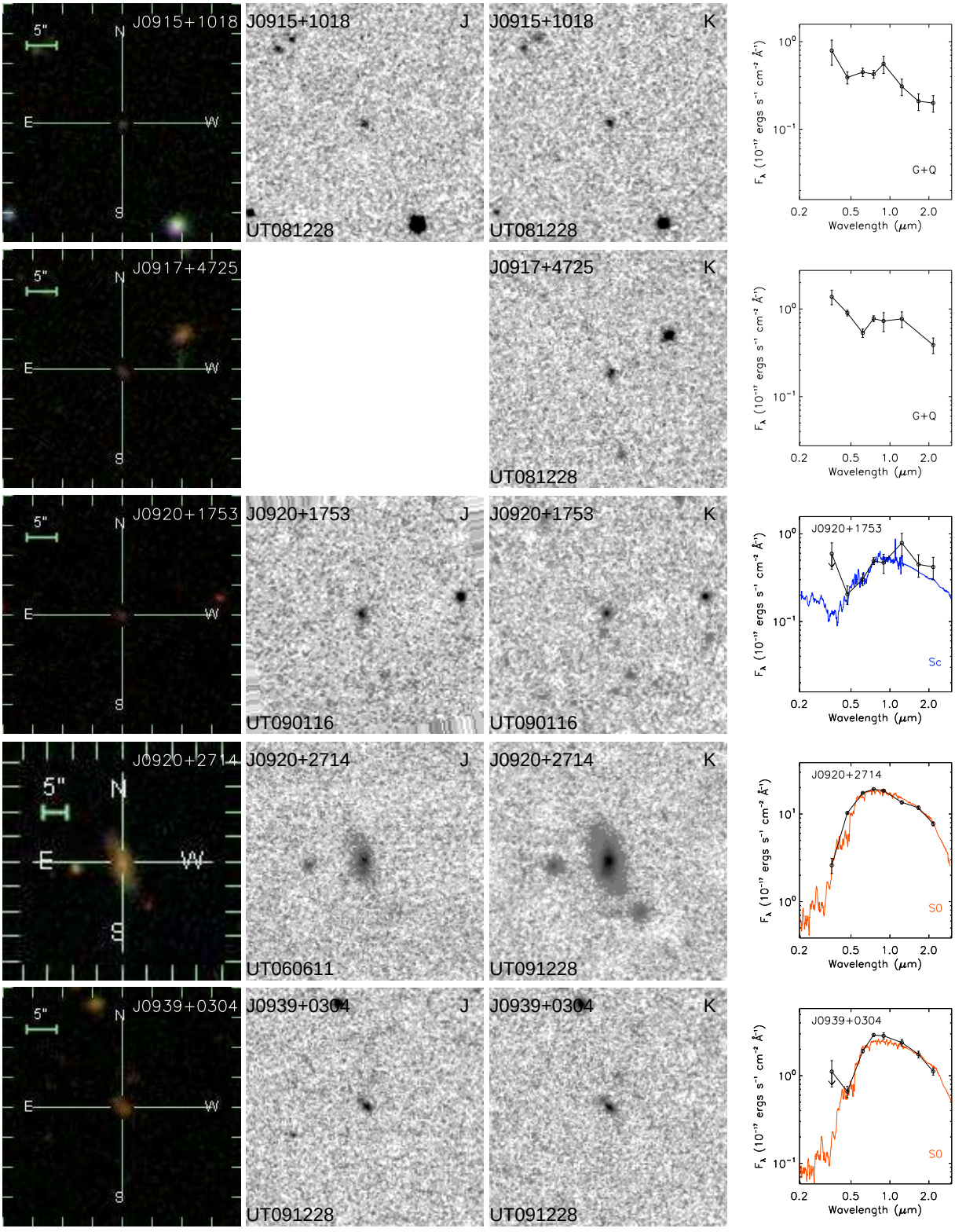

Figure A.1 Continued.

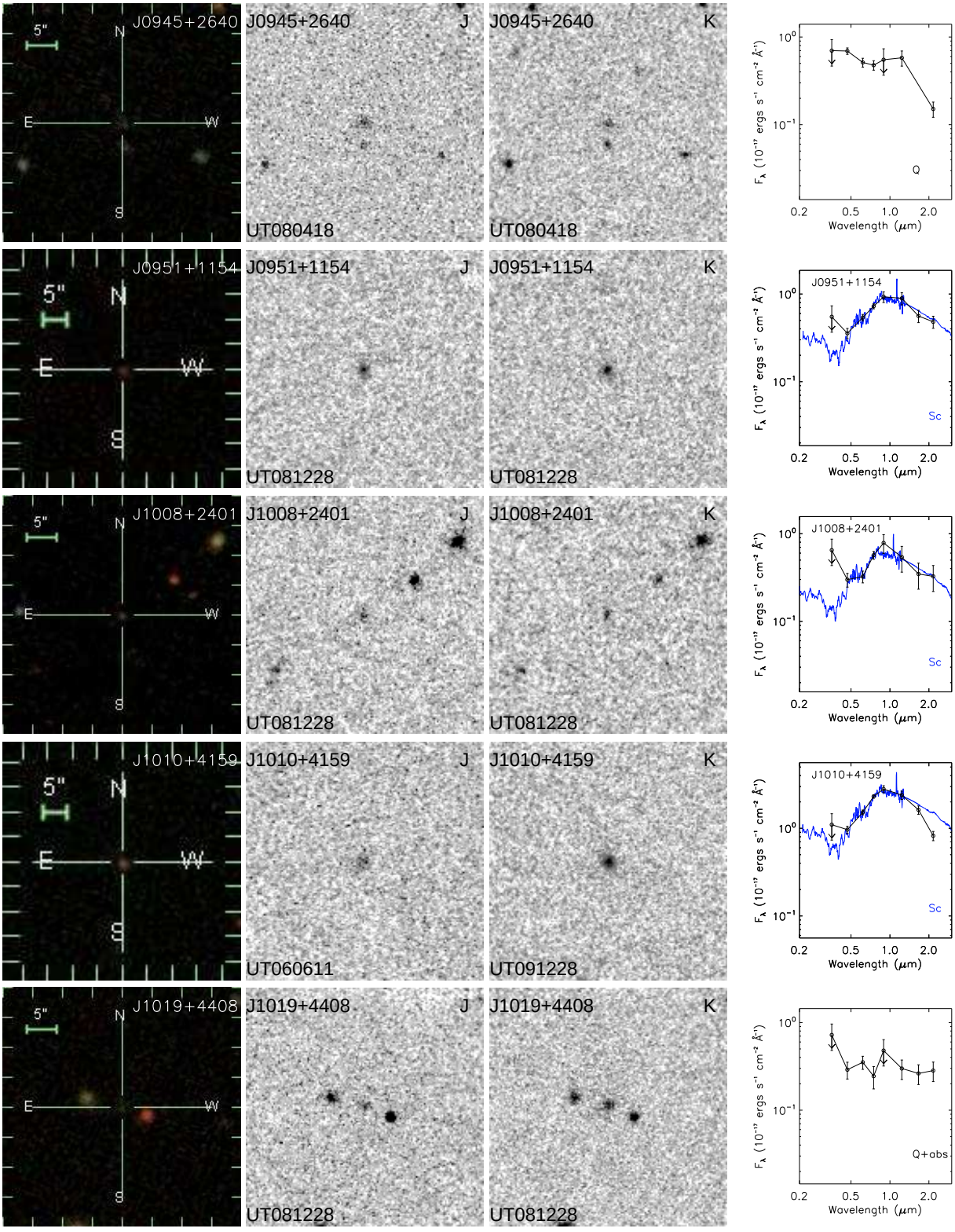

Figure A.1 Continued.

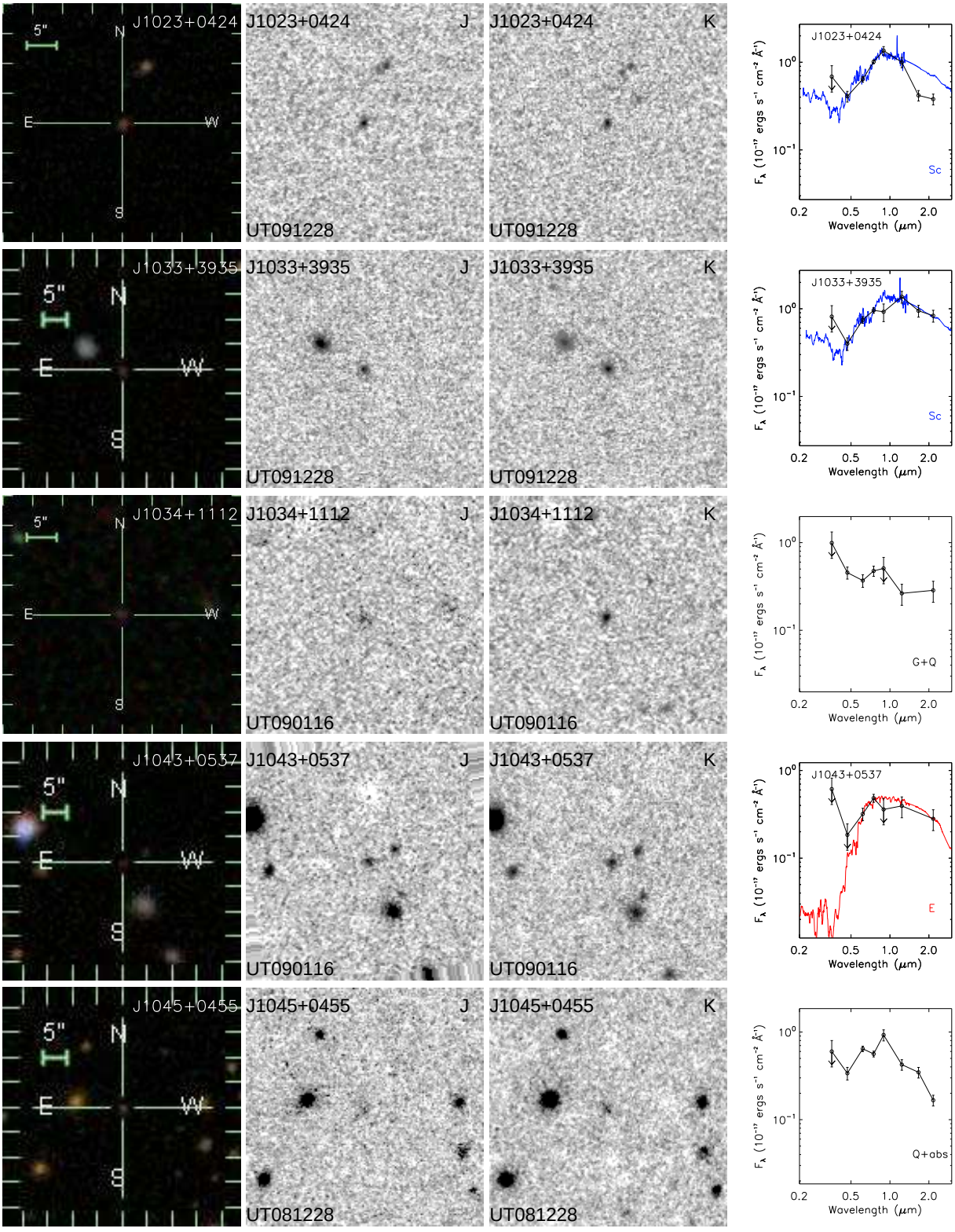

Figure A.1 Continued.

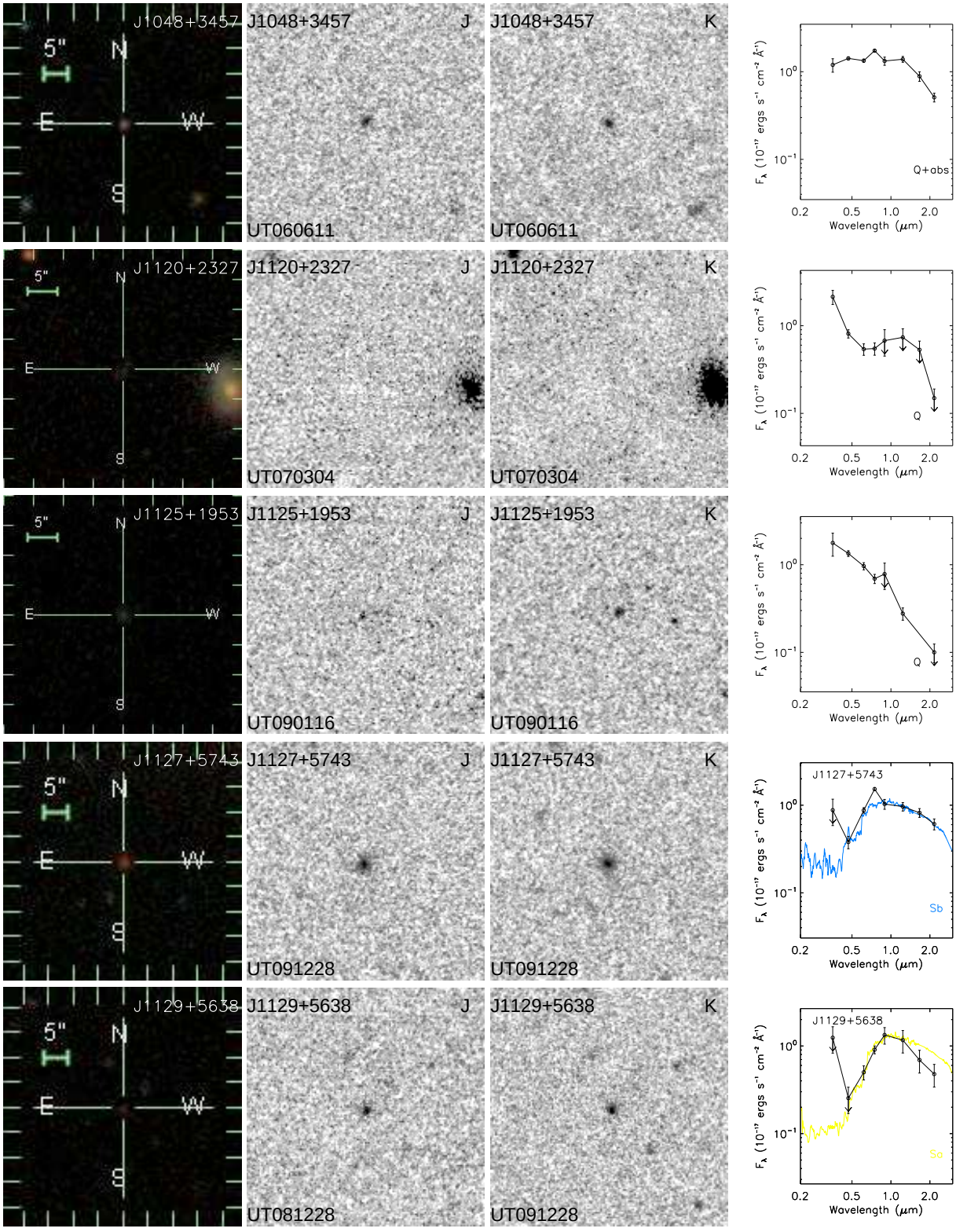

Figure A.1 Continued.

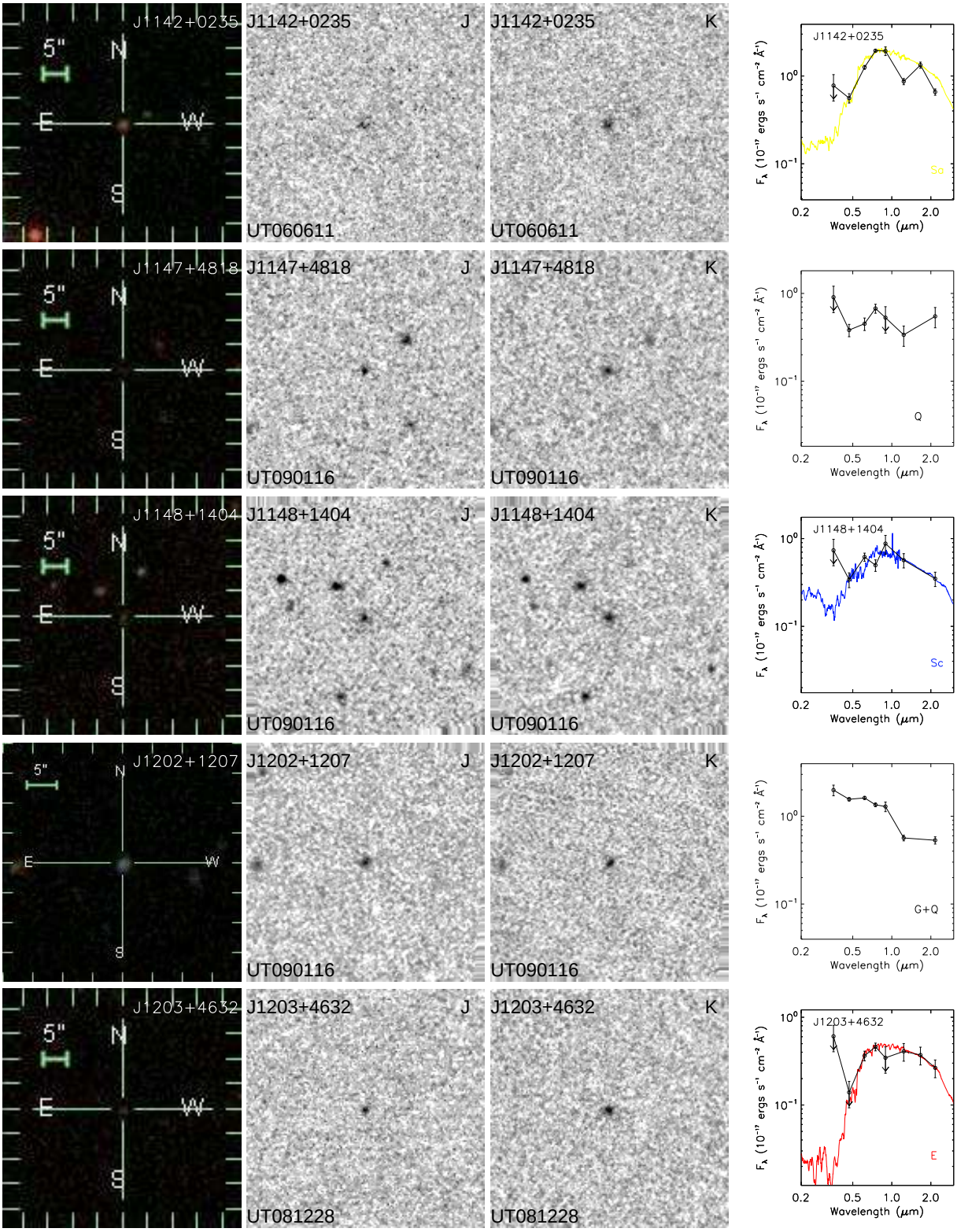

Figure A.1 Continued.

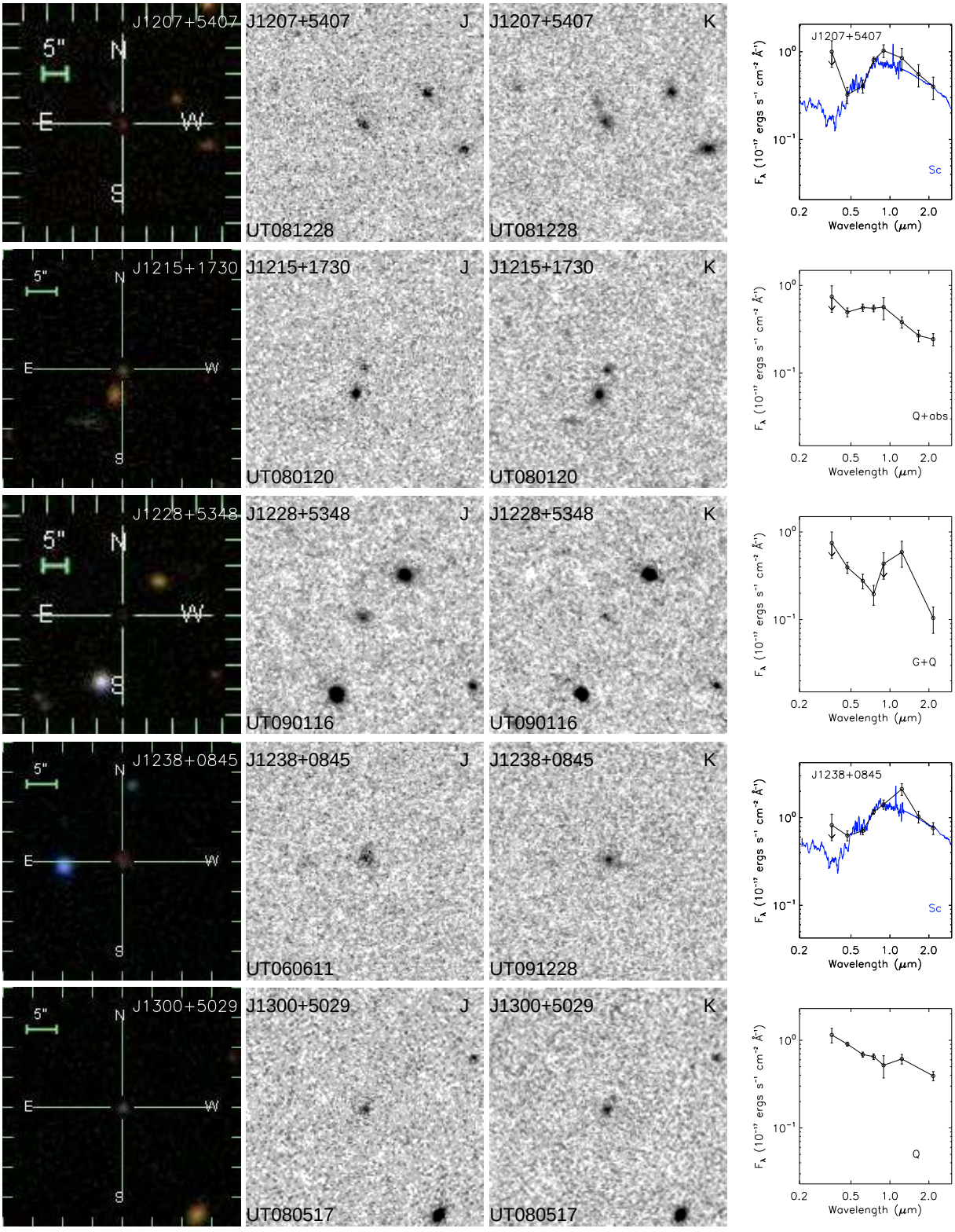

Figure A.1 Continued.

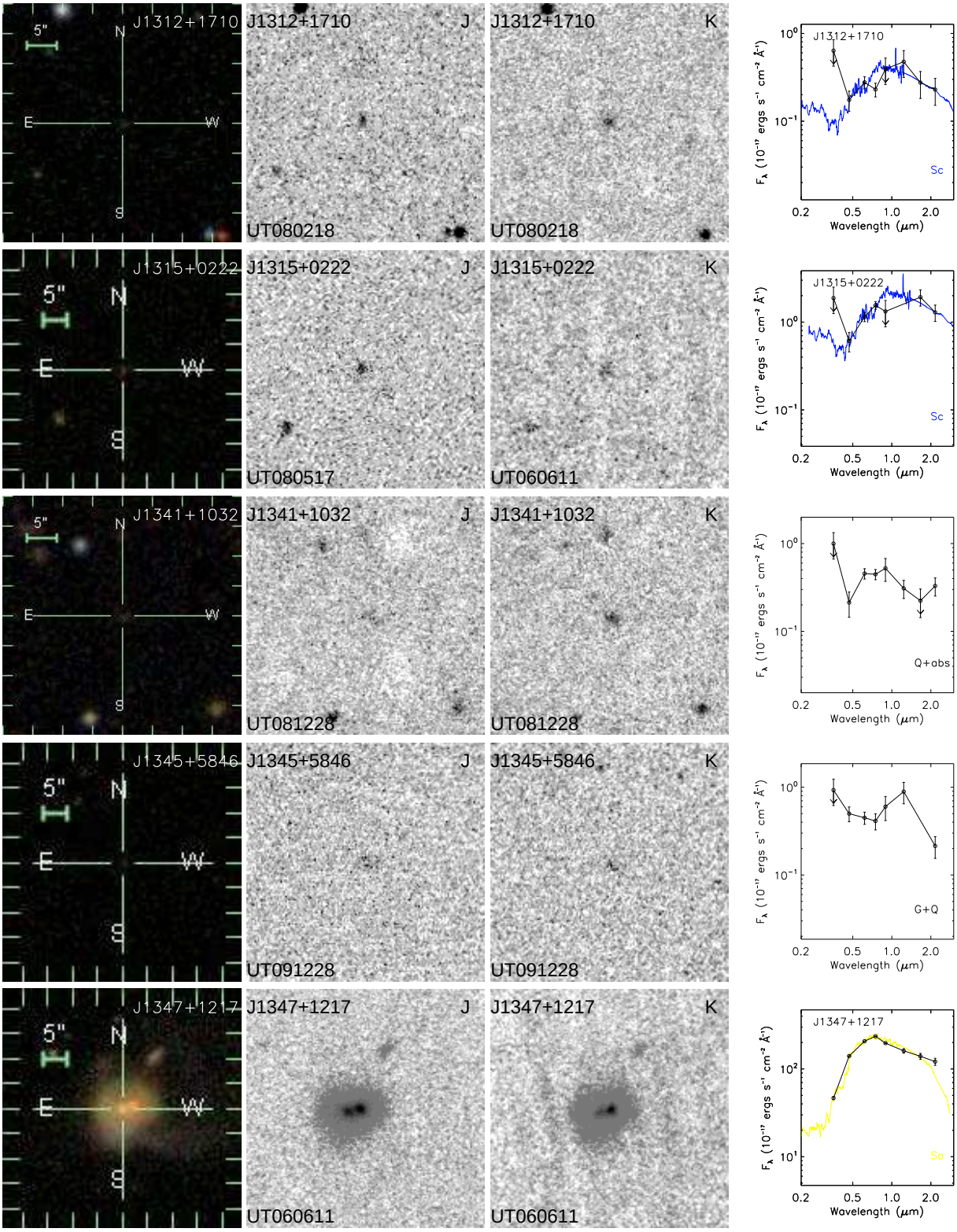

Figure A.1 Continued.

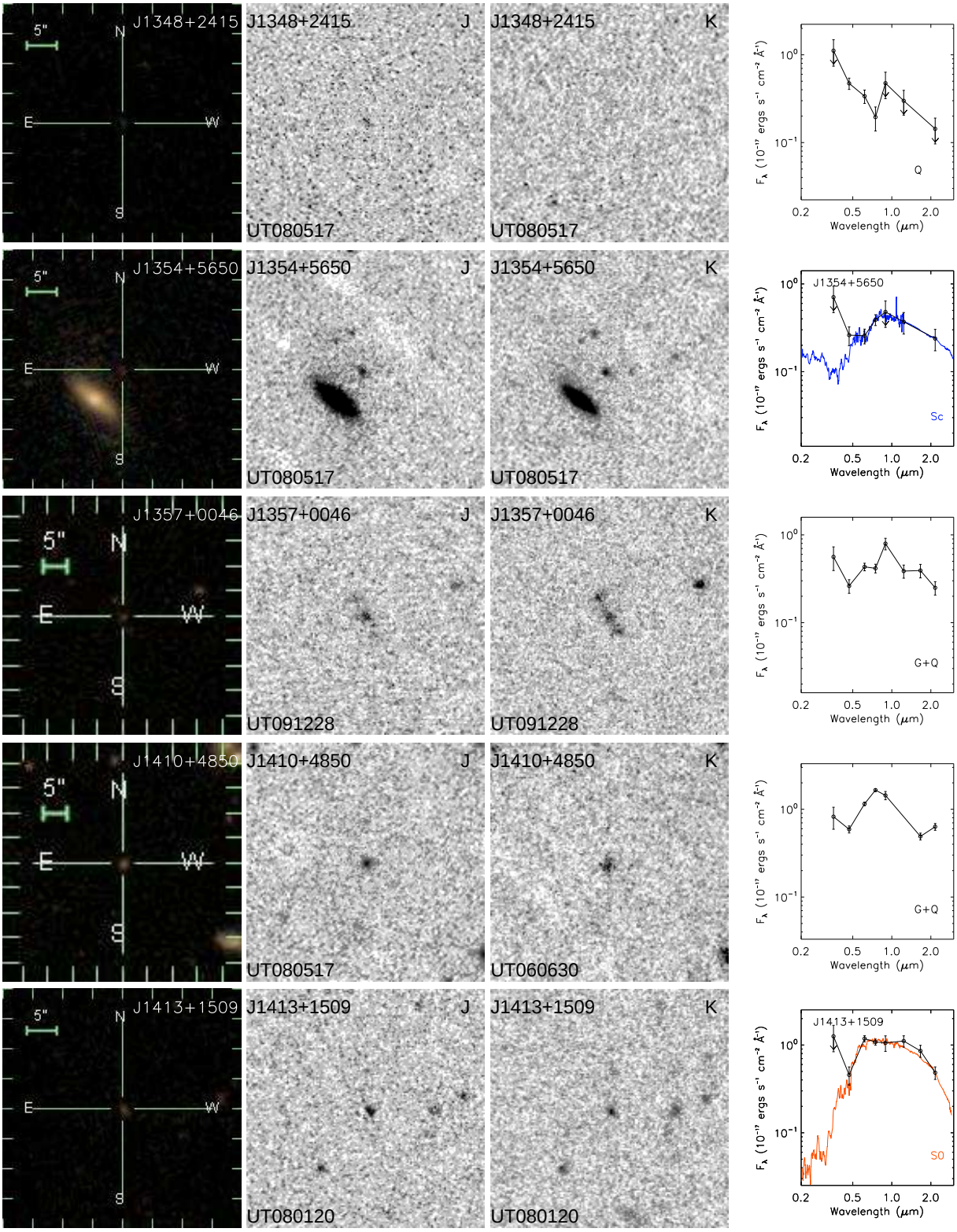

Figure A.1 Continued.

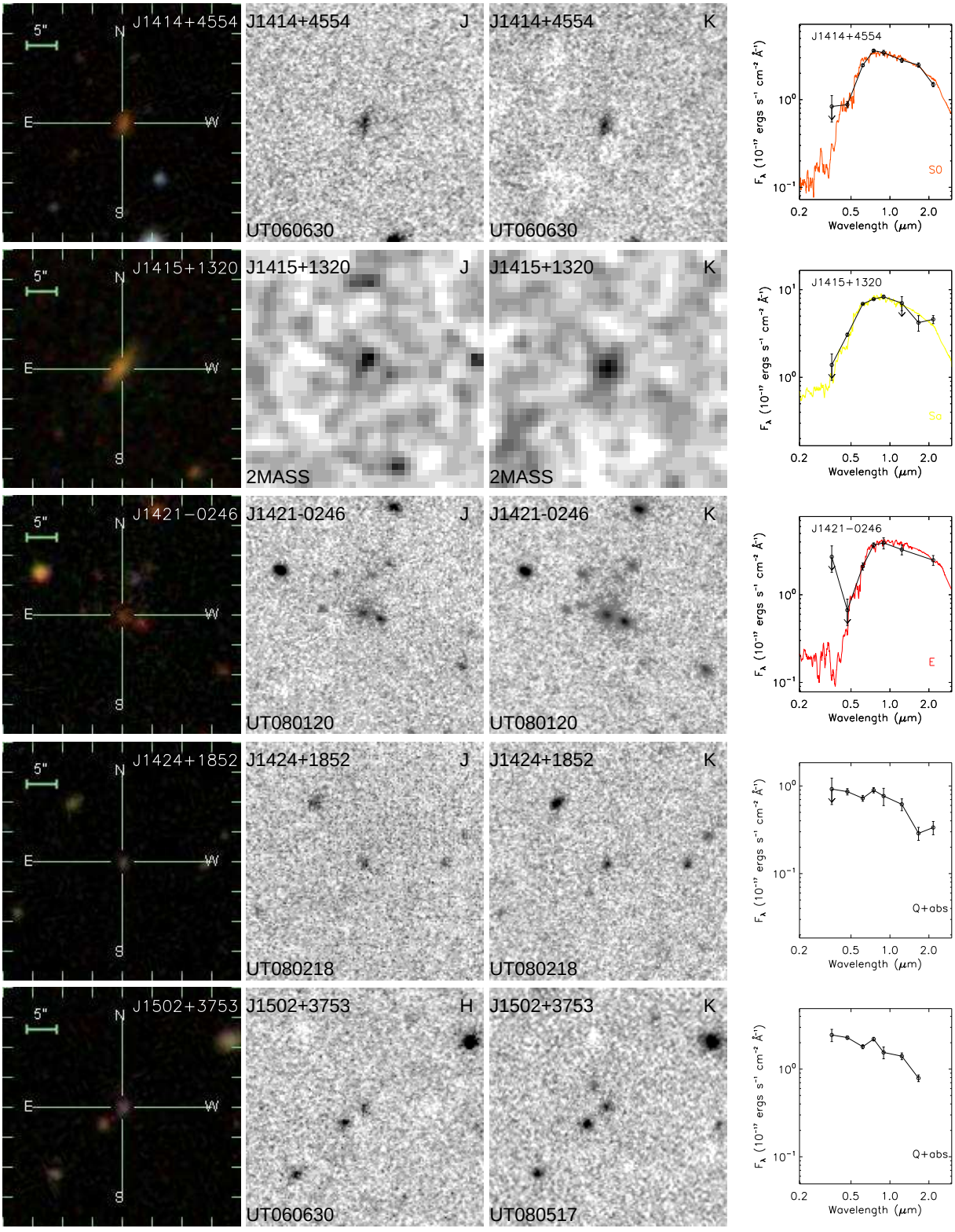

Figure A.1 Continued.

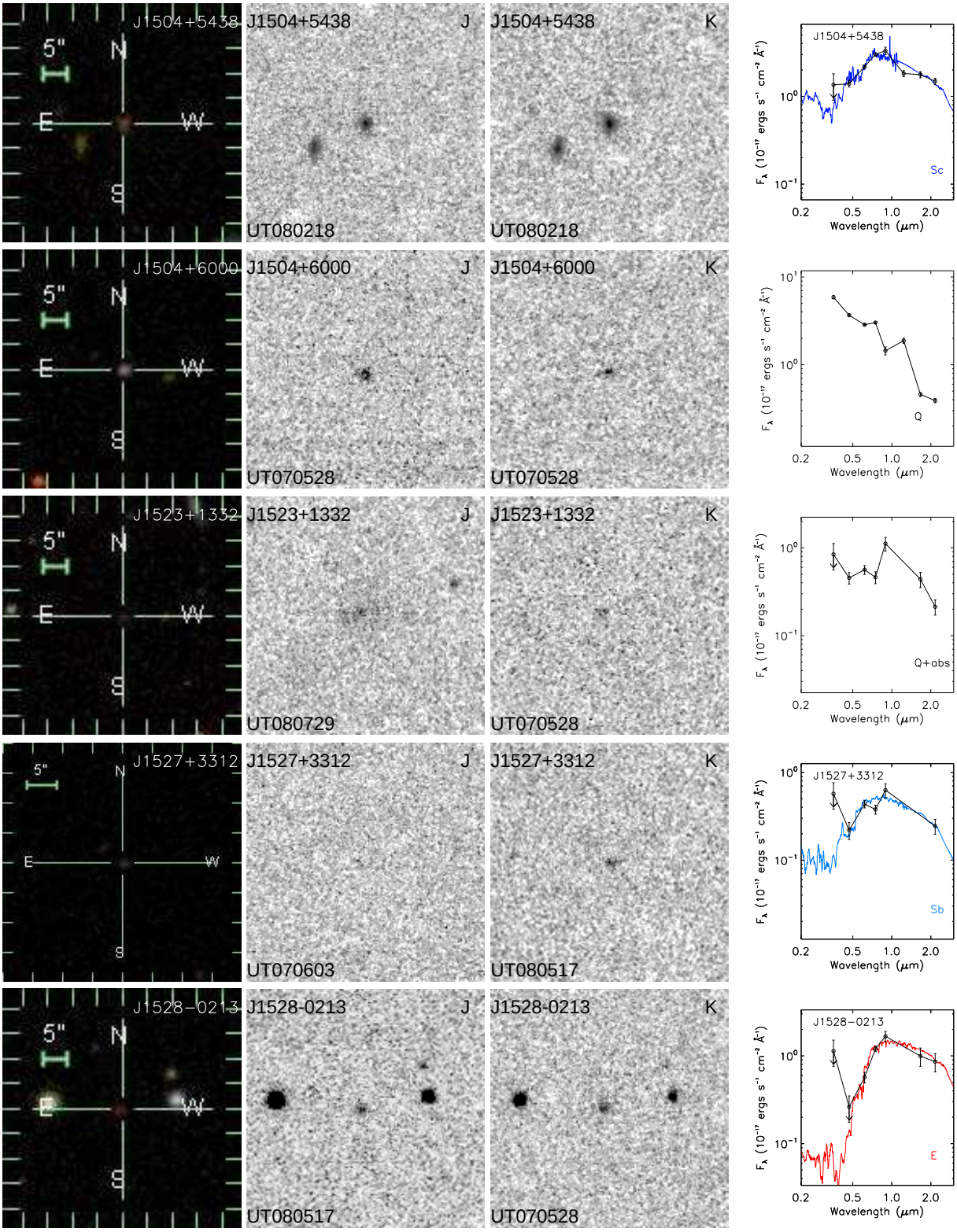

Figure A.1 Continued.

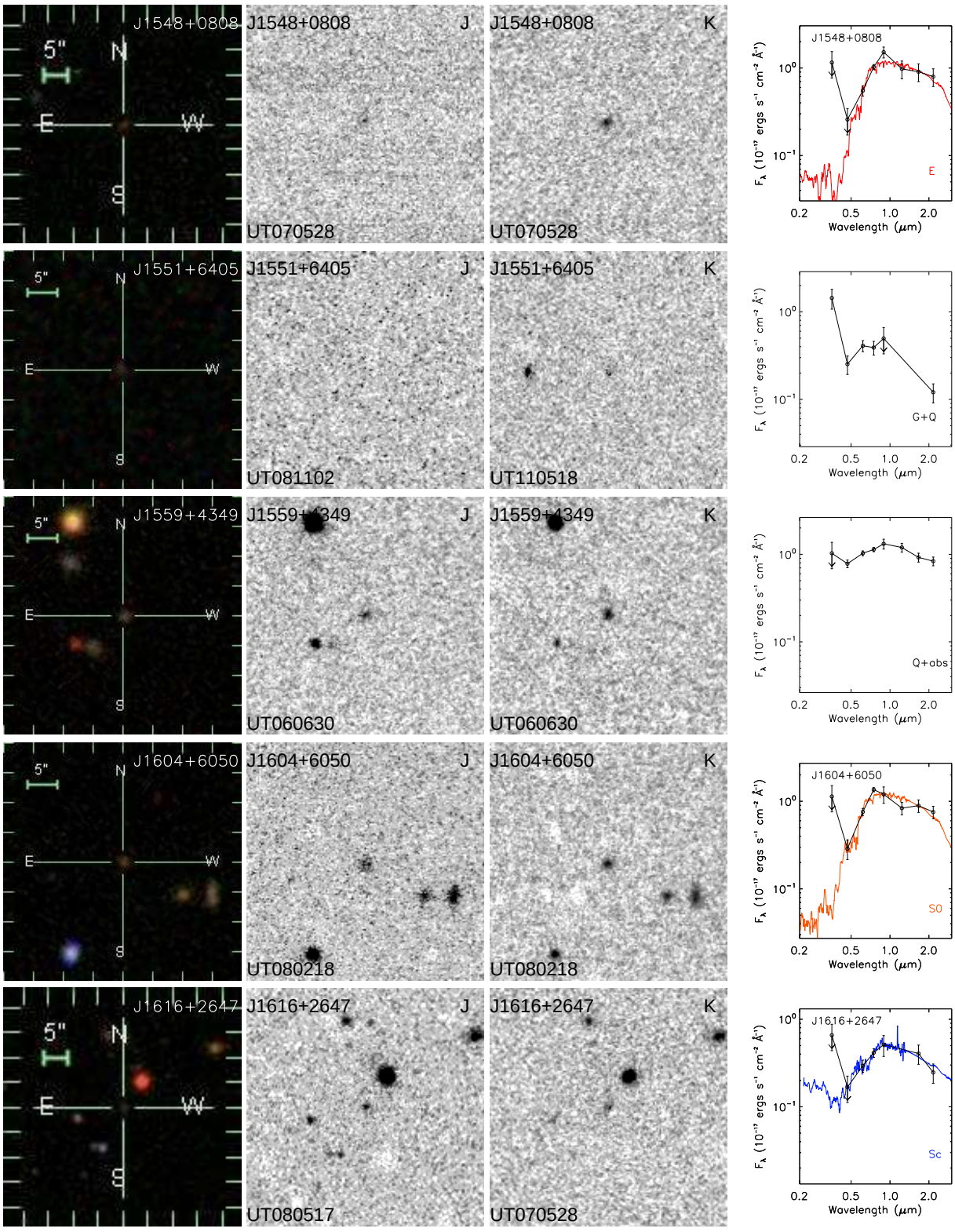

Figure A.1 Continued.

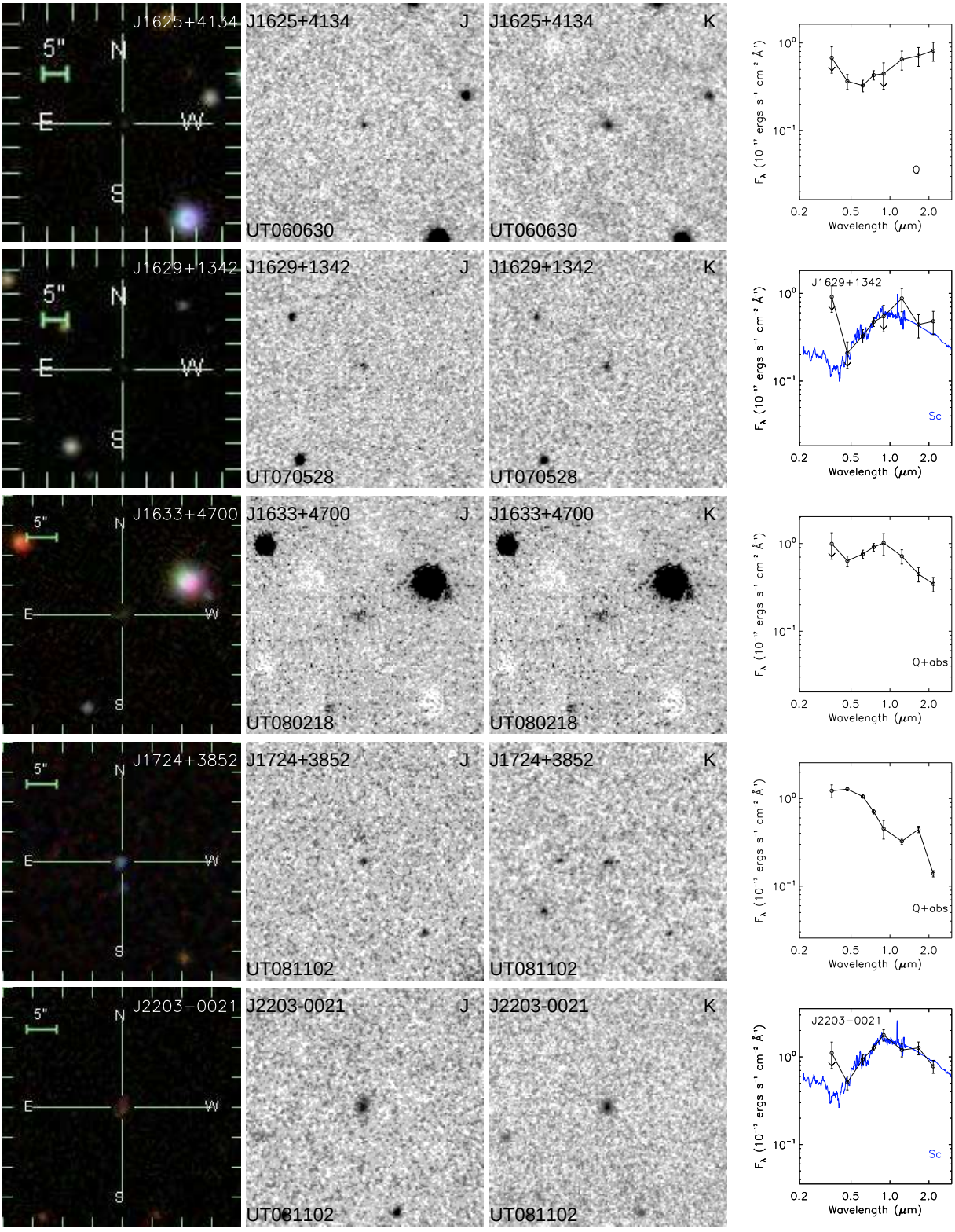

Figure A.1 Continued.

Appendix B

Radio Images

We show our VLA-A and VLBA images and tabulate image parameters in this appendix. Table B.1 lists basic image parameters including $r.m.s.$ (σ) and maximum flux densities, as well as the major and minor axis sizes, and position angle (P.A.) of the restored beam. Figure B.1 shows all the VLA-A 4.9 GHz, VLA-A 8.5 GHz, and VLBA 1.4 GHz images. We fit each image component with a Gaussian profile and list the fitting results in Tables B.2, B.3, and B.4 for the VLA-A 4.9 GHz, VLA-A 8.5 GHz, and VLBA 1.4 GHz images respectively. In Table B.3, the spectral indices between 4.9 GHz and 8.5 GHz are also included for each component.

Table B.1. Basic Observing Results of the Radio Imaging.

Object	VLA 4.9 GHz					VLA 8.5 GHz					VLBA 1.4 GHz				
	Maj. (″)	Min. (″)	P.A. (°)	RMS (mJy/ beam)	$F_{\rm m}$ (mJy/ beam)	Maj. (″)	Min. (″)	P.A. (°)	RMS (mJy/ beam)	$F_{\rm m}$ (mJy/ beam)	Maj. (mas)	Min. (mas)	P.A. (°)	RMS (mJy/ beam)	$F_{\rm m}$ (mJy/ beam)
J0000−1054	0.60	0.44	-6.3	0.15	34.9	0.35	0.25	174.3	0.11	17.6	...	...	...		...
J0003−1053	0.60	0.45	-3.3	0.17	31.1	0.37	0.26	175.6	0.14	27.4	...	...	...		...
J0134+0003	0.54	0.44	-22.7	0.57	541.5	...	...	...		...	...	...	...		...
J0249−0759	0.72	0.46	-39.8	0.33	117.9	0.44	0.26	-35.0	0.47	36.6	...	...	...		...
J0736+2954	...	...	...		...	...	...	...		...	...	...	...		...
J0747+4618	...	...	...		...	...	...	...		...	...	...	...		...
J0749+2129	0.81	0.46	39.8	0.14	45.0	0.33	0.27	-19.3	0.23	10.0	...	...	...		...
J0751+2716	...	...	...		...	...	...	...		...	...	...	...		...
J0759+5312	0.74	0.48	61.0	0.15	97.5	0.33	0.28	1.5	0.18	50.8	11.93	7.02	1.4	0.34	66.7
J0805+1614	0.61	0.46	64.0	0.19	114.0	0.28	0.23	37.5	0.29	89.5	14.43	8.48	9.3	1.00	97.2
J0807+5327	0.75	0.49	59.5	0.15	81.0	0.33	0.28	1.4	0.12	39.0	61.82	55.91	-33.9	2.74	45.3
J0824+5413	0.75	0.49	58.6	0.15	62.9	0.33	0.28	3.9	0.11	30.1	...	...	...		...
J0834+1700	...	...	...		...	0.26	0.24	-171.1	0.49	226.7	21.78	14.14	66.6	0.17	65.2
J0839+2403	0.43	0.41	-43.6	0.25	97.5	...	...	...		...	...	...	...		...
J0843+4215	...	...	...		...	...	...	...		...	...	...	...		...
J0901+0304	0.62	0.42	50.4	0.35	160.5	...	...	...		...	14.56	6.21	-1.3	0.30	184.9
J0903+5012	0.63	0.49	52.2	0.20	230.0	0.31	0.27	-13.3	0.07	39.4	...	...	...		...
J0905+4128	...	...	...		...	...	...	...		...	...	...	...		...
J0907+0413	0.58	0.47	-41.5	0.25	81.8	...	...	...		...	...	...	...		...

Table B.1 (continued)

Object	VLA 4.9 GHz					VLA 8.5 GHz					VLBA 1.4 GHz				
	Maj. (″)	Min. (″)	P.A. (°)	RMS (mJy/ beam)	$F_{\rm m}$ (mJy/ beam)	Maj. (″)	Min. (″)	P.A. (°)	RMS (mJy/ beam)	$F_{\rm m}$ (mJy/ beam)	Maj. (mas)	Min. (mas)	P.A. (°)	RMS (mJy/ beam)	$F_{\rm m}$ (mJy/ beam)
J0910+2419	0.44	0.41	-59.6	0.19	97.1	...	...	...		...	...	...	...		...
J0915+1018	0.54	0.40	-9.7	0.21	51.6	...	...	...		...	...	...	...		...
J0917+4725	0.75	0.48	71.0	0.19	63.0	0.31	0.27	-19.4	0.09	24.4	51.39	48.50	-11.1	0.56	7.5
J0920+1753	0.49	0.43	-87.6	0.29	177.2	...	...	...		...	...	...	...		...
J0920+2714	0.54	0.44	73.8	0.17	91.7	0.35	0.25	78.3	0.22	42.2	34.52	15.91	46.7	0.25	34.6
J0939+0304	0.68	0.41	-40.5	0.26	198.0	...	...	...		...	15.38	6.90	1.2	0.24	160.6
J0945+2640	0.97	0.47	61.2	0.15	162.0	...	...	...		...	13.66	10.10	8.2	0.11	64.6
J0951+1154	0.49	0.44	-3.0	0.18	26.3	0.74	0.39	-46.7	0.15	15.9	...	...	...		...
J1008+2401	0.47	0.41	-47.5	0.16	58.7	...	...	...		...	...	...	...		...
J1010+4159	...	...	...		...	...	...	...		...	...	...	...		...
J1019+4408	...	...	...		...	...	...	...		...	...	...	...		...
J1023+0424	0.51	0.42	-24.4	0.21	71.5	0.35	0.25	30.0	0.09	38.6	14.69	6.62	5.6	0.28	43.7
J1033+3935	...	...	...		...	...	...	...		...	...	...	...		...
J1034+1112	0.54	0.46	51.4	0.17	123.7	0.31	0.27	71.7	0.28	53.7	...	...	...		...
J1043+0537	0.53	0.44	38.7	0.12	46.7	...	...	...		...	...	...	...		...
J1045+0455	0.55	0.46	42.3	0.14	52.0	0.49	0.30	56.9	0.20	23.1	...	...	...		...
J1048+3457	...	...	...		...	...	...	...		...	8.12	4.86	-5.9	0.60	73.7
J1120+2327	...	...	...		...	...	...	...		...	...	...	...		...
J1125+1953	0.47	0.43	54.8	0.21	101.9	...	...	...		...	15.40	8.37	-13.1	0.20	18.2

Table B.1 (continued)

Object	VLA 4.9 GHz					VLA 8.5 GHz					VLBA 1.4 GHz				
	Maj. (″)	Min. (″)	P.A. (°)	RMS (mJy/ beam)	$F_{\rm m}$ (mJy/ beam)	Maj. (″)	Min. (″)	P.A. (°)	RMS (mJy/ beam)	$F_{\rm m}$ (mJy/ beam)	Maj. (mas)	Min. (mas)	P.A. (°)	RMS (mJy/ beam)	$F_{\rm m}$ (mJy/ beam)
J1127+5743	0.53	0.41	2.0	0.21	147.3	0.44	0.26	-33.4	0.20	79.3	24.87	15.68	65.1	0.36	219.9
J1129+5638	0.58	0.44	-2.0	0.28	108.3	0.47	0.26	-35.9	0.18	54.0	9.67	6.78	3.0	0.14	80.5
J1142+0235	0.57	0.41	-1.3	0.23	64.6	0.29	0.25	-175.8	0.46	40.9	...	...	...		...
J1147+4818	0.49	0.43	71.3	0.20	93.2	0.54	0.26	73.4	0.33	50.8	12.83	12.19	8.6	0.45	33.3
J1148+1404	0.47	0.44	-44.8	0.25	57.8	0.29	0.25	15.7	0.12	31.4	47.11	28.02	29.3	0.57	11.7
J1202+1207	0.48	0.43	24.3	0.17	130.4	0.29	0.28	70.8	0.10	88.7	13.23	6.76	3.4	0.15	32.3
J1203+4632	0.42	0.41	87.3	0.25	184.2	...	...	...		...	...	...	...		...
J1207+5407	0.57	0.49	12.6	0.19	71.4	0.41	0.29	109.6	0.33	33.0	...	...	...		...
J1215+1730	0.44	0.41	-55.5	0.40	356.1	...	...	...		...	...	...	...		...
J1228+5348	0.74	0.46	85.9	0.17	47.6	0.56	0.42	-16.1	0.35	30.8	...	...	...		...
J1238+0845	0.55	0.45	45.0	0.13	86.6	0.29	0.29	-27.9	0.07	41.6	33.93	15.65	47.5	0.64	30.5
J1300+5029	...	...	...		...	...	...	...		...	...	...	...		...
J1312+1710	0.44	0.42	14.1	0.21	94.3	0.26	0.25	-46.7	0.07	56.3	13.86	7.64	15.5	0.40	36.7
J1315+0222	0.56	0.42	-22.2	0.20	68.6	0.30	0.25	-26.2	0.11	33.9	...	...	...		...
J1341+1032	0.61	0.44	68.9	0.16	80.8	0.30	0.28	96.6	0.17	34.5	...	...	...		...
J1345+5846	0.69	0.41	73.2	0.15	72.7	0.32	0.29	77.4	0.12	37.1	22.12	13.74	78.2	0.50	20.5
J1347+1217	...	...	...		...	...	...	...		...	...	...	...		...
J1348+2415	...	...	...		...	...	...	...		...	...	...	...		...
J1354+5650	0.68	0.40	73.2	0.14	141.9	0.32	0.29	77.8	0.11	76.2	...	...	...		...

Table B.1 (continued)

Object	VLA 4.9 GHz					VLA 8.5 GHz					VLBA 1.4 GHz				
	Maj. (″)	Min. (″)	P.A. (°)	RMS (mJy/ beam)	$F_{\rm m}$ (mJy/ beam)	Maj. (″)	Min. (″)	P.A. (°)	RMS (mJy/ beam)	$F_{\rm m}$ (mJy/ beam)	Maj. (mas)	Min. (mas)	P.A. (°)	RMS (mJy/ beam)	$F_{\rm m}$ (mJy/ beam)
J1357+0046	0.54	0.49	30.7	0.36	475.1	0.33	0.28	-30.2	0.12	229.0	14.81	5.91	0.1	0.65	401.1
J1410+4850	0.43	0.41	-54.1	0.20	115.9	0.25	0.24	6.8	0.14	63.9	10.15	6.69	9.4	0.13	94.1
J1413+1509	0.43	0.41	-89.4	0.29	221.2	...	...	...		...	...	...	...		...
J1414+4554	...	...	...		...	...	...	...		...	...	...	...		...
J1415+1320	...	...	...		...	...	...	...		...	...	...	...		...
J1421−0246	0.68	0.46	33.7	0.13	21.6	0.32	0.24	10.1	0.11	11.9	...	...	...		...
J1424+1852	0.45	0.44	42.0	0.18	69.8	0.28	0.24	36.5	0.27	32.8	...	...	...		...
J1502+3753	0.47	0.42	61.4	0.19	32.5	0.24	0.24	46.7	0.11	11.8	...	...	...		...
J1504+5438	...	...	...		...	...	...	...		...	...	...	...		...
J1504+6000	0.55	0.44	77.0	0.41	297.1	0.35	0.29	81.3	0.15	175.1	10.29	8.68	19.1	0.60	132.5
J1523+1332	0.48	0.42	-43.0	0.15	63.1	0.29	0.26	-35.0	0.11	30.1	19.93	15.12	29.2	0.36	18.2
J1527+3312	...	...	...		...	...	...	...		...	13.11	7.23	9.2	0.19	59.9
J1528−0213	0.54	0.45	-13.8	0.18	60.4	0.33	0.27	-10.7	0.09	31.4	...	...	...		...
J1548+0808	0.68	0.41	-52.0	0.42	149.2	0.37	0.24	-51.0	0.09	59.0	49.00	37.85	17.3	3.50	113.6
J1551+6405	...	...	...	0.25	...	...	...	...		...	...	...	...		...
J1559+4349	0.51	0.42	80.6	0.19	134.3	...	...	...		...	18.49	15.02	66.5	0.33	30.0
J1604+6050	0.66	0.44	87.8	0.16	165.6	0.38	0.29	89.3	0.09	86.1	10.92	9.03	50.2	0.28	222.3
J1616+2647	0.46	0.41	-62.8	0.77	578.7	...	...	...		...	13.76	8.31	7.0	0.40	366.6
J1625+4134	...	...	...		...	...	...	...		...	...	...	...		...

Table B.1 (continued)

Object	VLA 4.9 GHz					VLA 8.5 GHz					VLBA 1.4 GHz				
	Maj. (″)	Min. (″)	P.A. (°)	RMS (mJy/ beam)	$F_{\rm m}$ (mJy/ beam)	Maj. (″)	Min. (″)	P.A. (°)	RMS (mJy/ beam)	$F_{\rm m}$ (mJy/ beam)	Maj. (mas)	Min. (mas)	P.A. (°)	RMS (mJy/ beam)	$F_{\rm m}$ (mJy/ beam)
J1629+1342	0.72	0.41	-56.5	0.14	79.8	0.40	0.24	122.3	0.07	41.2	...	...	...		...
J1633+4700	0.55	0.42	-84.4	0.13	73.9	0.32	0.24	89.4	0.06	35.8	27.64	23.72	27.9	0.65	26.7
J1724+3852	0.62	0.42	-71.0	0.19	126.1	0.36	0.24	102.8	0.20	68.7	12.26	8.96	-3.2	0.15	89.4
J2203−0021	0.62	0.43	38.1	0.33	131.4	...	...	...		...	...	...	...		...

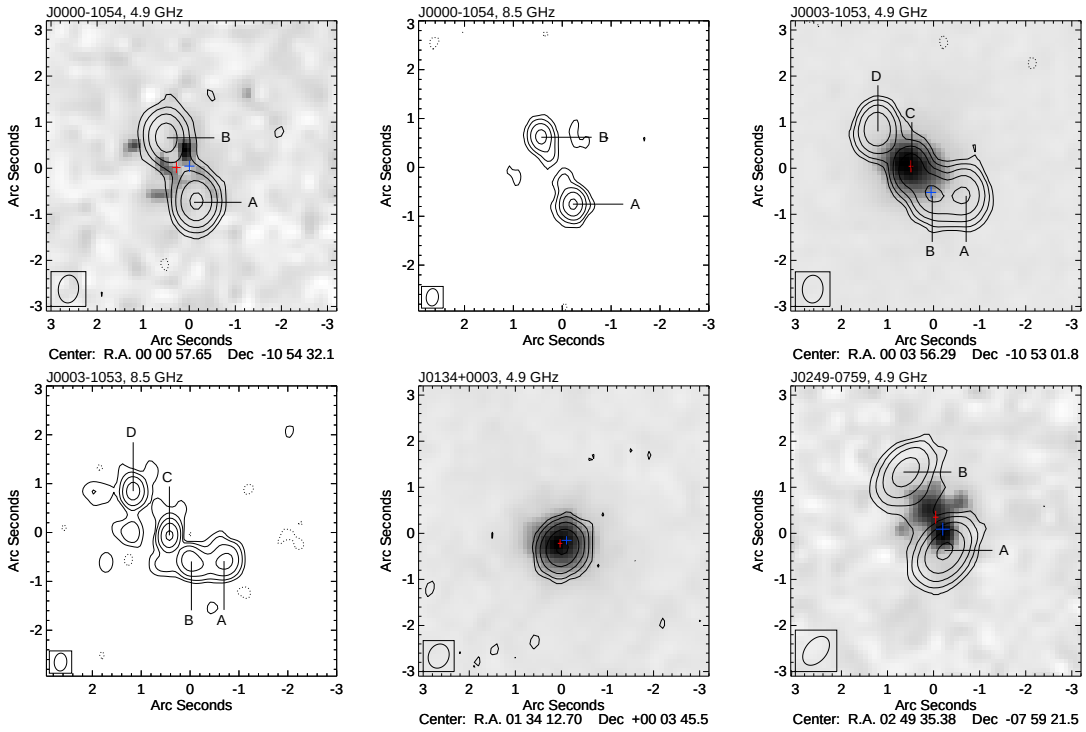

Figure B.1 VLA 4.9 GHz, VLA 8.5 GHz and VLBA 1.4 GHz images. Each image has five contour levels ranging from 3σ to $0.8F_{\rm m}$ logarithmically where $F_{\rm m}$ is the maximum of pixel counts, i.e., assuming $R = 0.8F_{\rm m}/3\sigma$, the contour levels are (1, $R^{1/4}$, $R^{2/4}$, $R^{3/4}$, R)$\times 3\sigma$. Negative 3σ is drawn in dashed line. On 4.9 GHz and 1.4 GHz images, r-band centroid position is labeled in blue with uncertainties along RA and Dec axis. Red cross is NIR centroid position and uncertainties primarily in $K_{\rm s}$-band. The crosses can be completely or partly outside 1.4 GHz images. Therefore, when 1.4 GHz image is available for an object, boundary of the represented field is illustrated by a green rectangle on its 4.9 GHz image. Center coordinates of 4.9 GHz and 1.4 GHz images are shown at the bottom. Relative positions along RA and Dec are labeled on X and Y axis respectively. Please note that absolute 8.5 GHz astrometry is problematic and center coordinates are thus not given. 4.9 GHz images are overlaid with NIR images. NIR images have been re-gridded and smoothed by cubic interpolation. Pixel counts are displayed by grayscale with the following approach. On a grayscale of 0 (white) to 1 (dark), 1 represents the maximum pixel counts of the object; 0 and 0.2 represents -2.5σ and 2.5σ noise of the sky background respectively; between 0 to 0.2 and 0.2 to 1, it scales linearly with pixel counts. The restored beam is shown at the lower left corner of each image. J0834+1700 and J1527+3312 have 8.5 GHz images but no 4.8 images; they are unresolved in 8.5 GHz. And we overlay their NIR images with the 8.5 GHz images. We also label the optical and NIR centroid positions on 8.5 GHz images as well as the field of 1.4 GHz images.

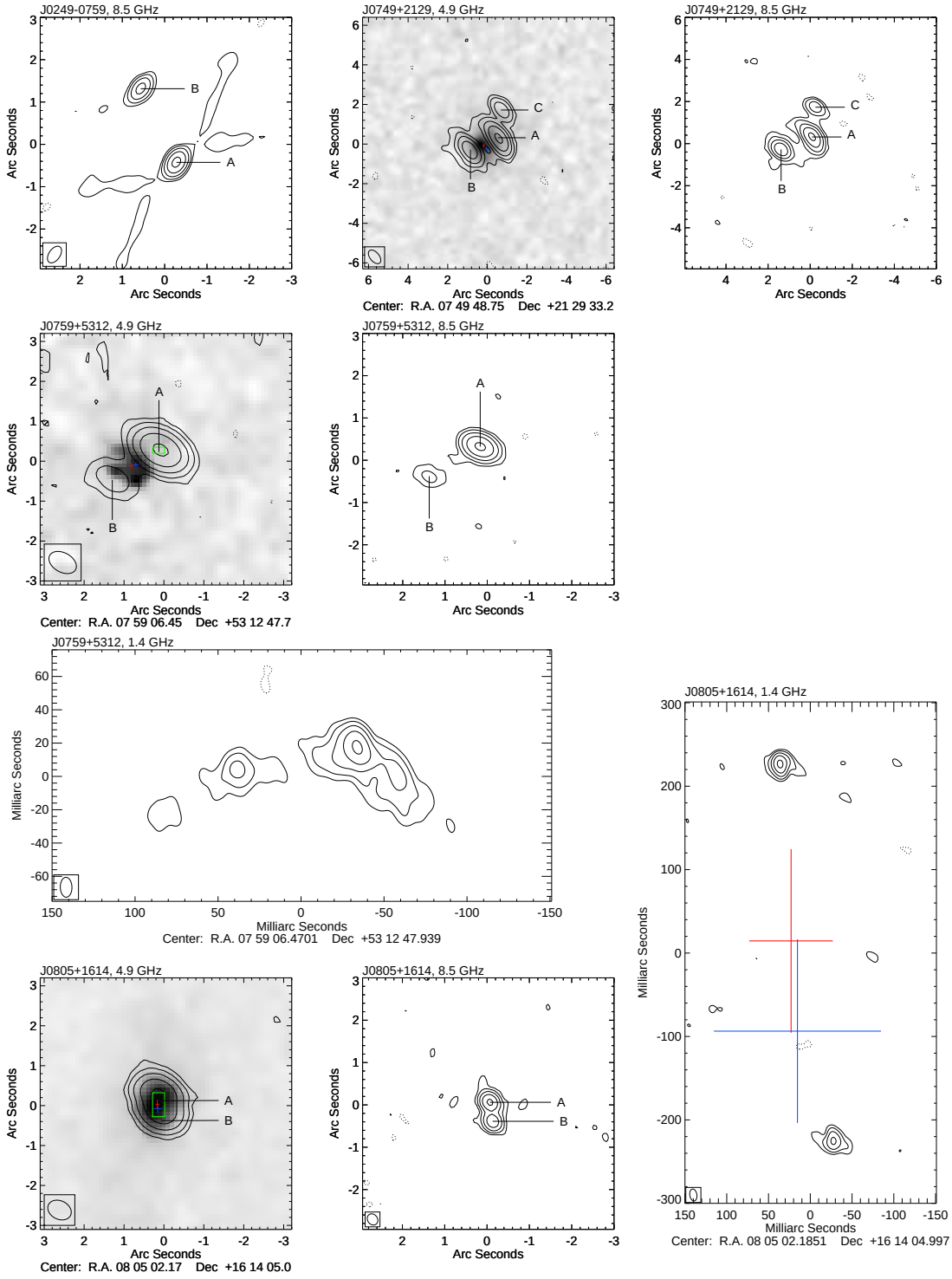

Figure B.1 (continued)

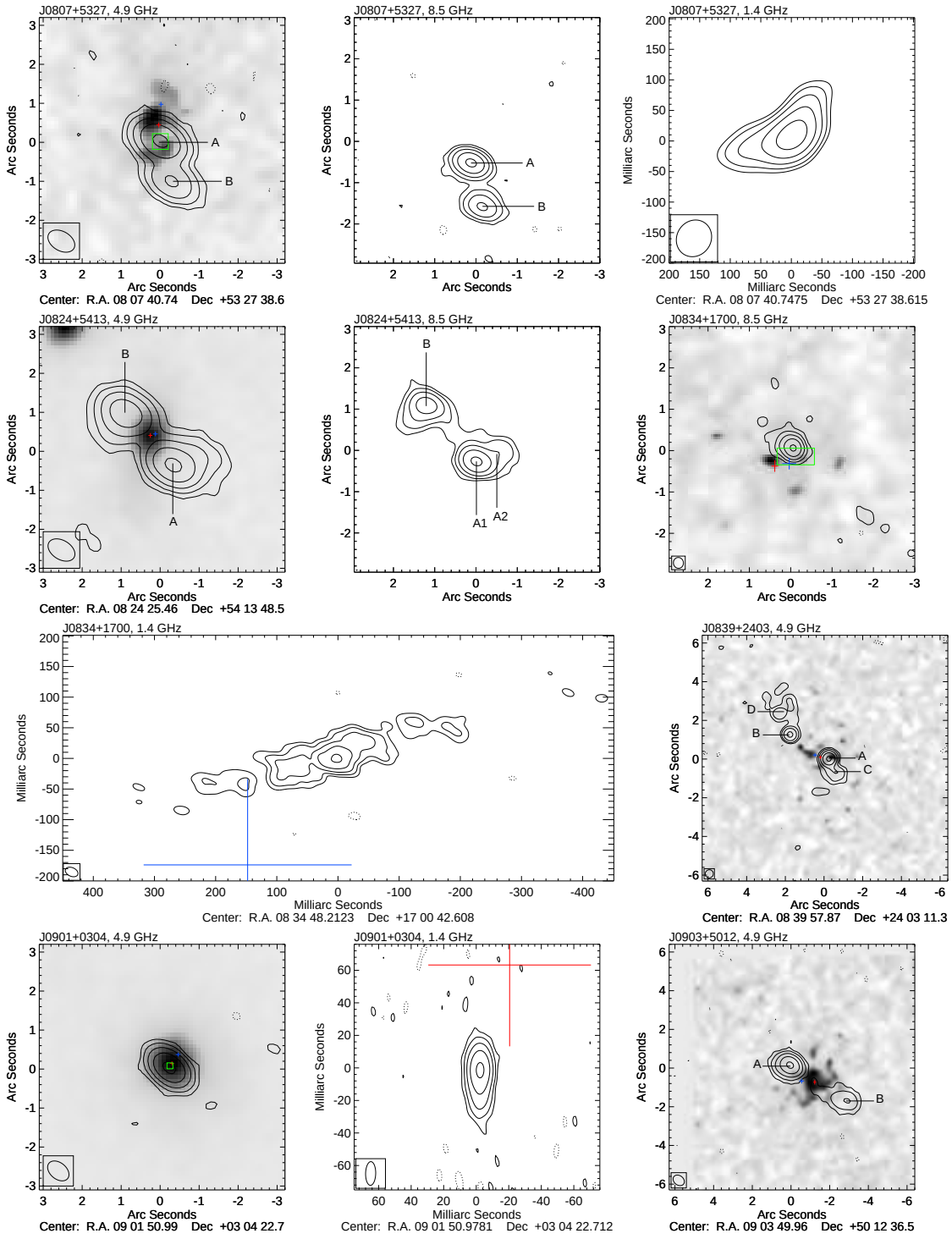

Figure B.1 (continued)

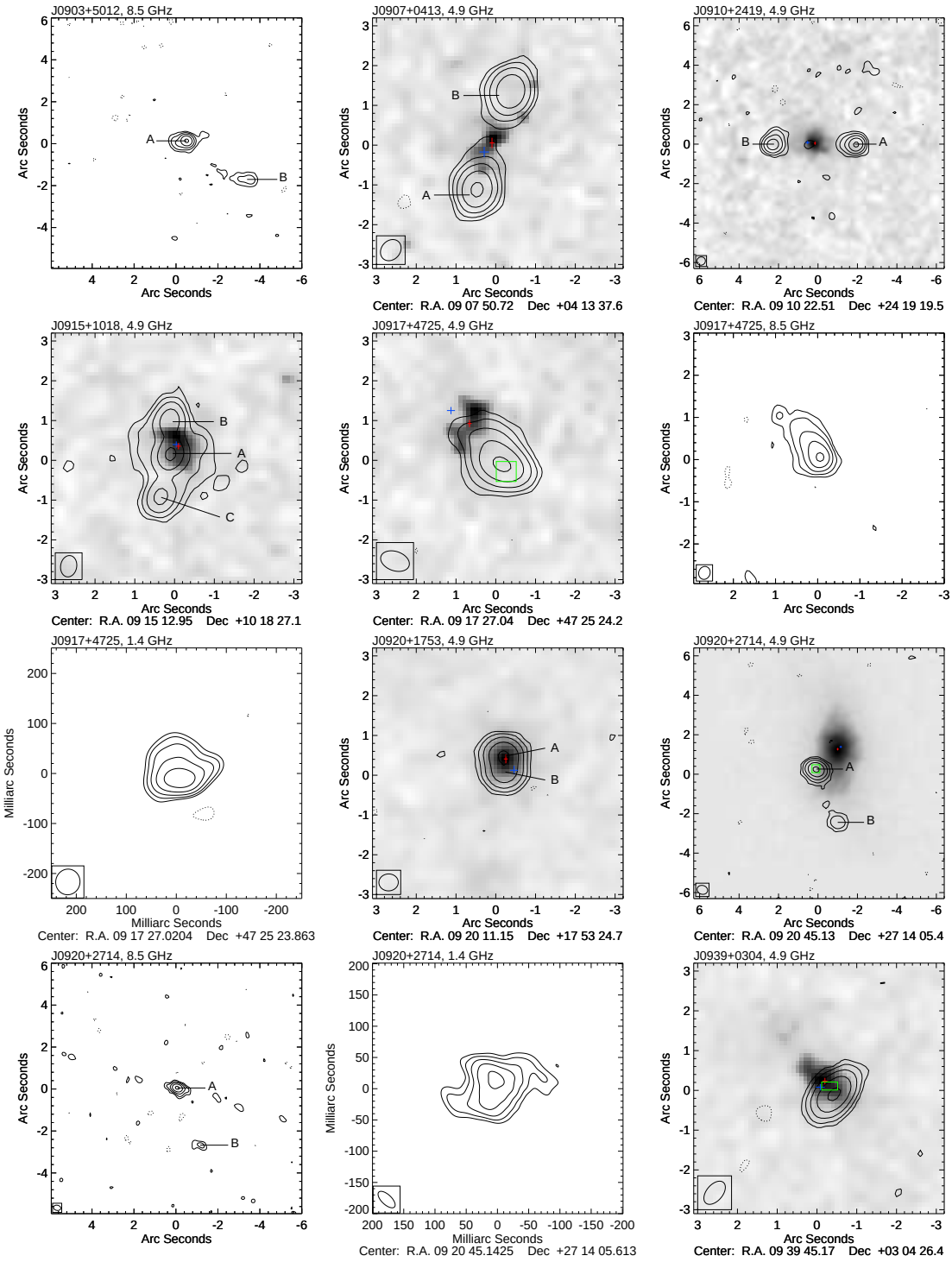

Figure B.1 (continued)

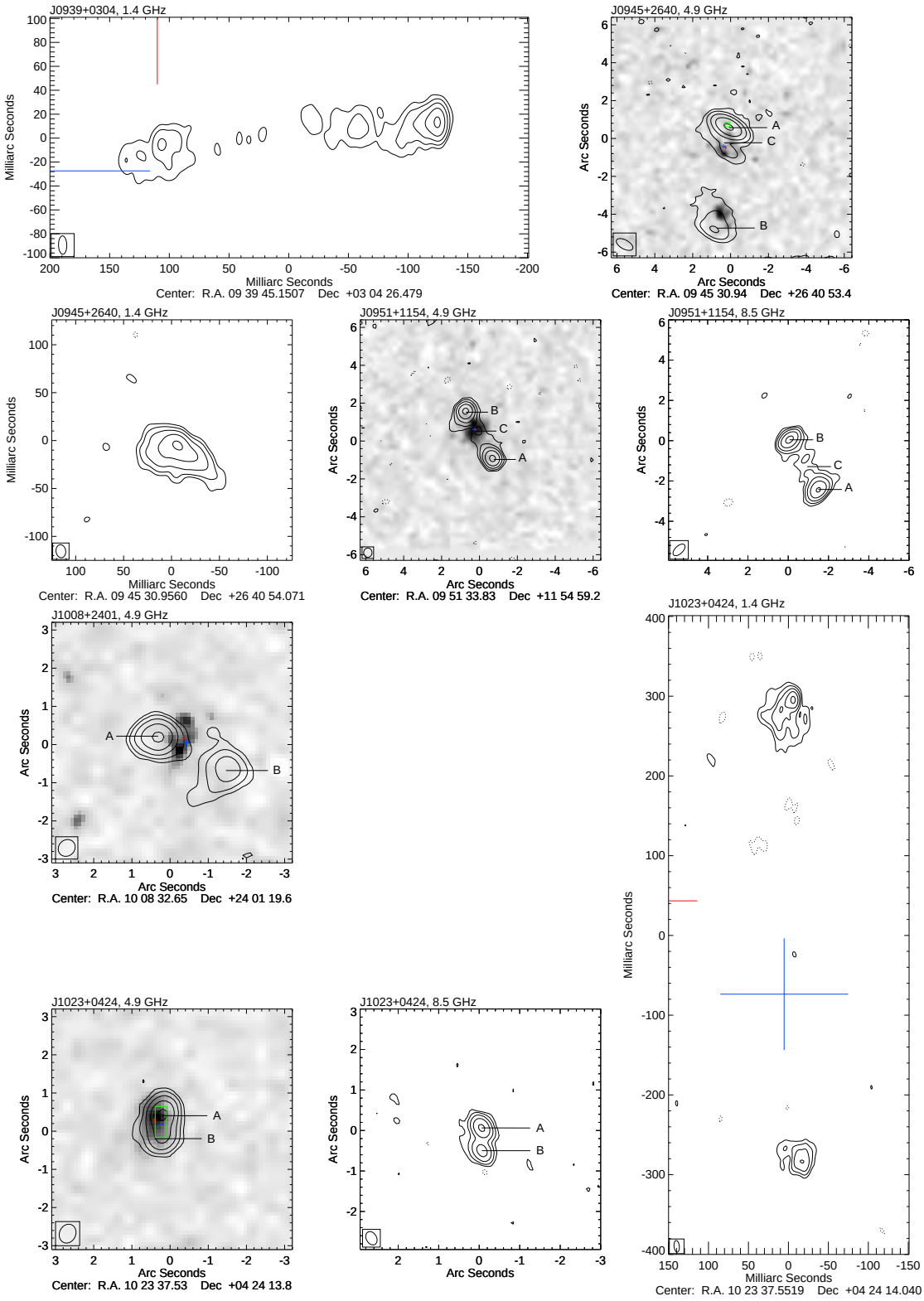

Figure B.1 (continued)

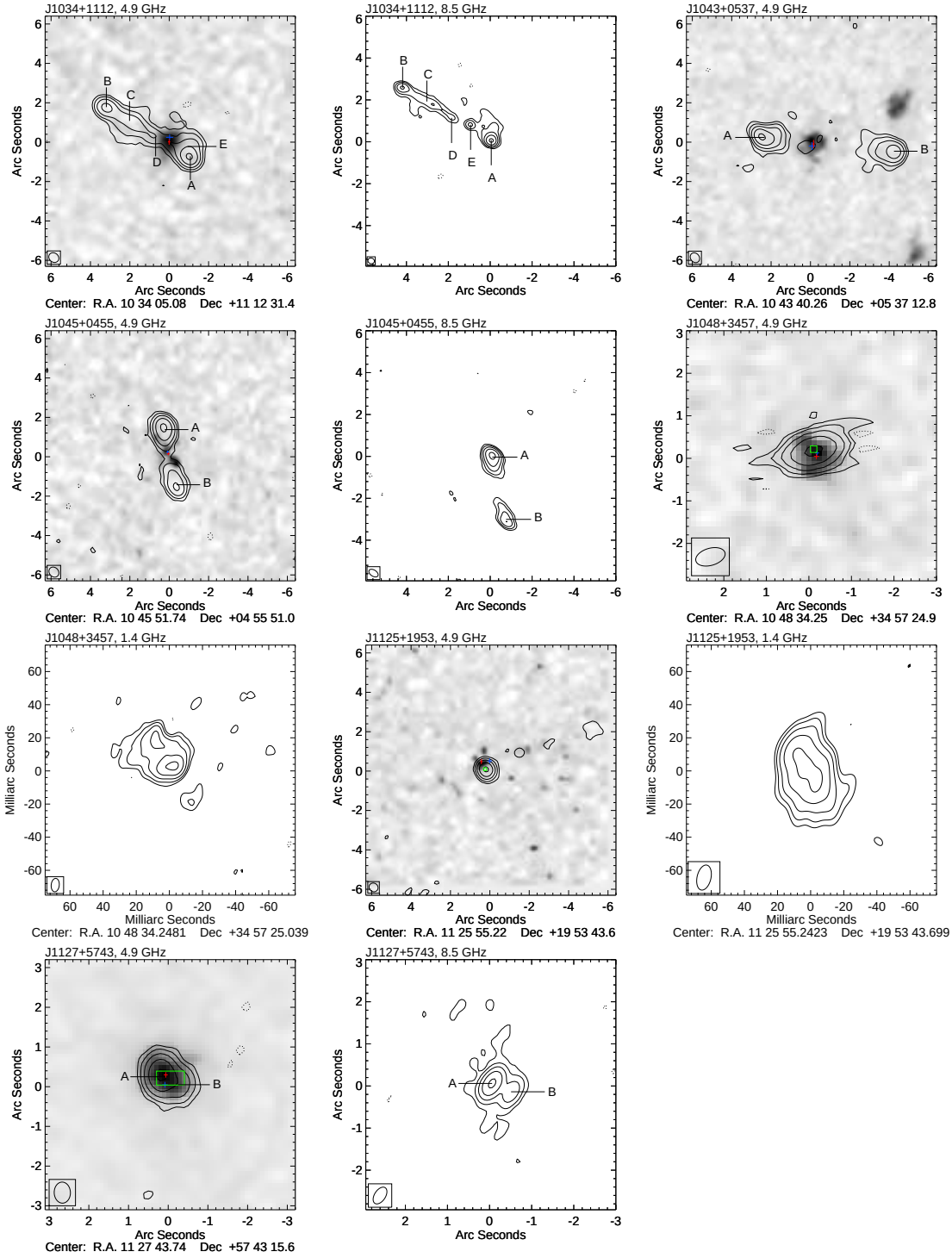

Figure B.1 (continued)

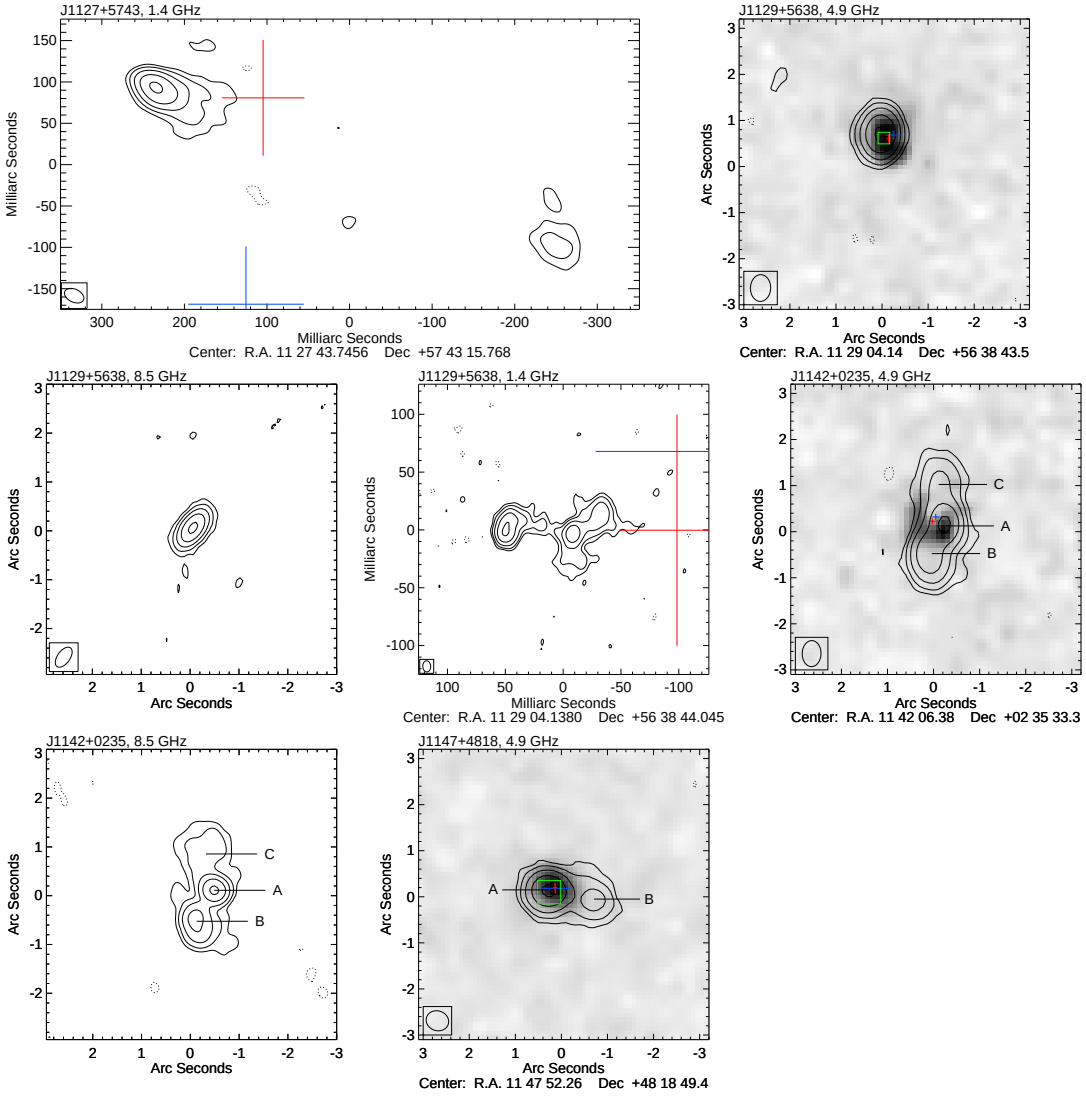

Figure B.1 (continued)

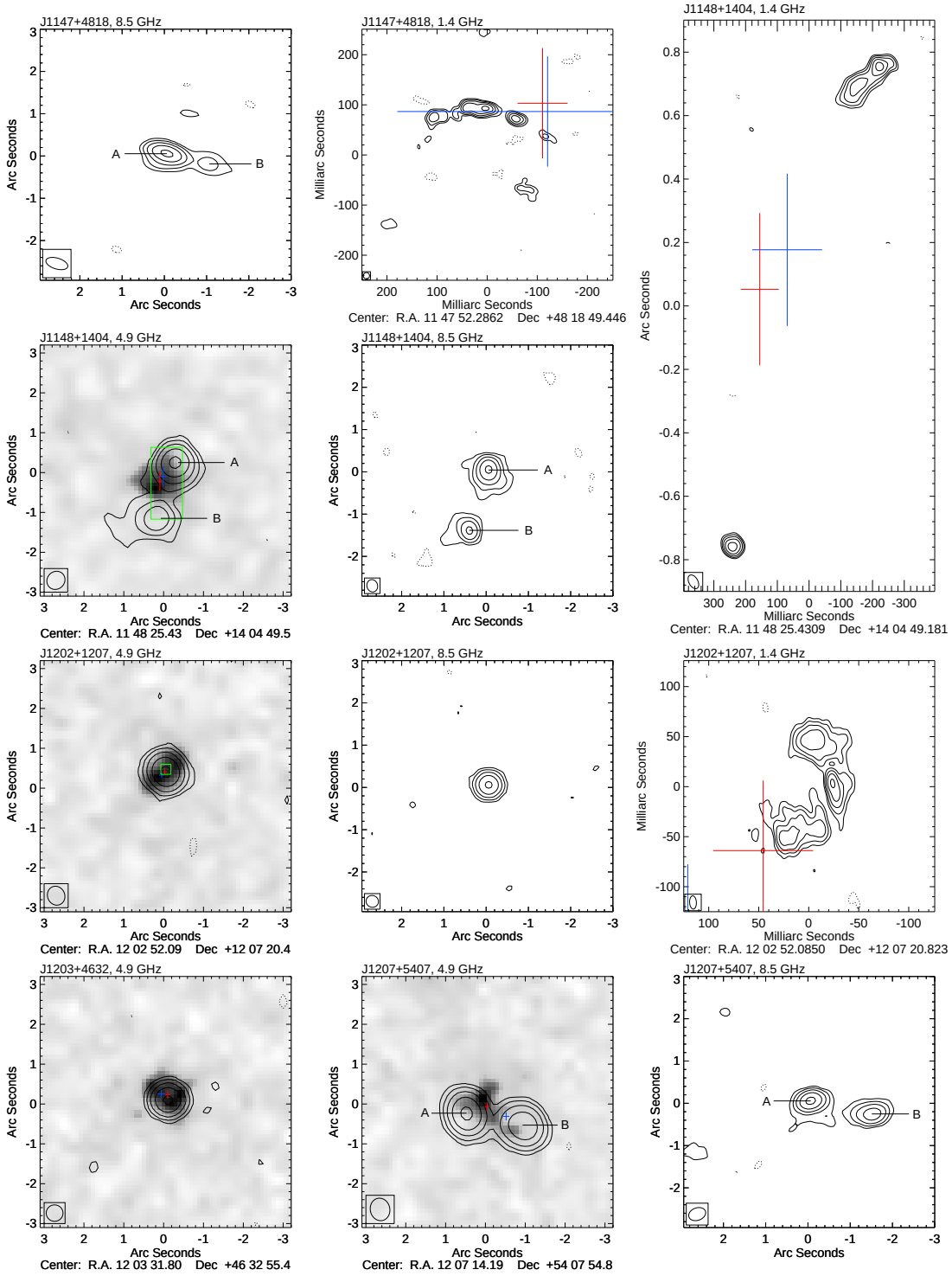

Figure B.1 (continued)

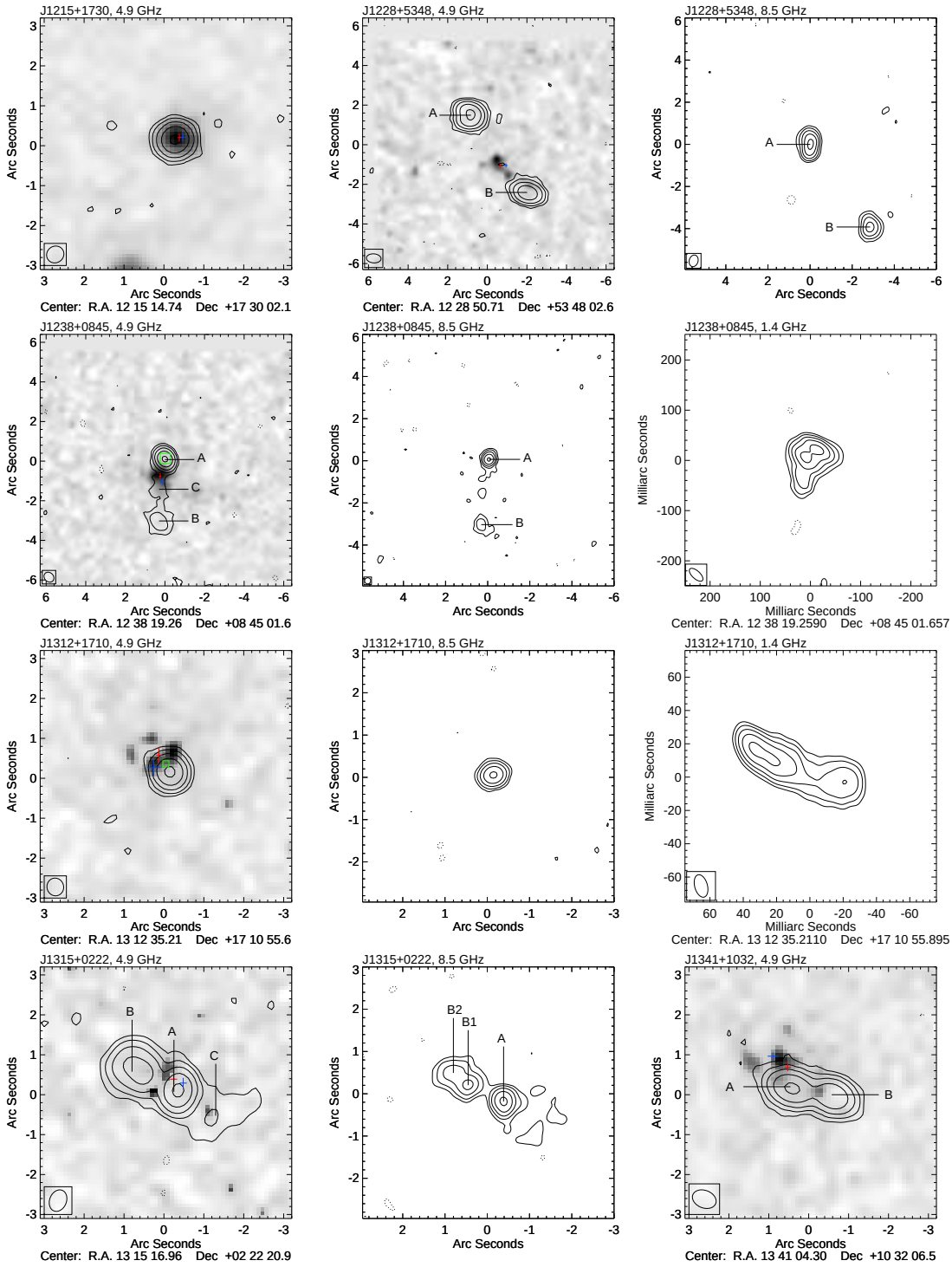

Figure B.1 (continued)

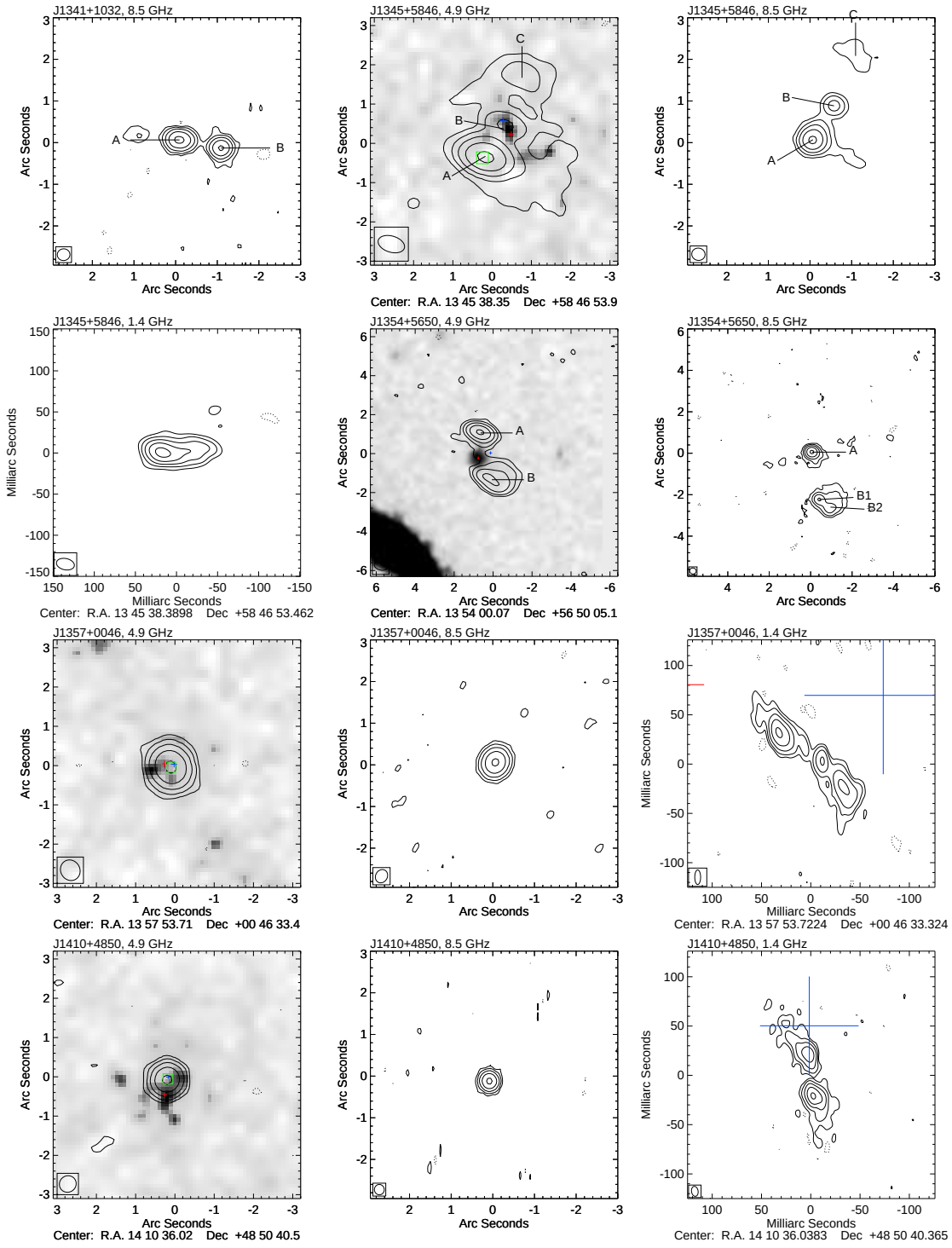

Figure B.1 (continued)

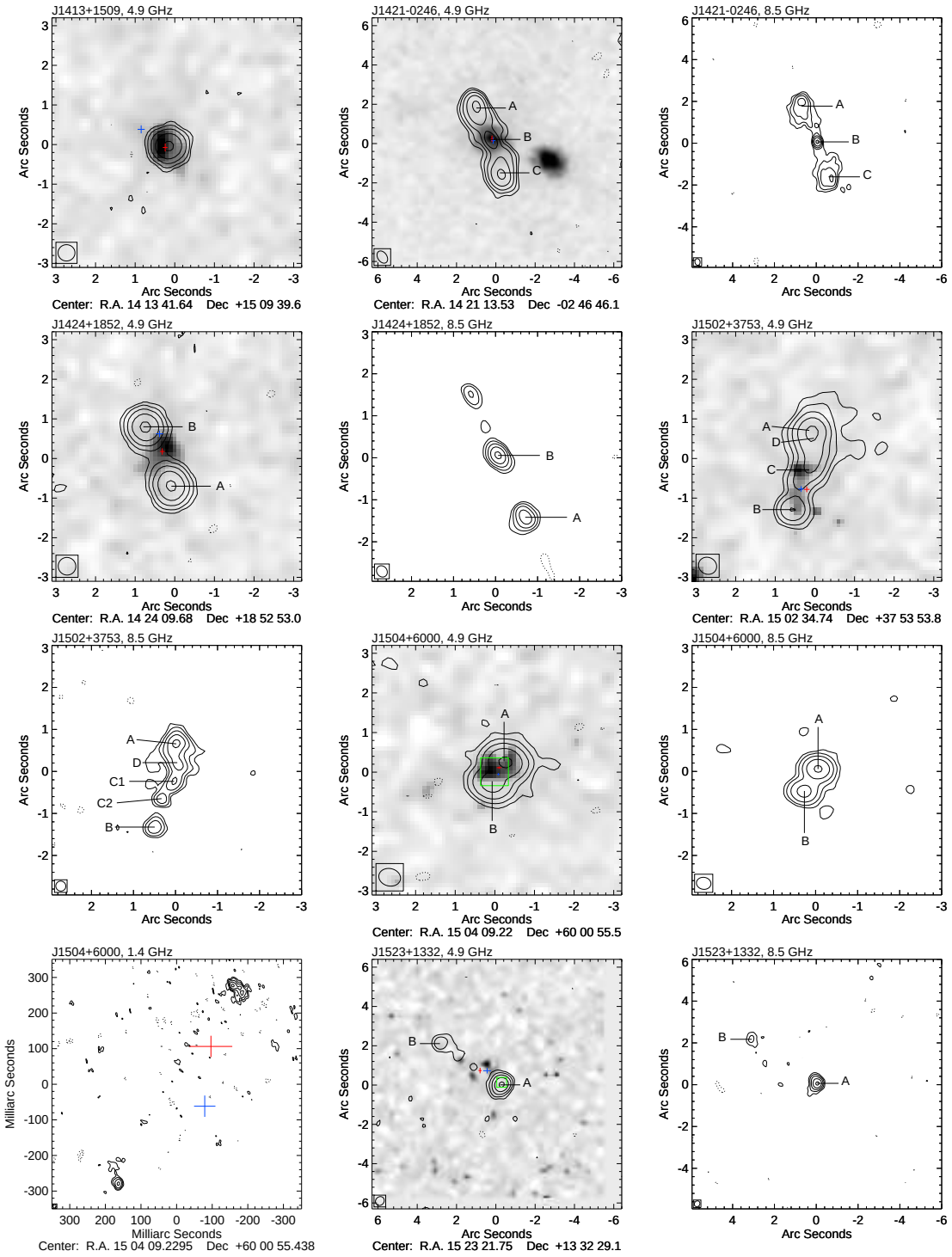

Figure B.1 (continued)

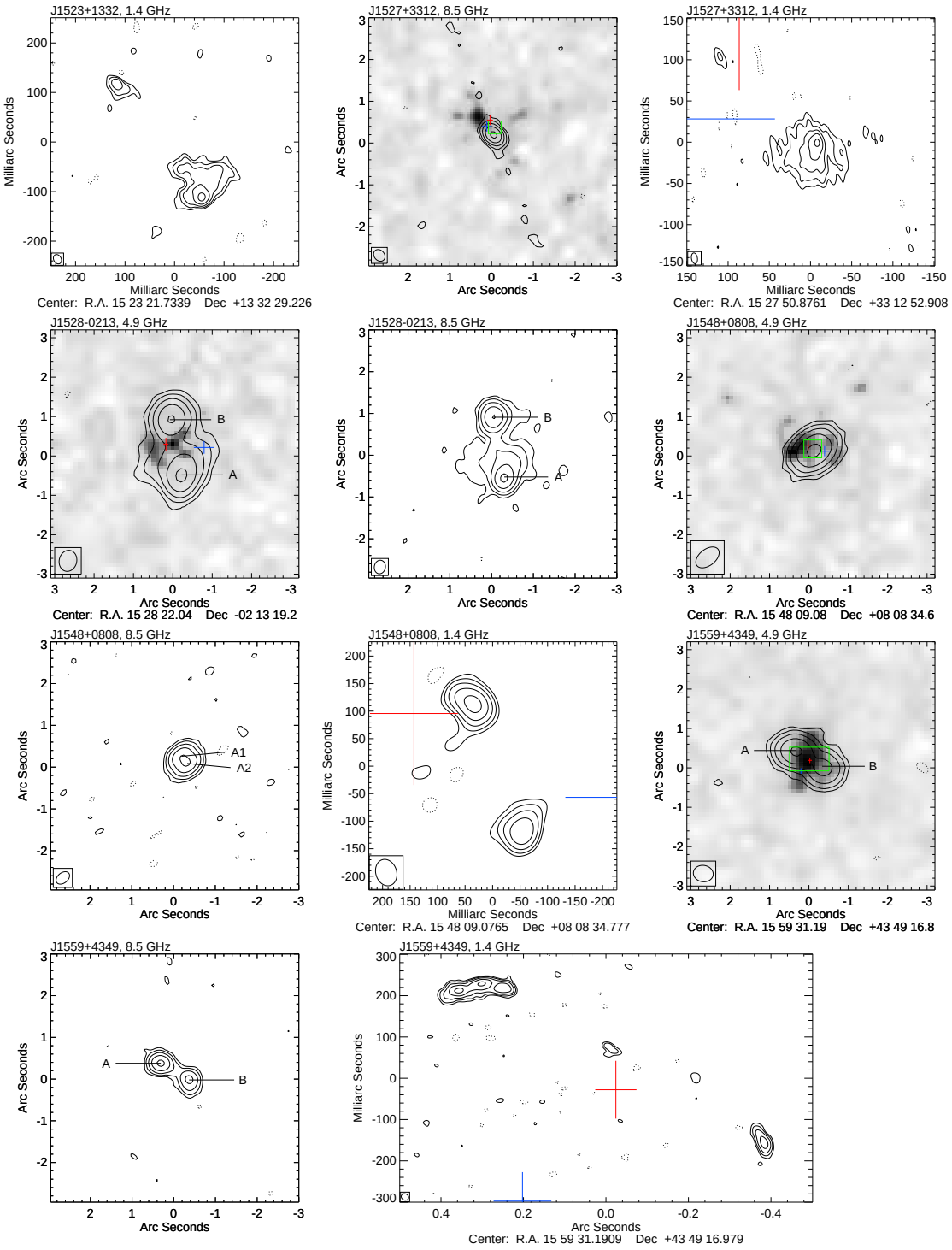

Figure B.1 (continued)

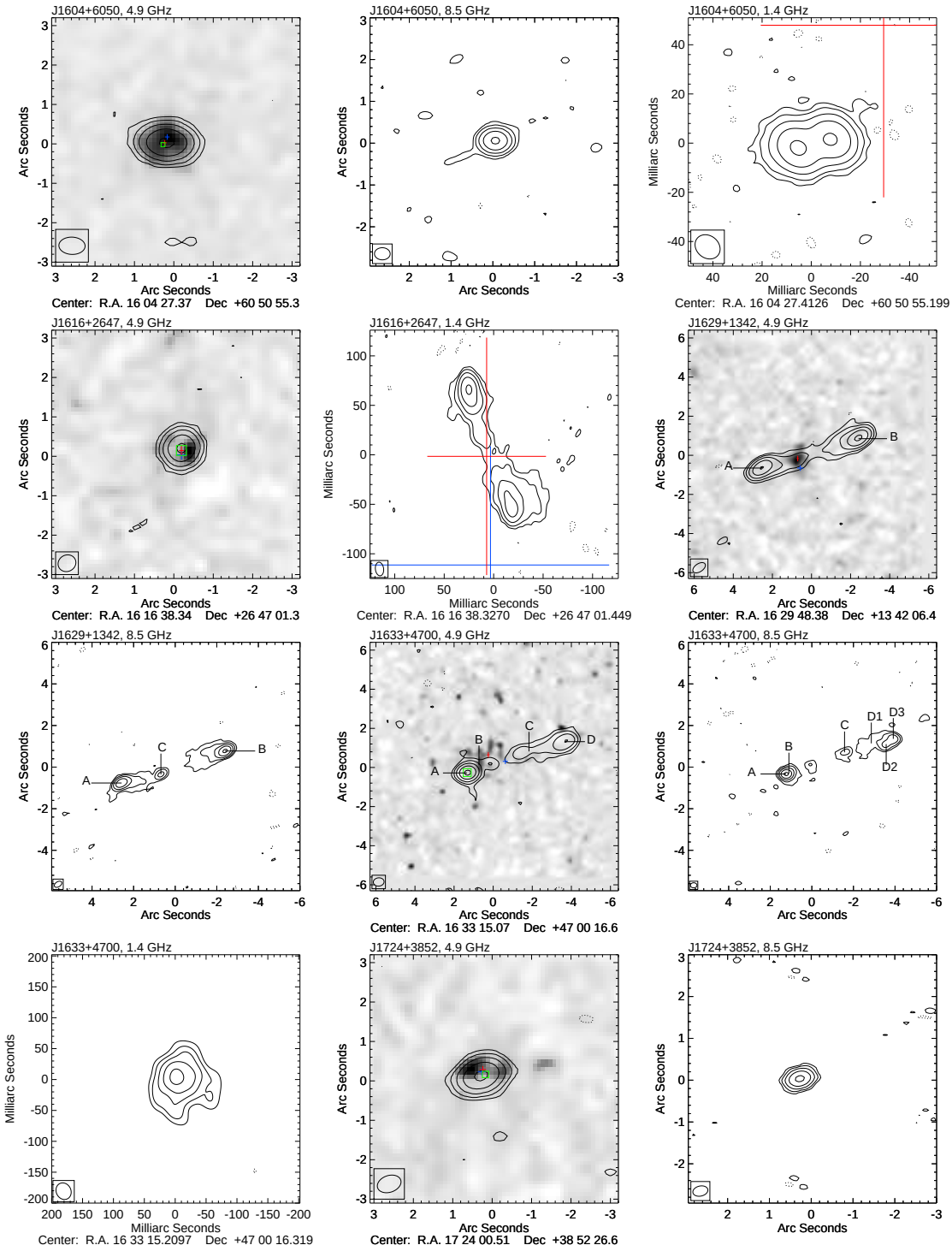

Figure B.1 (continued)

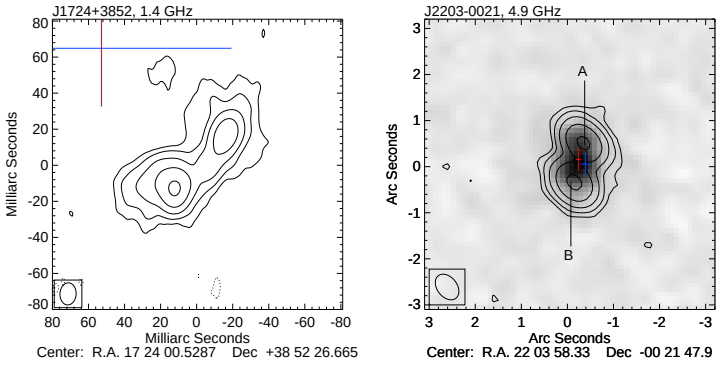

Figure B.1 (continued)

Table B.2. VLA 4.9 GHz Gaussian Fit Results.

Object	ID	R.A. (hh mm ss.sss)	Dec. (dd mm ss.ss)	S_p (mJy /beam)	S_{tot} (mJy)	Maj. (″)	Min. (″)	P.A. (°)
(1)	(2)	(3)	(4)	(5)	(6)	(7)	(8)	
J0000−1054	A	00 00 57.647	−10 54 32.87	35.3	42.6	0.28	0.17	40.2
	B	00 00 57.690	−10 54 31.50	18.8	23.8	0.36	0.14	32.0
J0003−1053	A	00 03 56.254	−10 53 02.49	30.7	39.6	0.30	0.23	96.1
	B	00 03 56.299	−10 53 02.47	30.5	40.5	0.40	0.07	60.0
	C	00 03 56.332	−10 53 01.92	22.3	23.0	0.11	0.07	140.9
	D	00 03 56.381	−10 53 01.06	24.3	27.8	0.21	0.17	48.7
J0134+0003		01 34 12.704	+00 03 45.14	548.3	553.9	0.05	0.05	106.0
J0249−0759	A	02 49 35.370	−07 59 21.92	118.9	136.1	0.23	0.18	5.9
	B	02 49 35.426	−07 59 20.21	55.6	67.1	0.29	0.23	149.8
J0749+2129	A	07 49 48.708	+21 29 33.47	44.7	63.5	0.68	0.18	27.6
	B	07 49 48.813	+21 29 32.87	28.2	36.0	0.45	0.22	27.5
	C	07 49 48.697	+21 29 34.90	8.6	10.3	0.34	0.21	43.5
J0759+5312	A	07 59 06.465	+53 12 47.95	97.8	100.1	0.11	0.07	40.5
	B	07 59 06.598	+53 12 47.23	3.7	4.5	0.34	0.24	79.9
J0805+1614	A	08 05 02.180	+16 14 05.10	107.1	114.2	0.18	0.10	72.6
	B	08 05 02.180	+16 14 04.60	69.2	73.0	0.16	0.09	72.4
J0807+5327	A	08 07 40.746	+53 27 38.63	81.9	86.3	0.15	0.10	152.9
	B	08 07 40.714	+53 27 37.60	22.1	24.9	0.27	0.16	35.9
J0824+5413	A	08 24 25.427	+54 13 48.06	62.5	79.4	0.36	0.23	112.3
	B	08 24 25.568	+54 13 49.37	35.2	48.0	0.39	0.29	139.0
J0839+2403	A	08 39 57.851	+24 03 11.27	100.8	108.0	0.12	0.10	50.9
	B	08 39 57.997	+24 03 12.52	33.9	36.9	0.15	0.09	58.2
	C	08 39 57.828	+24 03 10.57	8.2	21.9	0.70	0.39	55.5
	D	08 39 58.024	+24 03 13.72	4.5	18.6	1.00	0.52	120.9
J0901+0304		09 01 50.981	+03 04 22.66	166.5	172.5	0.14	0.06	44.9
J0903+5012	A	09 03 49.973	+50 12 36.55	233.3	268.4	0.26	0.15	105.6
	B	09 03 49.675	+50 12 34.73	11.2	22.7	0.76	0.38	81.7
J0907+0413	A	09 07 50.770	+04 13 36.30	82.5	106.9	0.38	0.14	8.6
	B	09 07 50.720	+04 13 38.80	64.0	89.7	0.41	0.23	7.5
J0910+2419	A	09 10 22.376	+24 19 19.48	97.5	118.3	0.22	0.17	91.1
	B	09 10 22.684	+24 19 19.48	51.8	78.3	0.33	0.28	109.0
J0915+1018	A	09 15 12.960	+10 18 27.20	50.2	67.5	0.31	0.21	113.1
	B	09 15 12.960	+10 18 28.00	28.3	40.6	0.34	0.27	135.1
	C	09 15 12.980	+10 18 26.10	19.9	28.5	0.36	0.23	120.2
J0917+4725		09 17 27.032	+47 25 24.07	60.9	95.7	0.58	0.29	29.3
J0920+1753	A	09 20 11.143	+17 53 25.12	167.8	181.6	0.15	0.10	24.7
	B	09 20 11.142	+17 53 24.70	106.2	113.6	0.13	0.10	159.4
J0920+2714	A	09 20 45.142	+27 14 05.58	93.0	105.0	0.20	0.15	39.1
	B	09 20 45.060	+27 14 02.90	5.7	6.9	0.23	0.20	166.1
J0939+0304		09 37 09.249	+03 18 03.33	199.9	216.0	0.17	0.12	111.6
J0945+2640	A	09 45 30.950	+26 40 53.90	161.2	171.8	0.16	0.13	154.3
	B	09 45 31.000	+26 40 48.60	7.9	16.1	0.72	0.51	170.1

Table B.2 (continued)

Object	ID	R.A.	Dec.	S_p (mJy	S_{tot}	Maj.	Min.	P.A.
		(hh mm ss.sss)	(dd mm ss.ss)	/beam)	(mJy)	(″)	(″)	(°)
(1)	(2)	(3)	(4)	(5)	(6)	(7)	(8)	
	C	09 45 30.970	+26 40 53.10	3.6	11.3	1.68	0.41	29.2
J0951+1154	A	09 51 33.780	+11 54 58.20	26.0	44.3	0.46	0.32	46.7
	B	09 51 33.880	+11 55 00.70	25.6	39.8	0.37	0.32	127.3
	C	09 51 33.850	+11 54 59.70	1.4	14.7	2.10	0.95	48.5
J1008+2401	A	10 08 32.681	+24 01 19.77	57.7	84.1	0.38	0.19	77.8
	B	10 08 32.548	+24 01 18.93	10.5	21.3	0.46	0.43	44.0
J1023+0424	A	10 23 37.550	+04 24 14.20	71.3	74.4	0.12	0.07	5.5
	B	10 23 37.560	+04 24 13.60	29.0	31.7	0.20	0.00	164.8
J1034+1112	A	10 34 05.014	+11 12 30.58	120.3	143.9	0.24	0.19	153.9
	B	10 34 05.299	+11 12 33.07	41.8	53.5	0.36	0.17	71.1
	C	10 34 05.216	+11 12 32.35	16.8	61.7	1.44	0.37	61.8
	D	10 34 05.132	+11 12 31.57	6.1	9.4	0.58	0.10	80.2
	E	10 34 05.024	+11 12 31.08	15.3	56.8	1.09	0.59	95.1
J1043+0537	A	10 43 40.425	+05 37 13.01	43.5	78.4	0.58	0.28	71.5
	B	10 43 39.984	+05 37 12.28	23.8	53.0	0.62	0.44	91.5
J1045+0455	A	10 45 51.764	+04 55 52.34	51.2	92.5	0.61	0.29	2.6
	B	10 45 51.723	+04 55 49.52	14.9	32.6	0.83	0.29	16.2
J1125+1953		11 25 55.240	+19 53 43.68	101.4	113.9	0.20	0.09	2.0
J1127+5743	A	11 27 43.773	+57 43 15.84	147.8	152.1	0.09	0.06	60.0
	B	11 27 43.718	+57 43 15.63	25.4	27.7	0.16	0.10	128.2
J1129+5638		11 29 04.147	+56 38 44.14	109.6	112.9	0.11	0.03	88.6
J1142+0235	A	11 42 06.370	+02 35 33.40	64.9	72.3	0.18	0.14	38.3
	B	11 42 06.390	+02 35 32.80	41.2	65.5	0.49	0.27	9.6
	C	11 42 06.380	+02 35 34.30	8.7	21.0	0.73	0.45	175.4
J1147+4818	A	11 47 52.288	+48 18 49.48	94.9	107.0	0.19	0.12	128.1
	B	11 47 52.193	+48 18 49.29	11.0	18.0	0.39	0.33	21.9
J1148+1404	A	11 48 25.410	+14 04 49.70	57.9	77.2	0.28	0.24	15.4
	B	11 48 25.440	+14 04 48.30	15.3	21.5	0.32	0.25	83.1
J1202+1207		12 02 52.086	+12 07 20.76	133.9	140.2	0.12	0.07	105.5
J1203+4632		12 03 31.795	+46 32 55.48	184.3	187.2	0.07	0.03	99.9
J1207+5407	A	12 07 14.249	+54 07 54.49	72.6	76.7	0.16	0.08	44.7
	B	12 07 14.088	+54 07 54.18	49.3	61.3	0.35	0.10	79.4
J1215+1730		12 15 14.724	+17 30 02.23	369.4	388.8	0.12	0.06	50.1
J1228+5348	A	12 28 50.815	+53 48 04.00	49.6	91.9	0.67	0.24	2.4
	B	12 28 50.487	+53 48 00.08	31.9	50.9	0.54	0.33	48.3
J1238+0845	A	12 38 19.260	+08 45 01.63	86.3	94.2	0.19	0.08	171.8
	B	12 38 19.282	+08 44 58.47	4.7	8.3	0.56	0.33	41.0
	C	12 38 19.277	+08 45 00.08	0.8	4.3	1.93	0.49	11.9
J1312+1710		13 10 07.820	+17 26 49.70	98.8	109.4	0.17	0.11	0.1
J1315+0222	A	13 15 16.950	+02 22 20.90	70.1	86.1	0.27	0.17	30.9
	B	13 15 17.020	+02 22 21.40	31.1	74.1	0.74	0.34	58.2
	C	13 15 16.880	+02 22 20.30	1.9	9.5	1.30	0.66	107.9

Table B.2 (continued)

Object	ID	R.A.	Dec.	S_p (mJy	S_{tot}	Maj.	Min.	P.A.
		(hh mm ss.sss)	(dd mm ss.ss)	/beam)	(mJy)	(″)	(″)	(°)
(1)	(2)	(3)	(4)	(5)	(6)	(7)	(8)	
J1341+1032	A	13 41 04.327	+10 32 06.56	83.0	92.3	0.25	0.11	80.3
	B	13 41 04.259	+10 32 06.36	62.2	65.3	0.13	0.10	48.4
J1345+5846	A	13 45 38.379	+58 46 53.48	74.5	87.9	0.22	0.21	96.8
	B	13 45 38.319	+58 46 54.24	5.6	10.5	0.54	0.39	140.2
	C	13 45 38.261	+58 46 55.54	3.0	7.8	0.84	0.56	78.0
J1354+5650	A	13 54 00.153	+56 50 06.13	141.1	157.1	0.21	0.15	57.0
	B	13 54 00.078	+56 50 03.70	38.5	99.4	0.98	0.42	57.5
J1357+0046		13 57 53.723	+00 46 33.32	483.0	495.6	0.10	0.06	18.4
J1410+4850		14 10 36.041	+48 50 40.35	117.0	118.7	0.07	0.01	11.9
J1413+1509		14 13 41.657	+15 09 39.51	233.7	236.4	0.06	0.01	151.3
J1421−0246	A	14 21 13.600	−02 46 44.33	21.0	52.9	0.87	0.53	7.1
	B	14 21 13.550	−02 46 45.94	12.6	27.3	1.01	0.31	32.0
	C	14 21 13.516	−02 46 47.63	20.2	53.3	0.87	0.57	176.2
J1424+1852	A	14 24 09.691	+18 52 52.21	68.0	85.3	0.29	0.14	20.6
	B	14 24 09.736	+18 52 53.69	71.2	79.8	0.18	0.13	40.6
J1502+3753	A	15 02 34.755	+37 53 54.49	14.4	19.9	0.44	0.00	102.4
	B	15 02 34.794	+37 53 52.50	10.5	12.4	0.25	0.06	127.0
	C	15 02 34.758	+37 53 53.54	9.0	22.0	0.92	0.09	142.8
	D	15 02 34.755	+37 53 54.27	21.0	46.9	0.79	0.17	175.1
J1504+6000	A	15 04 09.195	+60 00 55.68	306.8	323.7	0.12	0.11	13.4
	B	15 04 09.240	+60 00 55.16	128.8	138.9	0.16	0.11	119.1
J1523+1332	A	15 23 21.735	+13 32 29.11	62.5	76.5	0.23	0.20	171.0
	B	15 23 21.946	+13 32 31.23	1.9	3.0	0.38	0.26	80.7
J1528−0213	A	15 28 22.030	−02 13 19.67	56.4	91.3	0.47	0.31	165.7
	B	15 28 22.047	−02 13 18.30	52.1	67.5	0.29	0.25	9.1
J1548+0808		15 48 09.076	+08 08 34.73	152.4	187.4	0.29	0.05	36.8
J1559+4349	A	15 59 31.221	+43 49 17.18	135.3	143.7	0.16	0.06	82.2
	B	15 59 31.158	+43 49 16.77	50.0	59.5	0.25	0.11	16.5
J1604+6050		16 04 27.402	+60 50 55.25	168.4	168.6	0.03	0.00	121.5
J1616+2647		16 16 38.327	+26 47 01.50	579.3	610.2	0.14	0.00	107.6
J1629+1342	A	16 29 48.558	+13 42 05.71	65.8	81.5	0.38	0.16	102.4
	B	16 29 48.222	+13 42 07.23	77.5	96.6	0.36	0.19	101.7
J1633+4700	A	16 33 15.206	+47 00 16.31	74.6	82.8	0.18	0.13	138.9
	B	16 33 15.148	+47 00 16.74	1.3	3.9	1.30	0.25	82.3
	C	16 33 14.898	+47 00 17.42	2.7	13.2	1.95	0.38	104.6
	D	16 33 14.722	+47 00 17.89	17.2	32.4	0.64	0.28	124.0
J1724+3852		17 24 00.537	+38 52 26.63	127.7	130.3	0.09	0.06	112.7
J2203−0021	A	22 03 58.311	−00 21 47.46	127.7	144.8	0.21	0.15	85.6
	B	22 03 58.325	−00 21 48.31	134.4	152.9	0.22	0.13	107.0

Table B.3. VLA 8.5 GHz Gaussian Fit Results.

Object	ID	S_p (mJy /beam)	S_{tot} (mJy)	Maj. ($''$)	Min. ($''$)	P.A. ($^\circ$)	α
J0000−1054	A	17.5	23.3	0.19	0.13	66.4	-1.1
	B	7.9	11.9	0.27	0.14	33.4	-1.2
J0003−1053	A	12.0	25.4	0.37	0.25	105.1	-0.8
	B	17.7	29.0	0.32	0.08	71.3	-0.6
	C	27.2	28.4	0.12	0.00	167.9	0.4
	D	14.9	18.4	0.16	0.13	38.8	-0.7
J0249−0759	A	37.1	45.8	0.17	0.13	33.0	-2.0
	B	18.0	22.0	0.21	0.11	124.9	-2.0
J0749+2129	A	18.3	31.7	0.61	0.14	26.8	-1.2
	B	13.1	17.4	0.33	0.18	21.8	-1.3
	C	3.5	4.7	0.35	0.19	43.1	-1.4
J0759+5312	A	53.4	55.1	0.08	0.05	67.1	-1.1
	B	1.4	2.0	0.34	0.13	81.9	-1.5
J0805+1614	A	89.1	93.4	0.06	0.05	74.0	-0.4
	B	54.5	57.8	0.07	0.05	136.9	-0.4
J0807+5327	A	41.1	45.3	0.13	0.09	139.7	-1.2
	B	11.8	15.2	0.21	0.18	57.3	-0.9
J0824+5413	A1	32.8	40.8	0.19	0.16	157.8	-1.2
	A2	2.7	6.7	0.48	0.41	136.5	
	B	16.2	26.2	0.33	0.23	122.6	-1.1
J0834+1700		219.0	299.4	0.18	0.13	53.7	
J0903+5012	A	118.9	134.3	0.13	0.09	102.5	-1.2
	B	2.9	9.1	0.73	0.25	85.3	-1.6
J0917+4725		21.6	47.8	0.41	0.22	31.1	-1.2
J0920+2714	A	40.8	50.0	0.18	0.09	50.8	-1.3
	B	2.6	4.3	0.38	0.10	68.3	-0.9
J0951+1154	A	13.2	21.7	0.44	0.33	15.5	-1.1
	B	15.6	22.1	0.35	0.25	53.5	-1.2
	C	1.2	7.7	2.04	0.55	24.9	-1.2
J1023+0424	A	38.5	39.2	0.04	0.03	68.0	-1.2
	B	16.6	17.8	0.11	0.04	67.7	-1.0
J1034+1112	A	51.0	83.0	0.25	0.21	174.4	
	B	17.8	28.2	0.30	0.15	78.0	
	C	4.7	41.9	1.69	0.34	63.3	
	D	2.7	4.9	0.42	0.10	55.7	
	E	7.7	10.1	0.20	0.13	64.6	
J1045+0455	A	22.3	50.6	0.55	0.26	3.3	-1.1
	B	6.9	15.9	0.64	0.22	16.3	-1.3
J1127+5743	A	78.7	82.5	0.08	0.06	172.5	-1.1
	B	14.3	18.6	0.24	0.14	156.3	-0.7
J1129+5638		53.8	56.5	0.08	0.07	121.2	-1.2
J1142+0235	A	37.6	43.5	0.12	0.11	146.8	-0.9
	B	15.0	34.6	0.45	0.24	6.3	

Table B.3 (continued)

Object	ID	S_p (mJy /beam)	S_{tot} (mJy)	Maj. ($''$)	Min. ($''$)	P.A. ($^\circ$)	α
	C	1.9	13.1	0.85	0.61	162.7	
J1147+4818	A	50.0	55.5	0.14	0.09	99.6	-1.2
	B	3.6	7.2	0.48	0.29	83.9	-1.6
J1148+1404	A	30.3	44.4	0.20	0.17	166.8	-1.0
	B	10.8	13.2	0.14	0.12	36.2	-0.9
J1202+1207		88.6	93.9	0.09	0.05	150.9	-0.7
J1207+5407	A	32.4	36.1	0.16	0.06	78.4	-1.4
	B	19.0	26.4	0.32	0.11	86.9	-1.5
J1228+5348	A	30.6	54.5	0.64	0.25	2.1	-0.9
	B	15.1	27.2	0.49	0.36	27.8	-1.1
J1238+0845	A	40.9	48.3	0.16	0.08	169.4	-1.2
	B	1.9	4.4	0.43	0.25	14.4	-1.1
J1312+1710		56.5	60.5	0.09	0.06	157.2	-1.1
J1315+0222	A	30.3	50.5	0.26	0.14	26.3	-1.0
	B1	11.8	19.2	0.23	0.16	92.9	
	B2	5.3	17.2	0.46	0.31	98.1	
J1341+1032	A	35.1	47.3	0.25	0.07	83.5	-1.2
	B	31.2	33.6	0.09	0.07	54.9	-1.2
J1345+5846	A	36.2	47.2	0.20	0.13	147.5	-1.1
	B	5.3	6.1	0.14	0.10	136.8	-1.0
	C	0.6	5.8	1.07	0.77	57.8	-0.5
J1354+5650	A	75.0	88.0	0.14	0.11	66.9	-1.0
	B1	18.6	24.3	0.20	0.13	38.0	
	B2	8.2	31.1	0.59	0.43	118.4	
J1357+0046		229.0	240.0	0.09	0.02	51.5	-1.3
J1410+4850		65.5	66.4	0.04	0.00	13.2	-1.0
J1421−0246	A	4.7	34.2	0.88	0.56	179.2	
	B	11.6	12.9	0.14	0.04	7.9	
	C	4.1	31.9	0.84	0.63	177.9	
J1424+1852	A	20.1	32.4	0.25	0.17	26.7	-1.7
	B	32.1	42.8	0.22	0.08	34.8	-1.1
J1502+3753	A	11.4	24.3	0.28	0.23	145.1	
	B	3.8	5.7	0.20	0.14	128.0	
	C1	4.7	7.9	0.31	0.04	152.8	
	C2	3.2	3.6	0.11	0.04	13.8	
	D	5.7	13.1	0.40	0.15	46.4	
J1504+6000	A	173.7	183.7	0.09	0.05	143.4	-1.0
	B	59.3	71.5	0.19	0.08	135.1	-1.2
J1523+1332	A	28.9	38.6	0.18	0.12	31.1	-1.2
	B	1.3	3.1	0.38	0.25	13.0	
J1527+3312		73.8	81.0	0.13	0.03	46.6	
J1528−0213	A	28.6	48.1	0.30	0.19	164.0	-1.2
	B	25.6	39.4	0.22	0.21	28.5	-1.0

Table B.3 (continued)

Object	ID	S_p (mJy /beam)	S_{tot} (mJy)	Maj. ($''$)	Min. ($''$)	P.A. ($^\circ$)	α
J1548+0808	A1	42.5	43.9	0.06	0.04	166.8	-0.8
	A2	51.9	55.7	0.09	0.05	15.1	-0.5
J1559+4349	A	68.4	79.6	0.15	0.05	85.4	
	B	22.2	30.2	0.20	0.10	13.7	
J1604+6050		86.1	86.2	0.03	0.00	126.9	-1.2
J1616+2647		650.6	717.8	0.14	0.08	29.2	
J1629+1342	A	28.1	39.8	0.27	0.14	108.6	
	B	39.9	52.1	0.20	0.14	96.0	
	C	4.2	4.8	0.14	0.09	127.4	
J1633+4700	A	34.6	37.6	0.09	0.06	150.1	-1.4
	B	4.0	9.5	0.42	0.21	154.2	
	C	1.1	1.8	0.36	0.04	119.5	
	D1	0.4	6.8	1.99	0.52	122.6	
	D2	3.8	7.4	0.32	0.22	119.1	
	D3	6.2	9.1	0.22	0.15	44.0	
J1724+3852		71.6	72.8	0.06	0.01	140.9	-1.0

Table B.4. VLBA 1.4 GHz Gaussian Fit Results.

Object	ID	R.A. (hh mm ss.ssss)	Dec. (dd mm ss.sss)	S_p (mJy /beam)	S_{tot} (mJy)	Maj. (mas)	Min. (mas)	P.A. (°)
J0759+5312	a	07 59 06.4744	+53 12 47.943	8.4	20.9	13	8	97.9
	b	07 59 06.4792	+53 12 47.917	1.5	7.3	21	15	119.3
	c	07 59 06.4664	+53 12 47.956	62.7	132.3	11	7	51.0
	d	07 59 06.4638	+53 12 47.938	8.8	43.2	26	12	32.3
J0805+1614	a	08 05 02.1877	+16 14 05.223	92.7	175.5	11	9	118.5
	b	08 05 02.1832	+16 14 04.772	37.4	87.6	13	11	95.7
J0807+5327		08 07 40.7482	+53 27 38.624	43.3	103.1	109	34	125.1
J0834+1700	a	08 34 48.2174	+17 00 42.594	10.8	69.0	51	31	107.5
	b	08 34 48.2126	+17 00 42.608	61.8	184.1	31	18	100.7
	c	08 34 48.2102	+17 00 42.634	11.3	57.6	52	23	91.6
J0901+0304		09 01 50.9780	+03 04 22.709	181.8	295.0	11	5	1.2
J0917+4725		09 17 27.0198	+47 25 23.865	7.4	24.7	90	63	110.2
J0920+2714		09 20 45.1428	+27 14 05.620	32.1	157.2	52	36	149.7
J0939+0304	a	09 39 45.1424	+03 04 26.491	137.9	165.3	4	3	101.0
	b	09 39 45.1429	+03 04 26.491	38.1	94.3	15	5	98.7
	c	09 39 45.1459	+03 04 26.485	2.6	49.9	79	20	84.5
	d	09 39 45.1577	+03 04 26.472	9.2	38.5	21	14	118.4
J0945+2640		09 45 30.9555	+26 40 54.063	52.0	205.8	27	13	67.1
J1023+0424	a	10 23 37.5518	+04 24 14.332	29.9	124.4	24	10	135.0
	b	10 23 37.5508	+04 24 13.757	14.1	57.9	19	15	172.1
J1048+3457	a	10 48 34.2480	+34 57 25.042	69.4	203.0	12	4	104.8
	b	10 48 34.2487	+34 57 25.055	27.3	203.5	18	13	73.6
J1125+1953		11 25 55.2424	+19 53 43.699	19.4	100.0	31	16	26.2
J1127+5743	a	11 27 43.7751	+57 43 15.861	187.3	243.5	13	8	18.8
	b	11 27 43.7732	+57 43 15.852	56.7	158.4	31	22	86.7
	c	11 27 43.7144	+57 43 15.669	7.0	21.9	33	24	41.3
J1129+5638	a	11 29 04.1439	+56 38 44.047	80.7	237.7	16	8	158.4
	b	11 29 04.1370	+56 38 44.042	50.4	96.2	9	6	139.8
	c	11 29 04.1343	+56 38 44.056	12.7	61.5	21	12	145.3
J1147+4818	a	11 47 52.2965	+48 18 49.522	9.8	38.2	29	14	103.2
	b	11 47 52.2900	+48 18 49.541	24.0	61.6	21	10	108.7
	c	11 47 52.2868	+48 18 49.538	31.5	98.6	27	10	93.9
	d	11 47 52.2804	+48 18 49.518	20.4	40.7	18	6	72.0
	e	11 47 52.2744	+48 18 49.484	2.9	11.9	44	6	57.4
	f	11 47 52.2783	+48 18 49.375	3.6	20.8	37	19	67.6
J1148+1404	a	11 48 25.4153	+14 04 49.937	9.8	20.4	51	4	119.4
	b	11 48 25.4204	+14 04 49.869	7.9	37.6	106	34	130.8
	c	11 48 25.4474	+14 04 48.424	12.1	19.6	35	10	119.5
J1202+1207	a	12 02 52.0847	+12 07 20.869	20.4	103.0	22	14	83.7
	b	12 02 52.0833	+12 07 20.823	28.4	58.0	18	4	18.1
	c	12 02 52.0844	+12 07 20.781	7.4	21.3	13	11	100.0
	d	12 02 52.0863	+12 07 20.774	17.0	73.6	22	12	124.0
J1238+0845	a	12 38 19.2580	+08 45 01.677	29.2	78.9	41	21	71.3

Table B.4 (continued)

Object	ID	R.A. (hh mm ss.ssss)	Dec. (dd mm ss.sss)	S_p (mJy /beam)	S_{tot} (mJy)	Maj. (mas)	Min. (mas)	P.A. (°)
	b	12 38 19.2596	+08 45 01.660	24.4	53.4	36	17	57.1
	c	12 38 19.2601	+08 45 01.624	11.3	37.8	48	18	172.4
J1312+1710	a	13 12 35.2134	+17 10 55.914	23.0	27.3	8	0	72.2
	b	13 12 35.2125	+17 10 55.905	31.0	103.4	24	7	66.2
	c	13 12 35.2098	+17 10 55.892	12.9	43.6	20	10	97.9
J1345+5846		13 45 38.3909	+58 46 53.462	16.1	70.9	53	18	91.4
J1357+0046	a	13 57 53.7245	+00 46 33.354	390.7	929.4	15	5	46.8
	b	13 57 53.7216	+00 46 33.326	107.2	153.1	6	3	56.5
	c	13 57 53.7201	+00 46 33.298	117.1	449.5	23	9	34.0
J1410+4850	a	14 10 36.0386	+48 50 40.386	52.5	106.2	11	6	38.4
	b	14 10 36.0381	+48 50 40.344	88.1	147.0	9	4	52.3
J1504+6000	a	15 04 09.2075	+60 00 55.711	78.3	528.7	38	12	57.3
	b	15 04 09.2514	+60 00 55.158	45.7	131.1	15	11	175.6
J1523+1332	a	15 23 21.7418	+13 32 29.339	6.2	17.0	32	15	58.2
	b	15 23 21.7302	+13 32 29.113	14.1	27.7	19	14	112.6
	c	15 23 21.7321	+13 32 29.171	4.9	29.1	58	23	89.9
	d	15 23 21.7298	+13 32 29.139	6.7	87.0	92	37	126.6
J1527+3312		15 27 50.8757	+33 12 52.903	45.1	187.3	23	12	170.3
J1548+0808	a	15 48 09.0791	+08 08 34.890	112.5	180.4	43	22	60.7
	b	15 48 09.0730	+08 08 34.661	85.5	135.6	44	16	135.6
J1559+4349	a	15 59 31.2239	+43 49 17.191	27.1	99.9	40	17	99.5
	b	15 59 31.2188	+43 49 17.206	27.3	82.8	35	14	102.5
	c	15 59 31.2140	+43 49 17.197	23.5	66.3	31	15	91.3
	d	15 59 31.1898	+43 49 17.051	4.2	9.1	31	8	57.1
	e	15 59 31.1556	+43 49 16.825	15.5	54.2	42	13	22.6
J1604+6050	a	16 04 27.4134	+60 50 55.197	219.9	257.3	5	4	74.0
	b	16 04 27.4116	+60 50 55.201	208.8	234.5	4	2	108.9
J1616+2647	a	16 16 38.3289	+26 47 01.516	315.3	416.0	8	5	170.4
	b	16 16 38.3288	+26 47 01.505	93.6	255.3	17	11	25.2
	c	16 16 38.3258	+26 47 01.399	148.4	408.3	22	9	19.4
J1633+4700		16 33 15.2092	+47 00 16.321	22.6	107.0	54	45	152.7
J1724+3852	a	17 24 00.5298	+38 52 26.652	82.5	159.1	10	9	76.5
	b	17 24 00.5274	+38 52 26.680	49.2	97.9	17	4	150.0